Scuola Normale Superiore di Pisa

Classe di Scienze

Tesi di Perfezionamento in Methods and Models for Molecular Sciences

XXXV Ciclo

Modeling nanoplasmonics from an atomistic point of view: from theory to applications

Supervisor:
Prof. Chiara Cappelli
Scuola Normale Superiore

Co-supervisor
Dr. Tommaso Giovannini
Scuola Normale Superiore

Luca Bonatti

A.A. 2022-2023

To my parents, my sister and Rudy

Acknowledgements

First of all, I would like to sincerely thank my two supervisors, Prof. Chiara Cappelli and Dr. Tommaso Giovannini. The supervision of Prof. Cappelli has been crucial during the last few years, guiding me both professionally and personally. Her strong determination in scientific research and rigorous academic spirit will have a profound influence on my later life. Thanks to her guidance, I had the opportunity to attend several international conferences, take part in an internship, and participate in stimulating collaborations, which have been fundamental to my professional growth. Dr. Tommaso Giovannini, a great scientist, and friend, patiently helped me every single day. I do not exaggerate when I say that without his contribution during my Ph.D., there would be no results to present in the following of this Thesis.

I count myself very lucky to have been part of the EmbedLab group. For this reason, I want to express very special gratitude to all the best colleagues, and friends, I met during the years: Sara, Sveva, Sulejman, Emanuele, Matteo, Laura, Alessandra, Franco, Linda, Skev and the QED friends. Special thanks are due to the ω-room members: Pablo, Luca, and Piero. Heartfelt thanks go to Gioia and Chiara.

I am also grateful to Prof. Alessandro Tredicucci, Dr. Simone Zanotto, and Prof. Stefano Corni for their invaluable advice and meaningful conversations throughout my Ph.D. studies.

Next, I want to thank all my collaborators at Baker Hughes in Florence. In particular, I would like to express my gratitude to my supervisor, Gianni Orsi, Alberto Babbini, Alberta, and Francesca. Furthermore, I want to thank Dr. Stefania Pizzini for her commitment and invaluable help in organizing my internship at Baker Hughes.

Finally, I want to express my profound gratitude to my parents and my sister Elisa for always providing me with unfailing support and continuous encouragement. I am grateful to all the friends who supported me in this period. Specifically, I would like to thank Achille, Caterina, Lorenzo, Mario, Marco, Loris, Filippo, Gaspare, Valeria, Gwydyon, Luce, Matias, Daniele, Flavio and Spada, the best publisher ever.

I would like to thank everyone who helped me throughout my Ph.D., and I apologize to those who I might have forgotten to name here.

List of Publications

Attached Papers

1. Plasmonic resonances of metal nanoparticles: atomistic vs. Continuum approaches
   L. Bonatti, G. Gil, T. Giovannini, S. Corni, and C. Cappelli, *Front. Chem.*, **2020**, *8*, 340.

2. *In silico* design of graphene plasmonic hot-spots
   L. Bonatti,, L. Nicoli, T. Giovannini, and C. Cappelli, *Nanoscale Adv.*, **2022**, *4*, 2294-2302.

3. Strain-induced plasmon confinement in polycrystalline graphene
   S. Zanotto, **L. Bonatti**, F. M. Pantano, V. Mišeikis, G. Speranza, T. Giovannini, C. Coletti, C. Cappelli, A. Tredicucci, and A. Toncelli, *ACS Photonics*, **2023**, *10*, 394-400.

4. Do we really need quantum mechanics to describe plasmonic properties of metal nanostructures?
   T. Giovannini, **L. Bonatti**, P. Lafiosca, L. Nicoli, M. Castagnola, P. Grobas Illobre, S. Corni, and C. Cappelli, *ACS Photonics*, **2022**, *9*, 3025-3034.

5. QM/Classical Modeling of Surface Enhanced Raman Scattering Based on Atomistic Electromagnetic Models
   P. Lafiosca, L. Nicoli, **L. Bonatti**, T. Giovannini, S. Corni, and C. Cappelli, *under revision*.

Other papers not included in the Thesis

6. Graphene plasmonics: Fully atomistic approach for realistic structures
   T. Giovannini, **L. Bonatti**, M. Polini, and C. Cappelli, *J. Phys. Chem. Lett.*, **2020**, *11*, 7595-7602.

7. Fully Atomistic Modeling of Plasmonic Bimetallic Nanoparticles: Nanoalloys and Core-Shell Systems L. Nicoli, P. Lafiosca, P. Grobas Illobre, **L. Bonatti**, T. Giovannini, and C. Cappelli, *submitted*.

Contents

Chapter 1

Introduction

The aim of this thesis is the development of a fully atomistic classical model able to describe the plasmonic properties of metal nanomaterials and graphene, and how such plasmonic substrates can interact with a target molecule adsorbed on their surfaces, by enhancing the properties of the molecule itself. The interest in plasmonics,[1,2] a sub-discipline of photonics, derives from the opportunity to manipulate light via the surface plasmon polaritons (SPPs), the quanta of energy involved in the collective oscillations of valence electrons inside conducting materials.[3–6] Indeed, the increase in the control over the spectral and spatial properties of SPPs is responsible for huge advances in several fields of application, for example, photovoltaics,[7,8] nanoscale photometry and antennas,[9–11] improvement in imaging resolution,[12] quantum information devices,[13,14] cancer therapy[15,16] and, more in general, in biology and biomedicine.[17–19] Another field of application in which plasmons have a pivotal role, and that will be dealt with in detail in this thesis, is biosensing.[20,21]
In particular, surface-enhanced spectroscopies, like the Surface Enhanced Raman Scattering (SERS) technique,[22,23] are able to realize an ultrasensitive detection up to single-molecule level. These approaches rely on spatial confinement and, in turn, on the enhancement of light arising in the proximity of very confined regions of the metallic substrate, called *hot spots*.[24–30] When a target molecule interacts with the enhanced electric field, its properties are enhanced in turn, allowing its detection. The confinement of light that can be achieved in SERS experiments is extreme: light is typically caught in volumes of tens of nanometers (i.e. nanocavities), well beyond the diffraction limit.[24,31]

During the last decades, many efforts have been devoted to the development of particular geometrical arrangements of noble metal nanostructures to trap the light in a more efficient way, by allowing a more accurate detection of the analyte. As a result, to date light can be localized in volumes with a size below 1 nanometer (i.e. picocavities), allowing for the investigation of a single target molecule at the atomic scale.[27,32,33] To achieve picocavities, several engineered designs of the experimental setup can be exploited. For instance, in Tip Enhanced Raman Spectroscopy (TERS),[27,28,34,35] the picocavity is obtained by approaching the apex of a metallic tip to a metallic substrate, whereas in the nanoparticle-on-mirror (NPoM) arrangement,[32] the picocavity originates between a metal nanoparticle (NP) and a planar substrate (the mirror), that are separated by a molecular spacer, such as a

self-assembled monolayer (SAM) of biphenyl-4-thiol.[29,32,36]

Over the last decades, research has been focused mainly on noble metal plasmonics, that is today the cornerstone for the development of new plasmonic structures and gives, at the same time, the theoretical background to understand new optical phenomena involving nanostructured materials.[3,37] More recently, the interest of researchers has focused on graphene, a two-dimensional carbon-based material in which atoms are organized in a honeycomb lattice.[38–40] Graphene presents unique electronic, mechanical, and thermal properties, and has emerged as an alternative plasmonic material for its outstanding optical properties,[41–44] which are exploited in several technological applications, ranging from optoelectronic devices[42] to photodetection applications[45,46] and metamaterials design.[47] Graphene-based substrates have been used to realize surface-enhanced spectroscopies (Graphene enhanced Raman Spectroscopy, GERS),[48–51] allowing for the detection of the spectroscopic signals of several molecules. However, the electric field enhancement obtained in GERS is smaller as compared to the case of noble metal plasmonic substrates.[52]

The experimental achievements obtained for noble metals and graphene plasmonics have benefited from the development of theoretical methods, ranging from classical (atomistic or continuum) to purely *ab initio* methods, capable of describing the optical properties of plasmonic substrates.[53–57] Real-size systems are usually described by means of the Mie theory,[58,59] the Discrete Dipole Approximation (DDA),[60] the electromagnetic Finite Difference Time Domain (FDTD)[61,62] or the Boundary Element Method (BEM).[63–71] However such methods are based on classical electrodynamics principles and may fail when quantum effects play a substantial role, such as in the case of nanojunctions.[24,72] Also, the description of nanostructured surfaces by means of implicit methods becomes very challenging when the surfaces are characterized by atomically defined details and edges.[73,74] Both effects are correctly described by first-principle methods, for instance, the Tight Binding (TB),[57,75,76] Density Functional Theory[77] and its time-dependent counterpart (TD-DFT) approaches.[27,54,55,78–86] However, due to their high computational cost, such methods are limited to systems of a few thousand of atoms.[55]

In this context, classical, yet atomistic models have recently gained popularity as they can predict results close to *ab initio* methods while being computationally efficient and thus able to model real-sized systems.[87–93] Specifically, in recent years, a classical, fully atomistic model, called ωFQ[92] has been developed by the research group I joined during my Ph.D. experience. ωFQ extends the Fluctuating Charge (FQ) approach originally developed for bulk solutions[94–97] to the case of absorbing environments. In fact, ωFQ[92] extends the FQ formalism so as to describe the interaction of a plasmonic substrate with an oscillating external electric field. To this end, the charge interaction between the atoms of the nanostructure is modeled in terms of electric conduction between nearest neighbors via a simple Drude mechanism,[98] which is modulated by a Fermi-like step function that mimics quantum tunneling effects.[92] Within this approach, the optical properties of sodium nanoparticles (NPs) characterized by single atom junctions have been investigated, yielding almost perfect agreement with *ab initio* methods. During my master's Thesis, I extended the ωFQ model to describe the optical properties of 2D materials, such as graphene-based

nanostructures.[93] In particular, we have demonstrated the ability of ωFQ to describe plasmons arising in graphene samples with complex shapes and how they can be tuned by varying the Fermi energy of the system.[93]

In this Thesis, the ωFQ extensions performed during my Ph.D. research activity are discussed. The theoretical advancements have focused on two main lines: (i) the extension of ωFQ to model the optical properties of noble metal NPs (ωFQFμ), which are characterized by interband effects;[99] (ii) the coupling between a molecular system, treated at the QM level, and a plasmonic substrate, described by means of ωFQ(Fμ) models.[100] Additionally, ωFQ has been amply tested against the calculation of the optical properties of metallic and graphene-based nanostructures with complex geometries such as nanocavities, tips, and surfaces with defects, demonstrating its potential as compared to continuum and *ab initio* models.[93,101,102]

The Thesis is organized as follows. Chapter 2 provides an introduction to the theoretical fundamentals of plasmonics. It focuses on the interband contribution to the optical properties of metals, the electronic properties of graphene, and the electromagnetic enhancement mechanism underlying surface-enhanced spectroscopies. Chapter 3 provides an overview of the most popular theoretical models for nanoplasmonics. The chapter also specifically focuses on the ωFQ model, providing its theoretical derivation and discussing its extension for the correct description of graphene. Finally, Chapter 4 highlights the most important results of the papers included in this Thesis, which are attached in the next chapters (Chapters 5-9). Summary, conclusions, and future perspectives end the Thesis.

Chapter 2

Introduction to Plasmonics

In this chapter, the physical origin of plasmons is presented, starting with a discussion of the basic optical properties of metals and graphene-based nanostructures. The treatment of plasmons arising in metallic nanostructures is mainly drawn from Ref. 3 and 103, while the discussion concerning graphene plasmonics is primarily taken from Refs. 104, 105 and 44. Finally, selected plasmonic physical properties, such as plasmon confinement and near electric field enhancement, which is currently leveraged in surface-enhanced spectroscopies, are discussed.

2.1 Optical properties of metals

The optical properties of bulk metals are determined by their band structure. In metals, the valence and conduction bands overlap and can be partially filled under a certain value of the Fermi energy E_F. Free conduction electrons can move across the sample through intraband transitions, while bound electrons can be excited through interband transitions from the valence to the conduction band. The Drude model[98] provides a classical description of the motion of free carriers in intraband transitions and accurately reproduces the optical properties of metals over a wide range of frequencies. However, the Drude model fails to describe the optical properties of metals that are strongly affected by interband transitions. In addition, when defects, such as grain boundaries, affect the conduction of free carriers, back-scattering processes must be included in the Drude approach to correctly describe experimental observations.[106]

According to the Drude model, the motion of a free valence electron (negatively charged point particle) with respect to its nucleus (positive ion core) under the effect of an external time-dependent electric field $\mathbf{E}(t)$ can be described as the motion of a free carrier under the effect of a driving force $\mathbf{F}_{dri}$, which is expressed as:

$$\mathbf{F}_{dri} = -e\mathbf{E}(t) = -e\mathbf{E}_0 e^{-i\omega t} \tag{2.1}$$

where e is the universal charge constant, ω is the angular frequency of the incident electric field and $\mathbf{E}_0$ is the amplitude of the external radiation. The motion of an electron with respect to a positive ion core is described by the following equation:

$$\mathbf{F}_{dri} = m\frac{\partial \mathbf{r}^2}{\partial t^2} + m\gamma\frac{\partial \mathbf{r}}{\partial t} + m\omega_0^2\mathbf{r} \tag{2.2}$$

where m is the effective mass of the electron inside the material and γ is a damping term accounting for collisions between free charges and positive ion cores. The interaction between electron and nucleus can be classically described by the quadratic potential with a resonance frequency of ω_0 and a displacement from the equilibrium position equal to $\mathbf{r}$. According to the Drude model, only free (i.e. not bounded) electrons take part in the electric conduction across the metal. For this reason, the resonant term in Eq. 2.2 is neglected, and the damping term is defined as $\gamma = \frac{1}{\tau}$, where τ is the time between two subsequent collisions of a free valence electron with other carriers and ion cores. Consequently, Eq. 2.2 can be rewritten as:

$$\mathbf{F}_{dri} = -e\mathbf{E_0}e^{-i\omega t} = m\frac{\partial \mathbf{r}^2}{\partial t^2} + m\gamma\frac{\partial \mathbf{r}}{\partial t} \tag{2.3}$$

In order to obtain an expression for $\mathbf{r}(t)$ as a function of time, Eq. 2.3 is solved by using the ansatz $\mathbf{r}(t) = \mathbf{r}_0 e^{-i\omega t}$:

$$\mathbf{r}(t) = \frac{e}{m(\omega^2 + i\gamma\omega)}\mathbf{E}(t) \tag{2.4}$$

The polarization vector $\mathbf{P}$ can be defined as the product between the unit charge and the displacement vector between charges of opposite sign (i.e., from the negative electron to the positive nucleus), i.e.:

$$\mathbf{P} = -ne\mathbf{r}(t) \tag{2.5}$$

By substituting Eq. 2.3 in Eq. 2.5, $\mathbf{P}$ reads:

$$\mathbf{P} = -\frac{ne^2}{m(\omega^2 + i\gamma\omega)}\mathbf{E} \tag{2.6}$$

The dielectric displacement $\mathbf{D}$ for inhomogeneous media can be defined as $\mathbf{D} = \epsilon_0\mathbf{E} + \mathbf{P}$, in which ϵ_0 ($\approx 8.854 \cdot 10^{-12}$ F/m) is the electric permittivity of vacuum. $\mathbf{D}$ can be rewritten as follows:

$$\mathbf{D} = \epsilon_0\left(1 - \frac{\omega_p^2}{\omega^2 + i\gamma\omega}\right)\mathbf{E} \qquad \omega_p = \sqrt{\frac{ne^2}{m\epsilon_0}} \tag{2.7}$$

where ω_p is the bulk plasma frequency, i.e. the resonance frequency of the collective oscillations of the free-electron gas. In Eq. 2.7, the complex-valued dielectric constant $\epsilon(\omega)$ of the free electron gas appears. It can be defined as:

$$\epsilon(\omega) = 1 - \frac{\omega_p^2}{\omega^2 + i\gamma\omega} \tag{2.8}$$

The dielectric function acquires a key role in the description of the optical behavior of metals because, once it is defined, all the other optical quantities can be fully determined.[3]

2.1.1 Interband transitions

The Drude model fails in the description of the optical properties of metals in the ultraviolet-visible (UV-VIS) spectral range, in which interband transitions strongly affect the response. This limitation is especially true in the case of $d-$ metals, such as silver and gold, whereas interband effects have a negligible role in the case of alkali metals. As an example, Fig. 2.1 presents the real (ϵ_1) and imaginary (ϵ_2) parts of the dielectric function of silver, represented by green dots in panels (a) and (b), respectively, across the entire spectrum.[107] It is worth noting that in the high-frequency range ($>$ 3.5 eV), the Drude model fails to capture the observed behavior of silver (indicated by the deviation from the Drude Fit line in Fig. 2.1-a,b).

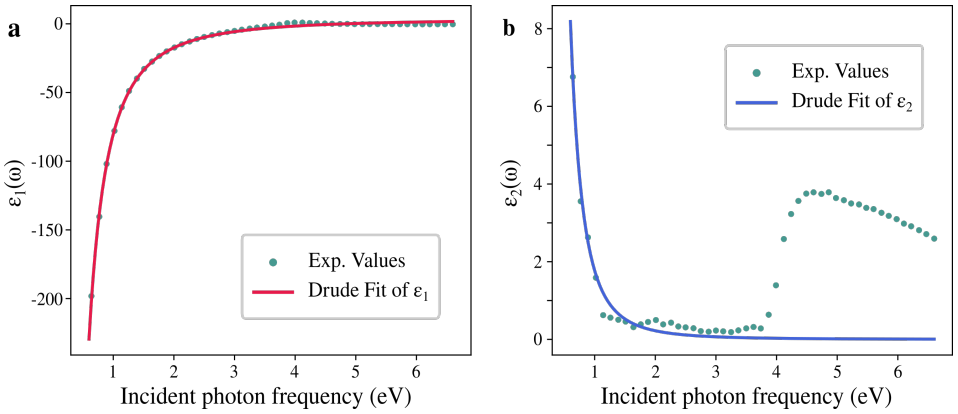

Figure 2.1. Comparison between the experimental values (green dots reproduced from Ref. 107) and the trends of the Drude model based on the fitting of the experimental values of ϵ_1 (**a**) and ϵ_2 (**b**) for silver.

It has been demonstrated[108–110] that the dielectric function $\epsilon(\omega)$ can be expressed as:

$$\epsilon(\omega) = \epsilon^{intra}(\omega) + \epsilon^{inter}(\omega) \tag{2.9}$$

where the contributions of intraband (ϵ^{intra}, free-electrons) and interband effects (ϵ^{inter}, bound-electrons) are explicitly separated. The intraband part can be described by the Drude model,[111] whereas a possible strategy to model interband transition is offered by the Lorentz model for dielectrics.[3,110,112] By resolving Eq. 2.2 with the same procedure described above in the case of the Drude model, but without neglecting the electron-nucleus interaction term, a new relation describing the dielectric function can be obtained:

$$\epsilon(\omega) = 1 + \frac{\omega_p^2}{\omega_0^2 - \omega^2 - i\omega\gamma} \tag{2.10}$$

where ω_0 is the natural frequency of the spring-like potential, which is used to model the interaction between a bound electron and the positive ion core. Eq. 2.10 can be generalized by taking into account higher orders of interband transitions, written in terms of Lorentz's oscillators:

$$\epsilon(\omega) = 1 + \sum_{m}^{K} \frac{f_m \omega_p^2}{\omega_m^2 - \omega^2 - i\omega\gamma_m} \tag{2.11}$$

where K is the total number of oscillators with frequency ω_m. $1/\gamma_m$ and f_m are the lifetime and the weighting coefficient related to the m-th oscillator, respectively.

Although the Lorentz model takes into account the contribution of bound electrons to the dielectric permittivity, it completely neglects the free electrons' motion related to intraband transitions. Thus, in order to model the optical properties of metals across the whole spectrum of frequencies, the contribution of both bound and free electrons has to be considered. A possible strategy to include both the intraband and interband effects on $\epsilon(\omega)$ relies on the union of the dielectric functions obtained with the Drude (see Eq. 2.8) and Lorentz (see Eq. 2.11) models respectively. This concept is at the basis of the so-called Lorentz-Drude (LD) formalism, in which the global dielectric function $\epsilon_{LD}(\omega)$ is expressed as:

$$\epsilon_{LD}(\omega) = 1 - \frac{\Omega_p^2}{\omega^2 + i\gamma\omega} + \sum_{m}^{K} \frac{f_m \omega_p^2}{\omega_m^2 - \omega^2 - i\omega\gamma_m} \tag{2.12}$$

where $\Omega_p = \sqrt{f_0}\omega_p$ is the plasma frequency associated with intraband transitions with oscillator strength f_0 and damping constant γ_0.[110]

Although the LD model is effective in reproducing experimental data for the dielectric functions of metals like aluminum and transition metals, it requires additional refinement to accurately handle noble metals.[110] Noble metals present a unique challenge because their optical properties are defined by several interband transitions, which require a large number of oscillators for proper characterization. Lorentz oscillators, which are typically used in the LD model, may not be adequate to describe the broadening of the dielectric function in noble metals, and Gaussian lineshapes may be a more suitable alternative.[110,113] This limitation is particularly significant for noble metals, and as an example, Fig. 2.2 demonstrates the LD model's performance by using Lorentzian oscillators (until the 4-th oscillator) in reproducing dielectric functions for aluminum and silver, along with their corresponding experimental values.

To address this problem, several approaches have been proposed in the past. For example, the Brendel-Bormann (BB) model,[113] which replaces Lorentzian oscillators with a superposition of an infinite number of Gaussian functions, has been suggested. More recently, the parametrization presented by Gharbi *et al.*[114] has also been proposed as a solution.

In parallel to the LD model, the optical properties of noble metals can be also analyzed by means of analytic models. In this scenario, the complex dielectric function of a metal in a certain frequency domain is described via a minimal set of parameters, explicitly tuned to obtain the best fit with the experimental data. As an example, Etchegoin *et al.*[115,116] proposed an analytic function accounting for both the Drude and interband contributions to the dielectric function of gold. Input parameters were fitted and compared to the experimental data reported by Johnson and Christy.[107]

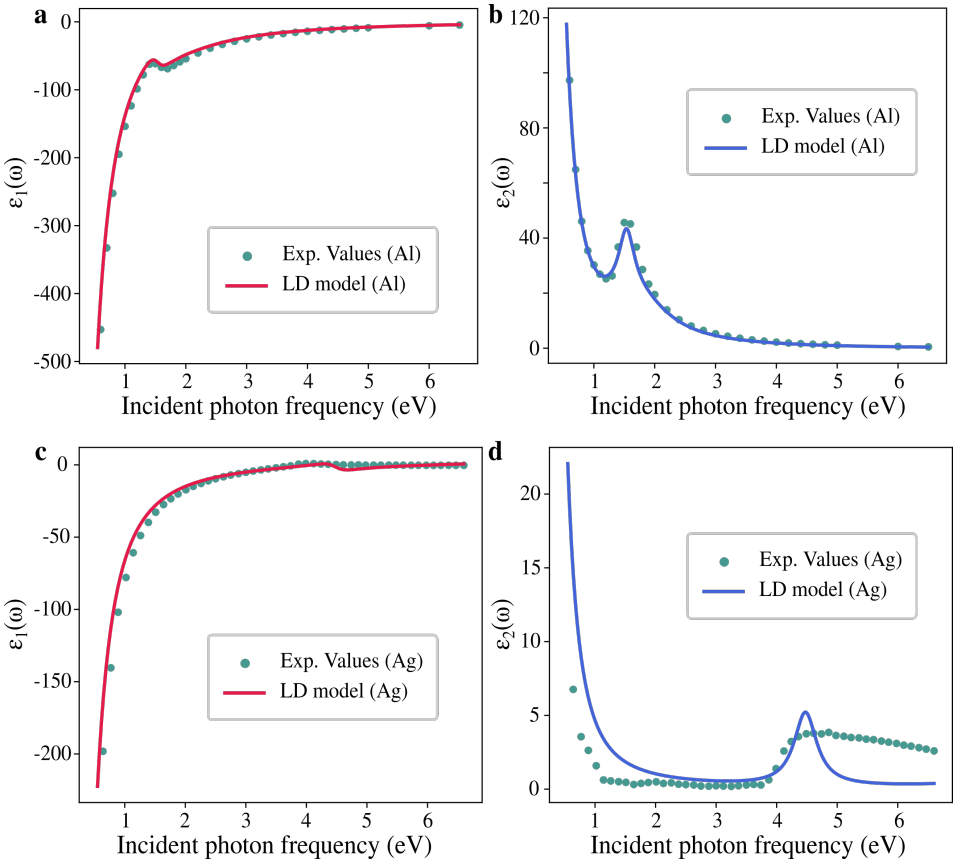

Figure 2.2. Comparison between the experimental data (green dots, reproduced from the Ref. 107) and the LD model fits for the real (ϵ_1) and imaginary (ϵ_2) parts of the dielectric function for aluminum (**a**-**b**) and silver (**c**-**d**) respectively.

2.1.2 Conductivity and Drude-Smith model

The expression of the displacement $\mathbf{r}(t)$ as a function of time (see Eq. 2.4), obtained from the Drude equation of motion in Eq. 2.3 reads:

$$\mathbf{r}(t) = \frac{e\tau}{m\omega(i+\omega\tau)}\mathbf{E}(t) \tag{2.13}$$

where $\tau = \gamma^{-1}$. From Eq. 2.13, the free electrons (intraband) contribution to the current density $\mathbf{J}$ reads:

$$\mathbf{J} = -ne\dot{\mathbf{r}}(t) = -ne(-i\omega)\mathbf{r}e^{-i\omega t} = \frac{ne^2\tau}{m}\frac{1}{1-i\omega\tau}\mathbf{E}e^{-i\omega\tau} \tag{2.14}$$

Thus, the contribution of the intraband part to the conductivity $\sigma(\omega)$ can be expressed as:

$$\sigma(\omega) = \sigma_0\frac{1}{1-i\omega\tau} \qquad \sigma_0 = \frac{ne^2\tau}{m} = \frac{\tau}{4\pi}\omega_p^2 \tag{2.15}$$

where σ_0 is the static conductivity (i.e. the value of conductivity when $\omega = 0$).
The real part of conductivity (see Eq. 2.15) exhibits a maximum at zero frequency, corresponding to the static conductivity σ_0, and decays with a Lorentzian shape by increasing the frequency. On the other hand, the imaginary part of conductivity vanishes at $\omega = 0$ and

shows a maximum at low frequencies. Then it slowly decreases to zero by increasing the frequency with a Lorentzian lineshape.

The Drude model provides a good representation of the conductivity of bulk metals, but breaks down when structural defects characterize the metal geometry.[106,117,118] In fact, when the disorder level in the sample increases, anisotropic scattering events may occur (even back-scattering events), leading to a non-Drude behavior of the conductivity. To address this issue, the Drude-Smith model was developed as an extension of the classical Drude model, specifically designed to describe materials where defects and grain boundaries have a strong impact on carrier transport.[106] The Drude-Smith equation for the conductivity reads:

$$\sigma(\omega) = \frac{ne^2\tau_{DS}}{m}\frac{1}{1-i\omega\tau_{DS}}\left(1+\sum_{p=1}^{\infty}\frac{c_p}{(1-i\omega\tau_{DS})^p}\right) \tag{2.16}$$

where τ_{DS} is the Drude–Smith transport relaxation time that, in principle, may be different from the Drude scattering time τ.[106] c_p is known as the *persistence of velocity* parameter and it defines the fraction of the carrier's initial velocity maintained after the p-th scattering event. The Drude-Smith model employs a single-scattering approximation, whereby each electron scatters only once and retains its initial velocity for the first collision only (i.e. $c_p > 0$ if $p > 1$).[106]

By applying such approximation to Eq. 2.16, the Drude-Smith equation becomes:

$$\sigma(\omega) = \frac{ne^2\tau_{DS}}{m}\left(1+\frac{c}{1-i\omega\tau_{DS}}\right) \tag{2.17}$$

where the c parameter is constrained between 0 and -1, and its value depends on the level of anisotropy of the system, as reported for the real part of conductivity σ_1 in Fig. 2.3. In particular, if $c = 0$, the isotropic scattering condition is recovered and the expression for σ_1 assumes a Drude-like form (see Fig. 2.3). As the value of c decreases, the electrons become increasingly confined within specific regions of the sample (such as grains of the metal), leading to a decrease in the static conductivity and a shift of the conductivity's peak towards higher frequencies. Specifically, when $-1 < c < 0$, backward scattering events occur in the sample, while for c = -1, the static conductivity is equal to zero and a distinct peak emerges, indicating a loss of the Drude-like behavior due to backscattering events (see Fig. 2.3)[106]

In the case of grain boundaries, complete charge trapping between the edges of the grains can lead to localization effects, causing opposite-sign charges to crowd the grain boundaries and form confined plasmons. Although the Drude-Smith model yields results in good agreement with experimental findings,[118] the single-scattering approximation lacks a clear physical interpretation.[119,120] For this reason, several theoretical models have been proposed in the past to provide a more physical interpretation of the Drude-Smith conductivity, trying to return a comprehensive explanation of the behavior of electrons under back-scattering events and extreme confinement.[120,121]

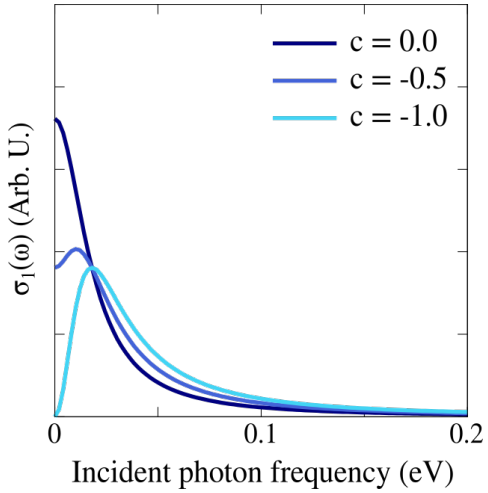

Figure 2.3. Drude-Smith $\sigma_1(\omega)$ trends for different values of the c parameter. The plot is obtained by using the parameters for silver reported in Ref. 122, which are equal to ω_p = 9.01 eV and $\gamma = \hbar/\tau$ = 0.018 eV.

2.2 Plasmons

Plasmons are the quanta of collective oscillations of the free-electron gas in metals. They are triggered when an external oscillating electric field matches their plasmon resonance frequency (PRF) and arise at the interface between a metal and a dielectric medium.
In this section, the physical properties of localized surface plasmons are discussed. Particular attention is paid to localized plasmons in noble metal nanoparticles (NPs), including their theoretical derivation and various applications for fine-tuning the PRF by adjusting the size and shape of the NPs.

2.2.1 Localized Surface Plasmons (LSPs)

Localized surface plasmons (LSPs) are non-propagating oscillations of the free-electron gas in metal nanostructures, like metal NPs, interacting with an external electromagnetic field. As the electric field polarizes the electron cloud, opposite charges accumulate at the ends of the nanostructure, leading to a restoring force that drives a collective oscillation of the free conduction electrons on the surface of the nanomaterial (see Fig. 2.4).
LSPs govern the optical properties of metal NPs in the visible (VIS) and near-infrared (NIR) frequency ranges. In particular, they determine the absorption frequency of the system and enable the tuning of the absorption frequency by adjusting the shape, size, and chemical composition of the nanomaterial.[53] The physics of LSPs can be easily understood by solving the scattering problem of a small metal NP dived into an oscillating electric field. To this end, a homogeneous metallic sphere of radius R and permittivity $\epsilon_m(\omega)$, placed in the origin $O\,(x, y, z = 0)$ of the system and surrounded by a dielectric medium, with dielectric function ϵ_d, can be considered. The Laplace equation can be solved and, by imposing the proper boundary conditions, the inner and outer potentials can be computed (see for instance Ref. 3 and Ref. 123).

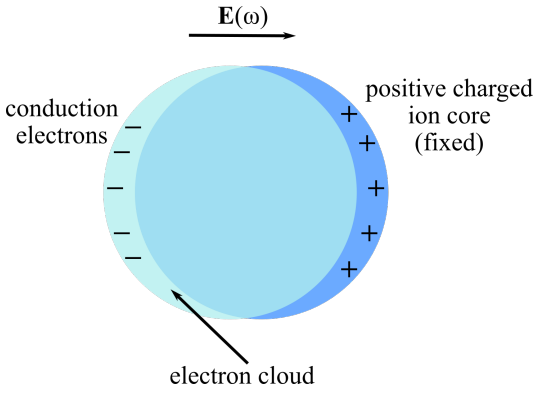

Figure 2.4. Dipolar plasmon oscillations confined on the surface of a metal NP. The shift of the electron cloud under the effect of an external electric field is highlighted.

An important result of this description is that, for spherical metal NPs, the PRF is related to the plasma frequency by means of the following relation:[3]

$$\omega_{PRF} = \frac{\omega_p}{\sqrt{3}} \tag{2.18}$$

The PRF can be evaluated by calculating the absorption cross section C_{abs} of the NP:[3]

$$C_{abs} = \frac{4\pi}{c}\omega R^3 Im\left[\frac{\epsilon_m - \epsilon_d}{\epsilon_m + 2\epsilon_d}\right] = \frac{4\pi}{c}\omega Im(\alpha) \tag{2.19}$$

Eq. 2.19 shows that the absorption cross-section only depends on the imaginary part of the isotropic polarizability of the NP (α) and on the frequency of the incident electric field and, remarkably, C_{abs} does not depend on the size of the metal NP. The expression for the scattering cross section C_{sca} instead reads:[3]

$$C_{sca} = \frac{8\pi}{3c^4}\omega^4 R^6 \left|\frac{\epsilon_m - \epsilon_d}{\epsilon_m + 2\epsilon_d}\right|^2 \tag{2.20}$$

Notice that, due to scaling of C_{sca} (see Eq. 2.20) with respect to the radius of the sphere (i.e. R^6), the absorption process (R^3) generally dominates over the scattering (R^6) for small size spheres. For this reason, the scattering cross-section can be neglected in the calculation of the extinction cross-section C_{ext}, which is obtained by summing up the C_{sca} and C_{abs}.

2.3 Graphene plasmonics

Graphene[38,39,124] is certainly the carbon allotrope[125–127] with the most interesting physical properties, which fueled to impressive scientific advances in several technological sectors.[128] Graphene has a 2D monolayer structure, like a single atomic plane extracted from a sample of graphite or as an unrolled single-wall carbon nanotube. Graphene's most peculiar property is its 2D p_z electron gas, which follows a linear dispersion relation similar to the behavior of relativistic massless Dirac fermions. This has significant implications for the electronic states, transport, and optical properties of the material.[104] In this section, the optical properties of graphene and its band structure are introduced, followed by an examination

of plasmons arising in graphene sheets, with a particular focus on their localization within graphene nanostructures.

2.3.1 Electronic properties of graphene

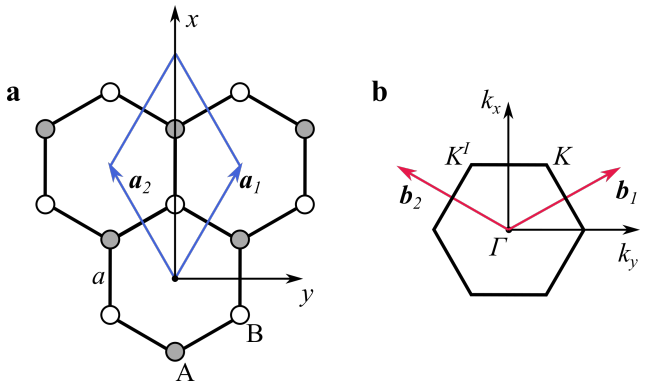

Figure 2.5. Crystalline structure of graphene in the real (**a**) and reciprocal (**b**) space respectively. The unit cell and the primitive vectors are highlighted in blue (**a**), whereas the primitive reciprocal vectors in the Brillouin zone are in red (**b**). Grey and white dots highlight the A and B triangular sublattices respectively, forming the final honeycomb lattice.

The primitive translation vectors of the unit cell in graphene are (see the blue vectors in Fig. 2.5-a):

$$\mathbf{a_1} = \frac{a}{2}(3, \sqrt{3}) \qquad \mathbf{a_2} = \frac{a}{2}(3, -\sqrt{3}) \tag{2.21}$$

where $a \approx 1.42$ Å is the carbon-carbon distance (see Fig. 2.5-a). In this way, the structure is represented as a superposition of two triangular sublattices A (grey dots) and B (white dots), with a basis made of two atoms per unit cell, one from each sublattice (see Fig. 2.5-a). In the momentum space, the primitive reciprocal vectors ($\mathbf{b}_1$, $\mathbf{b}_2$) and the coordinates for the high symmetry points (K,K') are given by Eq. 2.22a and 2.22b respectively (see Fig. 2.5-b).

$$\mathbf{b_1} = \frac{2\pi}{3a}(1, \sqrt{3}) \qquad \mathbf{b_2} = \frac{2\pi}{3a}(1, -\sqrt{3}) \tag{2.22a}$$

$$K = \left(\frac{2\pi}{3a}, \frac{2\pi}{3\sqrt{3}a}\right) \qquad K' = \left(\frac{2\pi}{3a}, -\frac{2\pi}{3\sqrt{3}a}\right) \qquad \Gamma = (0,0) \tag{2.22b}$$

where the K and K' point of the Brillouin zone are called Dirac points, and Γ is the center of the first Brillouin zone.

Although electrons in graphene exhibit a behavior similar to massless Dirac fermions, their dispersion relation can be studied by using simple models from solid state physics, such as the Tight Binding (TB) model.[129] Within the TB approach, the Hamiltonian for electrons in graphene can be written as (in atomic units):[104]

$$H = -t \sum_{\langle i,j \rangle, s} a^{\dagger}_{s,i} b_{s,j} + b^{\dagger}_{s,j} a_{s,i} - t' \sum_{\langle\langle i,j \rangle\rangle, s} (a^{\dagger}_{s,i} a_{s,j} + b^{\dagger}_{s,i} b_{s,j} + \text{H.c.}) \tag{2.23}$$

where $a^{\dagger}_{s,i}(a_{s,i})$ creates(annihilates) an electron of spin $s = (\uparrow, \downarrow)$ on the atomic site i of the sublattice A, whereas $b^{\dagger}_{s,i}(b_{s,i})$ creates(annihilates) an electron of spin s on the atomic site i of the sublattice B. In eq. 2.23, H.c. represents the Hermitian conjugated. The t parameter is equal to 2.8 eV and it represents the nearest-neighbor hopping energy, accounting for the hopping energy between atoms of different sublattices, whereas t' is a parameter describing the new-nearest-neighbor hopping parameter energy, returning the interaction between carbon atoms within the same sublattice ($t' \approx 0.1$ eV,[130] see Fig. 2.5-a). The energy dispersion relation derived from the Hamiltonian in Eq. 2.23 reads:[129]

$$E_{\pm}(\mathbf{k}) = \pm t \sqrt{3 + f(\mathbf{k})} - t' f(\mathbf{k}) \tag{2.24}$$

where $\mathbf{k}$ is the wave vector across the plane and $f(\mathbf{k})$ is defined as:

$$f(\mathbf{k}) = 2cos(\sqrt{3} k_y a) + 4cos\left(\frac{\sqrt{3}}{2} k_y a\right) cos\left(\frac{3}{2} k_x a\right) \tag{2.25}$$

in which the + and - signs are applied to the upper and lower $\pi^*(\pi)$ bands respectively. By expanding Eq. 2.25 close to the Dirac point (i.e. by substituting $\mathbf{k} = \mathbf{K} + \mathbf{q}$, with $\mathbf{q} \ll \mathbf{K}$ in Eq. 2.25), Eq. 2.24 becomes:[104]

$$E_{\pm}(\mathbf{q}) \approx v_F |\mathbf{q}| + O\left(\frac{q}{K}\right)^2 \tag{2.26}$$

where $\mathbf{q}$ is the momentum at the Dirac points and v_F is the Fermi velocity ($v_F \approx 10^6$ m/s).[42,44,104,131] Therefore, the energy band's profile near the K or K' points of the Brillouin zone shows a linear trend, as illustrated in Fig. 2.6. This linear trend has a conical shape throughout the entire reciprocal space. At the Dirac points, which correspond to the K-points of the Brillouin zone, the tips of the valence and conduction cones meet, forming what is known as Dirac cones.

The electron mass m^* is defined by the linear dispersion relation of massless Dirac fermions as:

$$m^* = \frac{1}{2\pi} \left[\frac{\partial A(E)}{\partial E}\right]\Bigg|_{E=E_F} \tag{2.27a}$$

$$A(E) = \pi \frac{E_F^2}{v_F^2} \tag{2.27b}$$

where $A(E)$ is the area in the momentum space enclosed by the orbit of electron. By substituting the definition for $A(E)$ in Eq. 2.27a, m^* reads:

$$m^* = \frac{\sqrt{\pi n}}{v_F} \tag{2.28}$$

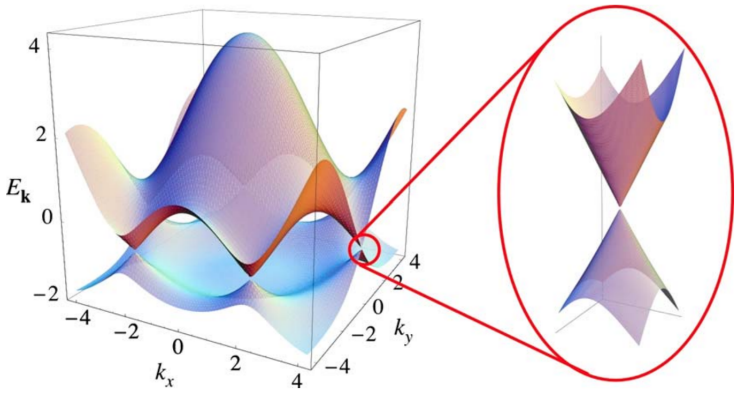

Figure 2.6. TB electronic dispersion relation in graphene obtained with $t = 2.7$ eV, and $t' = 0.2t$. The dispersion of the energy bands close to one of the Dirac points is highlighted. The image is reprinted with permission from Ref. 104. Copyright 2009 American Physical Society.

where the Fermi momentum is defined as $k_F = \sqrt{\pi n}$[132] and n is the surface electronic density. It is worth noting that, in contrast to the electron density for a metallic slab (see Eq. 2.7), the electron density of graphene is defined as a 2D quantity. In particular, the dependence $m^* \approx \sqrt{n}$ is a characteristic feature of the 2D electron gas in graphene and differs significantly from the constant mass obtained for the conventional parabolic dispersion. Furthermore, the electron density and, in turn, the cyclotron mass is related to the Fermi level through the following expression:[42,133]

$$E_F = \hbar v_F \sqrt{n\pi} \tag{2.29}$$

Because of the relation reported in Eq. 2.29, chemical doping and electric gating strongly affect the optical properties of graphene because they can move E_F upwards or downwards across the bands. Depending on the value of E_F, interband transitions in graphene can be forbidden or allowed according to the so-called Pauli blocking phenomenon.[44,105]

2.3.2 Localized plasmons in graphene

In graphene, localized plasmons are created when the system is geometrically confined, as in the case of graphene nanodisks[134,135] or graphene nanoribbons (GNRs).[136] GNRs, in particular, are excellent substrates for studying the confinement of free carriers in graphene due to their strong sensitivity to the polarization of the incident electric field (see Fig. 2.7-a,b). Consequently, the behavior of free electrons in GNRs can be confined or unconfined, depending on the width between the two opposite sides of the structure.

Fig. 2.7-a shows that when the incident electric field is polarized parallel to the ribbon's main length (i.e. along the y-axis, see Fig. 2.7-a), the electric response for the 2D electron gas (2DEG) in GNRs follows a Drude-like behavior, indicating that charges can freely move across the sample along that direction. However, when the incident light direction is perpendicular to the ribbon's main length (i.e. oriented along the x-axis in Fig. 2.7-a), the absorption peak exhibits a Lorentzian lineshape resulting from plasmon's oscillations

(see Fig. 2.7-b). Thus, GNRs host localized plasmons on their narrowest side. The same Lorentzian lineshape can also be observed in other graphene nanostructures, such as graphene nanodisks. In this case, because of the isotropic geometry of disks, free electrons are confined in all spatial directions, independently of the polarization of the incident electric field.[134]

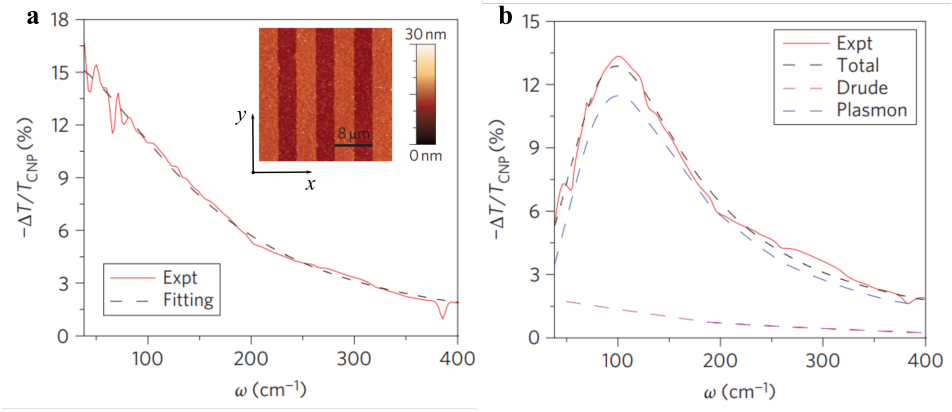

Figure 2.7. Absorption spectra for a GNRs array for an incident light polarized parallel (**a**, along the y axes) and perpendicular (**b**, along the x axis) to the ribbons main length, respectively. (**a**) Absorption spectrum for GNRs (red line) and fit of the absorption's trend by means of the Drude model (black dashed line) for an incident electric field polarized along the y direction. AFM representation of the GNRs array considered in the experiment: the width of each GNR and of each spacing between adjacent GNRs is equal to $W = 4$ μm respectively. (**b**) Absorption spectrum for GNRs (red line) for an incident electric field polarized along the x direction, and fits of the absorption's trend by means of the Lorentz model (blue dashed line), Drude model (magenta dashed line) and a combination of the two models (black dashed line) respectively. The discrepancy between experimental values and the Lorentz model (blue dashed line) derives from the Drude-like absorption of graphene outside the fabricated region area of the substrate. Image adapted from Ref. 136. Copyright 2011 Springer Nature.

The charge oscillation related to the plasmonic mode is also associated with the electric conductivity $\sigma(\omega)$, which can be computed for a spatially confined system in the quasistatic limit as:[134–137]

$$\sigma(\omega) \approx iD\frac{\omega}{(\omega^2 - \omega_p^2) + i\Gamma\omega} \tag{2.30}$$

where Γ is the plasmon resonance width, ω_p is the plasmon resonance frequency and D is the Drude weight.[44] In graphene, the Drude weight is defined as follows:[44]

$$D = \frac{4E_F\sigma_{uni}}{\hbar} \tag{2.31}$$

where σ_{uni} represents the universal (frequency-independent) optical conductivity for graphene:[44,138–141]

$$\sigma_{uni} = \frac{e^2}{4\hbar} \tag{2.32}$$

In confined graphene-based systems, with a characteristic dimension L, the plasma frequency can be written as:[134,142]

$$\omega_p \propto \sqrt{\frac{D}{\epsilon_0 \epsilon L}} \tag{2.33}$$

Eq. 2.33 clearly illustrates how the PRF in confined graphene systems can be adjusted by modifying the dimension of the sample. The PRF is also dependent on the Fermi level (see Eq. 2.31), which determines the electronic density of the system (see Eq. 2.29). Notably, the plasmon dispersion relation in graphene is proportional to $\omega_p \propto n^{\frac{1}{4}}$ (see Eq. 2.29), which differs from the plasmonic dispersion for a 2DEG in metals, where $\omega_p \propto n^{\frac{1}{2}}$ (see Eq. 2.7).

2.4 Electric field enhancement mechanism

Enhanced spectroscopies are one of the most exciting applications of plasmonics to date. They are based on the generation of a localized electric field in the proximity of a metal nanostructure, which enhances the Raman scattering of target molecules adsorbed on the nanostructure surface.[31] Among the several techniques proposed in literature to detect specific spectroscopic signals,[143–145] Surface enhanced Raman Scattering (SERS)[21–23,31,146–148] is the most commonly used due to its high detection limit, which has made it useful in applications ranging from real-time glucose sensing for diabetes testing[149,150] to real-time detection of drugs and pollutants[151] and ultra-sensitive DNA detection.[152] While rough noble metal slabs or clusters of noble metal NPs are typically used as plasmonic substrates in SERS experiments, it is possible to increase the confinement of plasmons by exploiting particular geometrical arrangements and NPs shapes, such as in the case of tip-enhanced Raman scattering (TERS).[27,28,34,35] Graphene has also been used as a substrate for surface-enhanced spectroscopy, but the electric field enhancement achieved with graphene-enhanced Raman spectroscopy (GERS) is several orders of magnitude lower than that obtained with noble metal substrates.[52]

In the following sections, the main physical mechanisms responsible for SERS/GERS are introduced, leading to the definition of the enhancement factors, which are commonly used to quantify the performance arising in specific configurations of plasmonic substrates.

2.4.1 SERS mechanism and enhancement factor

The Raman effect resides in the inelastic scattering process between a molecule and a photon. This mechanism is mediated by a vibrational (or rotational) mode of the molecule, resulting in the incoming photon of energy ($\hbar\omega_i$) being shifted in frequency by the energy of the molecule's vibration state ($\hbar\omega_m$).[153] In particular, when the molecule is in its vibrational ground state, the incident photon loses energy in the scattering event, leading to a red-shifted photon frequency (Stokes scattering). Conversely, when the molecule is in an excited vibrational state, the photon gains energy through the de-excitation process of the

excited mode (Anti-Stokes scattering).[153] Therefore, the frequencies of the Stokes (ω_s) and Anti-Stokes (ω_{as}) Raman bands can be expressed as follows:[153]

$$\omega_s = \omega_i - \omega_m \tag{2.34a}$$

$$\omega_{as} = \omega_i + \omega_m \tag{2.34b}$$

If the Raman scattering is related to a spontaneous scattering event, a linear proportional relation occurs between the total power of the scattered beam and the intensity of the incoming excitation (see Eq. 2.35). Under this condition, the power of the scattering beam in the case of the Stokes process (P_s) is:[154]

$$P_s(\omega_s) = N\sigma_{sca}I(\omega_i) \tag{2.35}$$

where N is the number of molecules in the probed volume, σ_{sca} is the Raman scattering cross section and $I(\omega_i)$ the intensity of the external radiation.
To estimate the SERS Stokes signal P_s^{SERS}, Eq. 2.35 needs to be modified to account for the electric field enhancement generated by a metal nanostructure. Specifically, the enhancement of the Raman signal is generally attributed to two mechanisms: the electromagnetic (EM) and chemical (CM) mechanisms.[31,155,156] The EM is due to the locally enhanced electromagnetic field generated by the excitation of localized surface plasmons in the nanostructure. For instance, isolated noble metal NPs can enhance the electromagnetic field by about 10^6-10^7.[3,31] However, when metallic substrates are engineered into geometrical arrangements that create very confined *hot spots*, the enhancement factors can reach values up to 10^{10}-10^{11},[157,158] allowing for single molecule detection. Differently, the physical origin of CM is still not fully understood.[31,159] It is thought to involve electron transfer between the adsorbed molecule and the metallic nanomaterial, occurring via two interconnected mechanisms.[155] The first involves changes in the electronic structure of the molecule's ground state due to a molecule-substrate charge transfer (CT) interaction.[160–163] The second process concerns the electron transfer in the excited states of the molecule-metal system.[164] However, quantifying the CT contribution to the total SERS enhancement is challenging, and generally provides enhancement factors of about 10^1-10^2.[31] EM is thus the main responsible for the enhancement of the Raman signal.[155] Therefore, in the following, the attention is focused on EM. Since the excitation of localized surface plasmons yields an enhancement of both the incoming and emitted light fields, the intensity of the enhanced Raman signal P_s^{SERS} (related to the Stokes process only) can be expressed as:[3]

$$P_s^{SERS} = N'\sigma_{sca}^{ads}|A(\omega_i)|^2|A(\omega_m)|^2I(\omega_i) \tag{2.36}$$

where N' is the number of molecules that are involved in the SERS process, which is might be smaller than the global number of molecules in the probed volume (N). σ_{sca}^{ads} represents the enhanced scattering cross-section of the Raman process for the molecule adsorbed on the metal nanostructure, whereas $|A(\omega_i)|$ and $|A(\omega_m)|$ are the enhancement factors for the incident and for the Raman scattered field, respectively.[3]

The enhancement factors of both the incoming and emitted fields can be expressed as:[3,154]

$$A(\omega) = \frac{|\mathbf{E}|}{|\mathbf{E}_0|} \tag{2.37}$$

where $\mathbf{E}$ (local field amplitude at the Raman active site) is the superposition of the field associated with the incident radiation $\mathbf{E}_0$ and the field of an induced dipole across the nanostructure $\mathbf{E}_{sp}$ (i.e. $\mathbf{E} = \mathbf{E}_0 + \mathbf{E}_{sp}$).[154]
Since the difference in energy between the incident and scattered photons ($\Delta\omega = \omega_i - \omega_m$) is generally smaller than the linewidth of localized surface plasmon modes, $|A(\omega_i)| \approx |A(\omega_m)|$. For this reason, the EM contribution to the total SERS enhancement R is proportional to the fourth power of the field enhancement factor:[3,165]

$$R = A(\omega)^4 = \frac{|\mathbf{E}|^4}{|\mathbf{E}_0|^4} \tag{2.38}$$

More precisely, by considering a molecule adsorbed at a distance d on a spherical metal NP having radius r and permittivity ϵ, surrounded by a medium with the dielectric function ϵ_0 (see Fig. 2.8), the definition of the enhancement factor reads:[154]

$$A(\omega) = \frac{\mathbf{E}}{\mathbf{E}_0} \approx \frac{\epsilon - \epsilon_0}{\epsilon + 2\epsilon_0}\left(\frac{r}{r+d}\right)^3 \tag{2.39}$$

Eq. 2.38 can be rewritten by highlighting the dependence of the total SERS enhancement on the geometrical parameters and the dielectric function of the plasmonic substrate:[154]

$$R = |A(\omega_i)|^2 |A(\omega_m)|^2 \approx \left|\frac{\epsilon(\omega_i) - \epsilon_0}{\epsilon(\omega_i) + 2\epsilon_0}\right|^2 \left|\frac{\epsilon(\omega_m) - \epsilon_0}{\epsilon(\omega_m) + 2\epsilon_0}\right|^2 \left(\frac{r}{r+d}\right)^{12} \tag{2.40}$$

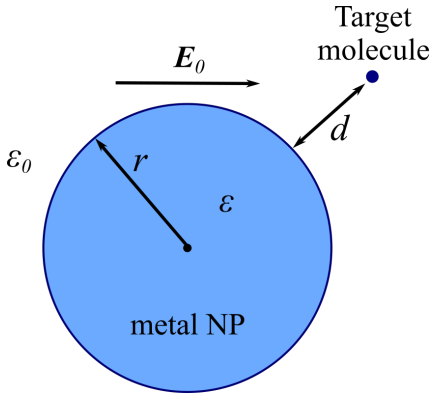

Figure 2.8. Metal NP with radius r and dielectric function ϵ placed at a distance d from a target molecule in a medium having permettivity ϵ_0. The diameter of the sphere has to be smaller compared to the wavelength of the incident light λ (Rayleigh limit, $2r/\lambda << 1$).[154]

2.4.2 Graphene Enhanced Raman Scattering (GERS)

In recent years, graphene has emerged as an ideal substrate for investigating the physical origins of the CM.[49,51,166–169] Indeed, its flat surface facilitates strong chemical interactions

between target analytes and the plasmonic substrate. Additionally, the lack of *hot spots* across the surface hampers the EM, making the CM the fundamental mechanism responsible for enhancement factors in graphene-enhanced Raman scattering (GERS).[52] Indeed, GERS enhancement factors are typically on the order of 10^1-10^2, thus they are much lower than those obtained using metal NPs as a substrate.[52,168]

The CM-based molecule-graphene interaction strongly depends on the physico-chemical properties of the target molecules, resulting in different enhancement factors.[52,169] This selectivity is determined by two main features of the molecular system. Firstly, an appropriate energy level alignment between the highest occupied molecular orbital (HOMO) and lowest unoccupied molecular orbital (LUMO) of the molecule and the Fermi level of the substrate is required, with higher enhancements observed when the Fermi level falls within the HOMO-LUMO energy gap of the molecule.[167] Secondly, the spatial orientation, structure, and symmetry of the target molecule also play a crucial role. In particular, molecules with planar structures exhibit stronger selectivity and return more intense signals in GERS.[52,167]

The Raman signal intensity strongly depends on the distance between the molecule and the substrate also, following an exponential decay of d^{10} (the so-called first layer effect).[166,170]

The lack of the EM contribution to the electric field enhancement has hindered the use of graphene as a substrate for enhanced Raman spectroscopies and sensing applications.[52] A possible way to overcome this limitation resides in the creation of very confined *hot spots* in precisely engineered graphene-based geometrical arrangements. During my Ph.D., I explored this idea, demonstrating that engineered plasmonic hot-spots in graphene, created by following similar strategies as proposed for metal nanoparticles, can yield electric field enhancement factors comparable to those obtained using common plasmonic substrates.[101]

Chapter 3

Modeling the optical response of metal NPs and graphene

Over the last few decades, theoretical models have had an impressive impact on the understanding of the optical response of noble metal NPs and graphene. In this chapter, the implicit and discrete modeling of plasmonic nanostructures are reviewed, by focusing on the Boundary Element Method (BEM), and classical atomistic approaches, such as the capacitance polarizability interaction model and ωFQ, which is developed in the research group I joined during my Ph.D. internship.

3.1 Boundary Element Method (BEM)

In BEM,[63,64,66,70,71,171,172] the plasmonic material is described as a continuum dielectric, characterized by a complex permittivity function $\epsilon(\omega)$. The scattering process between the incident light and the plasmonic structure produces a surface charge density that is numerically discretized in a set of surface charges.

Such surface charges are positioned on the surface of the plasmonic substrate and thus lie at the boundary between the inner and outer dielectric media, as reported in Fig. 3.1. Specifically, the plasmonic material has a dielectric function ϵ_1 and it is defined in a certain region of space (Ω), bounded by the surface $\partial\Omega$. The plasmonic material is surrounded by a medium with permettivity ϵ_2 (see Fig. 3.1). The solution of Maxwell's equations in the presence of arbitrarily shaped abrupt dielectric interfaces can be expressed in terms of the Poisson equation. In the quasistatic limit (i.e. retardation effects are neglected) it reads:

$$\nabla^2\Phi(\mathbf{r}) = -4\pi\rho(\mathbf{r}) \tag{3.1}$$

where Φ is the scalar potential and ρ is the total volume charge density. By considering the system represented in Fig. 3.1, Eq. 3.1 has the following solution:

$$\Phi(\mathbf{r}) = \Phi_j^{ext}(\mathbf{r}) + \int_{\partial\Omega} G_j(\mathbf{r}-\mathbf{s}')\sigma_j(\mathbf{s}')d\mathbf{s}' \qquad \mathbf{r}\in\Omega_j \qquad j=1,2 \tag{3.2}$$

where j indicates the region of space inside(1)/outside(2) the edge $\partial\Omega$, $\mathbf{r}$ and $\mathbf{r}'$ are the space positions inside the Ω region of space, whereas $\mathbf{s}$ and $\mathbf{s}'$ represent the points on the surface $\partial\Omega$. $\Phi_j^{ext}(\mathbf{r})$ is the solution of the free Helmholtz equation in the medium j, whereas $\sigma_j(\mathbf{s})$ are the surface charges placed on $\partial\Omega$ (see Fig. 3.1).

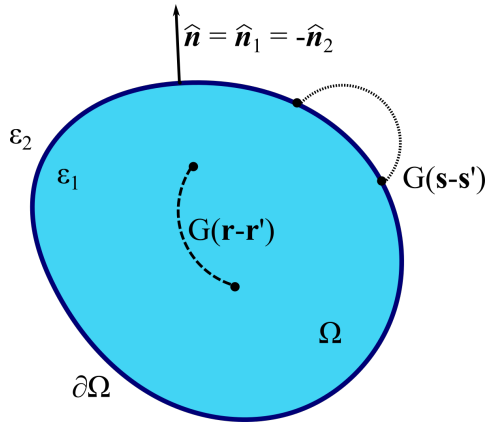

Figure 3.1. Metal NP with dielectric function ϵ_1 separated by means of the surface $\partial\Omega$ by a medium with permittivity ϵ_2. The normal component with respect to the surface is labeled as $\hat{\mathbf{n}}$. Points inside the NP are describe by the vector $\mathbf{r}$, whereas $\mathbf{s}$ indicates points on the surface $\partial\Omega$.

G is the Green function, defined as:[103]

$$\nabla^2 G(\mathbf{r} - \mathbf{r}') = -4\pi\delta(\mathbf{r} - \mathbf{r}') \tag{3.3}$$

Under the quasistatic approximation, the solution to Eq. 3.3 is:[103]

$$G(\mathbf{r} - \mathbf{r}') = \frac{1}{|\mathbf{r} - \mathbf{r}'|} = G(\mathbf{r}, \mathbf{r}') \tag{3.4}$$

Eq. 3.2 solves the Helmholtz equation (see Eq. 3.1) in the whole space, except for the boundary $\partial\Omega$. The surface charge $\sigma_j(\mathbf{s})$ are defined to fulfill the boundary conditions at the surface $\partial\Omega$. Thus, they are not a physical quantity but a mathematical tool to satisfy the boundary conditions only.[63] In particular, two boundary conditions have to be satisfied: the tangential component of the electric field and the normal component of the dielectric displacement have both to be continuous in $\partial\Omega$. The constrain on the tangential electric field implies that:

$$\Phi_1|_{\partial\Omega} = \Phi_2|_{\partial\Omega} \tag{3.5}$$

The key condition reported in Eq. 3.5 is guaranteed only if the charge densities on the opposite side of the surface $\delta\Omega$ are the same: $\sigma_1 = \sigma_2$. On the other hand, in order to satisfy the condition over the dielectric displacement, the normal derivative of $\Phi(\mathbf{r})$ (i.e. along the normal direction $\hat{\mathbf{n}}$ with respect to $\partial\Omega$, as reported in Fig. 3.1) has to be calculated:

$$\lim_{\mathbf{r}\to\mathbf{s}} \hat{\mathbf{n}} \cdot \nabla\Phi(\mathbf{r}) = \frac{\partial\Phi}{\partial n} = \int_{\partial\Omega} F(\mathbf{s}, \mathbf{s}')\sigma(\mathbf{s}')d\mathbf{s}' \pm 2\pi\sigma(\mathbf{s}) + \frac{\partial\Phi^{ext}}{\partial n} \tag{3.6}$$

where the sign of $2\pi\sigma(\mathbf{s})$ depends on the side of surface that is considered (i.e. positive sign inside the particle, negative outside), whereas $F(\mathbf{s},\mathbf{s}')$ is the normal derivative of the Green function. In BEM, the integral in Eq. 3.6 is calculated by approximating the surface charges as a discrete number of point located at the center of mass of each tessarae. Thus, Eq. 3.6 becomes:

$$\left(\frac{\partial\Phi}{\partial n}\right)_i = \sum_j F_{ij}\sigma_j \pm 2\pi\sigma_i + \left(\frac{\partial\Phi^{ext}}{\partial n}\right)_i \tag{3.7}$$

where the i and j indices run over the number of tesserae. Thus, the boundary condition concerning the normal component of the dielectric displacement reads:

$$\epsilon_1\left(\mathbf{F}\sigma + 2\pi\sigma + \frac{\partial\Phi^{ext}}{\partial n}\right) = \epsilon_2\left(\mathbf{F}\sigma - 2\pi\sigma + \frac{\partial\Phi^{ext}}{\partial n}\right) \tag{3.8}$$

Therefore, the BEM surface charges are:[103]

$$\sigma = -\left(2\pi\frac{\epsilon_1+\epsilon_2}{\epsilon_1-\epsilon_2}\mathbf{1} + \mathbf{F}\right)^{-1}\frac{\partial\Phi^{ext}}{\partial n} \tag{3.9}$$

where $\mathbf{F}$ is the surface derivative of the Green function, defined as:[173]

$$F_{ij} = \frac{(\mathbf{s}_i - \mathbf{s}_j)\cdot\mathbf{n}_j}{|\mathbf{s}_i - \mathbf{s}_j|^3}\cdot A_j \qquad \text{for} \quad i \neq j \tag{3.10}$$

$$F_{ii} = K\cdot\frac{\sqrt{4\pi A_i}}{2R_i} \qquad \text{for} \quad i = j \tag{3.11}$$

where R_i is the radius of the sphere the i-th tessera belongs, K is equal to -1.0694,[173] whereas A_i is the surface of each tessera. $\mathbf{n}_i$ is the normal vector corresponding to each tessera, going from the center of mass of the i-th tessera towards the outside part of the sphere (see Fig. 3.1). Finally, note that a more general treatment of the BEM model, in which retarded effects are also considered, can be found in Ref. 63.

3.2 Atomistic models

Although continuum models are capable of accurately reproducing the optical properties of metal NPs,[69,70] they might fail in describing nanostructures dominated by quantum effects, such as nanocavities and nanojunctions, and characterized by an atomistically defined morphology. As stated in the Introduction, to face such situations, atomistic approaches are generally exploited. *Ab initio* methods correctly model nonlocal, finite-size, and quantum effects, but the treatment of large, sizable structures is hampered due to the associated high computational cost. In this context, atomistic models based on classical physics can overcome the main limitations of both continuum and first-principle methods, while maintaining a low computational cost. In this Thesis, two atomistic classical approaches are reviewed: the capacitance polarizability interaction model (CPIM)[90,91] and the ωFQ model[92] (see section 3.3).

3.2.1 The capacitance polarizability interaction model (CPIM)

In the CPIM, the polarizability of a metal NP made of N atomic sites is described by endowing each atom of the nanostructure with a charge and a dipole, whose value depend on frequency-dependent atomic capacitances $c(\omega)$ and polarizabilities $\alpha_{\alpha\beta}(\omega)[\alpha, \beta = x, y, z]$. The atomic polarizability can be defined in terms of the bulk dielectric function $\epsilon(\omega)$ by using the Clausius-Mossotti relation:

$$\frac{\epsilon(\omega) - 1}{\epsilon(\omega) + 2} \frac{M}{D} = \frac{4\pi N_A \alpha(\omega)}{3} \tag{3.12}$$

where M and D are the molar mass and the density of the metal, respectively, $\alpha(\omega)$ is the polarizability of the system and N_A is Avogadro's constant. By defining the volume V of the atom i as:

$$V_i = \frac{M}{N_A D} \tag{3.13}$$

the atomic polarizability $\alpha_i(\omega)$ reads:

$$\alpha_i(\omega) = \frac{\epsilon(\omega) - 1}{\epsilon(\omega) + 2} \frac{3V_i}{4\pi} \tag{3.14}$$

As a result of the interaction between polarization sources placed on each atom, an induced charge q_i^{ind} and an induced dipole $\mu_{i,\alpha}^{ind}$ arise. Within this framework, the total energy of the system reads:[90]

$$\begin{aligned} E =& \frac{1}{2} \sum_i^N \frac{q_i^{ind} q_i^{ind}}{c_i} + \frac{1}{2} \sum_i^N \sum_{j \neq i}^N q_i^{ind} T_{ij}^{(0)} q_i^{ind} + \\ & \frac{1}{2} \sum_i^N \mu_{i,\alpha}^{ind} \alpha_{i,\alpha\beta}^{-1} \mu_{i,\beta}^{ind} - \frac{1}{2} \sum_i^N \sum_{j \neq i}^N \mu_{i,\alpha}^{ind} T_{ij,\alpha\beta}^{(2)} \mu_{j,\beta}^{ind} - \\ & \sum_i^N \sum_{j \neq i}^N \mu_{i,\alpha}^{ind} T_{ij,\alpha}^{(1)} q_j^{ind} + \sum_i^N q_i^{ind} \phi_i^{ext} - \\ & \sum_i^N E_\alpha^{ext} \mu_{i,\alpha}^{ind} - \lambda \left(q^c - \sum_i^N q_i^{ind} \right) \end{aligned} \tag{3.15}$$

where $T_{ij}^{(0)}$, $T_{ij}^{(1)}$ and $T_{ij}^{(2)}$ are the charge-charge, charge-dipole, dipole-dipole interaction kernels respectively, that are defined by following Ref. 174. ϕ^{ext} and $\mathbf{E}^{ext}$ are the electric potential and field associated with the external radiation. Finally, the last term contains the lagrangian multiplier λ, which is introduced to constrain the sum of all atomic charges of the cluster to be equal to q^c.

The induced charges and dipoles are obtained by minimizing Eq. 3.15 with respect to the induced atomic charges q_i^{ind}, atomic dipoles μ_i^{nd} and Lagrangian multiplier λ,[90] yielding the following set of linear equations:

$$\begin{pmatrix} E^{ext} \\ \phi^{ext} \\ q^c \end{pmatrix} = \begin{pmatrix} A & -M & 0 \\ -M^T & -C & 1 \\ 0 & 1 & 0 \end{pmatrix} \begin{pmatrix} \mu^{ind} \\ q^{ind} \\ \lambda \end{pmatrix} \tag{3.16}$$

where the matrix elements of are defined as:

$$A_{ii,\alpha\beta} = \alpha_{i,\alpha\beta}^{-1} \qquad M_{ii,\alpha} = 0 \qquad C_{ii} = c_i^{-1} \qquad i = j \tag{3.17a}$$

$$A_{ij,\alpha\beta} = -T_{ij,\alpha\beta}^{(2)} \qquad M_{ij,\alpha} = T_{ij,\alpha}^{(1)} \qquad C_{ij} = T_{ij}^{(0)} \qquad i \neq j \tag{3.17b}$$

By inverting the system in Eq. 3.16, the induced charges and dipoles can be computed by solving the following system of equations:

$$\begin{pmatrix} \mu^{ind} \\ q^{ind} \\ \lambda \end{pmatrix} = \begin{pmatrix} A & -M & 0 \\ -M^T & -C & 1 \\ 0 & 1 & 0 \end{pmatrix}^{-1} \begin{pmatrix} E^{ext} \\ \phi^{ext} \\ q^c \end{pmatrix} = \begin{pmatrix} B & G & H_1 \\ G^T & D & H_2 \\ H_1^T & H_2^T & H_3 \end{pmatrix} \begin{pmatrix} E^{ext} \\ \phi^{ext} \\ q^c \end{pmatrix} \tag{3.18}$$

where the B,G,D,H_1,H_2 and H_3 blocks come from the inversion of the matrix in Eq. 3.16. Once the B and D terms are known, the total polarizability of the system can be calculated as:[90]

$$\alpha_{\alpha\beta}^{mol} = \sum_{i,j}^{N} (B_{ij,\alpha\beta} - r_{i,\alpha} D_{ij,\alpha\beta} r_{j,\beta}) \tag{3.19}$$

where $B_{ij,\alpha\beta}$ considers the dipole-dipole interactions and $r_{i,\alpha} D_{ij,\alpha\beta} r_{j,\beta}$ represents the charge-transfer (CT) contribution to the molecular polarizability $\alpha_{\alpha\beta}^{mol}$.[90]

3.2.2 The frequency-dependent (FD)-CPIM

The frequency-dependent complex molecular polarizability can be obtained by extending the CPIM to a frequency-dependent (FD)-CPIM formulation, which describes the response of each atom to external oscillating radiation by using Lorentz oscillators.[91] Specifically, the atomic FD atomic polarizability $\alpha_{i,\alpha\beta}$ and capacitance c_i are written by means of a set of oscillators:

$$\alpha_{i,\alpha\beta}(\omega = 0) = \alpha_{i,\alpha\beta}^{s} \tag{3.20a}$$

$$\alpha_{i,\alpha\beta} = \alpha_{i,\alpha\beta}^{s} \left(\frac{\omega_{i,1}^2}{\omega_{i,1}^2 - \omega^2 - i\gamma_{i,1}\omega} + \frac{\omega(N)_{i,2}^2}{\omega(N)_{i,2}^2 - \omega^2 - i\gamma_{i,2}\omega} \right) \tag{3.20b}$$

$$c_i(\omega = 0) = c_i^s \tag{3.20c}$$

$$c_i = c_i^s \left(\frac{\omega_{i,1}^2}{\omega_{i,1}^2 - \omega^2 - i\gamma_{i,1}\omega} \right) \tag{3.20d}$$

where $\omega_{i,1}$ and $\omega_{i,2}$ are the oscillator's resonance frequencies and $\gamma_{i,1}$ and $\gamma_{i,2}$ the oscillator widths for the first and second oscillators respectively. When $\omega = 0$ (see Eq. 3.20a and

3.20c), the atomic capacitances and polarizabilities obtained in the static case are recovered (indicated with the s apex).[91]

The total polarizability $\alpha^{mol}_{\alpha\beta}$ is calculated by using 3.19, after solving the same set of linear equations in Eq. 3.18. The absorption σ_{abs} of the metal cluster can be computed as:[91]

$$\sigma_{abs} = \frac{4\pi\omega}{c} Im[\alpha_{iso}] \tag{3.21}$$

where c is the speed of light and $\alpha_{iso} = \frac{1}{3}(\alpha^{mol}_{xx} + \alpha^{mol}_{yy} + \alpha^{mol}_{zz})$ is the isotropic imaginary polarizability of the system.

3.3 The ωFQ model

In ωFQ, each atomic site has a complex charge that can vary in response to an external electric field and as a function of all the other charges in the system. ωFQ can be seen as a frequency-dependent extension of the Fluctuating Charges (FQ) Force Field (FF), first developed by Rick et al.,[94,95,175] and widely applied to liquid solutions in a quantum mechanics/molecular mechanics (QM/MM) framework.[96,97,176–182] Similarly, the FQ approach endows each atom of a molecular system with a charge (q) that can vary according to the Electronegativity Equalization Principle (EEP),[183] which states that at the equilibrium the electronegativity of each atom has the same value. In ωFQ, charges can move across adjacent atoms under two alternative regimes: the conductive regime, where electron exchange is governed by the dynamics of delocalized conduction electrons, as described in the Drude model; and the tunneling regime, where electron exchange is mediated by a quantum tunneling mechanism that resembles charge exchange phenomena in nanojunctions.[92] Under the conductive regime, the equation of motion for charges can be written according to the Drude model:

$$\frac{d\mathbf{p}}{dt} = \mathbf{E}(t) - \frac{\mathbf{p}}{\tau} \tag{3.22}$$

where $\mathbf{p}$ is the momentum of the electron, $\mathbf{E}(t)$ is the external electric field, and τ a friction-like constant taking into account the scattering events between electrons and between electrons and the fixed nuclei. The time derivative of the total charge on the atom i can be written as:

$$\frac{dq_i}{dt} = \sum_j A_{ij}(n_j < \mathbf{p} > \cdot\hat{l}_{ji} - n_i < \mathbf{p} > \cdot\hat{l}_{ij}) \tag{3.23}$$

where A_{ij} is an effective area dividing atom i by atom j, n_i is the electron density on atom i, $< \mathbf{p} >$ is the momentum of the electron averaged over the trajectories connecting i and j and $\hat{l}_{ji} = -\hat{l}_{ij}$ is the unit vector of the line connecting j to i. By assuming the total charge on each atom to be only marginally changed by the external perturbation, it is assumed that $n_i = n_j = n_0$. Thus, Eq. 3.23 becomes:

$$\frac{dq_i}{dt} = 2n_0 \sum_j A_{ij} < \mathbf{p} > \cdot \hat{l}_{ji} \tag{3.24}$$

In order to estimate the term $< \mathbf{p} > \cdot \hat{l}_{ji}$, an external monochromatic electric field is considered. Eq.(3.24) then translates to:

$$-i\omega q_i = 2n_0 \sum_j A_{ij} \frac{< \mathbf{E}(\omega) > \cdot \hat{l}_{ji}}{1/\tau - i\omega} \tag{3.25}$$

Notice that Eq. 3.25 is written in the frequency domain for a monochromatic electric field oscillating at frequency ω. To proceed further, $< \mathbf{E}(\omega) > \cdot \hat{l}_{ji}$ (the total electric field averaged over the line connecting j to i) needs to be connected to atomic properties. This can be done by assuming $< \mathbf{E}(\omega) > \cdot \hat{l}_{ji} \approx (\mu_j^{el} - \mu_i^{el})/l_{ij}$, where μ_i^{el} is the electrochemical potential of atom i and l_{ij} the distance between atoms i and j. Therefore, Eq. 3.25 becomes:

$$\begin{aligned} -i\omega q_i &= \frac{2n_0}{1/\tau - i\omega} \sum_j \frac{A_{ij}}{l_{ij}} (\mu_j^{el} - \mu_i^{el}) \\ &= \frac{2\sigma_0/\tau}{1/\tau - i\omega} \sum_j \frac{A_{ij}}{l_{ij}} (\mu_j^{el} - \mu_i^{el}) \\ &= \sum_j K_{ij}^{\mathrm{dru}} (\mu_j^{el} - \mu_i^{el}) \end{aligned} \tag{3.26}$$

where $n_0 = \sigma_0/\tau$ follows from the relationship between the electron density n_0 and the static conductance σ_0, whereas K^{dru} is a matrix containing the Drude-like terms defined inside Eq. 3.26. To avoid any overestimation of electron transfer effects, the number of atom pairs considered in Eq.3.26 has to be limited. To address this problem a purely geometrical criterion, based on the l_{ij} parameters is defined in order to limit the interaction between atoms to nearest neighbors only. However, in order to avoid any issue related to the specific definition of nearest neighbor atoms, a Fermi-like $f(l_{ij})$ damping function (see Eq. 3.28) can be introduced to mediate the Drude conductive mechanism. Thus, Eq. 3.26 becomes:

$$\begin{aligned} -i\omega q_i &= \sum_j (1 - f(l_{ij})) \cdot K_{ij}^{\mathrm{dru}} (\mu_j^{el} - \mu_i^{el}) \\ &= \sum_j K_{ij}^{\mathrm{tot}} (\mu_j^{el} - \mu_i^{el}) \end{aligned} \tag{3.27}$$

where:

$$f(l_{ij}) = \frac{1}{1 + \exp\left[-d\left(\frac{l_{ij}}{s \cdot l_{ij}^0} - 1\right)\right]} \tag{3.28}$$

and K_{ij}^{tot} contains the Drude-like terms mediated by the damping function (l_{ij}). In Eq.3.28 l_{ij}^0 is the equilibrium distance between two first neighbors atoms, whereas d and s determine

the position of the inflection point and the thickness of the curve respectively.[92] According to Eq. 3.27, when $f(l_{ij}) = 0$, the purely Drude conductive regime is recovered. On the contrary, when $f(l_{ij}) > 0$, the Drude mechanism is exponentially turned off as l_{ij} increases, leading to the tunneling regime of conduction. From a computational point of view, Eq. 3.27 can be rewritten as:[92]

$$\sum_j \left(-\sum_k K_{ik}^{\text{tot}} D_{ij} + \sum_k K_{ik}^{\text{tot}} D_{kj} + i\omega\delta_{ij} \right) q_j = \sum_j (V_i - V_j) K_{ij}^{\text{tot}} \tag{3.29}$$

where V_i is the potential of the external electric field acting on the atomic site i, ω is the external radiation, and $\mathbf{D}$ is a matrix containing the charge-charge interaction terms ($\mathbf{J}$).[96] In particular, in ωFQ the charge-charge interaction kernel is represented by means of Gaussian functions.[184–186] Therefore, the interaction kernel J_{ij} between the atomic sites i and j respectively is:[182]

$$J_{ij}(r_{ij}) = \int_{\mathbb{R}^3} d\mathbf{r} \int_{\mathbb{R}^3} d\mathbf{r}' \frac{|\varphi_i(\mathbf{r} - \mathbf{r}_i)|^2 |\varphi_j(\mathbf{r}' - \mathbf{r}_j)|^2}{|\mathbf{r} - \mathbf{r}'|} = \frac{1}{r_{ij}} \text{erf}\left(\frac{r_{ij}}{\sqrt{R_i^2 + R_j^2}} \right) \tag{3.30}$$

where

$$\varphi(\mathbf{r} - \mathbf{r}_i) = \frac{1}{(R_i^2 \pi)^{3/2}} e^{-\frac{|\mathbf{r} - \mathbf{r}_i|^2}{R_i^2}}$$

where $r_{ij} = |\mathbf{r}_i - \mathbf{r}_j|$ is the distance between atom i and atom j and R_i is the width of the Gaussian distribution on the atomic site i. The value associated with R_i can be obtained by imposing that the diagonal terms of the matrix correspond to the atomic chemical hardness η[175] as:

$$\lim_{r_j \to r_i} \frac{1}{r_{ij}} \text{erf}\left(\frac{r_{ij}}{\sqrt{R_i^2 + R_j^2}} \right) = \eta_i \Rightarrow R_i = \sqrt{\frac{2}{\pi}} \frac{1}{\eta}$$

Once the ωFQ frequency-dependent charges are obtained by solving Eq. 3.27, the complex polarizability $\overline{\alpha}$ can be evaluated. In particular, the complex electric dipole $\overline{\boldsymbol{\mu}}$ is defined as:

$$\overline{\boldsymbol{\mu}} = \sum_i q_i \cdot \mathbf{r}_i \tag{3.31}$$

where $\mathbf{r}_i$ is the distance between the atom i-th and the origin. From the dipole moment, the polarizability $\overline{\alpha}$ is calculated by solving:

$$\overline{\alpha} = \frac{\partial \overline{\boldsymbol{\mu}}}{\partial \mathbf{E}} \tag{3.32}$$

Thus, the absorption cross-section and the scattering one are obtained:

$$\sigma_{\text{abs}} = \frac{4\pi}{3c} \omega \, \text{tr}(\alpha_2) \qquad \sigma_{\text{sca}} = \left(\frac{8\pi}{3c} \right)^4 \omega^4 (\alpha_1^2 + \alpha_2^2) \tag{3.33}$$

where c is the speed of light, ω is the external frequency and α_1 and α_2 are respectively the real and imaginary part of the complex polarizability $\overline{\alpha}$. The extinction cross section is obtained by adding together the relations reported in Eq. 3.33. It is worth noting that the cross section for a particular polarization of the incident electric field can be obtained by selecting the corresponding spatial component of $\overline{\alpha}$.

3.3.1 ωFQ extension to graphene plasmonics

In this section, the ωFQ model extension to graphene plasmonics is discussed. Specifically, the contribution of graphene's linear dispersion relation is included in the conductive regime of the ωFQ model in Eq. 3.27 by means of the cyclotron mass m^*:

$$-i\omega q_i = \frac{2}{1-i\omega\tau}\frac{n_0\tau}{m^*}\sum_j \frac{A_{ij}}{l_{ij}}(\mu_j^{el}-\mu_i^{el}) \qquad m^* = \frac{\sqrt{\pi n}}{v_F} \tag{3.34}$$

To account for the 2D structure of graphene, two parameters entering in Eq. 3.27 have to be modified. First, the electron density n_0 accounts for 3D nanostructures, whereas graphene has a 2D electron density. Second, the effective area A_{ij} has to be defined as a planar surface across the graphene sheet. In the ωFQ model, the electron density n_0 is related to the 2D electron density n_{2D} through the following relation:[93]

$$n_{2D} = n_0 \cdot a_B \tag{3.35}$$

where a_B is the Bohr radius: $a_B \approx 0.53$ Å. n_{2D} can be obtained by calculating the ratio between the number of electrons inside the sheet N and the surface of the graphene sheet S.[93]

$$n_{2D} = \frac{\alpha N}{S} \tag{3.36}$$

where the dimensionless factor α relates the number of electrons to the number of carbon atoms and represents the fraction of electrons that are actually involved in the transport process. Its value can be estimated once the dimensions of the sample and n_{2D} are known. As an example, for a surface density $n_{2D} \approx 3.84 \cdot 10^{12}$ cm^{-2} in a sizable graphene sample, the estimated value for α is equal to 0.0001.[93]
On the other hand, the effective are A_{ij} is now defined as a square surface, with side R_I:

$$A_{ij} = R_I^2 \tag{3.37}$$

By substituting Eq. 3.36 and Eq. 3.37 in Eq. 3.34, the ωFQ Drude conduction term for graphene reads:

$$\begin{aligned} -i\omega q_i =& \frac{2R_I^2\tau v_F}{1-i\omega\tau}\sqrt{\frac{n_{2D}}{\pi}}\sum_j \frac{1}{l_{ij}}(\mu_j^{el}-\mu_i^{el}) \\ =& \sum_j K_{ij}^{\mathrm{dru}}(\mu_j^{el}-\mu_i^{el}) \end{aligned} \tag{3.38}$$

Therefore, the main physical properties of graphene enter the ωFQ model by means of a modification of the Drude-like conduction mechanism. Once again, in order to avoid an overestimation of the conduction of charges between adjacent atoms, the Drude conduction is hampered by using the same Fermi-like damping function reported in Eq. 3.27 and Eq. 3.28, as shown for the case of metal NPs.

3.3.2 Further developments of ωFQ model

The basic version of the ωFQ model (see section 3.3) and its extension to the description of graphene samples served as a starting point for my Ph.D. research activity. First, the performance of the developed approach is compared to the widely used continuum methods in the prediction of the optical properties of metal nanoparticles in chapter 5. Then, the extension of ωFQ to graphene-based nanostructures has been exploited to examine whether plasmonic *hot spots* can be generated by properly engineering the morphology of the material (see chapter 6). Finally, the potential of ωFQ to describe polycrystalline graphene structures in the THz regime is studied in chapter 7.

Furthermore, ωFQ in its basic form is unable to accurately describe the optical properties of metals affected by d-orbitals, responsible for interband transitions.[187–191] This is due to the model conduction mechanism which relies solely on the Drude model, and thus accounting for intraband transitions only. To address this issue, an extension of the ωFQ model, called ωFQFμ is proposed in this Thesis. In this approach, each atom is endowed with a charge q and an additional atomic polarizability, modeling d-shell polarizability, associated with an induced dipole moment μ. This allows ωFQFμ to account for the contribution of core electrons to the optical properties of the system, resulting in a successful description of the plasmonic properties of silver and gold NPs of varying sizes and shapes, as well as the optical properties of nanogaps between noble metal NPs.[99] A detailed treatment of the theoretical foundation of the ωFQFμ model and a collection of its applications to silver and gold NPs can be found in chapter 8.

Then, in my Ph.D. Thesis, I discuss a new computational protocol for describing the interaction between a target molecule and a plasmonic substrate, in order to calculate surface-enhanced Raman signals of the adsorbed molecule. Such a protocol is based on a multiscale QM/MM approach[97,179,192,193] that coupled a QM Hamiltonian[194] with the ωFQ(Fμ) model. The electronic properties of the molecule are treated at the QM level, whereas the substrate is described using the classical ωFQ(Fμ) approach. chapter 9 provides a detailed presentation of the QM/ωFQ(Fμ) multiscale approach, including its theoretical foundations and several applications, which encompass both metal NPs and graphene-based nanostructures.

Chapter 4

Overview of the attached papers

The papers that form the basis of this Thesis are conceptually divided into two categories. The first category deals with the testing of the basic formulation of ωFQ in describing the optical properties of complex-shaped metal and graphene-based nanostructures. The second category focuses on improving ωFQ so as to model interband transitions in noble metals and the generation of enhanced Raman signals of molecules adsorbed on plasmonic substrates.

Paper 1 compares *ab initio*, continuum, and ωFQ models in describing intraband transitions in sodium, silver, and gold NPs with complex shapes, such as nanorods and nanodomes. In particular, ωFQ absorption cross sections are compared to BEM[63–65,71] and TDDFT[78] values for several metal clusters of increasing size. The study finds that while the agreement between ωFQ and *ab initio* reference values is excellent for small metal clusters (up to ≈ 150 atoms), ωFQ results approach BEM data as the dimension of the systems increases. These findings demonstrate the ability of ωFQ to describe quantum-based effects in small-sized and complex shaped systems, overcoming the limitations of classical methods. However, because ωFQ is limited to describing intraband transitions, it can study optical properties of noble metals in the low-frequency range only.

The aim of **Paper 2** is to guide the design of novel graphene-based substrates for GERS applications, specially engineered to maximize the electric field enhancement in confined *hot spots*. Among the several geometries presented in the work, graphene nanocones[195–198] and polycrystalline graphene[199–203] samples are particularly interesting. The reason resides in the fact that enhancement factors computed for these geometrical arrangements are comparable to the values commonly reported for noble metal substrates. *Hot spots* are designed to increase the electromagnetic mechanism (EM) contribution to the electric field enhancement in graphene, thus overcoming the limitations commonly encountered in GERS experiments, where low enhancement factors are observed (usually 6-7 orders of magnitude lower than those obtained with noble metals).

In **Paper 3**, the atomistic nature of ωFQ is used to study the effect of defects and structural disorder on the conductivity of polycrystalline graphene sheets, under the application of isotropic strain. ωFQ results show a strong dependence of the absorption cross section on the grain separation, which in turn affects the conductivity. As the applied strain in-

creases, the reciprocal separation between adjacent grains also increases, causing electrons to become trapped inside the grains and plasmons to become confined within them. This trapping effect affects both optical and electronic properties, causing a blue-shift of the plasmon resonance frequency (PRF) and of the conductivity peak. Remarkably, the paper reports on a microscopic interpretation of the Drude-Smith model[106] to describe conduction in polycrystalline graphene samples.

The effort devoted to understanding the strengths and limitations of the basic version of ωFQ has led to significant improvements to the model, which are discussed in **Paper 4** and **Paper 5**.

Paper 4 extends ωFQ to describe the optical properties of metals featuring interband transitions. The new model, called ωFQFμ, endows each atom of the system with both a charge and a dipole, which can vary in response to the external electric field and to the interaction with other charges and dipoles. Dipoles are tuned to model interband effects and are introduced because *d*-orbitals (in noble metals) can efficiently be treated as polarizable shells placed at lattice positions.[190] The performance of ωFQFμ is tested against silver and gold NPs with different sizes and shapes, returning a good agreement with *ab initio* reference values. Notably, the atomistic description permits to study rough metal NPs and how they can be used to create nanogaps (i.e. *hot spots*) and, in turn, huge enhancement factors.

In order to simulate the Raman signal of a target molecule adsorbed on a plasmonic substrate, in **Paper 5** ωFQ and ωFQFμ are coupled to a quantum mechanical (QM) description of the molecular system,[194] in a multiscale QM/molecular mechanics (QM/MM) fashion.[97,179,192] The resulting models are applied to reproduce the Raman intensity enhancement for pyridine and methotrexate adsorbed on metal NPs and graphene, respectively. Enhanced Raman signals are also evaluated by varying the distance between molecules and substrates, the equilibrium position of the molecule adsorbed on the nanomaterial, the geometrical arrangement of the substrate, its chemical composition, and size.

Chapter 5

Plasmonic Resonances of Metal Nanoparticles: Atomistic vs. Continuum Approaches

frontiers in Chemistry

ORIGINAL RESEARCH
published: 07 May 2020
doi: 10.3389/fchem.2020.00340

Plasmonic Resonances of Metal Nanoparticles: Atomistic vs. Continuum Approaches

Luca Bonatti[1], *Gabriel Gil*[2,3], *Tommaso Giovannini*[4]*, *Stefano Corni*[3,5] *and Chiara Cappelli*[1]*

[1] Scuola Normale Superiore, Piazza dei Cavalieri 7, Pisa, Italy, [2] Institute of Cybernetics, Mathematics and Physics (ICIMAF), La Habana, Cuba, [3] Department of Chemical Sciences, University of Padova, Padova, Italy, [4] Department of Chemistry, Norwegian University of Science and Technology, Trondheim, Norway, [5] Institute of Nanoscience, National Research Council (CNR), Modena, Italy

The fully atomistic model, ωFQ, based on textbook concepts (Drude theory, electrostatics, quantum tunneling) and recently developed by some of the present authors in *Nanoscale*, **11**, 6004-6015 is applied to the calculation of the optical properties of complex Na, Ag, and Au nanostructures. In ωFQ, each atom of the nanostructures is endowed with an electric charge that can vary according to the external electric field. The electric conductivity between nearest atoms is modeled by adopting the Drude model, which is reformulated in terms of electric charges. Quantum tunneling effects are considered by letting the dielectric response of the system arise from atom-atom conductivity. ωFQ is challenged to reproduce the optical response of metal nanoparticles of different sizes and shapes, and its performance is compared with continuum Boundary Element Method (BEM) calculations.

Keywords: ωFQ, BEM, classical atomistic model, optical spectra, fluctuating charges

OPEN ACCESS

Edited by:
Costas Adam Charitidis, National Technical University of Athens, Greece

Reviewed by:
Christos Tserkezis, University of Southern Denmark, Denmark
Michał Zieliński, Nicolaus Copernicus University in Toruń, Poland

***Correspondence:**
Tommaso Giovannini
tommaso.giovannini@ntnu.no
Chiara Cappelli
chiara.cappelli@sns.it

Specialty section:
This article was submitted to Nanoscience, a section of the journal Frontiers in Chemistry

Received: *25 November 2019*
Accepted: *01 April 2020*
Published: *07 May 2020*

Citation:
Bonatti L, Gil G, Giovannini T, Corni S and Cappelli C (2020) Plasmonic Resonances of Metal Nanoparticles: Atomistic vs. Continuum Approaches. Front. Chem. 8:340. doi: 10.3389/fchem.2020.00340

1. INTRODUCTION

The study of the plasmonic excitation of metal nanoparticles (NPs) has attracted much interest in the last few decades (Moskovits, 1985; Nie and Emory, 1997; Maier, 2007; Anker et al., 2008; Atwater and Polman, 2010; Santhosh et al., 2016) due to the generation of very strong electric fields in the proximity of their surfaces, which has been exploited in many fields, including for the detection of molecular signals down to the single-molecule limit (Kneipp et al., 1997; Maier et al., 2003; Muehlschlegel et al., 2005; Lim et al., 2010; Giannini et al., 2011; Neuman et al., 2018). Among the plethora of physical features of metal substrates, one of the most relevant is the dependence of their resonance plasmon frequency on the shape, size, and actual material constituting the nanostructure, which permits a fine tuning of the final signal. From a theoretical point of view, the optical properties of nanostructures are generally treated, independently of their size and shape, by resorting to classical approaches (Jin et al., 2001; Hao et al., 2007; Jensen and Jensen, 2008, 2009; Myroshnychenko et al., 2008; Morton and Jensen, 2010, 2011; Pérez-González et al., 2010; Halas et al., 2011; Ciracì et al., 2012; Payton et al., 2012, 2013; Chen et al., 2015; Liu et al., 2017; Mennucci and Corni, 2019), such as the Mie Theory (Mie, 1908), the Discrete Dipole Approximation (DDA) (Draine and Flatau, 1994), and the finite difference time domain methods (FDTD) (Shuford et al., 2006). A viable alternative is to exploit the Boundary Element Method (BEM) (Corni and Tomasi, 2001; de Abajo and Howie, 2002; Hohenester and Trügler, 2012; Hohenester, 2015), in which the NP is treated as a homogeneous, continuum dielectric described by a frequency-dependent

permittivity function $\varepsilon(\omega)$, and the NP surface is modeled as a sharp interface Γ. BEM has been amply applied to reproduce the plasmonic response of NPs of different sizes and shapes, and it has also been extended to take into account quantum tunneling effects, which are relevant for the so-called subnanometer junctions (Esteban et al., 2012).

The wide applicability of the BEM approach is strictly related to its intrinsic low computational cost, which is due to the fact that the NP surface is discretized in terms of point complex charges that interact with the external electric field, giving rise to the resulting polarization. However, when finite size effects, together with edge effects, cannot be neglected, continuum models may fail. In these cases, the atomistic nature of the system needs to be explicitly taken into account. Fully atomistic *ab-initio* approaches, usually based on Density Functional Theory (DFT), address the problem; however, they cannot afford NPs of sizes larger than a few nanometers (hundreds of atoms) due to their high computational cost.

Fully atomistic, yet classical, approaches, able to reproduce both edge and finite size effects and bulk NP properties have been developed so to overcome the limitations of both *ab-initio* and continuum models (Mennucci and Corni, 2019). In particular, classical atomistic modeling of nanoplasmonics has been pioneered by Jensen and coworkers, who developed the Discrete Interaction Model (DIM) (Jensen and Jensen, 2008, 2009; Morton and Jensen, 2010, 2011; Payton et al., 2012, 2013; Chen et al., 2015; Liu et al., 2017). The original version of DIM assigns a frequency-dependent polarizability and a frequency-dependent capacity to each atom, the parameters of which are determined by accurate *ab-initio* calculations (Jensen and Jensen, 2009). However, most DIM applications only exploit the frequency-dependent polarizability (i.e., they neglect capacity terms), thus resulting in an atomistic picture of the Discrete Dipole Approximation (DDA) (Draine and Flatau, 1994; Chen et al., 2015).

An alternative fully atomistic classical model has recently been proposed by some of us (Giovannini et al., 2019e). Such an approach, named ωFQ (frequency-dependent Fluctuating Charges), is based on text-book concepts, i.e., the Drude model for conduction in metals, classical electrostatics, and quantum tunneling (Giovannini et al., 2019e). Each atom of the NP is endowed with an electric charge that is not fixed but can vary as a response to the externally applied oscillating electric field. Thus, ωFQ indeed adopts the atomistic description introduced by Jensen and coworkers, but it sticks to the simplest possible assumptions, e.g., Drude-like conductance even between two (bonded) atoms instead of parameterizing the model based on accurate calculations or empirical inputs (nanoparticle size, neighborhood of the single atom). Notably, ωFQ has been successfully applied to the optical response of subnanometer junctions, where quantum tunneling plays a crucial role. In this work, we apply the model to reproduce the optical properties of single NPs with different shapes and sizes.

The manuscript is organized as follows. In the next section, the main physical features of both ωFQ and BEM are briefly recalled and compared. Then, the computational methodology is presented, and the numerical results are discussed. In particular, ωFQ is tested against the reproduction of the absorption cross-sections of differently shaped Na, Ag, and Au NPs, and its performance is compared with BEM results so as to highlight the similarities and differences of the two models. A section focusing on conclusions and future perspectives for the approach ends the presentation.

2. MATERIALS AND METHODS

2.1. Theoretical Models

In this section, the main features of the atomistic ωFQ and continuum BEM approaches are briefly recalled. In particular, the working equations of the two models are presented, and the conceptual differences between the two are discussed in detail.

2.1.1. ωFQ

ωFQ is an atomistic approach aimed at describing the optical properties of a metal NP in the quasi-static limit. ωFQ has its theoretical foundation on the Fluctuating Charges (FQ) force field, which, combined with a QM description of a molecular solute, is usually exploited in the modeling of the spectroscopic properties of solvation phenomena (Cappelli, 2016; Giovannini et al., 2018, 2019b). In the FQ force field, each classical atom is described in terms of a charge, which value can vary as a response of the external sources. Similarly to FQ, in ωFQ, each NP atom is modeled as a charge that varies as a response to an external oscillating electric field [$\mathbf{E}(\omega)$]. Remarkably, from the mathematical point of view, ωFQ charges are complex because the metal response includes a dissipative part. In particular, their imaginary part is directly related to the absorption cross-section (vide infra).

The equation of motion of ωFQs is written in terms of the Drude model of conductance (Bade, 1957), adequately reformulated in case of charges (Giovannini et al., 2019e):

$$\frac{dq_i}{dt} = 2n_0 \sum_j A_{ij} < \mathbf{p} > \cdot \hat{l}_{ji} \tag{1}$$

where A_{ij} is the effective area dividing atom i by atom j and A_{ij} is a model parameter optimized to reproduce reference *ab-initio* data. n_0 is the atomic electron density, $< \mathbf{p} >$ is the momentum of an electron averaged over all trajectories connecting i and j, and $\hat{l}_{ji} = -\hat{l}_{ij}$ is the unit vector of the line connecting j to i. By replacing $\mathbf{p}$ with its expression in terms of the external electric field $\mathbf{E}(\omega)$ within the Drude model (Giovannini et al., 2019e), Equation (1) can be rewritten in the frequency domain as:

$$-i\omega q_i = 2n_0 \sum_j A_{ij} \frac{< \mathbf{E}(\omega) > \cdot \hat{l}_{ji}}{1/\tau - i\omega} \tag{2}$$

where τ is a friction-like constant due to scattering events. By then assuming $< \mathbf{E}(\omega) > \cdot \hat{l}_{ji} \approx (\mu_j^{el} - \mu_i^{el})/l_{ij}$, where μ_i^{el} is the electrochemical potential of atom i and l_{ij} the distance between

atoms i and j, Equation (2) becomes:

$$\begin{aligned} -i\omega q_i &= \frac{2n_0}{1/\tau - i\omega}\sum_j \frac{A_{ij}}{l_{ij}}(\mu_j^{el} - \mu_i^{el}) \\ &= \sum_j \left[\frac{2\sigma_0/\tau}{1/\tau - i\omega}\frac{A_{ij}}{l_{ij}}\right](\mu_j^{el} - \mu_i^{el}) \\ &= \sum_j K_{ij}^{\mathrm{dru}}(\mu_j^{el} - \mu_i^{el}) \end{aligned} \tag{3}$$

where $n_0 = \sigma_0/\tau$, with σ_0 being the static conductance of the considered metals. In Equation (3), a matrix named $\mathbb{K}^{\mathrm{dru}}$ with elements $K_{ij}^{\mathrm{dru}} = \frac{2n_0}{1/\tau - i\omega}\frac{A_{ij}}{l_{ij}}$ has been introduced.

Equation (3) describes the electron transfer between all atoms constituting the metal NP. However, in order to make the model physically consistent, i.e., to avoid electron transfer between atoms that are too far apart, in ωFQ, the pairs of atoms in Equation (3) are limited to nearest neighbors only. In order to impose such a limitation, a Fermi-like $f(l_{ij})$ damping function is introduced to weight the Drude conductive mechanism:

$$\begin{aligned} -i\omega q_i &= \sum_j (1 - f(l_{ij}))\cdot K_{ij}^{\mathrm{dru}}(\mu_j^{el} - \mu_i^{el}) \\ &= \sum_j K_{ij}^{\mathrm{tot}}(\mu_j^{el} - \mu_i^{el}) \end{aligned} \tag{4}$$

where:

$$f(l_{ij}) = \frac{1}{1 + \exp\left[-d\left(\frac{l_{ij}}{s\cdot l_{ij}^0} - 1\right)\right]} \tag{5}$$

In Equation (5), l_{ij}^0 is the equilibrium distance between two nearest neighbors, whereas d and s are parameters determining the position of the inflection point and the steepness of the curve. It is worth noticing that due to the exponential decay of the Fermi-like function in Equation (5) (Esteban et al., 2012; Giovannini et al., 2019e), ωFQ is also capable of treating the quantum tunneling that governs the electron transfer between the atoms in the NP (Giovannini et al., 2019e).

Finally, Equation (4) can be rewritten by defining the electrochemical potential μ in terms of the external potential V^{ext}:

$$\begin{aligned} &\sum_j \left(-\sum_k K_{ik}^{\mathrm{tot}} D_{ij} + \sum_k K_{ik}^{\mathrm{tot}} D_{kj} + i\omega\delta_{ij}\right) q_j \\ &= \sum_j (V_i^{\mathrm{ext}} - V_j^{\mathrm{ext}}) K_{ij}^{\mathrm{tot}} \end{aligned} \tag{6}$$

where D_{ij} is the electrostatic coupling kernel written in terms of Gaussian charges (Mayer, 2007; Giovannini et al., 2019c,e) and δ_{ij} is the Kronecker delta. Equation (6) finally gives the complex ωFQs charges from which the complex polarizability $\overline{\alpha}$ and thus the absorption cross-section σ^{abs} can be recovered:

$$\begin{aligned} \overline{\alpha}(\omega)_{kl} &= \frac{\partial \overline{\mu}_k(\omega)}{\partial E_l(\omega)} = \sum_i q_i(\omega)\cdot\frac{k_i}{E_l(\omega)} \\ &\Rightarrow \qquad \sigma^{\mathrm{abs}} = \frac{4\pi}{3c}\omega\,\mathrm{tr}\big(\mathrm{Im}(\overline{\alpha}(\omega))\big) \end{aligned} \tag{7}$$

where $\boldsymbol{\mu}$ is the complex dipole moment, i runs over NP atoms, k represents the x, y, z positions of the i-th atom, and l runs over the x,y,z directions of the external electric field. c is the speed of light, and $\mathrm{Im}(\overline{\alpha})$ is the imaginary part of the complex polarizability $\overline{\alpha}$.

ωFQ has recently been developed and applied to describe the optical response of sodium (Na) nanoparticles (Giovannini et al., 2019e). In fact, due to the specificity of the model, it describes the conductive electrons only by neglecting any possible contribution arising from d-electrons. Nevertheless, the model can be used in its present form to model the optical properties of any metal at frequencies that are far from interband transitions, i.e., those dominated by d-electrons.

2.1.2. Continuum Dielectric Model and Boundary Element Method

The Boundary Element Method (BEM) is a classical electrodynamics approach in which the NP is treated as a homogenous, continuum dielectric described by a frequency-dependent permittivity function $\varepsilon(\omega)$, and the NP surface is modeled as a sharp interface Γ (Fuchs, 1975; Corni and Tomasi, 2001; de Abajo and Howie, 2002; Vukovic et al., 2008; Hohenester and Trügler, 2012; Angioni et al., 2013; Mennucci and Corni, 2019). In this work, BEM quasi-static formulation, valid whenever the size of the NP is much smaller than the wavelength of the incident light, is exploited.

Under the action of an external oscillating electric field $\mathbf{E}(\omega)$, a surface charge density, which mimics the polarization, arises on the nanostructure. From the computational point of view, this electrodynamical phenomenon is solved by discretizing the NP surface by an ensemble of tesserae derived from the surface discretization. As a consequence, the surface charge density is modeled in terms of a set of point charges $\mathbf{q}$, which are called Apparent Surface Charge (ASCs) (Corni and Tomasi, 2001; de Abajo and Howie, 2002; Hohenester and Trügler, 2012). The BEM equation for solving the ASCs per tessera reads:

$$\mathbf{q}(\omega) = -\left[2\pi\left(\frac{\varepsilon(\omega)+1}{\varepsilon(\omega)-1}\right)\mathbf{A}^{-1} + \mathbf{D}^{\dagger}\right]^{-1}\mathbf{E}_n(\omega) \tag{8}$$

where $\mathbf{E}_n(\omega)$ is the normal component of the applied electric field calculated at each charge position, whereas $\mathbf{A}$ is a diagonal matrix containing the tessera areas. $\mathbf{D}$ is a matrix that is defined in terms of the tesserae positions $\mathbf{s}_i$ and the outgoing normal unit vector per tessera $\mathbf{n}_i$ as:

$$D_{ij} = \frac{(\mathbf{s}_i - \mathbf{s}_j)\cdot\mathbf{n}_j}{|\mathbf{s}_i - \mathbf{s}_j|^3} \quad \text{for} \quad i \neq j\,, \tag{9a}$$

$$D_{ii} = 2\pi - \sum_{j\neq i} D_{ij} \tag{9b}$$

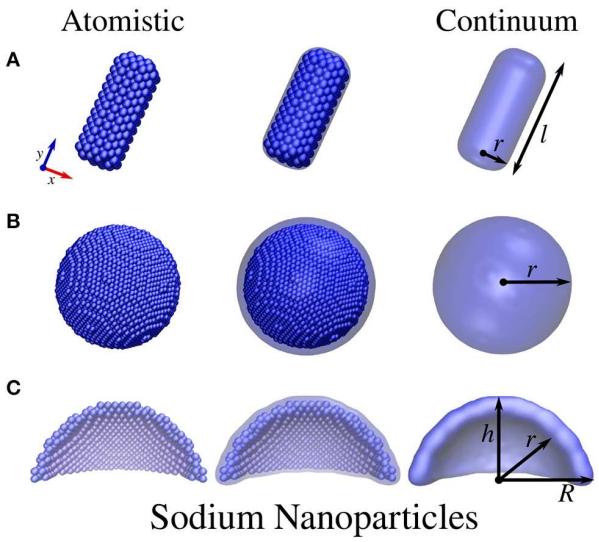

FIGURE 1 | Atomistic (left) and continuum (right) sodium NP structures. **(A)** Cylindrical nanorod with length *l* and radius *r*. **(B)** Spherical NP with radius *r*. **(C)** Spherical nanodome with internal radius *r*, external radius *R*, and dome height *h*. The dome has been cut in half so as to best represent the structure.

BEM Equation (8) depends on the NP geometry (**D** matrix) and material ($\varepsilon(\omega)$). It is worth noticing that Equation (8) formulates the optical response of NPs in vacuo. However, the generalization for any surrounding dielectric medium is straightforward and can be achieved by replacing $\Lambda = (\varepsilon(\omega) + 1)/(\varepsilon(\omega) - 1)$ by $\Lambda = (\varepsilon(\omega) + \varepsilon_{ext}(\omega))/(\varepsilon(\omega) - \varepsilon_{ext}(\omega))$ in Equation (8), where $\varepsilon_{ext}(\omega)$ is the dielectric function of the external medium (Corni et al., 2001; Corni and Tomasi, 2002). Similarly to ωFQ, ACSs are complex quantities because dielectric functions are complex themselves.

Finally, the absorption cross-section σ^{abs} is recovered from the definition of the complex polarizability $\overline{\alpha}_{ij}$, which in turn is defined in terms of the complex dipole moment $\overline{\boldsymbol{\mu}}$:

$$\overline{\boldsymbol{\mu}}(\omega) = \sum_{k=1}^{T} q_k(\omega)\mathbf{s}_k \qquad \Rightarrow \qquad \overline{\alpha}_{ij}(\omega) = \frac{\mu_i(\omega)}{E_j(\omega)}$$

$$\Rightarrow \quad \sigma_{\text{abs}} = \frac{4\pi}{3c}\omega \,\text{tr}\big(\text{Im}(\overline{\alpha}(\omega))\big) \tag{10}$$

where *k* runs over the number of tesserae, whereas *i* and *j* indicate Cartesian components.

2.2. Computational Details

Atomistic ωFQ and continuum BEM approaches were challenged to reproduce the optical response of Na, Ag, and Au nanoparticles of different shapes, varying from cylindrical and pentagonal nanorods and spherical nanodomes (see **Figures 1**, **2** for NP structures).

The geometries of atomistic Na nanorods (see **Figure 1A**) were constructed by imposing a cylindrical section (with radius *r* and length *l*) and Na lattice constant equal to 4.23 Å (Haynes, 2014) in a Body-Centered Cubic (BCC) packing. The geometries of atomistic Ag and Au nanorods (see **Figures 2A,B**) were instead created by imposing both a cylindrical and a pentagonal section (with radius *r* and length *l*) and Ag/Au lattice constant equal to 4.08 Å(Haynes, 2014) in a Face-Centered Cubic (FCC) packing. The geometries of Na, Ag, and Au spherical nanodomes (see **Figures 1C**, **2D**) were constructed by removing a semi-sphere of radius *r* from a concentric semi-sphere of radius $R > r$ (see **Figures 1B**, **2C**), retaining the same packing and distances mentioned above in the case of nanorods. Different heights of the obtained dome were considered by retaining all atoms that are placed at a certain distance *h* from the top of the dome.

All atomistic structures exploited for the following ωFQ calculations were obtained by using the Atomic Simulation Environment (ASE) Python module v. 3.17 (Larsen et al., 2017). The numbers of atoms in Na, Ag, and Au structures are reported in Tables S1–S8 (**Supplementary Material**).

The continuum structures for the same geometries described above were constructed by using the MNPBEM Matlab toolbox (v. 17) (Hohenester and Trügler, 2012). In particular, cylindrical nanorods are constructed out of a cylinder with two hemispheres covering the flat circular faces at its extremes. Analogously, pentagonal nanorods are build up from an extruded pentagon and two pentagonal hemispheres covering the flat pentagonal faces at the extremes. The pentagonal hemispheres are obtained by considering hemispheres discretized with five meridians, so as to generate an object with a pentagonal cross-section normal to the long axis of the nanorod. The pentagonal nanorods were smoothened out at the edges. The full tessellation of such nanorods resulted in 798 and 2212 tesserae, respectively. Spherical shells are built from two concentric spheres (see **Figures 1B,C**, **2C,D**), the inner of which is void. In the case of spherical nanodome portions, the full tessellation contains 600 tesserae.

ωFQ cross-sections were calculated on the obtained atomistic structures by using a stand-alone Fortran 95 package that is under development by some of the present authors. Equation (6) is solved for a set of frequencies given as input. All computed spectra reported in the manuscript were obtained by explicitly solving linear response equations for steps of 0.01 eV. For all studied Na and Ag nanosystems, the ωFQ parameters defined in Equations 3–4 were taken from Giovannini et al. (2019e). The parameters for Au nanostructures are instead reported here for the first time and were recovered from literature data where available: $\tau = 3.2 \cdot 10^{-14}$ s (Palik, 1997), $\sigma_0 = 2.4 \cdot 10^7$ S/m (Haynes, 2014), $A_{ij} = 3.38$ Å^2, $l^0_{ij} = 2.88$ Å (Haynes, 2014), $d = 12.00$, and $s = 1.10$ (Giovannini et al., 2019e). ωFQ Na, Ag, and Au parameters are given in Tables S9–S11 (**Supplementary Material**).

BEM cross-sections were computed by using the MNPBEM Matlab toolbox (v. 17) (Hohenester and Trügler, 2012). Similarly to ωFQ simulations, Equation (8) was solved for steps of 0.01 eV. The dielectric functions defined in Equation (8) were recovered from experimental data (Rakić et al., 1998 for Ag and Au and Althoff and Hertz, 1967; Smith, 1969 for Na).

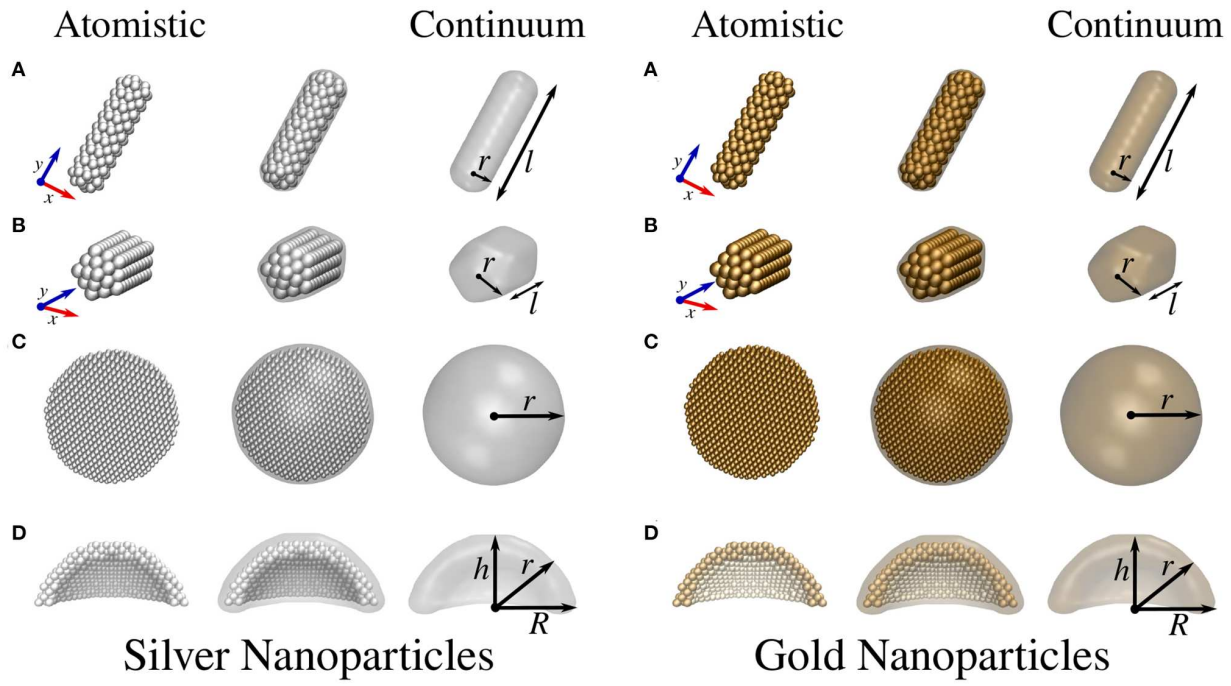

FIGURE 2 | Atomistic (left) and continuum (right) silver and gold NP structures. **(A)** Cylindrical nanorod with length *l* and radius *r*. **(B)** Pentagonal nanorod with length *l* and radius *r*. **(C)** Spherical NP with radius *r*. **(D)** Spherical nanodome with internal radius *r*, external radius *R*, and dome height *h*. The dome has been cut in half so as to best represent the structure.

Both ωFQ and MNPBEM simulations were limited to the quasi-electrostatic (non-retarded) approximation because the size of the largest studied nanoparticle (nanorods with $r = 50$ Å and $l = 150$ Å) is much smaller than the computed absorption wavelength.

3. RESULTS AND DISCUSSION

In this section, ωFQ and BEM absorption cross-sections (σ^{abs}) of sodium, silver, and gold NPs of different shapes (see **Figures 1**, **2**) are presented and compared so as to highlight the differences arising by exploiting atomistic/continuum approaches. The presentation of the computed results is divided into three sections, the first presenting a comparison between both ωFQ and BEM and *ab-initio* σ^{abs} for silver/gold pentagonal nanorods. The second and third sections are instead focused on Na NPs and Ag and Au NPs, respectively. This way of presenting the results is justified by the following: (i) the comparison with *ab-initio* results permits a quantitative analysis of the performance of the ωFQ and BEM approaches; (ii) Ag and Au are characterized by FCC packing, whereas Na has BCC packing, which makes the number of atoms of the structures rapidly incomparable; (iii) the Ag and Au structures are identical because they are characterized by the same lattice constant; (iv) both Ag and Au present inter-band transitions, whereas Na has a simpler dielectric response (interband transitions are, however, present above 2 eV).

3.1. ωFQ and BEM Benchmarking

In **Figure 3**, ωFQ and BEM σ^{abs} of silver/gold pentagonal nanorods (see **Figure 2B**) constituted by a different number of atoms (see labels) and r=2.8 Å are reported together with reference TD-DFT results reproduced from Sinha-Roy et al. (2017). As can be seen, all ωFQ and BEM results are characterized by an intense peak that redshifts as the length of the nanorod increases. Such a trend is perfectly in agreement with the reference data. In addition, the ωFQ Plasmon Resonance Frequencies (PRFs) are in better agreement with the corresponding TD-DFT values than are those of BEM, independently of the length of the nanorod. Such findings suggest that for these structures, which are characterized by atomically defined edges, ωFQ is more reliable than BEM. We also remark that the well-known explanation of the blueshift of small nanoparticles of noble metal was devised for spherical metal nanoparticles (Liebsch, 1993) whose resonance frequency is near to the interband absorption edge. There, the $d-$ electron screening is enhanced by the pre-resonance condition. The nanorods considered here have their resonance far from that region, and the shifts are dominated by atomistic effects that are grasped well by ωFQ.

3.2. Sodium Nanoparticles

Figure 4 presents BEM (**Figure 4A**) and ωFQ (**Figure 4B**) σ^{abs} of Na cylindrical nanorods with radius $r = 10$ Å as a function of the length *l*. BEM and ωFQ intensities were normalized with respect

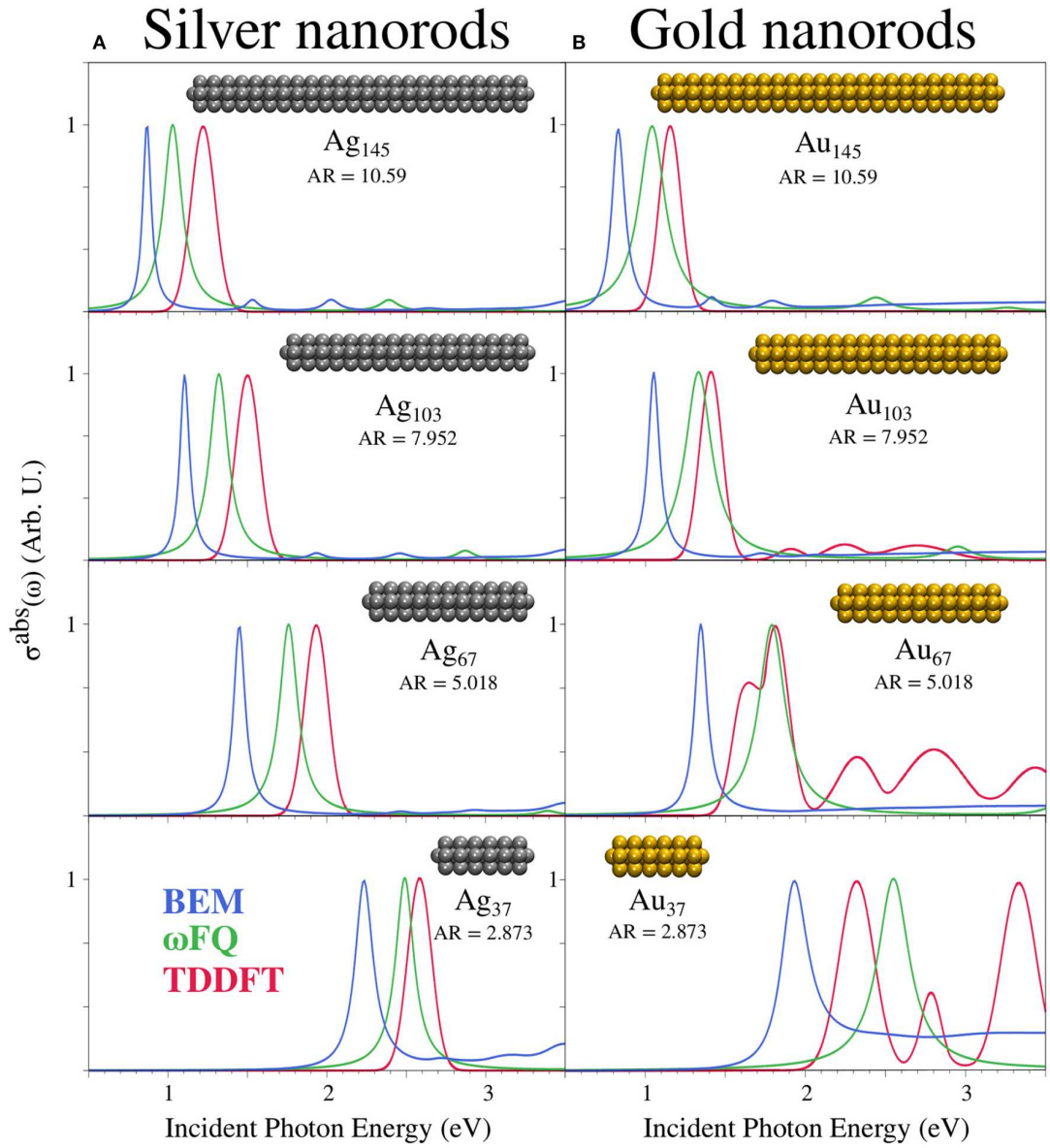

FIGURE 3 | BEM(blue), ωFQ (green), and TD-DFT (red) absorption cross-sections σ^{abs} of silver **(A)** and gold **(B)** pentagonal nanorods with different numbers of atoms (see labels). TD-DFT data are reproduced from Sinha-Roy et al. (2017). The aspect ratio (AR) of the selected nanorods is also given.

to nanorod volumes and NP numbers of atoms, respectively. The calculated absorption cross-sections are characterized by intense and sharp peaks, independently of the nanorod length and the exploited model (BEM or ωFQ). The nature of the plasmon associated to each peak is highlighted by plotting ωFQ imaginary charges calculated at the PRF for a sample structure with $l = 150$ Å (see **Figure 4C**). It is clear that the main band is related to a Boundary Dipolar Plasmon (BDP), which, remarkably, is in line with previous studies (Rossi et al., 2015; Sinha-Roy et al., 2017; Giovannini et al., 2019e).

Both BEM and ωFQ PRF redshift by increasing the length of the metal nanorod, in agreement with classical electrodynamics. By deepening in the comparison between the BEM and ωFQ results, we notice that, despite the trends being almost identically reproduced by both models, some deviations appear in the cases of the shortest nanorods (see **Figure 4**). This is probably due to the fact that finite-size effects cannot be neglected by decreasing the length of the nanorod. In addition, the PRF for such small structures shifts above 2 eV, thus indicating that interband transitions may play a relevant role. Also, it is worth

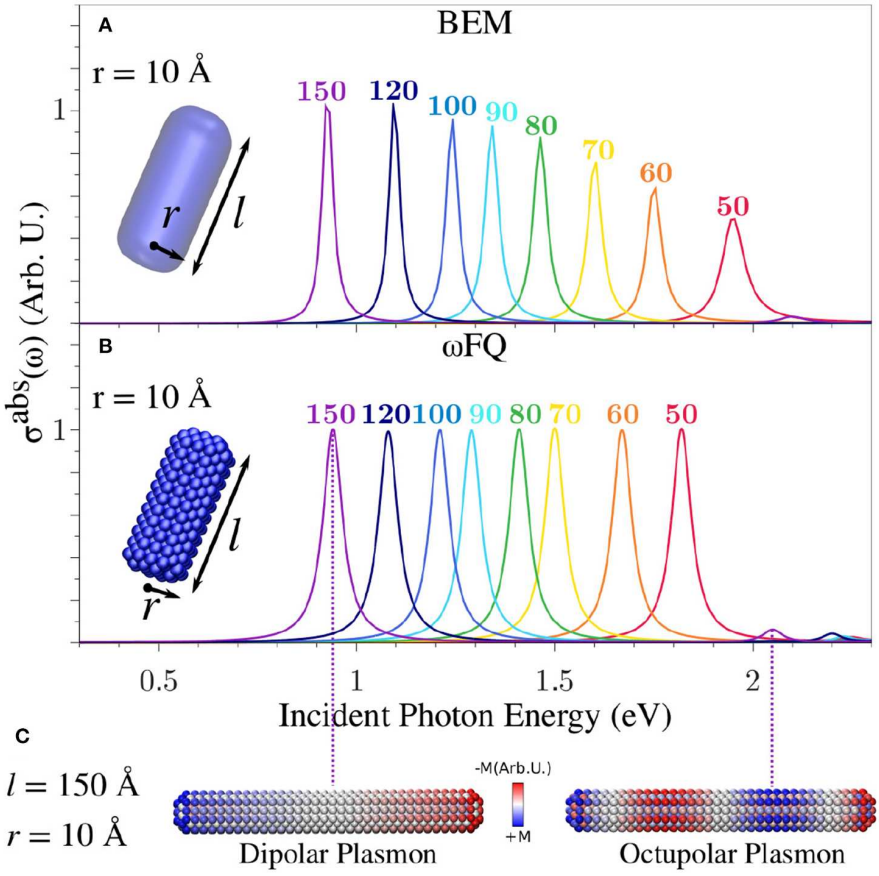

FIGURE 4 | Calculated BEM **(A)** and ωFQ **(B)** absorption cross-sections σ^{abs} of a sodium nanorod with $r = 10$ Å as a functions of l (see labels). **(C)** ωFQ imaginary charges for a Na nanorod with $r = 10$ Å and $l = 150$ Å calculated at the PRFs of the two peaks highlighted in **(B)**. All σ^{abs} are normalized with respect to the volume of the considered structure.

noticing that ωFQ intensities remain constant in all spectra, whereas BEM intensities decrease as the length of the nanorod decreases, with a simultaneous increase in the band broadening (Kreibig and Fragstein, 1969), which is not reported by ωFQ. In order to better understand the reasons for these discrepancies, the areas of all peaks have been computed and normalized with respect to the area of the peak of the longest nanorod (l = 150 Å, see **Figure S1**). We notice that all of the ωFQ peak areas almost perfectly match the BEM data, thus showing that the physics of the system is similarly described by the two approaches. It is worth remarking that an increase in the band broadening as the length of the nanorod decreases has been reported previously in the literature (Kreibig and Fragstein, 1969). Such an effect is correctly modeled by BEM, due to the fact that it exploits the experimental permittivity function. These features are not reproduced by ωFQ; however, several *ad-hoc* techniques, which have been developed in the past (Kreibig and Fragstein, 1969; Liebsch, 1993; Molina et al., 2002; Gao et al., 2011) to solve such issues, could in principle be coupled with our approach.

The general agreement between ωFQ and BEM in the cases of the largest structures is also confirmed by the presence of a second peak in the high-frequency region (see e.g., $l = 150$ Å at ~ 2.1 eV in **Figure 4**). The nature of such a band, which is very low in intensity, was investigated by plotting ωFQ imaginary charges similarly to the most intense band. From inspection of **Figure 4C**, the peak can be easily related to a boundary octupolar plasmon, confirming what has been reported in the literature (Rossi et al., 2015; Giovannini et al., 2019e). We remark that some mixing with the dipolar plasmon is needed to see $\sigma^{abs} \neq 0$.

To further investigate the performance of ωFQ and BEM, we selected a challenging system, i.e., a portion of a spherical Na (see **Figure 1C**), which has not been widely investigated before from both the theoretical and experimental points of view (Ye et al., 2009; Raja et al., 2016). In **Figure 5A**, the absorption cross-section of such structure as a function of the height h of the dome is reported. Notice that the internal r and external R radii are kept fixed to 40 and 50 Å, respectively. Three main features, common to both ωFQ and BEM absorption spectra, can be highlighted.

- All spectra are characterized by an intense and sharp peak at about 1.5 eV (ωFQ) and 1.8 eV (BEM) that redshifts by increasing the height of the dome (i.e., by moving from h=25 to h=45 Å). Such a trend is in agreement with what has been shown above in the case of nanorods (see **Figure 4**). In fact, increasing the height of the dome results in an increase in the number of atoms, which, as in the previous case, results in a redshift of the absorption spectrum. Differently from nanorods, BEM and ωFQ PRFs differ by almost 0.3 eV; this is probably due to a different description of the nanodome edges.
- All spectra present a second low-in-intensity peak in the region between 2 and 3 eV. Both the intensities and PRFs of such bands show the same trends already commented on for the first intense peak.
- Finally, two additional bands arise for all structures in the region between 3 and 4 eV (BEM) and 4-5 eV (ωFQ). It is worth noticing that for such a composite band, the trend reproduced by ωFQ PRFs is opposite with respect to the low-in-energy peaks, i.e., PRFs blueshift as the structures are enlarged. BEM PRFs are instead almost constant with an increase in the system's size.

In order to physically investigate these findings, imaginary ωFQ charges were depicted and rationalized in terms of the plasmon hybridization approach (Prodan et al., 2003a,b; Radloff and Halas, 2004; Wang et al., 2006a,b, 2007; Bardhan et al., 2009; Park and Nordlander, 2009). In particular, spherical nanodome plasmonic response can be represented by analyzing a simple model in which such a geometry is seen as resulting from the difference between a section of spherical NP and a section of a spherical cavity in an infinite Na structure (see **Figure 5B**). The direct consequence of such a model is that the plasmons arising in the nanodome can be viewed as the linear combination of the plasmons arising in the two pristine structures. In fact, the antisymmetric and symmetric combinations give rise to two plasmonic modes, which are named bonding and anti-bonding, respectively (see **Figures 5B,C**). Notice also that the studied nanodomes have cylindrical symmetry. Therefore, an electric field parallel or orthogonal to the symmetry axis activates three different plasmonic excitations. Two of them will be degenerate, i.e., where the external field is orthogonal to the symmetry axis. The two alternatives are graphically depicted in **Figures 5B,C**.

The main features of Na nanodome spectra can be rationalized in terms of the above simple model. In fact, the two excitations at lower energy can be related to bonding modes, as is confirmed by the graphical representation of the imaginary ωFQ charges calculated at PRFs (see **Figures 5D,E**, in which the two possible orientations of the electric field are considered). It is worth noticing that the two bonding modes are qualitatively different; in the case where the electric field is orthogonal to the symmetry axis (see **Figure 5D**), a BDP appears both in the external and in the internal surface of the shell, whereas in the other case (see **Figure 5E**), the basis of the shell is the only portion that is positively charged, and the external surface is globally negatively charged.

The two peaks at high energies (see **Figure 5A**) can instead be associated to the anti-bonding modes, which are placed at different PRFs depending on the direction of the external electric field. This is the reason why each computed spectrum is characterized by the presence of two peaks. Similarly to bonding modes, also in this case, we characterized the nature of the plasmonic modes by plotting the imaginary ωFQ charges calculated at PRFs (see **Figures 5D,E**). If the electric field is orthogonal to the symmetry axis, the anti-bonding mode is characterized by an opposite BDP on the internal and the external surfaces, exactly as predicted by the simple model in **Figure 5B**. In the orthogonal field polarization, such a mode is instead characterized by the internal surface negatively charged and the external positively charged, and the basis of the shell is almost zero charged. Again, all the present features can entirely be explained by the suggested model.

To conclude the discussion on Na nanodomes, it is worth remarking that **Figure 5A** reports isotropic cross-sections. Therefore, the bonding and antibonding modes result in a pair of peaks because co-axial and orthogonal polarizations are not degenerate. This can be further appreciated by looking at Figure S2 in **Supplementary Material**.

3.3. Silver and Gold Nanoparticles

Figure 6 presents BEM (top) and ωFQ (bottom) σ^{abs} of silver (left) and gold (right) pentagonal (**Figures 4A,B**) and cylindrical (**Figures 4C,D**) nanorods with radius $r = 2.8$ Å as a function of the length l (see **Figures 2A,B** for their structures). Similarly to the case of Na NPs, BEM and ωFQ intensities were normalized with respect to nanorod volumes and the number of NP atoms, respectively.

The ωFQ-calculated absorption cross-section of Ag nanorods (**Figure 6**, bottom, left) in both the considered geometries (i.e., pentagonal and circular section) is characterized by a sharp and intense peak independently of the length of the nanorod. Such a peak is related to BDP as in the case of Na nanorods (see **Figure 4**). A similar outcome is shown by Au NPs (**Figure 6**, bottom, right) in both geometrical arrangements, but in this case, the absorption band is much broader and lower in intensity. This is in agreement with previous work (Sinha-Roy et al., 2017) and is an expected consequence of the choice of ωFQ parameters, in particular τ, which in Au NPs is almost three times lower than in Ag NPs (see Equation 3 and **Tables S9–S11**). In both Ag and Au NPs, ωFQ computed PRFs redshift as the length of the nanorod is increased, again in agreement with previous work (Sinha-Roy et al., 2017) (see also **Figure 3**). We remark that Ag and Au ωFQ PRFs are in much better agreement with the corresponding *ab-initio* data reported by Sinha-Roy et al. (2017) (see **Figure 3**), thus confirming the validity of the proposed parametrization and the potentialities of ωFQ to describe the plasmonic character of noble metals, at least far from the inter-band region (Giovannini et al., 2019e). In addition, as already noticed in the case of Na nanorods (see **Figure 4**), each ωFQ spectrum is characterized by a second low-in-intensity peak at higher energies with respect to the most intense one, which can once again be related to high-order plasmons (octupolar, Rossi et al., 2015; Giovannini et al., 2019e).

Similarly to ωFQ, BEM Ag σ^{abs} (**Figure 6**, top, left) is characterized by a single absorption band whose maximum

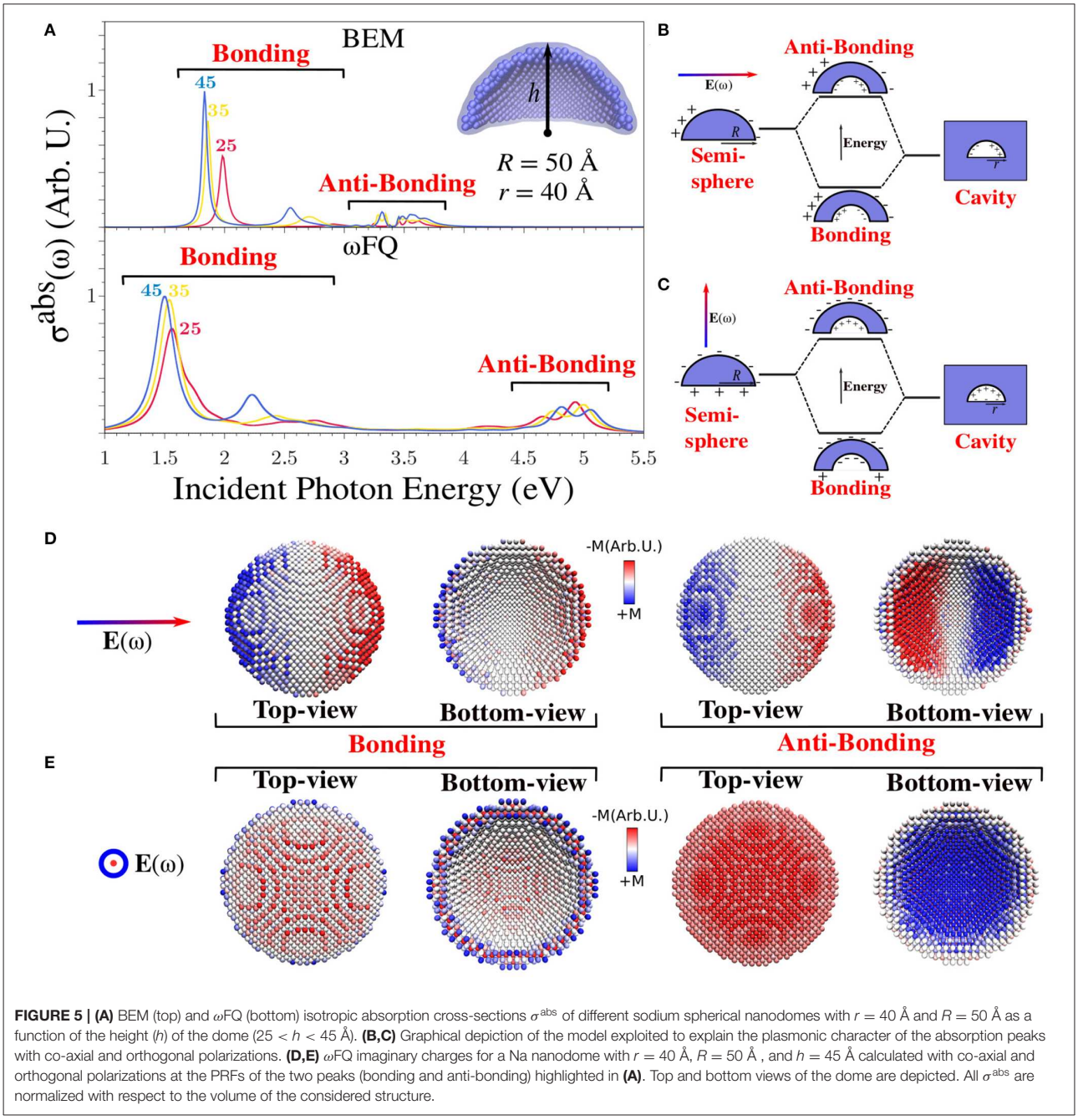

FIGURE 5 | (A) BEM (top) and ωFQ (bottom) isotropic absorption cross-sections σ^{abs} of different sodium spherical nanodomes with $r = 40$ Å and $R = 50$ Å as a function of the height (h) of the dome ($25 < h < 45$ Å). **(B,C)** Graphical depiction of the model exploited to explain the plasmonic character of the absorption peaks with co-axial and orthogonal polarizations. **(D,E)** ωFQ imaginary charges for a Na nanodome with $r = 40$ Å, $R = 50$ Å , and $h = 45$ Å calculated with co-axial and orthogonal polarizations at the PRFs of the two peaks (bonding and anti-bonding) highlighted in **(A)**. Top and bottom views of the dome are depicted. All σ^{abs} are normalized with respect to the volume of the considered structure.

redshifts, shrinks, and increases in intensity as the nanorod is elongated. Also, BEM spectra show an additional peak at higher energies, which is again related to octupolar plasmons. The same trend is also reported in the case of Au nanorods (**Figure 6**, top, right), which also exhibits a general decrease in the intensity that is in agreement with the ωFQ results. Deepening the comparison between ωFQ and BEM, the agreement between the two approaches increases as larger structures are considered. Such an agreement is not only due to the reproduction of PRFs but also to a general qualitative reproduction of the entire spectrum. Remarkably, such a finding might be justified by considering that small structures ($l \lesssim 26$ Å) are probably characterized by non-negligible edge effects, which cannot be modeled by continuum approaches such as BEM. In addition, we remark that the Drude function that is adopted in ωFQ (see Equation 3) does not consider possible interband transitions. Therefore, the observed discrepancies may also be connected to the differences between the experimental permittivity function

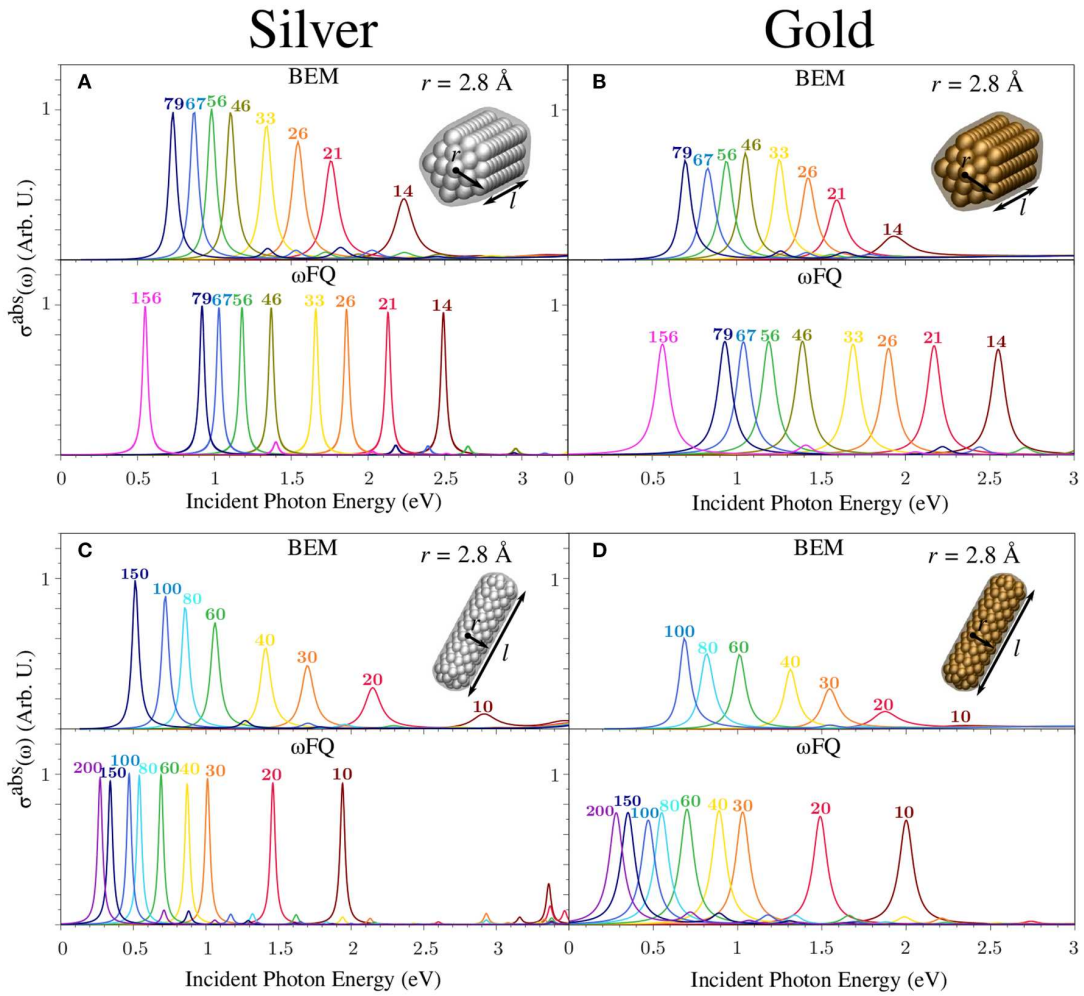

FIGURE 6 | BEM (top) and ωFQ (bottom) absorption cross-sections σ^{abs} of pentagonal **(A,B)** and cylindrical **(C,D)** silver (left) and gold (right) nanorods with r = 2.8 Å as a function of l (see labels). All σ^{abs} are normalized with respect to the volume of the considered structure.

$\varepsilon(\omega)$ (exploited in BEM) and the description given by the Drude model. We also notice that in the case of pentagonal nanorods, for both Ag and Au, BEM PRFs are redshifted with respect to the corresponding ωFQ values, whereas the opposite occurs in the case of cylindrical geometries. For pentagonal nanorods, this is in agreement with what has already been discussed in section 3.1. The reported discrepancies between ωFQ and BEM can be ascribed to the different geometrical arrangements of the nanorods. In fact, in the case that the geometry of the NP is characterized by the presence of edges (for BEM) or isolated atomic chains (for ωFQ), a redshift is expected. This is confirmed by comparing the BEM results for pentagonal (edges) and cylindrical (no edges) nanorods (**Figures 6A,C** top, respectively) and the ωFQ PRFs for pentagonal (no presence of atomic chains) and cylindrical (presence of atomic chains) nanorods (**Figures 6A,C** bottom, respectively). Therefore, the aforementioned differences between BEM and ωFQ are basically due to the fact that the BEM structures in **Figures 6A,B** are characterized by the presence of edges, whereas ωFQ structures do not have atomic chains. The opposite is seen in **Figures 6C,D**. Furthermore, we remark that the atomistic structures exploited in ωFQ are unambiguously determined by the lattice constant of the studied material. In BEM, in contrast, different approximations need to be done to represent a given atomistic structure (smooth/sharp edges, capping, etc.), and this constitutes a limitation of the BEM approach itself.

Let us now focus on calculated ωFQ (bottom) and BEM (top) σ^{abs} of a set of Ag and Au nanorods with fixed length l (150 Å) as a function of the radius r in both pentagonal and cylindrical shapes (see **Figure 7**). The comments presented above for **Figure 6** still hold. In fact, all ωFQ Ag absorption spectra are characterized by an intense and sharp peak followed by another low-in-intensity peak at higher energies. The former

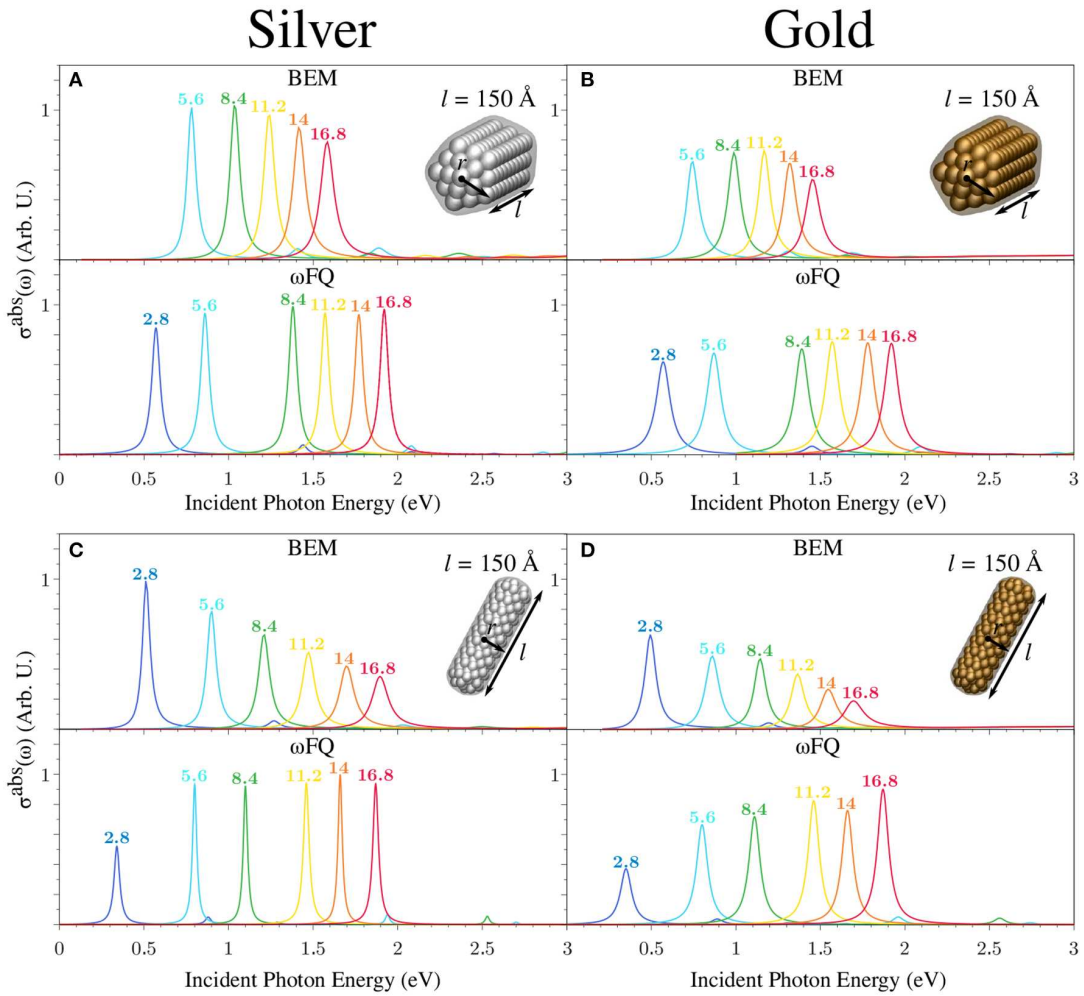

FIGURE 7 | BEM (top) and ωFQ (bottom) absorption cross-sections σ^{abs} of pentagonal **(A,B)** and cylindrical **(C,D)** silver (left) and gold (right) nanorods with $l = 150$ Å as a function of r (see labels). All σ^{abs} are normalized with respect to the volume of the considered structure.

is once again associated to a BDP, whereas the latter has an octupolar character. The most appreciable differences between Ag and Au spectra are associated with the smaller intensities and the larger broadening in the case of Au, as already commented on in the previous case. The same considerations applied to ωFQ results can be extended to BEM. It is worth noticing that, differently to the previous case (see **Figure 6**), the two approaches are nicely in agreement in reproducing PRFs of both Ag and Au cylindrical nanorods. Such an outcome can be explained by considering that the structures reported in **Figure 7** are much larger than those studied in **Figure 6**; thus, edge effects are expected to play a minor role. This, however, does not occur in the case of pentagonal nanorods, which show almost the same trend as that already discussed above for smaller nanorods. Such an outcome can be justified by the fact that BEM structures are affected by edge effects. In fact, BEM PRFs are redshifted with respect to BEM cylindrical nanorods (see **Figures 7A–C**, top). ωFQ PRFs for cylindrical/pentagonal nanorods are instead almost identical for the largest nanorods ($r \geq 11.2$ Å), thus confirming that edge effects become more and more negligible as the radius of the nanorod increases.

To conclude the discussion on Ag and Au NPs, we studied the absorption cross-section for a spherical nanodome with $r = 25$ Å and $R = 30$ Å as a function of the height of the dome, similarly to what we also reported in case of Na NPs. The results are graphically depicted in **Figures 8A,B** for Ag and Au structures, respectively. The outcomes already discussed in the case of Na nanodomes are, for the most part, confirmed. In fact, for both metals, σ^{abs} is characterized by an intense pair of peaks between 2 and 3 eV, of which the PRF redshifts as the NP size increases. Again, such bands are related to bonding plasmonic modes showing charge distributions almost identical to those depicted in **Figures 5D,E** (see also **Figure S2**). Notice

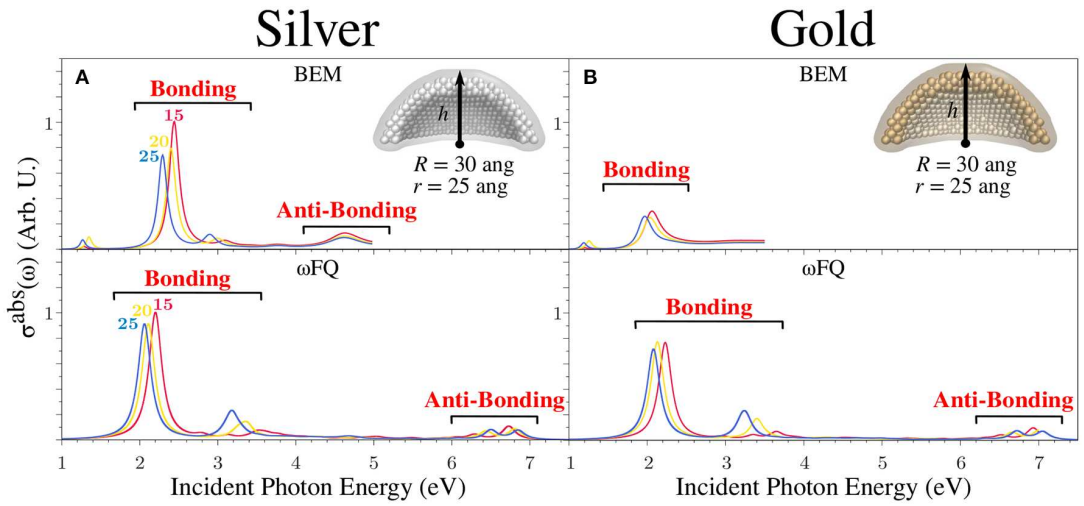

FIGURE 8 | BEM (top) and ωFQ (bottom) isotropic absorption cross-sections σ^{abs} of silver **(A)** and gold **(B)** spherical nanodomes with $r = 25$ Å and $R = 30$ Å as a function of h ($15 < h < 25$ Å). All σ^{abs} are normalized with respect to the volume of the considered structure.

that also in this case, the two polarizations (i.e., co-axial and orthogonal) give rise to two non-degenerate absorption peaks due to the symmetry breaking that has been introduced by cutting the pristine sphere in half (see also the Computational Details Section). In addition, ωFQ predicts a pair of two high-energy peaks, which can instead be related to antibonding plasmonic modes. Notice that the latter bands undergo a blueshift as the NP number of atoms increases, thus resulting in an opposite behavior with respect to that underlined in the case of the bonding modes. Finally, it is worth noticing that the discussed antibonding excitations are not fully reported for BEM. This is due to the fact that the experimental permittivity function ($\varepsilon(\omega)$) adopted to model the plasmonic response of the two metals (see Equation 8) is not defined in the considered energy range.

4. CONCLUSIONS

In this work, the potentialities of the atomistic ωFQ approach to describe the optical properties of sodium, silver, and gold NPs characterized by different geometrical arrangements have been investigated. The results have been compared with BEM, and theoretical analogies and differences between ωFQ and BEM have been discussed and analyzed in terms of the physical quantities underlying both approaches. The main difference between ωFQ and BEM lies in the fact that in the former, the atomistic nature of the NP is retained, whereas in the latter, the NP is modeled through its surface only. Despite such differences, both models describe the polarization in terms of complex charges, which are placed on each NP atom in the case of ωFQ, whereas, in BEM, they are located at points defined through the discretization procedure of the NP surface.

ωFQ and BEM have been applied to Na, Ag, and Au cylindrical and pentagonal (in the case of Ag and Au NPs) nanorods and spherical nanodomes. The results obtained with the two methods are nicely in agreement for Na nanorods, whereas some discrepancies are present for Na spherical nanodomes. For the latter, to explain the different plasmonic modes that arise in the absorption spectrum, the plasmon hybridization model has been applied (Bardhan et al., 2009; Park and Nordlander, 2009). In particular, both ωFQ and BEM predict bonding and anti-bonding plasmonic modes, which have been highlighted by plotting imaginary charges arising on the NP surfaces. Remarkably, the breaking of the spherical symmetry in the studied structures gives rise to two different non-degenerate plasmonic modes depending on the polarization of the incident electric field, i.e., co-axial or perpendicular to the symmetry axis. It is also worth noticing that some discrepancies are present in ωFQ and BEM PRFs of the different plasmonic modes, which may be related to edge effects and to interband transitions [which, in the case of Na, occur above 2 eV (Smith, 1969)].

Similar results have been obtained for Ag and Au structures. In the case of cylindrical and pentagonal nanorods, the discrepancies between ωFQ and BEM PRFs tend to disappear with an increase in the size of the studied structures. The results obtained with the two methods are similar in the case of metal nanodomes, for which bonding and anti-bonding plasmonic modes are correctly described by ωFQ. Antibonding excitations have not been studied by BEM, because the experimental permittivity function ($\varepsilon(\omega)$) of the two metals is not available in the considered energy range. Although this drawback can be easily overcome by modeling the permittivity function with a Drude model, the quality of BEM results would inevitably lose accuracy due to the inaccurate description of interband transitions.

To conclude, our results show that the novel ωFQ atomistic approach can effectively describe the optical properties of metal NPs far from the energy range of interband transitions. This

limitation can, however, be overcome by introducing in the ωFQ approach the physical features that are needed to correctly account for *d*-electrons in noble metals, e.g., by including an additional term in the response equations expressed in terms of an atomic dipole, similarly to what has recently been done by some of us in a different context (Giovannini et al., 2019a,c,d). Such an extension is currently under development and will be a topic of future communications.

DATA AVAILABILITY STATEMENT

The datasets generated for this study are available on request to the corresponding author.

AUTHOR CONTRIBUTIONS

LB ran the ωFQ calculations. GG ran the BEM calculations. TG wrote the stand-alone Fortran95 code for ωFQ calculations. TG, LB, and GG analyzed data and wrote the manuscript. TG, SC, and CC discussed and supervised the whole project. All authors revised and checked the draft.

FUNDING

This work has received funding from the European Research Council (ERC) under the European Union's Horizon 2020 research and innovation program (grant agreement No. 818064). GG and SC acknowledge funding from ERC under the grant ERC-CoG-681285 TAME-Plasmons. TG acknowledges funding from the Research Council of Norway through the grant TheoLight (grant no. 275506).

ACKNOWLEDGMENTS

We are thankful for the computer resources provided by the high-performance computer facilities of the SMART Laboratory (http://smart.sns.it/).

SUPPLEMENTARY MATERIAL

The Supplementary Material for this article can be found online at: https://www.frontiersin.org/articles/10.3389/fchem.2020.00340/full#supplementary-material

REFERENCES

Althoff, R., and Hertz, J. (1967). Measurement of the optical constants of Na and K in the range of wavelength from 2.5 to 10 μ. *Infrared Phys.* 7, 11–16. doi: 10.1016/0020-0891(67)90025-5

Angioni, A., Corni, S., and Mennucci, B. (2013). Can we control the electronic energy transfer in molecular dyads through metal nanoparticles? A QM/continuum investigation. *Phys. Chem. Chem. Phys.* 15, 3294–3303. doi: 10.1039/c2cp44010e

Anker, J. N., Hall, W. P., Lyandres, O., Shah, N. C., Zhao, J., and Van Duyne, R. P. (2008). Biosensing with plasmonic nanosensors. *Nat. Mater.* 7, 442–453. doi: 10.1038/nmat2162

Atwater, H. A., and Polman, A. (2010). Plasmonics for improved photovoltaic devices. *Nat. Mater.* 9:205. doi: 10.1038/nmat2629

Bade, W. (1957). Drude-model calculation of dispersion forces. I. General theory. *J. Chem. Phys.* 27, 1280–1284. doi: 10.1063/1.1743991

Bardhan, R., Mukherjee, S., Mirin, N. A., Levit, S. D., Nordlander, P., and Halas, N. J. (2009). Nanosphere-in-a-nanoshell: a simple nanomatryushka. *J. Phys. Chem. C* 114, 7378–7383. doi: 10.1021/jp9095387

Cappelli, C. (2016). Integrated QM/polarizable MM/continuum approaches to model chiroptical properties of strongly interacting solute-solvent systems. *Int. J. Quantum Chem.* 116, 1532–1542. doi: 10.1002/qua.25199

Chen, X., Moore, J. E., Zekarias, M., and Jensen, L. (2015). Atomistic electrodynamics simulations of bare and ligand-coated nanoparticles in the quantum size regime. *Nat. Commun.* 6:8921. doi: 10.1038/ncomms9921

Ciraci, C., Hill, R., Mock, J., Urzhumov, Y., Fernández-Dominguez, A., Maier, S., et al. (2012). Probing the ultimate limits of plasmonic enhancement. *Science* 337, 1072–1074. doi: 10.1126/science.1224823

Corni, S., Cappelli, C., Cammi, R., and Tomasi, J. (2001). Theoretical approach to the calculation of vibrational Raman spectra in solution within the polarizable continuum model. *J. Phys. Chem. A* 105, 8310–8316. doi: 10.1021/jp011079c

Corni, S., and Tomasi, J. (2001). Enhanced response properties of a chromophore physisorbed on a metal particle. *J. Chem. Phys* 114:3739. doi: 10.1063/1.1342241

Corni, S., and Tomasi, J. (2002). Surface enhanced Raman scattering from a single molecule adsorbed on a metal particle aggregate: a theoretical study. *J. Chem. Phys.* 116, 1156–1164. doi: 10.1063/1.1428349

de Abajo, F. G., and Howie, A. (2002). Retarded field calculation of electron energy loss in inhomogeneous dielectrics. *Phys. Rev. B* 65:115418. doi: 10.1103/PhysRevB.65.115418

Draine, B. T., and Flatau, P. J. (1994). Discrete-dipole approximation for scattering calculations. *JOSA A* 11, 1491–1499. doi: 10.1364/JOSAA.11.001491

Esteban, R., Borisov, A. G., Nordlander, P., and Aizpurua, J. (2012). Bridging quantum and classical plasmonics with a quantum-corrected model. *Nat. Commun.* 3:825. doi: 10.1038/ncomms1806

Fuchs, R. (1975). Theory of the optical properties of ionic crystal cubes. *Phys. Rev. B* 11:1732. doi: 10.1103/PhysRevB.11.1732

Gao, Y., Yuan, Z., and Gao, S. (2011). Semiclassical approach to plasmon-electron coupling and landau damping of surface plasmons. *J. Chem. Phys.* 134:134702. doi: 10.1063/1.3575185

Giannini, V., Fernández-Dominguez, A. I., Heck, S. C., and Maier, S. A. (2011). Plasmonic nanoantennas: fundamentals and their use in controlling the radiative properties of nanoemitters. *Chem. Rev.* 111, 3888–3912. doi: 10.1021/cr1002672

Giovannini, T., Ambrosetti, M., and Cappelli, C. (2018). A polarizable embedding approach to second harmonic generation (SHG) of molecular systems in aqueous solutions. *Theor. Chem. Acc.* 137:74. doi: 10.1007/s00214-018-2247-7

Giovannini, T., Grazioli, L., Ambrosetti, M., and Cappelli, C. (2019a). Calculation of ir spectra with a fully polarizable qm/mm approach based on fluctuating charges and fluctuating dipoles. *J. Chem. Theory Comput.* 15, 5495–5507. doi: 10.1021/acs.jctc.9b00574

Giovannini, T., Macchiagodena, M., Ambrosetti, M., Puglisi, A., Lafiosca, P., Lo Gerfo, G., et al. (2019b). Simulating vertical excitation energies of solvated dyes: from continuum to polarizable discrete modeling. *Int. J. Quantum Chem.* 119:e25684. doi: 10.1002/qua.25684

Giovannini, T., Puglisi, A., Ambrosetti, M., and Cappelli, C. (2019c). Polarizable QM/MM approach with fluctuating charges and fluctuating dipoles: the QM/FQFμ model. *J. Chem. Theory Comput.* 15, 2233–2245. doi: 10.1021/acs.jctc.8b01149

Giovannini, T., Riso, R. R., Ambrosetti, M., Puglisi, A., and Cappelli, C. (2019d). Electronic transitions for a fully polarizable qm/mm approach based on fluctuating charges and fluctuating dipoles: linear and corrected

linear response regimes. *J. Chem. Phys*. 151:174104. doi: 10.1063/1.5121396

Giovannini, T., Rosa, M., Corni, S., and Cappelli, C. (2019e). A classical picture of subnanometer junctions: an atomistic drude approach to nanoplasmonics. *Nanoscale* 11, 6004–6015. doi: 10.1039/C8NR09134J

Halas, N. J., Lal, S., Chang, W.-S., Link, S., and Nordlander, P. (2011). Plasmons in strongly coupled metallic nanostructures. *Chem. Rev*. 111, 3913–3961. doi: 10.1021/cr200061k

Hao, F., Nehl, C. L., Hafner, J. H., and Nordlander, P. (2007). Plasmon resonances of a gold nanostar. *Nano Lett*. 7, 729–732. doi: 10.1021/nl062969c

Haynes, W. (2014). *CRC Handbook of Chemistry and Physics*. Boca Raton, FL: CRC Press.

Hohenester, U. (2015). Quantum corrected model for plasmonic nanoparticles: a boundary element method implementation. *Phys. Rev. B* 91:205436. doi: 10.1103/PhysRevB.91.205436

Hohenester, U., and Trügler, A. (2012). MNPBEM–A Matlab toolbox for the simulation of plasmonic nanoparticles. *Comp. Phys. Commun*. 183, 370–381. doi: 10.1016/j.cpc.2011.09.009

Jensen, L. L., and Jensen, L. (2008). Electrostatic interaction model for the calculation of the polarizability of large noble metal nanoclusters. *J. Phys. Chem. C* 112, 15697–15703. doi: 10.1021/jp804116z

Jensen, L. L., and Jensen, L. (2009). Atomistic electrodynamics model for optical properties of silver nanoclusters. *J. Phys. Chem. C* 113, 15182–15190. doi: 10.1021/jp904956f

Jin, R., Cao, Y., Mirkin, C. A., Kelly, K., Schatz, G. C., and Zheng, J. (2001). Photoinduced conversion of silver nanospheres to nanoprisms. *Science* 294, 1901–1903. doi: 10.1126/science.1066541

Kneipp, K., Wang, Y., Kneipp, H., Perelman, L. T., Itzkan, I., Dasari, R. R., et al. (1997). Single molecule detection using surface-enhanced Raman scattering (SERS). *Phys. Rev. Lett*. 78:1667. doi: 10.1103/PhysRevLett.78.1667

Kreibig, U., and Fragstein, C. V. (1969). The limitation of electron mean free path in small silver particles. *Z. Physik* 224, 307–323. doi: 10.1007/BF01393059

Larsen, A. H., Mortensen, J. J., Blomqvist, J., Castelli, I. E., Christensen, R., Dulak, M., et al. (2017). The atomic simulation environment–A python library for working with atoms. *J. Phys. Condens. Matter*. 29:273002. doi: 10.1088/1361-648X/aa680e

Liebsch, A. (1993). Surface-plasmon dispersion and size dependence of Mie resonance: silver versus simple metals. *Phys. Rev. B* 48:11317. doi: 10.1103/PhysRevB.48.11317

Lim, D.-K., Jeon, K.-S., Kim, H. M., Nam, J.-M., and Suh, Y. D. (2010). Nanogap-engineerable Raman-active nanodumbbells for single-molecule detection. *Nat. Mater*. 9, 60–67. doi: 10.1038/nmat2596

Liu, P., Chulhai, D. V., and Jensen, L. (2017). Single-molecule imaging using atomistic near-field tip-enhanced Raman spectroscopy. *ACS Nano* 11, 5094–5102. doi: 10.1021/acsnano.7b02058

Maier, S. A. (2007). *Plasmonics: Fundamentals and Applications*. New York, NY: Springer Science & Business Media. doi: 10.1007/0-387-37825-1

Maier, S. A., Kik, P. G., Atwater, H. A., Meltzer, S., Harel, E., Koel, B. E., et al. (2003). Local detection of electromagnetic energy transport below the diffraction limit in metal nanoparticle plasmon waveguides. *Nat. Mater*. 2:229. doi: 10.1038/nmat852

Mayer, A. (2007). Formulation in terms of normalized propagators of a charge-dipole model enabling the calculation of the polarization properties of fullerenes and carbon nanotubes. *Phys. Rev. B* 75:045407. doi: 10.1103/PhysRevB.75.045407

Mennucci, B., and Corni, S. (2019). Multiscale modelling of photoinduced processes in composite systems. *Nat. Rev. Chem*. 3, 315–330. doi: 10.1038/s41570-019-0092-4

Mie, G. (1908). Beiträge zur optik trüber medien, speziell kolloidaler metallösungen. *Ann. Phys*. 330, 377–445. doi: 10.1002/andp.19083300302

Molina, R. A., Weinmann, D., and Jalabert, R. A. (2002). Oscillatory size dependence of the surface plasmon linewidth in metallic nanoparticles. *Phys. Rev. B* 65:155427. doi: 10.1103/PhysRevB.65.155427

Morton, S. M., and Jensen, L. (2010). A discrete interaction model/quantum mechanical method for describing response properties of molecules adsorbed on metal nanoparticles. *J. Chem. Phys*. 133:074103. doi: 10.1063/1.3457365

Morton, S. M., and Jensen, L. (2011). A discrete interaction model/quantum mechanical method to describe the interaction of metal nanoparticles and molecular absorption. *J. Chem. Phys*. 135:134103. doi: 10.1063/1.3643381

Moskovits, M. (1985). Surface-enhanced spectroscopy. *Rev. Mod. Phys*. 57:783. doi: 10.1103/RevModPhys.57.783

Muehlschlegel, P., Eisler, H.-J., Martin, O. J., Hecht, B., and Pohl, D. (2005). Resonant optical antennas. *Science* 308, 1607–1609. doi: 10.1126/science.1111886

Myroshnychenko, V., Rodriguez-Fernández, J., Pastoriza-Santos, I., Funston, A. M., Novo, C., Mulvaney, P., et al. (2008). Modelling the optical response of gold nanoparticles. *Chem. Soc. Rev*. 37, 1792–1805. doi: 10.1039/b711486a

Neuman, T., Esteban, R., Casanova, D., Garcia-Vidal, F. J., and Aizpurua, J. (2018). Coupling of molecular emitters and plasmonic cavities beyond the point-dipole approximation. *Nano Lett*. 18, 2358–2364. doi: 10.1021/acs.nanolett.7b05297

Nie, S., and Emory, S. R. (1997). Probing single molecules and single nanoparticles by surface-enhanced raman scattering. *Science* 275, 1102–1106. doi: 10.1126/science.275.5303.1102

Palik, E. D. (1997). *Handbook of Optical Constants of Solids*. San Diego, CA: Elsevier.

Park, T.-H., and Nordlander, P. (2009). On the nature of the bonding and antibonding metallic film and nanoshell plasmons. *Chem. Phys. Lett*. 472, 228–231. doi: 10.1016/j.cplett.2009.03.029

Payton, J. L., Morton, S. M., Moore, J. E., and Jensen, L. (2012). A discrete interaction model/quantum mechanical method for simulating surface-enhanced Raman spectroscopy. *J. Chem. Phys*. 136:214103. doi: 10.1063/1.4722755

Payton, J. L., Morton, S. M., Moore, J. E., and Jensen, L. (2013). A hybrid atomistic electrodynamics-quantum mechanical approach for simulating surface-enhanced Raman scattering. *Acc. Chem. Res*. 47, 88–99. doi: 10.1021/ar400075r

Pérez-González, O., Zabala, N., Borisov, A., Halas, N., Nordlander, P., and Aizpurua, J. (2010). Optical spectroscopy of conductive junctions in plasmonic cavities. *Nano Lett*. 10, 3090–3095. doi: 10.1021/nl1017173

Prodan, E., Nordlander, P., and Halas, N. (2003a). Electronic structure and optical properties of gold nanoshells. *Nano Lett*. 3, 1411–1415. doi: 10.1021/nl034594q

Prodan, E., Radloff, C., Halas, N. J., and Nordlander, P. (2003b). A hybridization model for the plasmon response of complex nanostructures. *Science* 302, 419–422. doi: 10.1126/science.1089171

Radloff, C., and Halas, N. J. (2004). Plasmonic properties of concentric nanoshells. *Nano Lett*. 4, 1323–1327. doi: 10.1021/nl049597x

Raja, W., Bozzola, A., Zilio, P., Miele, E., Panaro, S., Wang, H., et al. P. (2016). Broadband absorption enhancement in plasmonic nanoshells-based ultrathin microcrystalline-si solar cells. *Sci. Rep*. 6:24539. doi: 10.1038/srep24539

Rakić, A. D., Djurisić, A. B., Elazar, J. M., and Majewski, M. L. (1998). Optical properties of metallic films for vertical-cavity optoelectronic devices. *Appl. Opt*. 37, 5271–5283. doi: 10.1364/AO.37.005271

Rossi, T. P., Zugarramurdi, A., Puska, M. J., and Nieminen, R. M. (2015). Quantized evolution of the plasmonic response in a stretched nanorod. *Phys. Rev. Lett*. 115:236804. doi: 10.1103/PhysRevLett.115.236804

Santhosh, K., Bitton, O., Chuntonov, L., and Haran, G. (2016). Vacuum RABI splitting in a plasmonic cavity at the single quantum emitter limit. *Nat. Commun*. 7:11823. doi: 10.1038/ncomms11823

Shuford, K. L., Ratner, M. A., Gray, S. K., and Schatz, G. C. (2006). Finite-difference time-domain studies of light transmission through nanohole structures. *Appl. Phys. B* 84, 11–18. doi: 10.1007/s00340-006-2218-x

Sinha-Roy, R., Garcia-Gonzalez, P., Weissker, H.-C., Rabilloud, F., and Fernandez-Dominguez, A. I. (2017). Classical and ab initio plasmonics meet at sub-nanometric noble metal rods. *ACS Photonics* 4, 1484–1493. doi: 10.1021/acsphotonics.7b00254

Smith, N. (1969). Optical constants of sodium and potassium from 0.5 to 4.0 eV by split-beam ellipsometry. *Phys. Rev*. 183:634. doi: 10.1103/PhysRev.183.634

Vukovic, S., Corni, S., and Mennucci, B. (2008). Fluorescence enhancement of chromophores close to metal nanoparticles. optimal setup revealed by the polarizable continuum model. *J. Phys. Chem. C* 113, 121–133. doi: 10.1021/jp808116y

Wang, H., Brandl, D. W., Le, F., Nordlander, P., and Halas, N. J. (2006a). Nanorice: a hybrid plasmonic nanostructure. *Nano Lett*. 6, 827–832. doi: 10.1021/nl060209w

Wang, H., Brandl, D. W., Nordlander, P., and Halas, N. J. (2007). Plasmonic nanostructures: artificial molecules. *Acc. Chem. Res*. 40, 53–62. doi: 10.1021/ar0401045

Wang, H., Wu, Y., Lassiter, B., Nehl, C. L., Hafner, J. H., Nordlander, P., and Halas, N. J. (2006b). Symmetry breaking in individual plasmonic nanoparticles. *Proc. Natl. Acad. Sci. U.S.A*. 103, 10856–10860. doi: 10.1073/pnas.0604003103

Ye, J., Lagae, L., Maes, G., Borghs, G., and Van Dorpe, P. (2009). Symmetry breaking induced optical properties of gold open shell nanostructures. *Opt. Express* 17, 23765–23771. doi: 10.1364/OE.17.023765

Conflict of Interest: The authors declare that the research was conducted in the absence of any commercial or financial relationships that could be construed as a potential conflict of interest.

Chapter 6

In silico design of graphene plasmonic hot-spots

Nanoscale Advances

ROYAL SOCIETY OF CHEMISTRY

PAPER

View Article Online
View Journal | View Issue

Cite this: *Nanoscale Adv.*, 2022, **4**, 2294

Received 7th February 2022
Accepted 15th April 2022

DOI: 10.1039/d2na00088a

rsc.li/nanoscale-advances

In silico design of graphene plasmonic hot-spots†

Luca Bonatti, Luca Nicoli, Tommaso Giovannini * and Chiara Cappelli *

We propose a route for the rational design of engineered graphene-based nanostructures, which feature enormously enhanced electric fields in their proximity. Geometrical arrangements are inspired by nanopatterns allowing single molecule detection on noble metal substrates, and are conceived to take into account experimental feasibility and ease in fabrication processes. The attention is especially focused on enhancement effects occurring close to edge defects and grain boundaries, which are usually present in graphene samples. There, very localized hot-spots are created, with enhancement factors comparable to noble metal substrates, thus potentially paving the way for single molecule detection from graphene-based substrates.

1. Introduction

Graphene is capable of strongly confining light down to the nanometer scale due to the formation of highly localized surface plasmons under the effect of external electromagnetic radiation.[1–3] Also, plasmons in graphene have the peculiar property that their plasmon resonance frequency (PRF) can be tuned by adjusting shape, size, gating or doping of the samples.[1] For these reasons, plasmons are the cornerstone of several technological applications, ranging from quantum information and telecommunication to biological sensing.[1,4,5] Similarly to metal nanoparticles (MNPs), graphene may be exploited to enhance the spectral response of adsorbed molecular systems, due to its plasmonic properties[6–13] that give rise to local electric field enhancement.[14–21] However, for specific MNP geometrical arrangements, single molecule detection becomes possible due to huge field enhancements (*i.e.* the creation of the so-called hot-spots),[22–27] whereas such behavior has not been confirmed for graphene nanostructures. In fact, pristine graphene has been used as a substrate for the so-called graphene enhanced Raman scattering (GERS), but the measured enhancement in the molecular Raman signal is orders of magnitude lower than for MNPs.[28] For this reason, the measured GERS enhancement has been attributed to chemical/charge transfer effects and only marginally related to electric field confinement,[28,29] thus substantially hampering the broad application of graphene as a substrate for surface enhanced Raman spectroscopies (SERS).[5,28] However, is it possible to achieve the desired field enhancement to effectively exploit graphene-based nanostructures in enhanced spectroscopy? In this work, we propose a computationally driven rational design of structural patterns, based on a fully atomistic approach that we have recently developed.[30–33] Remarkably, our design route can guide *a priori* the definition of ideal structural patterns with the desired enhancement features.

The geometrical patterns investigated fall within two categories. Firstly, we take inspiration from metal nanoaggregates that allow single molecule detection,[34–37] and that bear plasmonic nanocavity hot-spots. Examples are MNP dimers or oligomers commonly endowed with tips defined at the atomic level.[38–41] Although these geometries have already been extensively studied for the case of metal substrates,[26,34,38,40,42–45] full understanding on how such arrangements can tune field enhancement in graphene-based materials is still missing.

The second set of structures that we investigate are specifically tailored to reach enhancement factors that would allow single molecule detection on graphene. More specifically, we design atomically defined hot-spots arising in the proximity of edge defects and grain boundaries. In particular, we focus on systems that can be experimentally obtained, *e.g.* bite defects arising in graphene nanoribbons (GNRs)[46–50] or cracks propagating in polycrystalline graphene (PCG) under the effect of mechanical strain.[51–53] Therefore, we showcase the pivotal role of atomically defined defects in increasing enhancement and field confinement in graphene-based nanostructures.

The manuscript is organized as follows. In the next section, we briefly validate the accuracy of our computational model to predict enhancement factors. Such kind of investigation is necessary to move on to predict field enhancement and localization in carbon-based systems inspired by MNPs geometrical patterns, such as graphene nanocones monomers and dimers. Then, we study electric field enhancement in systems endowed with edge defects, grain boundaries and cracks, thus suggesting novel experimental setups for single molecule detection

Scuola Normale Superiore, Piazza dei Cavalieri 7, 56126 Pisa, Italy. E-mail: tommaso.giovannini@sns.it; chiara.cappelli@sns.it

† Electronic supplementary information (ESI) available: ωFQ induced electric field. Computational details. Further validation of ωFQ model. Plasmonic properties of the systems studied in Fig. 3–5. See https://doi.org/10.1039/d2na00088a

applications. Finally, a brief summary and future perspectives of this work end the manuscript.

2. Methods

The optical properties of graphene-based nanostructures are studied by exploiting ωFQ, which is a classical, fully atomistic approach, which modulates Drude conduction with quantum tunneling effects.[30–33] In particular, each atom is endowed with a complex-valued charge q_i, which adjusts to the external oscillating electric field $E(\omega)$. The set of charges $\mathbf{q}$ is obtained by solving an equation of motion, where charge-exchange between atoms is governed by a Drude mechanism, and modulated through quantum tunneling. In the frequency domain, the classical ωFQ equation of motion for charges $\mathbf{q}$ in graphene-based materials reads:[32]

$$-i\omega q_i = \frac{2\tau v_F}{1-i\omega\tau}\sqrt{\frac{n_{2D}}{\pi}}\sum_j f(l_{ij})\frac{A_{ij}}{l_{ij}}\left(\mu_j^{el}-\mu_i^{el}\right) \quad (1)$$

where ω is the frequency of the external electric field, τ the relaxation time, v_F the Fermi velocity, and n_{2D} the 2D-density of graphene. A_{ij} is the effective area connecting the atoms i and j, l_{ij} their distance, μ_i^{el} the electrochemical potential of atom i and $f(l_{ij})$ is a damping function taking into account quantum tunneling, by allowing charge exchange among nearest neighbor atoms and exponentially decreasing when distance increases. Thus, $f(l_{ij})$ introduces an additional charge-exchange mechanism different from that governed by the classical Drude model.[32] Notice that in this way ωFQ can perfectly reproduce the plasmonic behavior of metal nanoparticles characterized by subnanometer junctions, where quantum tunneling effects are crucial.[30,42,54–58] The $f(l_{ij})$ step function, defining the quantum tunneling mechanism, reads:

$$f(l_{ij}) = \frac{1}{1+\exp\left[-d\left(\frac{l_{ij}}{sl_{ij}^0}-1\right)\right]} \quad (2)$$

where l_{ij}^0 is the equilibrium distance between two first neighbors (*i.e.* $l_{ij}^0 = 1.42$ Å),[59] whereas d and s determine the position of the inflection point and the thickness of the curve, respectively.[30,32] Also, notice that spill-out and surface-enabled Landau damping are not currently included in our classical modeling of graphene.[56,60–62] The effective mass is set to $m^* = \sqrt{\pi n_{2D}}/v_F$,[59] whereas the Fermi energy is defined as $E_F = \hbar v_F\sqrt{\pi n_{2D}}$, leading to an electronic density which depends on E_F, which can be tuned according to the experimentally applied gating. The external electric field induces an electric field on the nanostructure, which is calculated from the Gaussian charge distributions on each atom. Unless otherwise stated, in all calculations we set $E_F = 400$ meV, $\tau = 600$ a.u. (*i.e.* 14.5 fs) and $v_F = 10^6$ m s^{-1} τ is fitted against reference *ab initio*[63] data in order to take into account scattering processes leading to plasmon relaxation (see Fig. 1). In particular, for plasmon energies above the phonon threshold energy (of ≈0.2 eV), the electron–phonon coupling dominates the plasmon decay and the scattering time becomes of the order of 10^{-14} s.[64–68] Therefore, the fitted τ = 14.5 fs takes into account both decay channels.

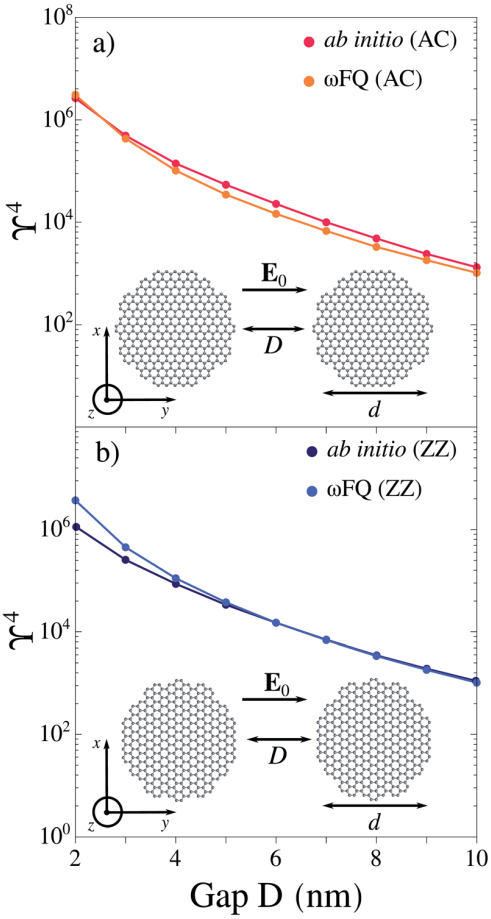

Fig. 1 ωFQ and *ab initio* (reproduced from ref. 63) Υ^4 values for (a) AC–AC and (b) ZZ–ZZ graphene dimers (d = 20 nm) as a function of the gap width D. The graphene Fermi energy is E_F = 0.4 eV for each configuration.

3. Results and discussion

3.1 Model validation

We first study the electric field enhancement ($\Upsilon = |\mathbf{E}|/|\mathbf{E}_0|$) exhibited by planar graphene dimeric nanoantennas (see Sec. S1 and S3 in the ESI†). In particular, we consider monomers with circular shape (with diameter $d \sim 20$ nm), and dimers obtained by coupling armchair (AC) or zig-zag (ZZ) graphene monomers at a distance D (see Fig. 1a and b for their structures). In our simulations, the external electric field is polarized along the y direction (see Fig. 1a and b). We calculate the field enhancement associated with GERS process, which is proportional to Υ^4,[21] at the center of mass of the whole system, in the graphene plane (*i.e.* $z = 0$ nm), at the PRF of each dimer (see also Sec. S3 in the ESI†). For both AC and ZZ configurations, the considered PRF is associated with a boundary dipolar plasmon (BDP), *i.e.* a dipolar plasmon arises in each monomer. In Fig. 1a and b, ωFQ results are compared with *ab initio* data reproduced

from ref. 63; the agreement between the two methods is impressive, thus demonstrating the level of reliability of the classical ωFQ method. Only a minor discrepancy is observed for ZZ–ZZ with $D = 2$ nm gap. This is probably due to edge effects which cause an increase of the field confinement in the proximity of the gap and, as a consequence, a slight increase in the field enhancement. Such edge effects become negligible by increasing the gap ($D \geq 4$ nm). In line with *ab initio* results,[63] ωFQ predicts the maximum field enhancement for the smallest gap ($D = 2$ nm) and a rapid decrease as the width of the nanojunction increases. Additional comparison between ωFQ and *ab initio* results for selected circular and triangular graphene-based arrangements are reported in Sec. S3 of the ESI,† showing again almost perfect agreement. These findings confirm the reliability of ωFQ to describe the electric field enhancement in graphene-like structures.

3.2 Pristine graphene sheets

We now take advantage of ωFQ favourable computational scaling,[33] to study electric field enhancement in several graphene disks of increasing size (see also Sec. S4 in the ESI†), with a diameter D from 2 nm (112 atoms) to 200 nm (more than 1.1 million atoms). In Fig. 2, the electric field is computed at the center of the disk, at $d = 3.5$ Å from the substrate (in line with the average adsorption distance of molecules on graphene[7,69,70]), and at distance $s = 3.5$ Å from the side of the disk. Both enhancements are computed at the PRF of the dipolar plasmon mode of each disk (see inset in Fig. 2). We first focus on the enhancement computed at the center of the disk. Υ^4 decreases as the disk size increases, however, for small diameters, Υ^4 increases due to edge effects, which become negligible for $D \geq$ 20 nm. Remarkably, for diameters typically exploited in GERS experimental setups (*i.e.* $D \gg 50$ nm), the enhancement is strongly reduced and tends to $\Upsilon^4 \sim 40$ for $D = 200$ nm. On the other hand, Υ^4 calculated at the edges is three orders of magnitude larger than the values at the center (see right axis in Fig. 2). In particular, Υ^4 increases with the dimension of the disk and converges to $\Upsilon^4 \approx 8.0 \times 10^5$ for $D \geq 120$ nm. However, notice that such large Υ^4 values rapidly decay by receding from the edges, bringing no benefit to potential spectral enhancements in case of adsorbed molecular systems, which are generally placed away from edges.

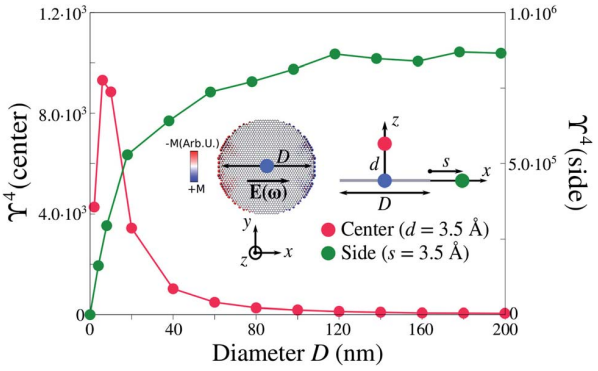

Fig. 2 Calculated Υ^4 for pristine graphene disks as a function of the diameter D. Values are computed at the dipolar plasmon mode (see inset for a graphical representation) at two specific points: the center of the disk (blue dot) at distance $d = 3.5$ Å (red dot), and at a distance $s = 3.5$ Å from the edge (green dot). The Fermi energy is equal to $E_F = 0.4$ eV in all calculations.

3.3 Graphene tips

We focus on graphene tips based on 3D bow-tie antennas obtained by pairing two hollow carbon nanocones forming a nanocavity (see Fig. 3a). Such structures are inspired by the graphene 2D bow-tie antennas which we studied above to validate the method.[63,71,72] Hollow graphene nanocones have been experimentally reported.[73–76] In addition, graphene nanocones are currently exploited for the encapsulation of gold tips in atomic force microscopy (AFM) experiments to increase their mechanical stability.[77] The studied geometries are constructed by removing a slice of α angle from a circular graphene sheet, and welding together the two parts, for a given height h (see Fig. 3a). By varying both α and h, the β angle defining the sharpness can easily be tuned. Here we select $\beta = 30°$ and $\beta = 40°$ to study the dependence of Υ^4 on the nanocone shrinking. In fact, the nanocones have a very sharp, atomistically defined, vertex, which is constituted of 3 ($\beta = 30°$) or 4 carbon atoms ($\beta = 40°$). The considered 3D bow-ties are formed by coupling two facing nanocones at distance D; electric field is always polarized along the axis connecting them.

Computed Υ^4 values for the boundary dipolar plasmon mode (see S5 in the ESI†) at the center of the gap as a function of D are reported in Fig. 3b. The maximum value of $|\mathbf{E}|/|\mathbf{E}_0|$ (2.0×10^3) corresponds to $D = 2$ Å for both configurations, and rapidly decreases as D increases. $|\mathbf{E}|/|\mathbf{E}_0|$ is larger for the structures with $\beta = 30°$, due to the presence of a sharper tip, although computed fields are of the same order of magnitude. Also, $|\mathbf{E}|/|\mathbf{E}_0|$ is strongly reduced for $D = 1$ Å, however the two monomers are almost covalently bonded at this distance and thus a dramatic change in their optical properties is expected.

In order to fully characterize the field enhancement, the local character of the enhanced electric field can be quantified. Such a feature is deeply connected to the actual resolution of surface enhanced spectral signals. By following ref. 44 and 78, the effective localization area A is defined as:

$$A = \frac{1}{h}\int_V \frac{|E(x,\ y,\ z)|^2}{|E_{\max}|^2}\mathrm{d}V \qquad (3)$$

where E and $E_{\max}$ are the induced field and its maximum values calculated in a thin slab of volume V and thickness $h = 2$ Å parallel to the field direction, centered in the middle of the gap for each distance D. Computed A values as a function of D are reported in Fig. 3b. The localization of the electric field rapidly increases as the gap between the two cones increases (for both β angles), however A remains well below 1 nm^2, *i.e.* much lower than typical values for metal picocavities. The field locality can be further appreciated by plotting the electric field values in the plane parallel to the field direction (see Fig. 3b for the 3D bow-tie with $D = 5$ Å). Clearly, structures with $\beta = 30°$ show the

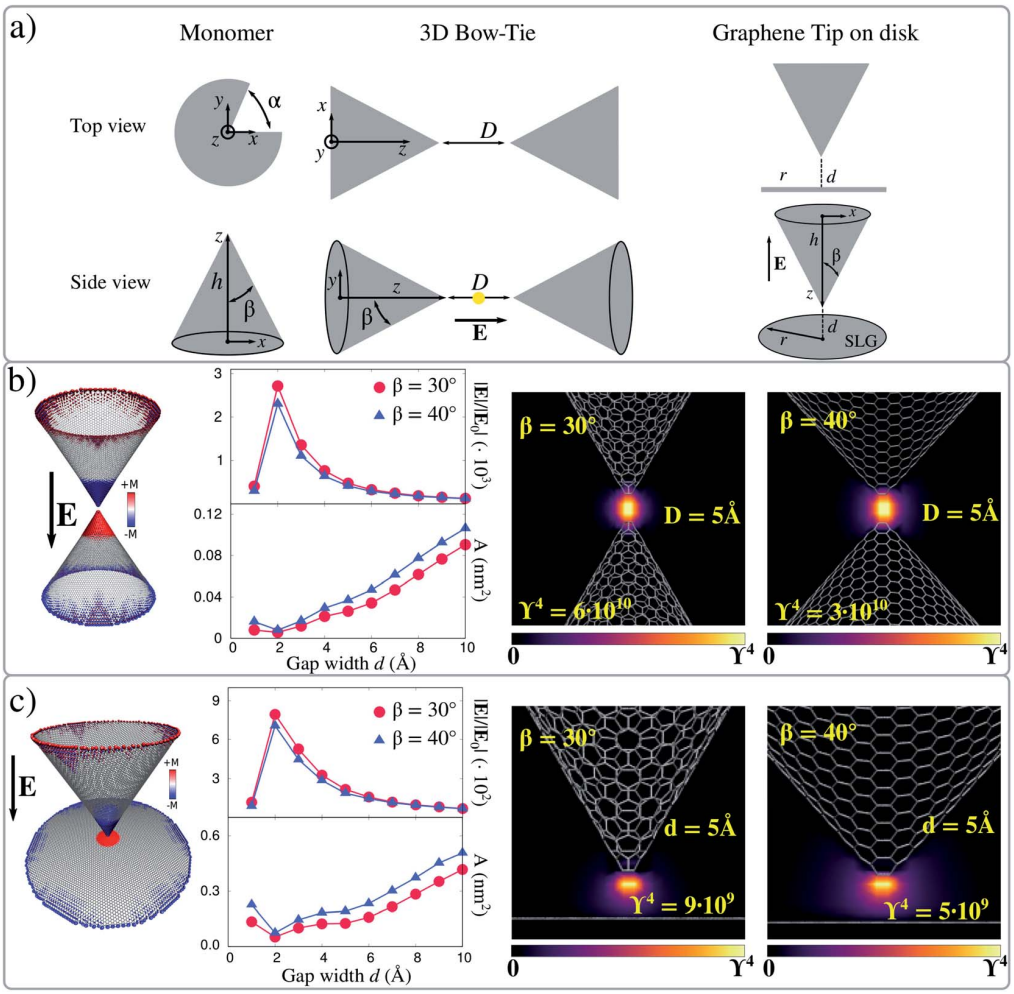

Fig. 3 (a) Geometrical parameters of graphene-based nanocones, 3D bow-ties and graphene tip-disks. (b) 3D bow-tie electric field enhancement factors ($|\mathbf{E}|/|\mathbf{E}_0|$ and Υ^4) and localization area (A) for both $\beta = 30°$ and $\beta = 40°$, as a function of the gap width (D) calculated at the boundary dipolar plasmon (see left panel) in the center of the gap. $\beta = 30°$ and $\beta = 40°$ electric field enhancement factors color map for 3D bow-tie nanostructure with $D = 5$ Å. (c) Graphene tip-disk electric field enhancement factors ($|\mathbf{E}|/|\mathbf{E}_0|$ and Υ^4) and localization area (A) for both $\beta = 30°$ and $\beta = 40°$, as a function of the gap width (d) calculated at the boundary dipolar plasmon (see left panel) in the center of the gap. $\beta = 30°$ and $\beta = 40°$ electric field enhancement factors color maps for graphene tip-disk nanostructure with $d = 5$ Å. The Fermi level is set to $E_F = 0.4$ eV for each configuration.

largest enhancement values, due to the higher cone sharpness, which, as stated above, is responsible for a larger plasmon confinement. However, for both β angles, Υ^4 is of the order of 10^{10}, thus a huge electric field enhancement comparable to what can be obtained with MNPs is expected. Also, notice that the obtained Υ^4 is four orders of magnitude larger that the value we obtained for the monomeric moiety, thus demonstrating the relevance of creating a subnanometric junction (see Sec. 5 in the ESI†).

An alternative geometrical arrangement can be designed by coupling a tip and a sheet, where a molecular system can potentially be deposited, similarly to what is done in case of tip enhanced spectroscopies.[34,38–40] Therefore, plasmonic picocavities can be created by placing a graphene sheet (in our case, a graphene disk with radius 10 nm) at close distance from the apex of a nanocone (see Fig. 3a). Also in this case, we perform the same simulations as for the 3D bow-tie system, by varying the gap between the sheet and the apex (d) from 1 to 10 Å. The electric field enhancement is calculated at the boundary dipolar plasmon resonance frequency, which is associated with a dipolar mode involving both the cone and the graphene disk (see Fig. 3c). $|\mathbf{E}|/|\mathbf{E}_0|$ rapidly decreases as the gap increases, while the opposite trend is observed for the effective localization area A, which is in this case computed for a slice centered in the middle of the gap. The same also holds for small gaps, for which the two structures are bonded. Finally, Υ^4 is graphically reported for both $\beta = 30$ and $\beta = 40°$ and $d = 5$ Å, as computed in the plane parallel to the electric field direction. For both angles, Υ^4 is about 10^9, thus one order of magnitude lower than for 3D bow-ties. This behavior is expected, because in tip-disk

structures a single tip is responsible for the huge electric field enhancement. However, this geometrical arrangement is promising and could be exploited in GERS experiments. In fact, it returns enhancement factors that, according to our calculations, could be up to seven orders of magnitude larger than those commonly reached in current GERS experiments exploiting pristine graphene as substrates. Also, it might provide huge field localization, thus allowing excellent spectral resolution. To conclude, for both 3D bow-ties and tip-disk arrangements, we focused on the dipolar plasmon where charges accumulate near the tips of both structures. Remarkably, the dipolar nature of these plasmon modes does not change by increasing the size of these systems.

3.4 Bite defects

We now move to investigate structures bearing atomic-scale defects. We first focus on AC and ZZ graphene nanoribbons. Their geometries are constructed according to the experimental structures reported in ref. 46 (see Fig. 4). In particular, the number of missing rings forming the bite defects and the relative distance between two adjacent defects resemble those experimentally measured.[46] There, atomically precise fabrication methods are exploited, which in principle allow for a deep control of the system's geometry.[50] However, the resulting samples may contain a certain percentage of structural disorder due to missing benzene rings resulting from the synthesis.[48,49]

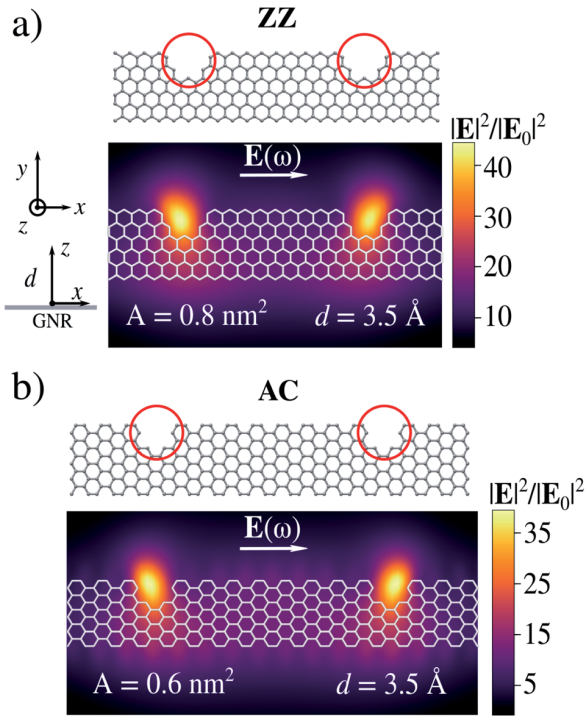

Fig. 4 Geometries and electric field enhancement factor ($|\mathbf{E}|^2/|\mathbf{E}_0|^2$) color maps for ZZ (a) and AC (b) graphene nanoribbons with bite defects. Color maps are calculated at distance d = 3.5 Å from the nanostructure. The Fermi energy is set equal to E_F = 0.4 eV.

These defects are known as bite defects and affect charge transport along the nanoribbon through charge confinement.[46,47]

Electric field enhancements ($|\mathbf{E}|^2/|\mathbf{E}_0|^2$) for both AC and ZZ GNRs with bite defects are computed at their PRFs, on a plane placed at d = 3.5 Å (see Fig. 4). When the incident electric field is polarized along the x-direction, *i.e.* the system main axis, the plasmon excitation is associated with a localization of charge around the bite, in both AC or ZZ configurations. Such localization is associated with Υ^4 larger than 10^3 at d = 3.5 Å. Thus, bite defects strongly trap plasmons, leading to the formation of hot-spots. Similar to the previous cases, we can quantify the local character of the enhanced electric field by means of its effective localization area A, which is reported in Fig. 4. The induced electric field is localized inside the bite and the effective area is subnanometric. Interestingly, in this case the huge atomistic localization of the electric field follows the presence of a hole in the structure, whereas in more common nanostructures tips/needles are exploited.

From the numerical point of view, the enhancement is much lower than in the case of cone-based structures (see above). A possible strategy to increase the induced fields would consist of exploiting one of the most peculiar properties of graphene, *i.e.* the Fermi level tunability. In fact, by increasing the Fermi energy (E_F), the number of electrons involved in the collective excitation increases, and in turn also the electric field. Thus, we vary E_F from 0.2 eV to 1.0 eV (see Section S6 in the ESI†), which is a range experimentally achievable.[4,79] The enhancement factors increase by increasing E_F, without any loss in the induced fields local character. We finally notice that, similar to the corresponding experimental setups, the systems are composed of a relatively small number of atoms; therefore, even larger field enhancement factors are expected for bigger nanostructures.

3.5 Strained polycrystalline graphene sheets

In this section we focus on a 40 nm × 40 nm polycrystalline graphene (PCG) sheet, as shown in Fig. 5a. The interest in studying such structure is driven by two reasons. First, PCGs are experimentally accessible.[51–53,80–84] Secondly, as we have already

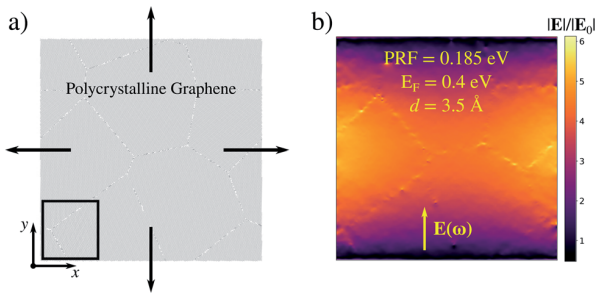

Fig. 5 (a) Graphical representation of the stretching process of a PCG sheet of 40 nm of side. The black box highlights the region where the maximum field enhancement for the stretched structure is computed. (b) Υ color map arising for the pristine PCG sheet at rest. The Fermi energy is set to 0.4 eV.

shown and discussed above, the generation of high field enhancement and confinement, *i.e.* hot-spots, in large graphene-based systems is particularly challenging.[28]

To create regions characterized by large electric field enhancement and confinement, we apply a mechanical stress to PCG in terms of an isotropic strain. Note that dimensions comparable with those exploited in the present work (40 nm × 40 nm) have been used to model the cracking of experimentally studied graphene sheets.[51,85,86] To simulate the stretching process, we perform a reactive molecular dynamics (MD) calculation employing ReaxFF[87,88] on PCG, where a strain rate of $\dot{\varepsilon}(t) = \frac{1}{L_0}\frac{dL}{dt} = 2.161\ \text{ns}^{-1}$ is applied along the x and y directions for 56 ps (see Fig. 5a and Sec. S2 in the ESI† for more details about the computational protocol). From the MD we extract six snapshots (see Sec. S7 in the ESI†) at different strain percentages ϵ. Each geometry is then excited by an external monochromatic electric field polarized along the y direction and oscillating at the PRF of the considered geometry see Fig. 5a. For all the snapshots, the maximum field enhancement

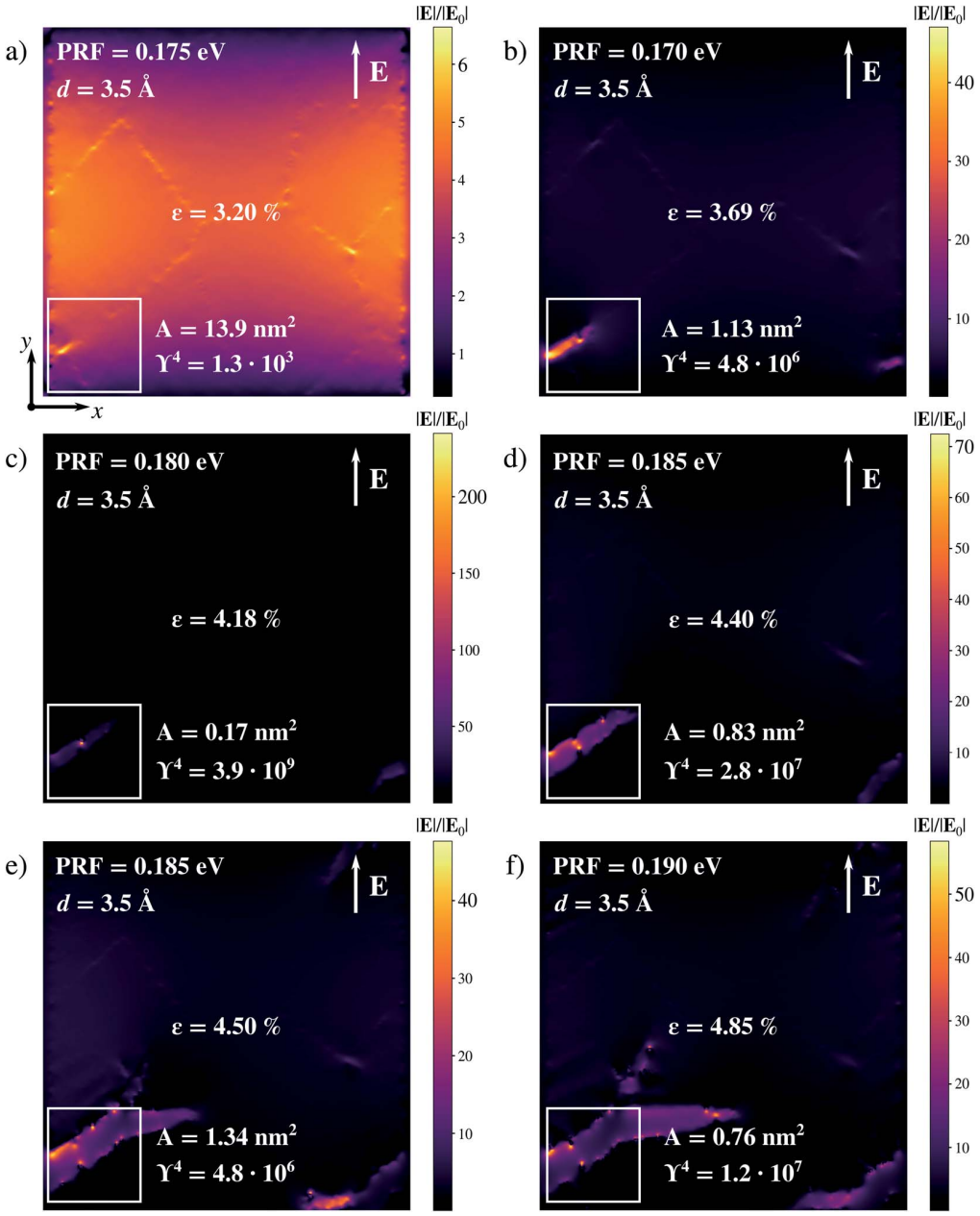

Fig. 6 Computed $|\mathbf{E}|/|\mathbf{E}_0|$ color maps of PCG under isotropic strain ϵ = 3.20% (a), 3.69% (b), 4.18% (c), 4.40% (d), 4.50% (e) and 4.85% (f). The maximum enhancement is calculated in the region highlighted in the white box. The Fermi level is set to E_F = 0.4 eV for all calculations.

Y^4 is computed in the region highlighted in the black box in Fig. 5a, on a plane parallel to the PCG and placed at 3.5 Å from it. This region has been chosen because it corresponds to the area where the first crack starts to form (see Sec. S7 in the ESI†).

To evaluate the effects of defects formation, we compare the field enhancement computed for each geometry with those of the structure at rest. Pristine PCG features a dipolar plasmon at 0.185 eV; the charge density is localized at the edge of the structure (not shown), similarly to what we observed previously (*e.g.* see Fig. 2). The field enhancement away from the edge is low, *i.e.* $Y^4 = 1.2 \times 10^3$ (see Fig. 5b).

As a result of the application of a tensile stress, cracks are first formed in the substrate, then they propagate across the sample, in agreement with previous observations.[51] Thus, narrow gaps between adjacent regions appear and, by further increasing the strain, the graphene sheet breaks completely (see Sec. S7 in the ESI†). As soon as defects are formed, plasmon confinement and field enhancement are observed in regions away from PCG edges (see Fig. 6a–f). A clear dependence of the enhancement upon the applied strain is not observed (see Fig. 6), whereas plasmon charges are indeed confined on edges and defects along the cracks. This suggests that once a crack starts forming, the kinetics of the cracking process is correlated to the reported enhancement more than the actual strain which is applied. However, high field enhancement and sub-nanometric localization are simultaneously reached in certain surface regions for different ϵ values. The highest enhancement occurs for $\epsilon = 4.18\%$, being $Y^4 = 3.9 \times 10^9$ and the effective localization area $A = 0.17$ nm^2 (see Fig. 6c). Therefore, the isotropic strain deformation of PCG seems to induce the formation of highly confined and enhanced fields, *i.e.* hot-spots, along the cracks. Moreover, it is known that graphene edges and vacancies can act as adsorption sites for various types of analytes.[89–92] Although this is not directly proven in this work, our results suggest that morphological defects not only behave as hot-spots, but can be ideal candidates for adsorption of target analytes, in order to allow their probing through surface-enhanced spectral signals. Therefore, common shortcomings of graphene substrates in the context of surface-enhanced spectroscopies might be solved through defect engineering.

4. Summary and conclusions

We have shown that high electric field enhancement and confinements can arise in engineered graphene-based nanostructures. The latter are designed by following two approaches. The first mimics geometrical arrangements commonly exploited to create hot-spots with noble MNPs, such as 3D bow-tie antennas. The second exploits graphene peculiar properties, such as edge defects and cracks propagating in polycrystalline substrates. Computed field enhancement and confinement factors show that in all these structures hot-spots are induced, which can be used as potential substrate for surface-enhanced spectroscopies. Notably, in some cases the computed field enhancement is comparable with the values which are observed in widely-used metal nanosubstrates exploited in SERS, thus suggesting that single-molecule detection is potentially accessible also in graphene-based nanostructures. In addition, computed confinement factors go down to the subnanometric scale, thus also suggesting a huge potentiality of graphene to strongly confine plasmon-induced enhancement. To conclude, the findings of this study suggest that by proper engineering graphene-based structures, the common shortcomings reported for graphene when it is exploited as a substrate for surface-enhanced spectroscopies can be solved. We hope that our work can inspire further experimental investigations to confirm our theoretical predictions.

Conflicts of interest

There are no conflicts to declare.

Acknowledgements

This work has received funding from the European Research Council (ERC) under the European Union's Horizon 2020 research and innovation program (grant agreement No. 818064). We acknowledge the Center for High Performance Computing (CHPC) at SNS for providing the computational infrastructure.

References

1 A. Grigorenko, M. Polini and K. Novoselov, *Nat. Photonics*, 2012, **6**, 749–758.
2 F. H. Koppens, D. E. Chang and F. J. Garcia de Abajo, *Nano Lett.*, 2011, **11**, 3370–3377.
3 Z. Fang, S. Thongrattanasiri, A. Schlather, Z. Liu, L. Ma, Y. Wang, P. M. Ajayan, P. Nordlander, N. J. Halas and F. J. García de Abajo, *ACS Nano*, 2013, **7**, 2388–2395.
4 F. J. Garcia de Abajo, *ACS Photonics*, 2014, **1**, 135–152.
5 A. C. Ferrari, F. Bonaccorso, V. Fal'Ko, K. S. Novoselov, S. Roche, P. Bøggild, S. Borini, F. H. Koppens, V. Palermo, N. Pugno, *et al.*, *Nanoscale*, 2015, **7**, 4598–4810.
6 X. Ling, S. Huang, S. Deng, N. Mao, J. Kong, M. S. Dresselhaus and J. Zhang, *Acc. Chem. Res.*, 2015, **48**, 1862–1870.
7 S. Huang, X. Ling, L. Liang, Y. Song, W. Fang, J. Zhang, J. Kong, V. Meunier and M. S. Dresselhaus, *Nano Lett.*, 2015, **15**, 2892–2901.
8 F. Schedin, E. Lidorikis, A. Lombardo, V. G. Kravets, A. K. Geim, A. N. Grigorenko, K. S. Novoselov and A. C. Ferrari, *ACS Nano*, 2010, **4**, 5617–5626.
9 W. Xu, X. Ling, J. Xiao, M. S. Dresselhaus, J. Kong, H. Xu, Z. Liu and J. Zhang, *Proc. Natl. Acad. Sci.*, 2012, **109**, 9281–9286.
10 H. Lai, F. Xu, Y. Zhang and L. Wang, *J. Mater. Chem. B*, 2018, **6**, 4008–4028.
11 Y. Liu, X. Dong and P. Chen, *Chem. Soc. Rev.*, 2012, **41**, 2283–2307.
12 X.-M. Lin, Y. Cui, Y.-H. Xu, B. Ren and Z.-Q. Tian, *Anal. Bioanal. Chem.*, 2009, **394**, 1729–1745.
13 F. J. G. de Abajo, *Science*, 2013, **339**, 917–918.

14 M. G. Albrecht and J. A. Creighton, *J. Am. Chem. Soc.*, 1977, **99**, 5215–5217.
15 D. L. Jeanmaire and R. P. Van Duyne, *J. Electroanal. Chem. Interfacial Electrochem.*, 1977, **84**, 1–20.
16 A. Campion and P. Kambhampati, *Chem. Soc. Rev.*, 1998, **27**, 241–250.
17 K. A. Willets and R. P. Van Duyne, *Annu. Rev. Phys. Chem.*, 2007, **58**, 267–297.
18 R. Alvarez-Puebla, L. M. Liz-Marzán and F. J. García de Abajo, *J. Phys. Chem. Lett.*, 2010, **1**, 2428–2434.
19 E. Le Ru and P. Etchegoin, *Principles of Surface-Enhanced Raman Spectroscopy: And Related Plasmonic Effects*, Elsevier, 2008.
20 S. A. Maier, *Plasmonics: Fundamentals and Applications*, Springer Science & Business Media, 2007.
21 J. Langer, D. Jimenez de Aberasturi, J. Aizpurua, R. A. Alvarez-Puebla, B. Auguié, J. J. Baumberg, G. C. Bazan, S. E. Bell, A. Boisen, A. G. Brolo, *et al.*, *ACS Nano*, 2019, **14**, 28–117.
22 K. Kneipp, Y. Wang, H. Kneipp, L. T. Perelman, I. Itzkan, R. R. Dasari and M. S. Feld, *Phys. Rev. Lett.*, 1997, **78**, 1667.
23 S. Nie and S. R. Emory, *Science*, 1997, **275**, 1102–1106.
24 H. Xu, J. Aizpurua, M. Käll and P. Apell, *Phys. Rev. E: Stat. Phys., Plasmas, Fluids, Relat. Interdiscip. Top.*, 2000, **62**, 4318.
25 A. B. Zrimsek, N. Chiang, M. Mattei, S. Zaleski, M. O. McAnally, C. T. Chapman, A.-I. Henry, G. C. Schatz and R. P. Van Duyne, *Chem. Rev.*, 2017, **117**, 7583–7613.
26 R. Zhang, Y. Zhang, Z. Dong, S. Jiang, C. Zhang, L. Chen, L. Zhang, Y. Liao, J. Aizpurua, Y. e. Luo, *et al.*, *Nature*, 2013, **498**, 82–86.
27 S. Jiang, Y. Zhang, R. Zhang, C. Hu, M. Liao, Y. Luo, J. Yang, Z. Dong and J. Hou, *Nat. Nanotechnol.*, 2015, **10**, 865–869.
28 X. Ling, L. Xie, Y. Fang, H. Xu, H. Zhang, J. Kong, M. S. Dresselhaus, J. Zhang and Z. Liu, *Nano Lett.*, 2010, **10**, 553–561.
29 X. Ling, L. Moura, M. A. Pimenta and J. Zhang, *J. Phys. Chem. C*, 2012, **116**, 25112–25118.
30 T. Giovannini, M. Rosa, S. Corni and C. Cappelli, *Nanoscale*, 2019, **11**, 6004–6015.
31 L. Bonatti, G. Gil, T. Giovannini, S. Corni and C. Cappelli, *Front. Chem.*, 2020, **8**, 340.
32 T. Giovannini, L. Bonatti, M. Polini and C. Cappelli, *J. Phys. Chem. Lett.*, 2020, **11**, 7595–7602.
33 P. Lafiosca, T. Giovannini, M. Benzi and C. Cappelli, *J. Phys. Chem. C*, 2021, **125**, 23848–23863.
34 F. Benz, M. K. Schmidt, A. Dreismann, R. Chikkaraddy, Y. Zhang, A. Demetriadou, C. Carnegie, H. Ohadi, B. De Nijs, R. Esteban, *et al.*, *Science*, 2016, **354**, 726–729.
35 S. F. Tan, *Molecular Electronic Control over Tunneling Charge Transfer Plasmons Modes*, Springer, 2018, pp. 51–67.
36 J. J. Baumberg, J. Aizpurua, M. H. Mikkelsen and D. R. Smith, *Nat. Mater.*, 2019, **18**, 668–678.
37 A. Xomalis, X. Zheng, A. Demetriadou, A. Martínez, R. Chikkaraddy and J. J. Baumberg, *Nano Lett.*, 2021, **21**, 2512–2518.
38 R. Chikkaraddy, B. De Nijs, F. Benz, S. J. Barrow, O. A. Scherman, E. Rosta, A. Demetriadou, P. Fox, O. Hess and J. J. Baumberg, *Nature*, 2016, **535**, 127–130.
39 B. Yang, G. Chen, A. Ghafoor, Y. Zhang, Y. Zhang, Y. Zhang, Y. Luo, J. Yang, V. Sandoghdar, J. Aizpurua, *et al.*, *Nat. Photonics*, 2020, **14**, 693–699.
40 P. Liu, D. V. Chulhai and L. Jensen, *ACS Nano*, 2017, **11**, 5094–5102.
41 J. Lee, N. Tallarida, X. Chen, P. Liu, L. Jensen and V. A. Apkarian, *ACS Nano*, 2017, **11**, 11466–11474.
42 I. Romero, J. Aizpurua, G. W. Bryant and F. J. G. De Abajo, *Opt. Express*, 2006, **14**, 9988–9999.
43 N. A. Hatab, C.-H. Hsueh, A. L. Gaddis, S. T. Retterer, J.-H. Li, G. Eres, Z. Zhang and B. Gu, *Nano Lett.*, 2010, **10**, 4952–4955.
44 M. Barbry, P. Koval, F. Marchesin, R. Esteban, A. G. Borisov, J. Aizpurua and D. Sánchez-Portal, *Nano Lett.*, 2015, **15**, 3410–3419.
45 E. Hao and G. C. Schatz, *J. Chem. Phys.*, 2004, **120**, 357–366.
46 M. Pizzochero, G. B. Barin, K. Cernevics, S. Wang, P. Ruffieux, R. Fasel and O. V. Yazyev, *J. Phys. Chem. Lett.*, 2021, **12**, 4692–4696.
47 M. Pizzochero, K. Čerņevičs, G. B. Barin, S. Wang, P. Ruffieux, R. Fasel and O. V. Yazyev, *2D Mater.*, 2021, **8**, 035025.
48 S. Sun, Y. Guan, Z. Hao, Z. Ruan, H. Zhang, J. Lu, L. Gao, X. Zuo and J. Cai, *Nano Res.*, 2021, 1–6.
49 P. S. Costa, J. D. Teeter, A. Enders and A. Sinitskii, *Carbon*, 2018, **134**, 310–315.
50 J. Cai, P. Ruffieux, R. Jaafar, M. Bieri, T. Braun, S. Blankenburg, M. Muoth, A. P. Seitsonen, M. Saleh, X. Feng, *et al.*, *Nature*, 2010, **466**, 470–473.
51 K. Kim, V. I. Artyukhov, W. Regan, Y. Liu, M. Crommie, B. I. Yakobson and A. Zettl, *Nano Lett.*, 2012, **12**, 293–297.
52 Z. Zhang, X. Zhang, Y. Wang, Y. Wang, Y. Zhang, C. Xu, Z. Zou, Z. Wu, Y. Xia, P. Zhao, *et al.*, *ACS Nano*, 2019, **13**, 10327–10332.
53 S. R. Na, X. Wang, R. D. Piner, R. Huang, C. G. Willson and K. M. Liechti, *ACS Nano*, 2016, **10**, 9616–9625.
54 K. J. Savage, M. M. Hawkeye, R. Esteban, A. G. Borisov, J. Aizpurua and J. J. Baumberg, *Nature*, 2012, **491**, 574–577.
55 R. Esteban, A. G. Borisov, P. Nordlander and J. Aizpurua, *Nat. Commun.*, 2012, **3**, 1–9.
56 W. Zhu, R. Esteban, A. G. Borisov, J. J. Baumberg, P. Nordlander, H. J. Lezec, J. Aizpurua and K. B. Crozier, *Nat. Commun.*, 2016, **7**, 1–14.
57 M. Urbieta, M. Barbry, Y. Zhang, P. Koval, D. Sánchez-Portal, N. Zabala and J. Aizpurua, *ACS Nano*, 2018, **12**, 585–595.
58 X. Chen, J. E. Moore, M. Zekarias and L. Jensen, *Nat. Commun.*, 2015, **6**, 1–8.
59 A. C. Neto, F. Guinea, N. M. Peres, K. S. Novoselov and A. K. Geim, *Rev. Mod. Phys.*, 2009, **81**, 109.
60 E. J. Skjølstrup, T. Søndergaard and T. G. Pedersen, *Phys. Rev. B*, 2018, **97**, 115429.
61 L. Stella, P. Zhang, F. García-Vidal, A. Rubio and P. García-González, *J. Phys. Chem. C*, 2013, **117**, 8941–8949.
62 S. Raza, S. I. Bozhevolnyi, M. Wubs and N. A. Mortensen, *J. Phys.: Condens. Matter*, 2015, **27**, 183204.

63 S. Thongrattanasiri and F. J. G. de Abajo, *Phys. Rev. Lett.*, 2013, **110**, 187401.
64 M. Jablan, H. Buljan and M. Soljačić, *Phys. Rev. B: Condens. Matter Mater. Phys.*, 2009, **80**, 245435.
65 T. Low and P. Avouris, *ACS Nano*, 2014, **8**, 1086–1101.
66 F. Karimi and I. Knezevic, *Phys. Rev. B*, 2017, **96**, 125417.
67 D. Novko, *Nano Lett.*, 2017, **17**, 6991–6996.
68 R. Beams, L. G. Cançado and L. Novotny, *Nano Lett.*, 2011, **11**, 1177–1181.
69 E. Voloshina, D. Mollenhauer, L. Chiappisi and B. Paulus, *Chem. Phys. Lett.*, 2011, **510**, 220–223.
70 K. Kneipp, Y. Ozaki and Z.-Q. Tian, *Recent Developments In Plasmon-supported Raman Spectroscopy: 45 Years of Enhanced Raman Signals*, World Scientific, 2017.
71 H. Liu, S. Sun, L. Wu and P. Bai, *Plasmonics*, 2014, **9**, 845–850.
72 W. Wang, T. Christensen, A.-P. Jauho, K. S. Thygesen, M. Wubs and N. A. Mortensen, *Sci. Rep.*, 2015, **5**, 1–9.
73 J. A. Jaszczak, G. W. Robinson, S. Dimovski and Y. Gogotsi, *Carbon*, 2003, **41**, 2085–2092.
74 C.-T. Lin, C.-Y. Lee, H.-T. Chiu and T.-S. Chin, *Langmuir*, 2007, **23**, 12806–12810.
75 S. N. Naess, A. Elgsaeter, G. Helgesen and K. D. Knudsen, *Sci. Technol. Adv. Mater.*, 2009, **10**, 065002.
76 N. Wohner, P. Lam and K. Sattler, *Carbon*, 2014, **67**, 721–735.
77 A. G. Cano-Marquez, W. G. Schmidt, J. Ribeiro-Soares, L. G. Cançado, W. N. Rodrigues, A. P. Santos, C. A. Furtado, P. A. Autreto, R. Paupitz, D. S. Galvão, *et al.*, *Sci. Rep.*, 2015, **5**, 1–5.
78 X. Chen and L. Jensen, *Nanoscale*, 2018, **10**, 11410–11417.
79 C.-F. Chen, C.-H. Park, B. W. Boudouris, J. Horng, B. Geng, C. Girit, A. Zettl, M. F. Crommie, R. A. Segalman, S. G. Louie, *et al.*, *Nature*, 2011, **471**, 617–620.
80 O. V. Yazyev and S. G. Louie, *Nat. Mater.*, 2010, **9**, 806–809.
81 O. V. Yazyev and Y. P. Chen, *Nat. Nanotechnol.*, 2014, **9**, 755–767.
82 K. Kim, Z. Lee, W. Regan, C. Kisielowski, M. Crommie and A. Zettl, *ACS Nano*, 2011, **5**, 2142–2146.
83 F. Banhart, J. Kotakoski and A. V. Krasheninnikov, *ACS Nano*, 2011, **5**, 26–41.
84 P. Y. Huang, C. S. Ruiz-Vargas, A. M. Van Der Zande, W. S. Whitney, M. P. Levendorf, J. W. Kevek, S. Garg, J. S. Alden, C. J. Hustedt, Y. Zhu, *et al.*, *Nature*, 2011, **469**, 389–392.
85 P. Zhang, L. Ma, F. Fan, Z. Zeng, C. Peng, P. E. Loya, Z. Liu, Y. Gong, J. Zhang, X. Zhang, *et al.*, *Nat. Commun.*, 2014, **5**, 1–7.
86 T. Zhang, X. Li and H. Gao, *Int. J. Fract.*, 2015, **196**, 1–31.
87 A. C. Van Duin, S. Dasgupta, F. Lorant and W. A. Goddard, *J. Phys. Chem. A*, 2001, **105**, 9396–9409.
88 K. Chenoweth, A. C. Van Duin and W. A. Goddard, *J. Phys. Chem. A*, 2008, **112**, 1040–1053.
89 S. N. Kim, Z. Kuang, J. M. Slocik, S. E. Jones, Y. Cui, B. L. Farmer, M. C. McAlpine and R. R. Naik, *J. Am. Chem. Soc.*, 2011, **133**, 14480–14483.
90 N. Ghaderi and M. Peressi, *J. Phys. Chem. C*, 2010, **114**, 21625–21630.
91 L. Kong, A. Enders, T. S. Rahman and P. A. Dowben, *J. Phys.: Condens. Matter*, 2014, **26**, 443001.
92 Y.-H. Zhang, Y.-B. Chen, K.-G. Zhou, C.-H. Liu, J. Zeng, H.-L. Zhang and Y. Peng, *Nanotechnology*, 2009, **20**, 185504.

Chapter 7

Strain-induced plasmon confinement in polycrystalline graphene

ACS Photonics

pubs.acs.org/journal/apchd5

Article

Strain-Induced Plasmon Confinement in Polycrystalline Graphene

Simone Zanotto, Luca Bonatti, Maria F. Pantano, Vaidotas Mišeikis, Giorgio Speranza, Tommaso Giovannini, Camilla Coletti, Chiara Cappelli, Alessandro Tredicucci,* and Alessandra Toncelli

Cite This: *ACS Photonics* 2023, 10, 394−400

Read Online

ABSTRACT: Terahertz spectroscopy is a perfect tool to investigate the electronic intraband conductivity of graphene, but a phenomenological model (Drude-Smith) is often needed to describe disorder. By studying the THz response of isotropically strained polycrystalline graphene and using a fully atomistic computational approach to fit the results, we demonstrate here the connection between the Drude-Smith parameters and the microscopic behavior. Importantly, we clearly show that the strain-induced changes in the conductivity originate mainly from the increased separation between the single-crystal grains, leading to enchanced localization of the plasmon excitations. Only at the lowest strain values explored, a behavior consistent with the deformation of the individual grains can instead be observed.

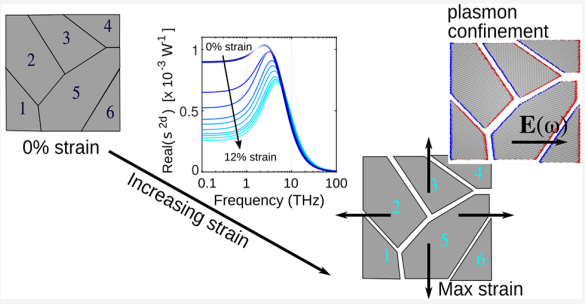

KEYWORDS: *graphene, terahertz, plasmons, strain, Drude-Smith, conductivity of polycrystalline 2D materials, atomistic simulations*

INTRODUCTION

Extremely simple in its crystal structure, graphene has revealed an outstandingly complex and rich spectrum of fundamental physical phenomenologies, with unique perspectives toward technological applications.[1] One of such peculiar features is the presence of an effective gauge field − analogous to the electromagnetic vector potential − when a strain is applied to an otherwise homogeneous, unperturbed graphene lattice.[2] If an inhomogeneous strain belonging to a specific symmetry class is considered, the effective gauge field can be linked to a homogeneous pseudomagnetic field (PMF), capable − on par with a real magnetic field − of reorganizing the electronic states into discrete levels with a characteristic $\sqrt{n}$ energy behavior.[3,4] The possibility of controlling electronic properties through strain, which gave birth to a whole field of research usually named straintronics,[5−9] in graphene coexists with many other appealing properties of such material, like high carrier mobility, universal optical conductance, tunability by electrostatic and ionic gating, mechanical flexibility, and peculiar plasmonic properties. It is especially in the terahertz (THz) frequency range that graphene plasmonics and magnetoplasmonics deserve special attention, thanks to the small plasmon confinement length and high Faraday rotation power, enabling applications such as modulators, nonreciprocal elements, coherent absorbers, polaritonic components, detectors, and metasurfaces.[10−15] Considering strained graphene, THz can be regarded both as an application domain and as a diagnostic tool. From the first perspective, THz manipulation can benefit from appropriate graphene strain engineering;[16] in addition, pseudo-LL could be employed for ultrastrong coupling experiments, without the need for high magnetic field environments.[17−20] From the second, one may leverage on the various THz spectroscopic techniques that proved powerful in understanding the micro- and mesoscopic structure of materials.[21,22] Indeed, technologies to fabricate graphene samples of sufficient quality and size with an engineered strain are currently still challenging. On the other hand, the use of THz as a diagnostic tool has proven often extremely powerful. In the present article we investigate the THz conductivity of a variably strained polycrystalline graphene sample, unveiling the origin of the observed Drude-Smith behavior.[23−25] We analyzed our experimental data by means of an atomistic technique, ωFQ,[26−28] highlighting the presence of strain-induced carrier reflection at the grain boundaries and strain-induced mutual separation between grains. The ensuing localization of the plasmon excitations confirms that the conductivity trend of the macroscopic Drude-Smith model finds its roots in the creation of actual atom-size gaps between graphene grains of realistic size. Our study extends prior knowledge on the THz conductance of strained graphene where uniaxial strain was considered,[29,30] but, most importantly, reports for the first time

Received: July 24, 2022
Published: January 12, 2023

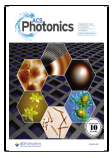

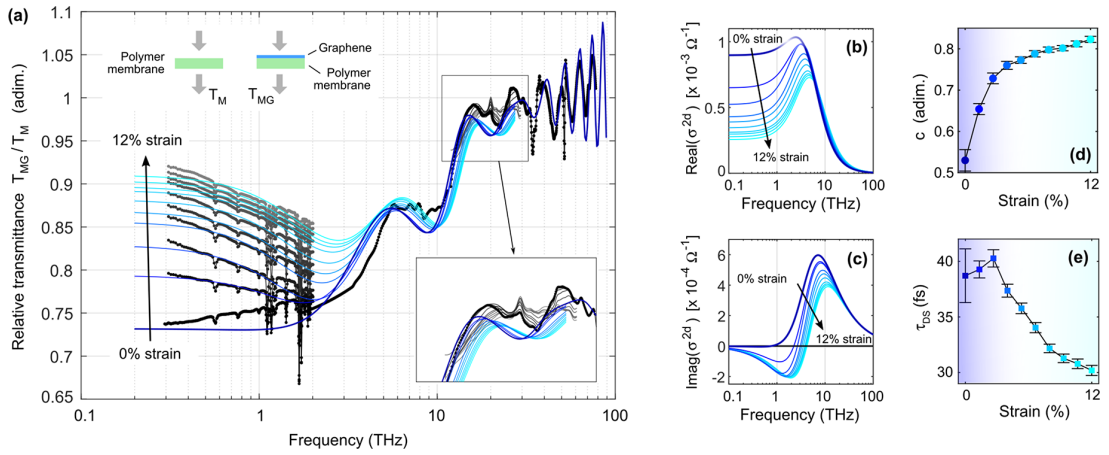

Figure 1. Spectroscopic evidence of the Drude-Smith behavior observed in the far-infrared response of strained polycrystalline graphene. (a) Experimental (black to gray dotted traces) and calculated (blue to cyan solid lines) relative transmittance spectra, defined as the ratio between the transmittance of the investigated sample (graphene on polymer membrane) and a reference sample (bare polymer membrane). The spectral region mostly affected by the Drude-Smith strain-dependent response is that between 0.2 and 3 THz. The inset shows a small effect mostly due to membrane thickness reduction. (b, c) Real and imaginary parts of graphene conductivity giving rise to the calculated spectra in (a). The suppression of Re(σ) at low frequencies is a fingerprint of Drude-Smith behavior. (d, e) Strain dependence of the Drude-Smith model parameters c (quantifying the carrier backscattering) and τ_{DS} (effective scattering time). Large strain imply stronger backscattering and smaller effective scattering time (more on this in the main text).

the application of a fully atomistic approach to quantify the deviation from the Drude model and, at the same time, provides a novel microscopic interpretation of the Drude-Smith behavior, which is a widespread tool for the analysis of THz conductance in nanostructured disordered materials.

RESULTS AND DISCUSSION

To perform the aforementioned study, we have designed a special sample and sample holder. Sample fabrication began with chemical vapor deposition (CVD) synthesis of a polycrystalline monolayer graphene film on copper foil (Alfa-Aesar, 25 μm thick) using an Aixtron BM Pro cold-wall CVD reactor. Wet transfer[31] was used to deposit the graphene film on a thin (≈8 μm thick) circular polyvinyl chloride (PVC)-based membrane of about 20 mm diameter. The membrane was cut from a foil by means of a hollow punch in order to provide the desired geometry. The graphene sample was spin-coated with a protective layer of poly(methyl methacrylate) (PMMA), and the copper was etched away using iron chloride ($FeCl_3$). The remaining PMMA/graphene film was rinsed in deionized water several times and was picked up from water using the PVC membrane. The sample was dried under ambient conditions. A reference sample consisting of the sole PVC membrane was also fabricated. The sample holder is a manual chuck with four jaws, on which the membrane sample can be accommodated and fixed by means of glue. By actuating the chuck, the four jaws move apart from one another, thus applying a biaxial deformation field to the sample, as illustrated in Figure S1 in the Supporting Information (SI). The usage of a four-jaw chuck allows to deliver a mostly homogeneous and isotropic strain distribution, avoiding position-dependent strain profiles that could give rise to specific PMF effects. In any case, it should be highlighted that the polycrystallinity of our sample prevents the creation of directionality-dependent effects, as the unstrained sample is isotropic. The sample is then inserted in the main optical path of two kinds of spectrometers: (i) a THz-TDS instrument, operating in the 0.3−2 THz spectral range, (ii) a FTIR instrument, operating either in the FIR (2−10 THz) or in the MIR (10−100 THz) spectral ranges depending on the employed beam splitter and detector. In Figure 1a we plot, as traces with black to gray color, the transmittance spectra collected under different strain levels, from 0 to 12%. For strained samples, only the 0.3−2 THz and 10−100 THz regions have been characterized, owing to setup limitations. The strain strongly affects the 0.3−2 THz region, while the 10−100 THz region is affected only weakly. All the spectra in Figure 1a are of relative transmittance, in the sense that they are the ratio between the spectra of a polymer+graphene sample with respect to the reference polymer sample. To interpret the spectra, we modeled the transmittance employing the scattering-matrix method for electromagnetic wave propagation through unpatterned layered media, following the theory in ref 32 after reduction to a single spatial harmonic, and generalization of the interface matrix to account for graphene as a zero-thickness sheet with local conductivity.[1] As a first attempt, we employed a pure Drude form for the graphene conductivity; with this approach, however, it was not even possible to fit the zero-strain spectrum with reasonable parameters. The simple Drude form would be the (asymptotic) form expected for the conductivity of graphene in the frequency range below the onset of interband transitions, i.e., in the case of a sample grown with our technique, for frequencies smaller than around 150 THz.[33] A deviation from the Drude behavior is however expected in polycrystalline samples; indeed, the Drude model is unable to capture the backscattering of carriers at the grain boundaries, as it only describes a time-domain Poissonian process of inelastic scattering events that is suitable for describing bulk scattering only. We thus moved to the Drude-Smith model, that, for graphene, is given by the expression

$$\sigma(\omega) = \sigma_0 E_F \frac{\tau_{DS}}{\hbar} \frac{1}{1 - i\omega\tau_{DS}} \left(1 - \frac{c}{1 - i\omega\tau_{DS}}\right) \quad (1)$$

https://doi.org/10.1021/acsphotonics.2c01157
ACS Photonics 2023, 10, 394−400

where $\sigma_0 = 2e^2/h \approx 7.75 \times 10^{-5}\ \Omega^{-1}$ is the conductance quantum, E_F is the Fermi energy, τ_{DS} is the Drude-Smith scattering time (related, but distinct from the bulk scattering time), and $c \in [0, 1]$ is a parameter that quantifies the deviation from the pure Drude model.[23] The choice $c = 0$ recovers the Drude model; the effect of $c > 0$ is to suppress the DC conductivity and to move the maximum of $\mathrm{Re}(\sigma)$ from $\omega = 0$ (as in the Drude model) to a finite value $\omega > 0$. Such effects are interpreted, in the original view of the model given by Smith, as a "memory effect" experienced by the carriers, whose velocity distribution is not fully randomized after the first collision, and rather retains a net backward component.[23] Otherwise, it can be interpreted as the consequence of a finite reflectivity felt by the carriers while moving across the sample, modeled as a disordered assembly of grains with partially impenetrable boundaries.[24]

The transmittance spectra following from the fit to experimental data using our multilayer model and eq 1 for the graphene conductivity are reported in Figure 1a as blue to cyan lines. No data are shown for the strained samples above 30 THz since in that spectral region one only observes a shift of the oscillations, an effect connected to the change of the polymer thickness rather than to a modification of the Drude-Smith parameters of graphene. More on this, and additional information on the fitting procedure, are given in SI, section 2. The slight increase with frequency in the 0.5−2 THz range (of the order of just a few percent) in the experimental transmission for the unstrained spectrum is likely due to deviations from flatness of the membrane in the absence of any applied tension (with possible formation of small bends and wrinkles) or to residuals of the polymer absorption. Consistently with the general behavior of the Drude-Smith model with nonzero c, the real part of the conductance has a maximum at finite values of the frequency (≈3 THz, see Figure 1b). As the strain increases, the DC conductance decreases, reducing absorption at low frequency. This is a consequence of c shifting from 0.5 to 0.82, which means a strong deviation from the Drude model at large strains (Figure 1d). A peculiar trend is also observed in the τ_{DS} parameter (Figure 1e). Here, the best estimates for τ_{DS} first increase and then decrease; however, especially when considering the data with error bars (95% CI statistical error), the initial increasing τ_{DS} trend is not unambiguous and the data could also be consistent with a global decrease, albeit with different slopes for strains below or above ≈3.5%. A microscopic interpretation of this effect is given later. The data of Figure 1 complement literature reports about the conductance in strained graphene, where either the maximum strain was much smaller than ours[30] or uniaxial strain was employed.[29]

To move toward a microscopic interpretation of the trends observed in Figure 1d,e, one can resort to the model proposed by Cocker et al.,[24] where the carriers motion in a multidomain sample is studied by a Montecarlo approach and by considerations on the diffusion current. In this model, new parameters are involved: the diffusion time in each domain (t_0), the domain wall reflectivity (R), and the bulk scattering time (τ). However, the two models are connected, since relatively simple algebraic relations between the above-mentioned parameters and the "original" Drude-Smith parameters (c, τ_{DS}) can be derived. Exploiting such relations, we report in the SI (section 3.6) details on the analysis of our data in view of the model by Cocker et al. In summary, the domain diffusion time decreases with increasing strain, the reflectivity increases with increasing strain, and the bulk scattering time remains almost constant. These observations support the vision that the strain applied to the polycrystalline sample leads to a progressive separation between the monocrystals (connected to reflectivity increase) and to the creations of cracks within each crystal (connected to diffusion time decrease, assuming that diffusion time equals a drift velocity multiplied by the domain size). Effects connected to the stretch of carbon−carbon bonds seem instead negligible[34] (see section 3.8 in the SI), and the consequent opening of a bandgap, yet expected at even larger strains, would rather affect mostly the optical spectral region.[35] It should be recalled, however, that the model by Cocker et al. was derived for massive charges, which is not the case of graphene.

To provide a more solid analysis of Dirac Fermions dynamics in a multidomain graphene sample, we then exploit a fully atomistic, yet classical, model, called ωFQ,[26−28,36] which is able to correctly describe how the grain boundaries morphology affects the electron conduction across the sample (see also Methods).[37] In ωFQ, each carbon atom is endowed with a net charge q_i, which responds to an external oscillating electric field. The conduction properties of graphene samples are directly obtained from computed ωFQ charges, by exploiting their complex (i.e., real + imaginary) nature. In fact, the charge's imaginary part enters the definition of the dipole moment of the whole system and, as a consequence, the calculation of the complex polarizability ($\alpha(\omega)$), that can be easily related to the conductivity (see section 3.1 in the SI). Also, the charge exchange between nearest neighbor atoms is described in terms of the Drude model of conductance, which is further modulated by means of a Fermi-like damping function, which introduces an exponential decay, typical of quantum tunneling (see Methods section).[26,27] In this work, ωFQ needs to be applied to graphene samples with a size of tens of μm. Although ωFQ can afford graphene sheets constituted by more than 1 million atoms due to its low computational cost,[28] a fully atomistic modeling of graphene samples of size of the order of μm is still computationally unfeasible. However, it has been shown that by modulating the graphene 2D electron density, or equivalently its Fermi level, the plasmonic properties of a graphene sheet of arbitrary size can be reproduced.[38] Indeed, ωFQ is able to correctly reproduce the peculiar property of graphene-based materials to yield plasmon degeneracy (i.e., the same Plasmon Resonance Frequency - PRF) by modulating both the intrinsic dimensions of the considered substrate and the Fermi energy by the same numerical factor.[27,38] In this scenario, a graphene-based nanostructure showing a PRF in the THz regime, which is unfeasible from a computational point of view due to the prohibitive number of atoms to be described, can be modeled as a smaller system by decreasing the Fermi level to make the electron density equal to that of the real-size structure. Remarkably, ωFQ retains this important physical feature;[27] therefore, in the present work, we adopt a special parametrization, which is able to correctly describe the initial experimental system at rest (see section 3.2 in the SI). In this way, graphene samples characterized by a PRF in the THz regime can be described by actually computing much smaller structures (i.e., tens of nm) and the results of calculations can be directly compared with experimental data. We model the experimental unstressed polycrystalline graphene as a multi-domain graphene sheet constituted of 6 grains of different size as the starting geometry at rest (see Figure 2 a). Obviously,

https://doi.org/10.1021/acsphotonics.2c01157
ACS Photonics 2023, 10, 394−400

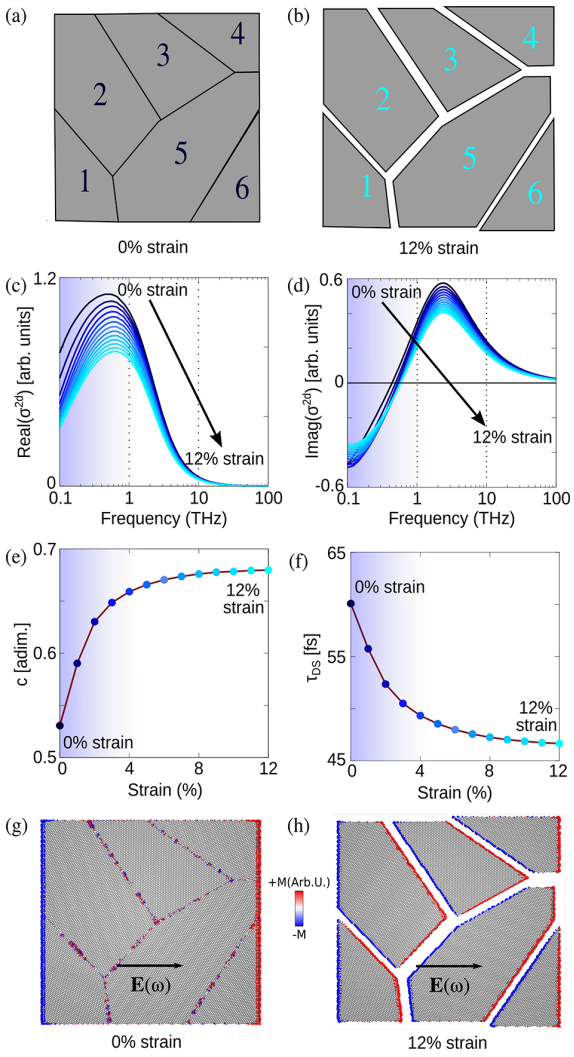

Figure 2. Polycrystalline graphene sheet composed of 6 grains at rest (a) and under the effect of biaxial strain (b). ωFQ values for the real (c) and imaginary (d) part of σ^{2d} as a function of the external frequency. Drude-Smith parameters c (e) and τ_{DS} (f) as a function of the applied strain. Charge density plots for the system at rest (g) and at 10% strain (h).

multiple starting structures could be exploited; additional results obtained by using a multidomain graphene sheet constituted of 12 and 17 grains are reported in section S3.7 in the SI. Such data show that similar trends are obtained independently of the number of grains. Drude-Smith parameters are extrapolated from conduction trends with a fitting procedure (see section 3.3 in the SI). Also, in order to allow for a direct comparison between our modeling and the experimental data, we impose the Drude-smith parameter c = 0.53 at 0% strain (see eq 1 and Figure 1 d), by tuning the free parameter β (see sections 3.2 and 3.4 in the SI). ωFQ is then tasked to explain at the microscopic level experimental macroscopic trends as a function of the applied strain (see Figure 1). We first assume that, by starting from the unstressed polycrystalline graphene, in which all grains are linked together, the grains start to drift away as the applied strain increases. Thus, gaps between adjacent grains are first formed and then their size increases as a function of the applied strain, so that cracks between grains appear (see Figure 2a,b). Computed ωFQ real and imaginary parts of the conductivity (σ^{2d}) for each strained geometry (from 0% to 12% external applied strain, with a constant step of 1%) are reported in Figure 2c and d, respectively.

The ωFQ Re(σ^{2d}) maximum for graphene at rest falls at about 0.7 THz, which differs from the experimental result. However, such a shift does not affect the overall description of the behavior of the conduction peak as a function of the applied strain. In fact, as reported in Figure 1c,d, the conductivity blue shifts as the applied strain increases, coherently with experimental findings. In addition, ωFQ reproduces well the experimental decrease of the peak's intensity as the applied strain increases.

By exploiting the fitting procedure explained in section 3.3 in the SI, the c and τ_{DS} parameters entering the Drude-Smith model (see eq 1) can be obtained as a function of the applied strain (see Figure 2e,f). Also in this case, the agreement between ωFQ results and the experiment is extremely good. Indeed, not only the general behavior as a function of the strain is correctly reproduced for applied strains >2−3%, but also ωFQ results are numerically comparable with experiments. These findings are particularly relevant, because they confirm the reliability of our modeling of the experimental strain process. The decreasing of τ_{DS} as the applied strain increases can be explained by considering that for large strains, grains tend to behave as independent islands and the electron conduction between adjacent domains is strongly damped. As a result, the plasmonic density is blocked inside each single grain and the overall scattering time drops. In Figure 2g,h, we show that the charge density is diffused over the whole unstressed sample, whereas a confinement of the plasmon density arises when gaps originate in the structure. Although we are able to mimic with very good accuracy the experimental trends for strains >3.5%, our theoretical picture does not capture the change in the slope of τ_{DS} as a function of strain occurring when we move to values below ∼3.5%. Such a discrepancy probably reflects that in weakly stressed graphene an additional relaxation mechanism, more relevant than grain separation, is playing an active role. In fact, the results reported in Figure 2c−f are obtained by assuming the internal relaxation of the C−C bonds within each grain to be instantaneous. This is an approximation which may be valid for large strain values, but may fail at low strain values (1−3%).

To support this vision, we consider the alternative situation produced by the strain: the multidomain unstressed graphene is elongated, stretching the chemical bonds without detaching the grains (see Figure 3a and section 3.8 in the SI). At the grain boundaries amorphous C phases could indeed be present, and they might prevent a clear separation of the islands until the strain is large enough, leading to a complex interplay of mechanisms. If grains deform without moving away from each other, an overall increase of the system size, and, as a consequence, of the scattering time, is expected, without major changes in the plasmon confinement. In fact, the computed ωFQ trend of τ_{DS} as a function of the applied strain shows in this case a small linear increase (see Figure 3b). Such findings support the experimental observations that, for strains lower than 3.5%, the values of τ_{DS} are relatively unchanged (within the errors).

In summary, two different mechanisms have been investigated by our computational modeling: the elongation

https://doi.org/10.1021/acsphotonics.2c01157
ACS Photonics 2023, 10, 394−400

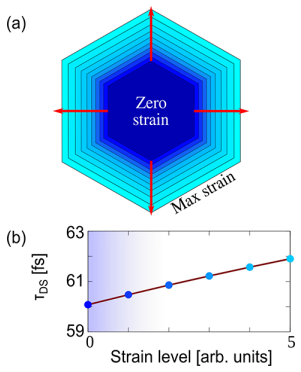

Figure 3. (a) Graphical representation of the elongation of a single graphene ring under the effect of an increasing level of isotropic strain. (b) Drude-Smith parameter τ_{DS} as a function of the applied strain by imposing a stretching of C−C bonds only.

of the C−C bonds in the whole polycrystalline structure and the formation of different cracks across the grain boundaries of the structure, leading to narrow gaps between adjacent grains, providing a confinement of the plasmons within the different grains. Opposite τ_{DS} trends are obtained from the simulations in the two cases, which allows interpreting the experimental results as deriving from the interplay of the two processes: while at low applied strains both elongation of the C−C bonds' length and separation between adjacent grains may be involved, at high levels of strain, the latter effect clearly dominates the THz response.

CONCLUSIONS

We have investigated the THz conductivity of polycrystalline graphene as a function of isotropically applied strain by both time domain/FTIR spectroscopy and theoretical atomistic simulations. It is found that the dependence can be properly described by considering two different effects: a uniform deformation of the graphene lattice, which dominates for low strain, and a progressive detachment of the individual monocrystal grains at high strain. The latter affects the THz conductivity through the progressive localization of plasmon excitations in each grain.

Furthermore, by fitting both experimental and theoretical spectra with a phenomenological Drude-Smith model, a connection is drawn between the parameters accounting for disorder in the formula and the microscopic physics they are expected to convey.

The results highlight the potential of the ωFQ approach in studying systems where macroscopic electro-dynamic theories cannot cope with the presence of underlying micro/nanoscale structures at the atomic scale, if not through the introduction of average parameters of limited quantitative significance. They also finally provide a clear picture of how polycrystalline disorder affects graphene plasmon resonances, suggesting a new interesting mechanism by which strain could be used as the external control knob in the implementation of graphene-based tunable THz devices.

METHODS

In this work, we describe the optical properties of multidomain graphene nanostructures, with an emphasis on structural defects created by a biaxial strain applied to a sample initially at rest. We model the optical response of such structures by using a classical, fully atomistic approach, called ωFQ.[26−28,36,37,39] In this method, a net complex charge q_i is placed at each atomic site, and atom−atom charge flow occurs in response to a time dependent external electric field. Charge exchange is described in terms of the Drude model of conduction, modulated by quantum tunneling effects. In this way, charge transfer is restricted to nearest neighboring atoms, and the typical quantum tunneling exponential decay is considered. ωFQ charges ($\mathbf{q}$) are determined through the following equation:[27]

$$-i\omega q_i = \frac{2\tau v_F}{1 - i\omega\tau}\sqrt{\frac{n_{2D}}{\pi}}\sum_j f(l_{ij})\frac{A_{ij}}{l_{ij}}(\phi_j^{el} - \phi_i^{el}) \quad (2)$$

where $q_i(\omega)$ is a complex-valued charge placed at atom i, oscillating at frequency ω. v_F is the Fermi velocity, n_{2D} is the 2D-density of graphene, and τ the scattering time. l_{ij} is the distance between atoms i and j, whereas A_{ij} is the effective area connecting i and j atoms. The electrochemical potential acting on each atomic site is labeled as ϕ^{el}. Finally, $f(l_{ij})$ is a Fermi-like damping function mimicking quantum tunneling effects, which reads as the following:

$$f(l_{ij}) = \frac{1}{1 + \exp\left[-d\cdot\left(\frac{l_{ij}}{s\cdot l_{ij}^0} - 1\right)\right]} \quad (3)$$

where l_{ij}^0 is the equilibrium distance between two adjacent carbon atoms at rest (i.e., l_{ij}^0 = 1.42 Å[40]). The position of the inflection point and the steepness of the step function are determined by the parameters d and s, respectively.

ASSOCIATED CONTENT

Supporting Information

The Supporting Information is available free of charge at https://pubs.acs.org/doi/10.1021/acsphotonics.2c01157.

Details on the sample holder used during the experimental procedure and on the fitting procedure for the experimental data. ωFQ equations for conductivity and parametrization of the system. Computational details. Comparison between experimental and computational trends for Cocker parameters. Role of the grain size on the Drude-Smith and Cocker parameters. Alternative strain modeling: elongation of C−C bonds (PDF)

AUTHOR INFORMATION

Corresponding Author

Alessandro Tredicucci − *Dipartimento di Fisica "E. Fermi" and CISUP, Università di Pisa, and Istituto Nanoscienze - CNR, Pisa 56127, Italy;* orcid.org/0000-0003-3619-3011; Email: alessandro.tredicucci@unipi.it

Authors

Simone Zanotto − *NEST, Istituto Nanoscienze − CNR and Scuola Normale Superiore, Pisa 56127, Italy;* orcid.org/0000-0001-7180-3335

Luca Bonatti − *Scuola Normale Superiore, Pisa 56126, Italy*

Maria F. Pantano − *Department of Civil, Environmental and Mechanical Engineering, University of Trento, Trento 38123, Italy;* orcid.org/0000-0001-5415-920X

Vaidotas Mišeikis − *Center for Nanotechnology Innovation @ NEST - Istituto Italiano di Tecnologia, Pisa 56127, Italy*

Giorgio Speranza − *Centre for Materials and Microsystems, Fondazione Bruno Kessler, Trento I-38123, Italy;* orcid.org/0000-0003-1478-0995
Tommaso Giovannini − *Scuola Normale Superiore, Pisa 56126, Italy;* orcid.org/0000-0002-5637-2853
Camilla Coletti − *Center for Nanotechnology Innovation @ NEST - Istituto Italiano di Tecnologia, Pisa 56127, Italy;* orcid.org/0000-0002-8134-7633
Chiara Cappelli − *Scuola Normale Superiore, Pisa 56126, Italy;* orcid.org/0000-0002-4872-4505
Alessandra Toncelli − *Dipartimento di Fisica "E. Fermi" and CISUP, Università di Pisa, and Istituto Nanoscienze - CNR, Pisa 56127, Italy;* orcid.org/0000-0003-4400-8808

Complete contact information is available at: https://pubs.acs.org/10.1021/acsphotonics.2c01157

Funding

This work has received funding from the European Research Council (ERC) under the European Union's Horizon 2020 research and innovation program (Grant Agreement No. 818064) and from the Italian Ministry of University and Research under the PRIN 2017 Project Monstre-2D.

Notes

The authors declare no competing financial interest.

■ ACKNOWLEDGMENTS

We gratefully acknowledge the Center for High Performance Computing (CHPC) at SNS for providing the computational infrastructure.

■ REFERENCES

(1) Ferrari, A. C.; Bonaccorso, F.; Fal'Ko, V.; Novoselov, K. S.; Roche, S.; Bøggild, P.; Borini, S.; Koppens, F. H.; Palermo, V.; Pugno, N.; et al. Science and technology roadmap for graphene, related two-dimensional crystals, and hybrid systems. *Nanoscale* **2015**, *7*, 4598−4810.
(2) Guinea, F.; Katsnelson, M.; Geim, A. Energy gaps and a zero-field quantum Hall effect in graphene by strain engineering. *Nat. Phys.* **2010**, *6*, 30−33.
(3) Levy, N.; Burke, S.; Meaker, K.; Panlasigui, M.; Zettl, A.; Guinea, F.; Neto, A. C.; Crommie, M. F. Strain-induced pseudo−magnetic fields greater than 300 T in graphene nanobubbles. *Science* **2010**, *329*, 544−547.
(4) Nigge, P.; Qu, A.; Lantagne-Hurtubise, É.; Mårsell, E.; Link, S.; Tom, G.; Zonno, M.; Michiardi, M.; Schneider, M.; Zhdanovich, S.; et al. Room temperature strain-induced Landau levels in graphene on a wafer-scale platform. *Science Advances* **2019**, *5*, No. eaaw5593.
(5) Bukharaev, A. A.; Zvezdin, A. K.; Pyatakov, A. P.; Fetisov, Y. K. Straintronics: a new trend in micro-and nanoelectronics and materials science. *Physics-Uspekhi* **2018**, *61*, 1175.
(6) Si, C.; Sun, Z.; Liu, F. Strain engineering of graphene: a review. *Nanoscale* **2016**, *8*, 3207−3217.
(7) Zhu, S.; Stroscio, J. A.; Li, T. Programmable extreme pseudomagnetic fields in graphene by a uniaxial stretch. *Physical review letters* **2015**, *115*, 245501.
(8) Zhang, D.-B.; Seifert, G.; Chang, K. Strain-induced pseudo-magnetic fields in twisted graphene nanoribbons. *Physical review letters* **2014**, *112*, 096805.
(9) Castro-Villarreal, P.; Ruiz-Sánchez, R. Pseudomagnetic field in curved graphene. *Phys. Rev. B* **2017**, *95*, 125432.
(10) Li, Y.; Tantiwanichapan, K.; Swan, A. K.; Paiella, R. Graphene plasmonic devices for terahertz optoelectronics. *Nanophotonics* **2020**, *9*, 1901−1920.
(11) Liu, P. Q.; Luxmoore, I. J.; Mikhailov, S. A.; Savostianova, N. A.; Valmorra, F.; Faist, J.; Nash, G. R. Highly tunable hybrid metamaterials employing split-ring resonators strongly coupled to graphene surface plasmons. *Nat. Commun.* **2015**, *6*, 1−7.
(12) Tamagnone, M.; Moldovan, C.; Poumirol, J.-M.; Kuzmenko, A. B.; Ionescu, A. M.; Mosig, J. R.; Perruisseau-Carrier, J. Near optimal graphene terahertz non-reciprocal isolator. *Nat. Commun.* **2016**, *7*, 1−6.
(13) Asgari, M.; Riccardi, E.; Balci, O.; De Fazio, D.; Shinde, S. M.; Zhang, J.; Mignuzzi, S.; Koppens, F. H.; Ferrari, A. C.; Viti, L.; et al. Chip-Scalable, Room-Temperature, Zero-Bias, Graphene-Based Terahertz Detectors with Nanosecond Response Time. *ACS Nano* **2021**, *15*, 17966−17976.
(14) Zanotto, S.; Bianco, F.; Miseikis, V.; Convertino, D.; Coletti, C.; Tredicucci, A. Coherent absorption of light by graphene and other optically conducting surfaces in realistic on-substrate configurations. *APL Photonics* **2017**, *2*, 016101.
(15) Miao, Z.; Wu, Q.; Li, X.; He, Q.; Ding, K.; An, Z.; Zhang, Y.; Zhou, L. Widely tunable terahertz phase modulation with gate-controlled graphene metasurfaces. *Physical Review X* **2015**, *5*, 041027.
(16) Nguyen, V. H.; Lherbier, A.; Charlier, J.-C. Optical Hall effect in strained graphene. *2D Materials* **2017**, *4*, 025041.
(17) Hagenmüller, D.; Ciuti, C. Cavity QED of the graphene cyclotron transition. *Phys. Rev. Lett.* **2012**, *109*, 267403.
(18) Chirolli, L.; Polini, M.; Giovannetti, V.; MacDonald, A. H. Drude weight, cyclotron resonance, and the Dicke model of graphene cavity QED. *Physical review letters* **2012**, *109*, 267404.
(19) Pellegrino, F.; Chirolli, L.; Fazio, R.; Giovannetti, V.; Polini, M. Theory of integer quantum Hall polaritons in graphene. *Phys. Rev. B* **2014**, *89*, 165406.
(20) Mann, C.-R.; Horsley, S. A.; Mariani, E. Tunable pseudo-magnetic fields for polaritons in strained metasurfaces. *Nat. Photonics* **2020**, *14*, 669−674.
(21) Ulbricht, R.; Hendry, E.; Shan, J.; Heinz, T. F.; Bonn, M. Carrier dynamics in semiconductors studied with time-resolved terahertz spectroscopy. *Rev. Mod. Phys.* **2011**, *83*, 543.
(22) Buron, J. D.; Petersen, D. H.; Bøggild, P.; Cooke, D. G.; Hilke, M.; Sun, J.; Whiteway, E.; Nielsen, P. F.; Hansen, O.; Yurgens, A.; et al. Graphene conductance uniformity mapping. *Nano Lett.* **2012**, *12*, 5074−5081.
(23) Smith, N. Classical generalization of the Drude formula for the optical conductivity. *Phys. Rev. B* **2001**, *64*, 155106.
(24) Cocker, T. L.; Baillie, D.; Buruma, M.; Titova, L. V.; Sydora, R. D.; Marsiglio, F.; Hegmann, F. A. Microscopic origin of the Drude-Smith model. *Phys. Rev. B* **2017**, *96*, 205439.
(25) Joyce, H. J.; Boland, J. L.; Davies, C. L.; Baig, S. A.; Johnston, M. B. A review of the electrical properties of semiconductor nanowires: insights gained from terahertz conductivity spectroscopy. *Semicond. Sci. Technol.* **2016**, *31*, 103003.
(26) Giovannini, T.; Rosa, M.; Corni, S.; Cappelli, C. A classical picture of subnanometer junctions: an atomistic Drude approach to nanoplasmonics. *Nanoscale* **2019**, *11*, 6004−6015.
(27) Giovannini, T.; Bonatti, L.; Polini, M.; Cappelli, C. Graphene Plasmonics: Fully Atomistic Approach for Realistic Structures. *journal of physical chemistry letters* **2020**, *11*, 7595−7602.
(28) Lafiosca, P.; Giovannini, T.; Benzi, M.; Cappelli, C. Going beyond the limits of classical atomistic modeling of plasmonic nanostructures. *J. Phys. Chem. C* **2021**, *125*, 23848−23863.
(29) Kim, J.; Lee, C.; Bae, S.; Jin Kim, S.; Soo Kim, K.; Hee Hong, B.; Choi, E. Effect of uni-axial strain on THz/far-infrared response of graphene. *Appl. Phys. Lett.* **2012**, *100*, 041910.
(30) Chhikara, M.; Gaponenko, I.; Paruch, P.; Kuzmenko, A. B. Effect of uniaxial strain on the optical Drude scattering in graphene. *2D Materials* **2017**, *4*, 025081.
(31) Li, X.; Cai, W.; An, J.; Kim, S.; Nah, J.; Yang, D.; Piner, R.; Velamakanni, A.; Jung, I.; Tutuc, E.; et al. Large-area synthesis of high-quality and uniform graphene films on copper foils. *science* **2009**, *324*, 1312−1314.
(32) Whittaker, D.; Culshaw, I. Scattering-matrix treatment of patterned multilayer photonic structures. *Phys. Rev. B* **1999**, *60*, 2610.

(33) Ivanov, I.; Bonn, M.; Mics, Z.; Turchinovich, D. Perspective on terahertz spectroscopy of graphene. *EPL (Europhysics Letters)* **2015**, *111*, 67001.
(34) Pellegrino, F.; Angilella, G.; Pucci, R. Strain effect on the optical conductivity of graphene. *Phys. Rev. B* **2010**, *81*, 035411.
(35) Pereira, V. M.; Castro Neto, A. H.; Peres, N. M. R. Tight-binding approach to uniaxial strain in graphene. *Phys. Rev. B* **2009**, *80*, 045401.
(36) Bonatti, L.; Gil, G.; Giovannini, T.; Corni, S.; Cappelli, C. Plasmonic Resonances of Metal Nanoparticles: Atomistic vs. Continuum Approaches. *Frontiers in Chemistry* **2020**, *8*, 340.
(37) Bonatti, L.; Nicoli, L.; Giovannini, T.; Cappelli, C. In silico design of graphene plasmonic hot-spots. *Nanoscale Advances* **2022**, *4*, 2294−2302.
(38) Yu, R.; Cox, J. D.; Saavedra, J.; Garcia de Abajo, F. J. Analytical modeling of graphene plasmons. *ACS Photonics* **2017**, *4*, 3106−3114.
(39) Giovannini, T.; Bonatti, L.; Lafiosca, P.; Nicoli, L.; Castagnola, M.; Illobre, P. G.; Corni, S.; Cappelli, C. Do We Really Need Quantum Mechanics to Describe Plasmonic Properties of Metal Nanostructures? *ACS photonics* **2022**, *9*, 3025−3034.
(40) Castro Neto, A. H.; Guinea, F.; Peres, N. M. R.; Novoselov, K. S.; Geim, A. K. The electronic properties of graphene. *Reviews of Modern Physics* **2009**, *81*, 109.

https://doi.org/10.1021/acsphotonics.2c01157
ACS Photonics 2023, 10, 394−400

Chapter 8

Do We Really Need Quantum Mechanics to Describe Plasmonic Properties of Metal Nanostructures?

ACS Photonics

pubs.acs.org/journal/apchd5

Article

Do We Really Need Quantum Mechanics to Describe Plasmonic Properties of Metal Nanostructures?

Tommaso Giovannini,* Luca Bonatti, Piero Lafiosca, Luca Nicoli, Matteo Castagnola, Pablo Grobas Illobre, Stefano Corni, and Chiara Cappelli*

Cite This: *ACS Photonics* 2022, 9, 3025−3034

Read Online

ACCESS | Metrics & More | Article Recommendations | Supporting Information

ABSTRACT: Optical properties of metal nanostructures are the basis of several scientific and technological applications. When the nanostructure characteristic size is of the order of few nm or less, it is generally accepted that only a description that explicitly describes electrons by quantum mechanics can reproduce faithfully its optical response. For example, the plasmon resonance shift upon shrinking the nanostructure size (red-shift for simple metals, blue-shift for *d*-metals such as gold and silver) is universally accepted to originate from the quantum nature of the system. Here we show instead that an atomistic approach based on classical physics, ωFQFμ (frequency dependent fluctuating charges and fluctuating dipoles), is able to reproduce all the typical "quantum" size effects, such as the sign and the magnitude of the plasmon shift, the progressive loss of the plasmon resonance for gold, the atomistically detailed features in the induced electron density, and the non local effects in the nanoparticle response. To support our findings, we compare the ωFQFμ results for Ag and Au with literature time-dependent DFT simulations, showing the capability of fully classical physics to reproduce these TDDFT results. Only electron tunneling between nanostructures emerges as a genuine quantum mechanical effect, that we had to include in the model by an ad hoc term.

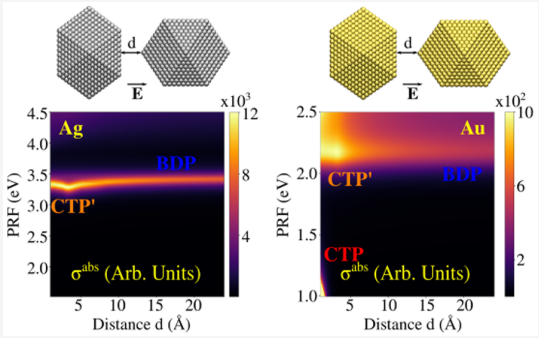

KEYWORDS: *atomistic, interband, gold, silver, tunneling, field enhancement*

1. INTRODUCTION

The recent progress in nanoscience has allowed to experimentally reach the atomistic detail in the geometrical arrangement of metal nanoaggregates.[1−5] This has paved the way for many technological applications, including the creation of local hot-spots featuring enormously enhanced electric field, that has allowed single molecule detection, and even submolecular resolutions, when coupled to surface enhanced spectral techniques.[6−13] A deep understanding of the peculiarities of these structures may benefit of an unavoidable interplaying between theory and experiments. At subnanometric scales such as for atomistically defined needles/tips, quantum effects play an important role in the plasmonic response and therefore need to be considered.[14−23] As a result, a unified theoretical approach to describe the plasmonic properties of metal nanoaggregates under different regimes needs to consistently take into account the physical phenomena underlying the quantum and classical response.[19,24,25]

Large-size nanoparticles are typically described by means of classical electrodynamics, such as the Mie theory,[26] the Discrete Dipole Approximation (DDA),[27] the electromagnetic Finite Difference Time Domain (FDTD),[28] or the Boundary Element Method (BEM).[29−34]

Nonlocal corrections can be considered by exploiting spatially dependent dielectric function based models[35] or hydrodynamic models,[36−38] which are also able to account for the electron spill-out effect that determines the near-field generated in plasmonic hot-spots of *d*-metals.[39−41] However, these models substantially discard atomistic details, which could become relevant when studying surface-assisted spectroscopic properties.[42] It is also worth noting that electron spill-out and nonlocal effects can effectively be treated by means of surface response functions, which would need to be specified for different surface planes.[43,44] Limitations of these approaches for nanoparticles have recently been discussed.[45] In this context, ab initio modeling, at the Time-Dependent Density Functional Theory (TDDFT) level, is still considered the most accurate approach to deal with these effects;[46−50] however, it can only treat relatively small metal nanoparticles (NP; with diameter < 5 nm); therefore, real-size systems

Received: May 20, 2022
Published: September 1, 2022

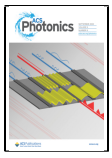

https://doi.org/10.1021/acsphotonics.2c00761
ACS Photonics 2022, 9, 3025−3034

cannot be afforded due to the prohibitively large computational cost. Such a situation naturally leads to the conclusion that an explicit quantum mechanical treatment of electrons, such as DFT and TDDFT, is mandatory to provide a realistic picture of plasmonic phenomena in this size regime. Such a conclusion is not really challenged by the existing classical atomistic approaches to nanoplasmonics,[51−57] that, while delivering accurate results, are based on fitting very general classical response expressions on TDDFT calculations, retaining therefore the physical basis of the latter.

In this paper, we explore whether a classical atomistic method based on essentially classical ingredients (Drude conduction mechanism and classical polarizabilities to reproduce interband polarization) can reproduce the optical response of complex plasmonic nanostructures. To this goal, we propose a physically robust approach to describe the plasmonic properties of sizable metal nanoaggregates characterized by the presence of interband transitions. Together with collective electronic excitations, they determine the plasmonic response of noble metal nanoparticles. The model is based on the recently developed ωFQ method,[32,58−61] in which each metal atom is endowed with a net charge, which varies as a response of the external electric field. The charge-exchange between atoms is governed by the Drude mechanism. As an element of mere quantum mechanical origin that we found essential to add to our classical atomistic picture, the Drude charge exchange is modulated by quantum tunneling, which guarantees a correct description of the optical response for subnanometric junctions.[15,16,18,20,22,58,62,63] Although the method has been successfully applied to sodium nanostructures and graphene-based materials,[58,59] the basic formulation of ωFQ overlooks interband contributions, thus, it is unsuitable to describe the plasmonic properties of nanostructures based on *d*-metals.[64−68] Here, we substantially extend ωFQ so to assign each metal atom with an atomic complex-valued polarizability (i.e., a complex-valued dipole moment), appropriately tuned to model interband effects. The resulting approach is called ωFQFμ (frequency-dependent fluctuating charges and fluctuating dipoles) by analogy with a parent polarizable approach, which has been proposed by some of the present authors to treat completely different chemical systems.[69−71] The theoretical basis of the approach stems from the evidence that *d*-states can efficiently be treated as polarizable shells placed at lattice positions.[67]

Notice that ωFQFμ was developed from a different perspective compared to other classical atomistic approaches.[51−54] Indeed, ωFQFμ is built from textbook bulk metal physics rather than fitting of generic polarizability and capacity frequency-dependent expressions. This provides practical benefits as well. In fact, Drude-tunneling and interband regimes are perfectly decoupled in the two terms that depend on ωFQs[58] and ωFμs, thus allowing for a fine, physically guided, tuning of the plasmonic response. In the following, we show that ωFQFμ is able to correctly reproduce the plasmonic properties of Ag and Au nanostructures as a function of size and shape, and also their plasmonic response when forming subnanometer junctions. Remarkably, the favorable scaling of the method permits to afford large systems (more than 10^4 atoms), which cannot be treated at the quantum-mechanical level. Also, the ability of ωFQFμ to fully retain the atomistic detail is crucial to reproduce not only the plasmonic response but also near-field enhancements, which play a key-role in near-field enhanced spectroscopies.[72,73]

2. THEORETICAL MODEL

ωFQFμ is a fully atomistic, classical approach which substantially extends ωFQ, which assigns to each metal atom a time dependent charge. Under the action of a time dependent external electric field, metal atoms exchange charge via the Drude conduction mechanism, which is further assisted by quantum tunneling, which limits the charge transfer among nearest neighboring atoms and makes the interaction decrease with the typical exponential decay.[58] In particular, ωFQ charge equation of motion in the frequency domain (ω) reads:[58]

$$-i\omega q_i(\omega) = \frac{2n_0\tau}{1-i\omega\tau}\sum_j [1-f(l_{ij})]\frac{\mathcal{A}_{ij}}{l_{ij}}(\phi_j^{el}-\phi_i^{el}) = \sum_j K_{ij}(\phi_j^{el}-\phi_i^{el}) \quad (1)$$

where $q_i(\omega)$, a complex-valued quantity, is the Fourier component at the frequency ω of the oscillating atomic charge on atom *i*. n_0 is the metal density, τ the friction time, $\mathcal{A}_{ij}$ is the effective area connecting *i*th and *j*th atoms, and l_{ij} is their distance. ϕ^{el} is the electrochemical potential acting on each metal atom, which takes into account the interactions between the different atoms and their interaction with the external electric field, which oscillates at frequency ω. $f(l_{ij})$ is a Fermi-like function mimicking quantum tunneling:[58]

$$f(l_{ij}) = \frac{1}{1+\exp\left[-d\left(\frac{l_{ij}}{s\cdot l_{ij}^0}-1\right)\right]} \quad (2)$$

where l_{ij}^0 is the equilibrium atom−atom distance, whereas *d* and *s* are dimensionless parameters that determine the sharpness and the center of the Fermi function $f(l_{ij})$, respectively. Their values can be determined by comparing computed results with reference ab initio data (see also Section S1 in the Supporting Information (SI)). In eq 1, Drude and tunneling terms are collected in the **K** matrix. The parameters entering ωFQ all have a clear microscopic physical meaning. Therefore, their values can be either chosen by an independent experiment or fitted to reproduce higher level results, and then the soundness of their values can be judged. We took the latter perspective, as discussed in the SI.

Due to its physical foundations, ωFQ cannot describe the specificity of metals featuring *d*-electrons, which contribute to interband transitions and that substantially affect the plasmon response.[64−68] Therefore, we here extend ωFQ into a novel method, ωFQFμ, in which each atom is assigned a charge and an additional source of polarization, that is, an atomic polarizability (to which an induced dipole moment is associated). The presence of the dipole moments is included in eq 1 by taking into account the interaction between charges and dipoles in the electrochemical potential. The induced dipole moments $\boldsymbol{\mu}_i$ are instead obtained by solving the following set of linear equations:

$$\boldsymbol{\mu}_i = \alpha_i^{\omega}(\mathbf{E}_i^{ext} + \mathbf{E}_i^{\mu} + \mathbf{E}_i^{q}) \quad (3)$$

where, $\mathbf{E}^{ext}$, $\mathbf{E}^{\mu}$, and $\mathbf{E}^{q}$ are the external electric field and those generated by the other dipole moments and charges, respectively. α^{ω} is the atomic complex polarizability, which is introduced to describe interband transitions. Remarkably, α^{ω} can easily be obtained by extracting interband contributions

https://doi.org/10.1021/acsphotonics.2c00761
ACS Photonics 2022, 9, 3025−3034

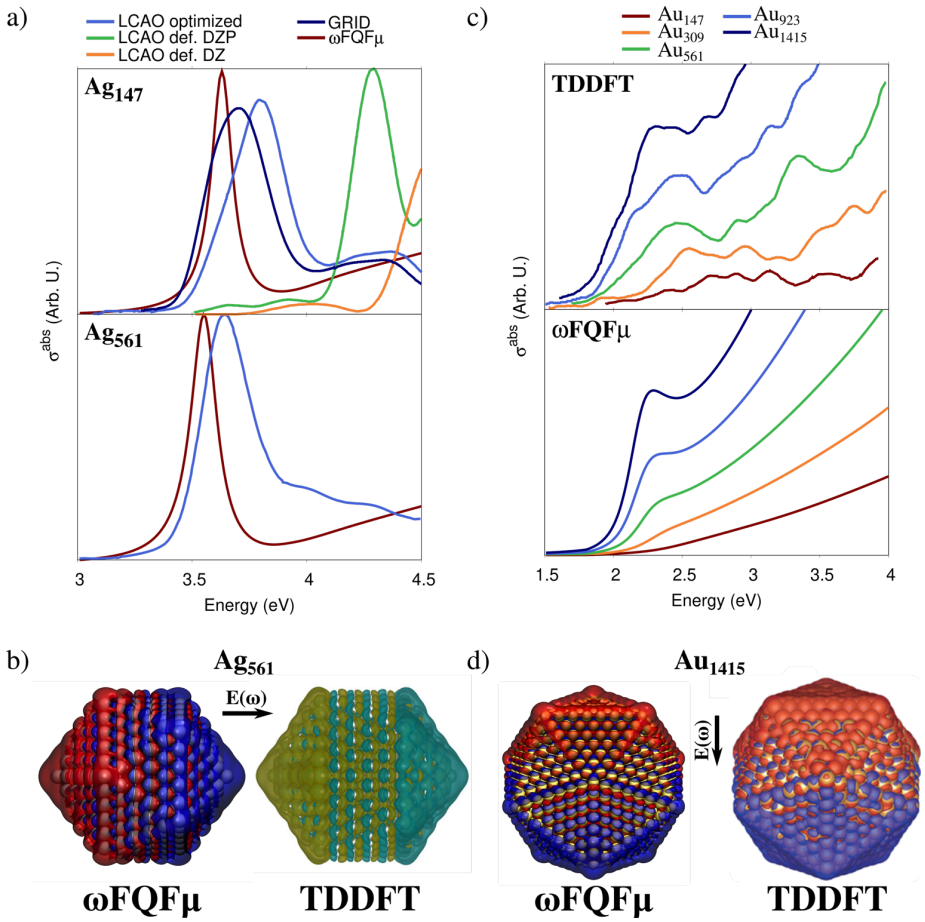

Figure 1. (a) Computed ωFQFμ and TDDFT σ^{abs} for Ag_{147} (~0.8 nm radius) and Ag_{561} (~1.4 nm radius). TDDFT results are reproduced from ref 87 and obtained by exploiting different basis sets (LCAO optimized, def. DZ (double-ζ), def. DZP (double-ζ polarized)) and on a real-space grid (GRID). (b) ωFQFμ and TDDFT[87] plasmon densities for Ag_{561}. TDDFT plasmon densities adapted with permission from ref 87. Copyright 2015 APS Publications. (c) ωFQFμ and TDDFT[88] σ^{abs} for Au_{147}–Au_{1415} (~1.9 nm radius). (d) ωFQFμ and TDDFT[88] plasmon densities for Au_{1415}. TDDFT plasmon densities adapted with permission from ref 88. Copyright 2014 ACS Publications. ωFQFμ isovalues are set to 0.002 and 0.0005 au for Ag and Au, respectively.

from the experimental permittivity function (see Section S1 in the SI), with no need to introduce a posteriori adjustable parameters.

To effectively couple charges and dipoles, that is, to simultaneously account for Drude and interband transitions, eqs 1 and 3 need to be solved simultaneously. By explicitly indicating all terms, the problem can be recast as the following set of linear equations:

$$\sum_{j=1}^{N}\left(\sum_{k=1}^{N} K_{ik}(T_{kj}^{qq} - T_{ij}^{qq}) + i\omega\delta_{ij}\right)q_j + \sum_{j=1}^{N}\left(\sum_{k=1}^{N} K_{ik}(T_{kj}^{q\mu} - T_{ij}^{q\mu})\right)\boldsymbol{\mu}_j = \sum_{k=1}^{N} K_{ik}(V_i^{ext} - V_k^{ext}) \quad (4)$$

$$\sum_{j\neq i}^{N} T_{ij}^{\mu q} q_j + \sum_{j\neq i}^{N} T_{ij}^{\mu\mu}\boldsymbol{\mu}_j + \frac{1}{\alpha_i^{\omega}}\boldsymbol{\mu}_i = \mathbf{E}_i^{ext} \quad (5)$$

where T^{qq}, $T^{q\mu}$, and $T^{\mu\mu}$ define charge–charge, charge–dipole, dipole–dipole interactions, respectively. By imposing $T^{\mu\mu}$ diagonal elements to correspond to $1/\alpha^{\omega}$, eqs 4 and 5 can be written in a compact matrix formulation as

$$\begin{pmatrix} \mathbf{A}^{qq} & \mathbf{A}^{q\mu} \\ \mathbf{T}^{\mu q} & \mathbf{T}^{\mu\mu} \end{pmatrix}\begin{pmatrix} \mathbf{q} \\ \boldsymbol{\mu} \end{pmatrix} = \begin{pmatrix} \mathbf{f}^{q} \\ \mathbf{f}^{\mu} \end{pmatrix} \quad (6)$$

where the complex $\mathbf{A}$ matrices include interaction kernels and the K_{ij} terms (see Section S1 in the SI for more details). The right-hand side of eq 6 accounts for external polarization sources, that is, the electric potential and field calculated at atomic positions:

$$f_i^{q} = \sum_j K_{ij}(V_i^{ext} - V_j^{ext})$$

$$\mathbf{f}_i^{\mu} = \mathbf{E}_i^{ext}$$

Notably, any kind of plasmonic materials can be modeled by ωFQFμ because it integrates all relevant physical ingredients (i.e., Drude conduction, electrostatics, quantum tunneling and interband transition) via eq 1 and eq 3. Also, once complex-

https://doi.org/10.1021/acsphotonics.2c00761
ACS Photonics 2022, 9, 3025–3034

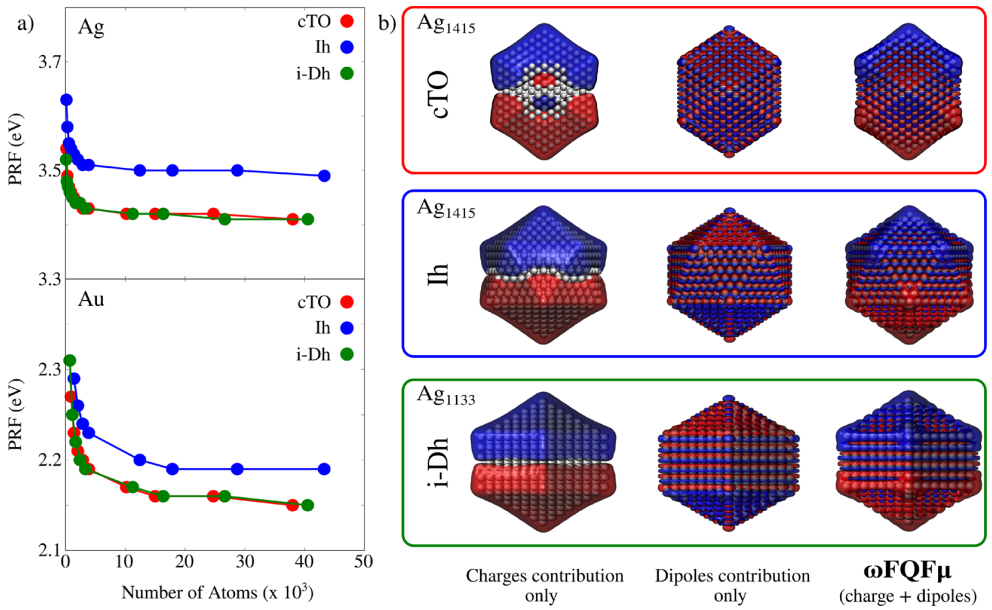

Figure 2. (a) Ag and Au PRF for cTO, Ih, and i-Dh NPs as a function of the number of atoms. (b) Ag densities calculated at the PRF for cTO (top), Ih (middle), and i-Dh (bottom) geometries. Charge and dipole contributions are plotted together with ωFQFμ plasmon densities. Isovalues are 0.002 and 0.0005 au for Ag and Au, respectively.

valued charges and dipoles are computed, the absorption cross section σ^{abs} and the induced electric field can easily be calculated (see Section S1 in the SI for more details).

To conclude this section, it is worth noting that other atomistic, classical models, belonging to the Discrete Interaction Model (DIM) class, have been proposed to describe the plasmonic response of noble-metal nanoparticles.[54,74] Among them, the coordination-dependent–Discrete Interaction Model (cd-DIM)[74] is able to properly describe the size dependency of the Plasmon Resonance Frequency (PRF) for Ag NPs and the plasmonic response of Ag dimers, which is governed by quantum tunneling. Within this model, both effects arise from a modification of the coordination of surface atoms and the consequent modification of the atomic polarizability that is considered to be a parametrized function of the coordination number. In our approach the first effect genuinely originates from the screening effect of *d*-electrons, which is physically modeled by the presence of the α^{ω} term. A correct description of the plasmonic response of dimers arises from the phenomenological introduction of the quantum tunneling via the Fermi function in eq 2.

3. RESULTS AND DISCUSSION

3.1. Optical Response of Metal Nanoparticles: ωFQFμ versus TDDFT Results. Here the capability of ωFQFμ at describing typical plasmonic response properties of single metal nanoparticles is discussed.[75] Although the model is completely general, it is here applied to Ag and Au nanoparticles (NP), for which α^{ω} values are obtained from the permittivity functions reported by Etchegoin et al. in ref 76 and fitted in ref 77 (see also Section S1 in the SI). For both metals, we first consider NPs with three different geometrical arrangements, namely, truncated cuboctahedron (cTO), icosahedral (Ih), and ino-decahedron (i-Dh), which are all characterized by atomistically defined edges.[54] Their plasmonic properties are studied as a function of the size (from a minimum of 85 atoms, ∼5 Å radius, to a maximum of 43287 atoms, ∼65 Å radius).[78−80] Note that geometry relaxation is not considered, because it only slightly affects optical responses.[23,81−86]

Although sizable NPs cannot be afforded by ab initio methods, they can indeed be treated by ωFQFμ,[60] at a reasonable computational time (on average, 59 min on Intel(R) Xeon(R) Gold 5120 CPU @ 2.20 GHz, 28 processors, for each frequency given in input for the structure composed of 43287 atoms). As an example of the performance of ωFQFμ, Kuisma et al.[87] have reported that the calculation of the optical spectrum of Ag_{561} (∼1.4 nm radius) in Ih geometry with the time-propagation (TP) approach to TDDFT requires a wall time of 42.0 h with 512 cores.[87] For the same system, ωFQFμ only requires 25 s on the aforementioned platform. Remarkably, ωFQFμ and reference TDDFT data are very similar (see Figure 1a, bottom panel). Slight discrepancies in the PRF and band broadening among the two models can be justified by considering that TDDFT results substantially vary as a function of the basis set; this is demonstrated by the data shown in Figure 1a (top panel), which are taken from ref 87. Clearly, reference ab initio data display large variability of almost 1 eV when moving from linear combinations of atomic orbitals (LCAO) with different basis sets to real space grid calculation (GRID) results. We also remark that the width of peaks is chosen arbitrarily in TDDFT calculations.

A similar comparison can be performed for Au Ih NPs. TDDFT absorption cross sections reproduced from ref 88 and calculated at the ωFQFμ level are reported in Figure 1c,d. Also, in this case, ωFQFμ can correctly reproduce PRF trends as a function of the NP size and the relative intensities of the bands for the different NPs.

One of the most peculiar features of noble metal NPs and, in general, of *d*-metals is that the PRF blue shifts as the size of the

https://doi.org/10.1021/acsphotonics.2c00761
ACS Photonics 2022, 9, 3025−3034

system decreases, in contrast to what happens for simple metals (and correctly reproduced by ωFQ[58]). The physical origin of this blue-shift has been studied in the past.[67] The screening of the Coulomb interaction among conduction electrons (that determines the plasmon frequency) by the localized *d*-electron core interplays with conduction electrons spill-out at the cluster surface. In short, the *d*-electron core screens electron−electron repulsion, thus decreasing the *d*-metal plasmon frequency compared to what is expected on the basis of the free-electron density of the metal. At the surface, conduction electrons spill out of the structure; in ωFQ and ωFQFμ, the finite size of each atomic distribution accounts for this effect. In parallel, the *d*-electron core, which is localized on the metal atom (described by a point dipole in ωFQFμ) cannot effectively screen the electron−electron repulsion. As a result, the plasmon frequency moves back to the nonscreened, free-electron value. Remarkably, ωFQFμ can indeed describe this mechanism because it provides the right result for the right reason. In fact, if the *d*-electron core response is artificially switched-off (i.e., $\alpha^{\omega} \rightarrow 0$ in eq 3), the plasmon frequency (which is overall increased), red shifts for metal nanoparticles, as it is expected based on spill-out effects only.[58,82] This is demonstrated by the plots reported in Figure S3 in the SI.

The dependence of computed PRFs on the number of atoms is reported in Figure 2a for different geometries; the plots clearly demonstrate that ωFQFμ can indeed correctly reproduce the previously reported trends. Also, the linear fit of Ag Ih PRFs as a function of the inverse of the NP diameter permits to linearly extrapolate PRF = 3.47 eV for an infinite diameter. This value is in almost perfect agreement with the mesoscopic limit of 3.43 eV, as obtained at the quasi-static FDTD (QSFDTD) level,[87] and in excellent agreement with the extrapolated ab initio value of 3.35 eV (see also Figure S4 in the SI).[87]

The investigation of plasmon densities (i.e., the imaginary part of the charge density induced by a monochromatic electromagnetic field oscillating at the PRF) is of fundamental importance for correctly characterizing the plasmon resonance. Computed densities at the PRF for the largest structures in each geometrical arrangement are depicted in Figure 2b. In all cases, they represent a dipolar plasmon. Our result can be compared with reference ab initio data for Ag_{561} (∼1.4 nm radius, see Figure 1b) and Au_{1415} (∼1.9 nm radius, see Figure 1d). In both cases, the agreement is almost perfect.

For the purpose of a deeper theoretical analysis, ωFQFμ can also be used to decouple the contributions of Drude and interband transitions to the total plasmon density. Charge and dipole contributions are graphically depicted in Figure 2b for selected Ag NPs (see Figure S5 in the SI for Au NPS). Clearly, the two plasmon densities are associated with dipole moments in opposite directions. This finding remarks the screening role of the *d*-electrons response.[41,67] As explained above, this results in the typical blue shift observed for *d*-metals.

To further demonstrate the ability of ωFQFμ to correctly take into account screening effects in *d*-metal NPs, we can compare density distributions in inner regions. Computed ωFQFμ and TDDFT densities for Au_{1415} Ih NP (∼1.9 nm radius), in the central region of the cluster (defined for $-2 < z < 2$ Å), are depicted in Figure 3. Notice that densities are computed at the corresponding PRFs, which only differ by 0.01 eV. Coherently with the results reported in Figure 1d, positive and negative charges are located at the top and bottom surface regions, respectively. However, ωFQFμ and TDDFT densities are mainly characterized by a local charge distribution around each Au atom, which is polarized along an opposite direction with respect to the polarization of the surface density. Such a behavior is related to screening effects, which are correctly taken into account by our atomistic, yet classical model.

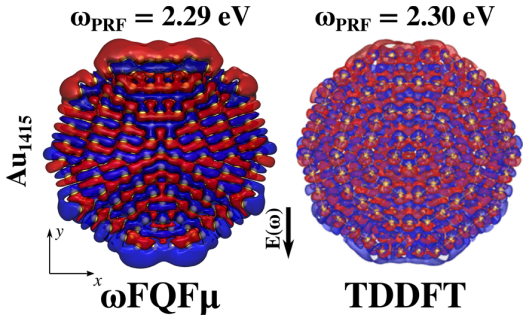

Figure 3. ωFQFμ and TDDFT[88] Au_{1415} (∼1.9 nm radius) plasmon densities in the central region of the cluster ($-2 < z < 2$ Å). TDDFT plasmon densities adapted with permission from ref 88. Copyright 2014 ACS Publications.

In Figure 4a,b the total enhanced electric field ($|\mathbf{E}|/|\mathbf{E}_0|$, where $\mathbf{E}_0$ is the external electric field intensity) at the PRF is reported. Such quantity (elevated to the fourth power) is related to field enhancement factors that are measured in SERS experiments.[10] The dependence of $|\mathbf{E}|/|\mathbf{E}_0|$ factors as a function of the number of atoms and the NPs radius is reported in Figure 4a and b, respectively. Notice that enhancement factors are computed at a distance of 3 Å from the tip of each structure; according to many previous reports, it corresponds to the typical adsorption distance of molecular systems.[89] $|\mathbf{E}|/|\mathbf{E}_0|$ color maps at the PRF for each geometrical arrangement are graphically displayed in Figures 4c. As expected, $|\mathbf{E}|/|\mathbf{E}_0|$ maximum values correspond to tips, and are reported for cTO geometries (for both gold and silver), where edges are the sharpest. Interestingly, for all arrangements, $|\mathbf{E}|/|\mathbf{E}_0|$ follows a $\sqrt[3]{N}$ trend (N being the number of atoms) and, thus, a linear trend with respect to NP radius, because the difference in the electric potential linearly increases with the NP intrinsic size. Remarkably, ωFQFμ is also able to quantify the differences between Ag and Au NPs, being the latter associated with much lower enhancement factors as compared to the former, as expected in this frequency range.

As a final comment, it is remarkable that ωFQFμ is able to describe nonlocal effects. To demonstrate that, we artificially changed the total electric potential and field acting on a specific atom placed at the surface or at the centroid of Ag_{147} (∼0.8 nm radius) and Ag_{3871} (∼2.7 nm radius) structures in the Ih configuration. As a result, independently of the atom position, not only charge and the dipole of the perturbed atom are modified, but also those of other atoms (see Figure S6 in the SI).

3.2. Subnanometer Junctions. In this section we will show that ωFQFμ has the potential to describe hot-spots in subnanometer junctions in a physically consistent manner. This is possible due to the account for quantum tunneling (eq 1), which dominates the plasmon response in these systems. To showcase ωFQFμ performances, we study Ag_{2869}/Au_{2869} (∼2.6 nm radius) cTO dimers. In particular, we select two different morphologies obtained by approaching two NPs so to obtain surface−tip or surface−surface geometrical arrange-

https://doi.org/10.1021/acsphotonics.2c00761
ACS Photonics 2022, 9, 3025−3034

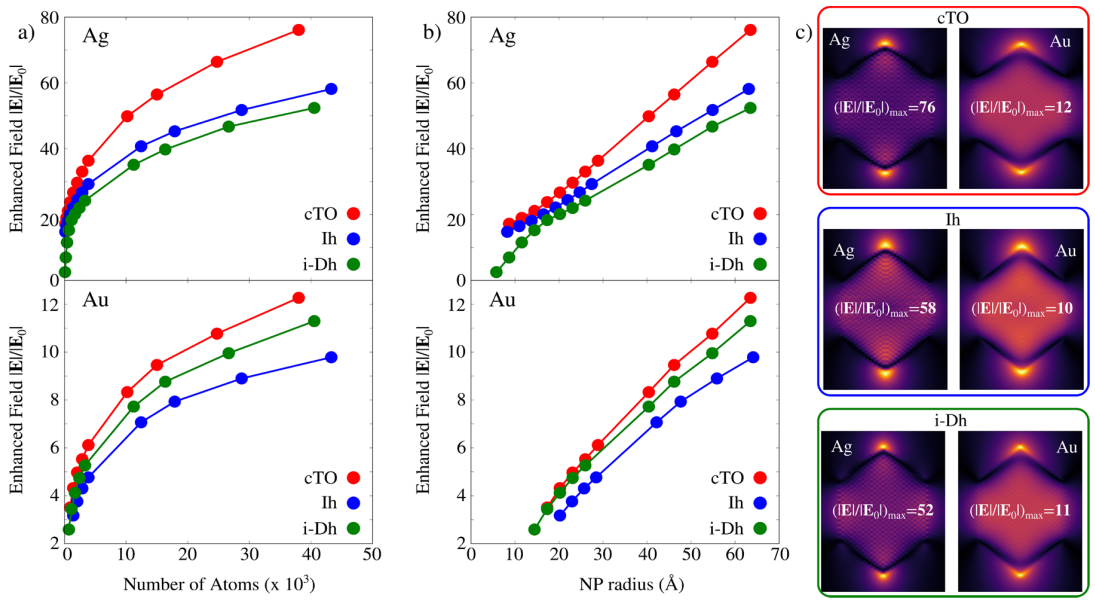

Figure 4. Ag and Au enhanced electric field $|\mathbf{E}|/|\mathbf{E}_0|$ calculated at 3 Å from the tips for cTO, Ih, and i-Dh NPs as a function of the number of atoms (a) and NP radius (b). (c) Ag and Au $|\mathbf{E}|/|\mathbf{E}_0|$ color maps for cTO (top), Ih (middle), and i-Dh (bottom) geometries.

ments (see Figures 5 and 6).[90] Note that for both structures the structural relaxation effects are not taken into account,

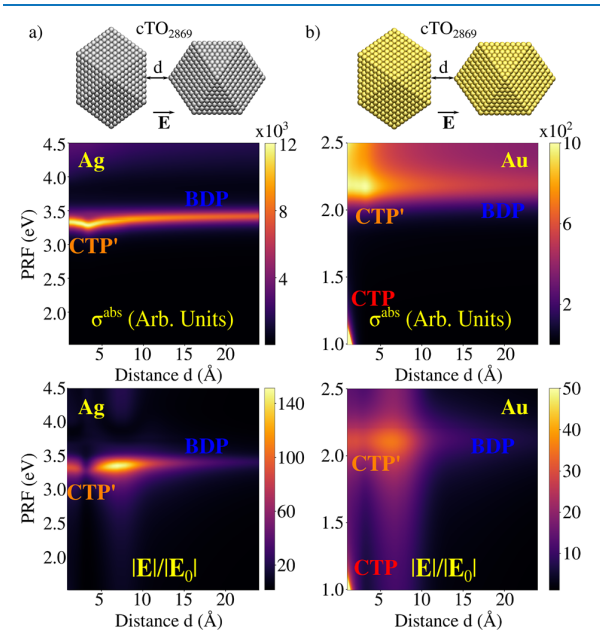

Figure 5. Ag (a) and Au (b) cTO_{2869} dimers in surface−tip geometrical arrangement. Color maps of σ^{abs} and $|\mathbf{E}|/|\mathbf{E}_0|$ as a function of the PRF and the distance between the two NPs are reported in the middle and bottom panels, respectively.

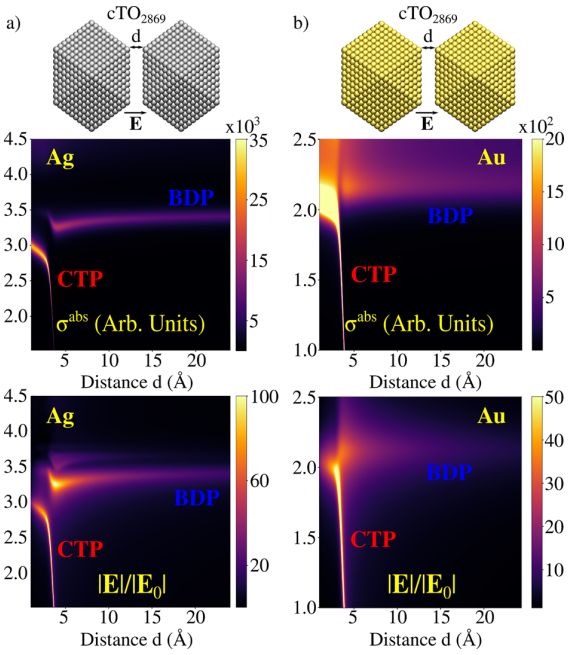

Figure 6. Ag (a) and Au (b) cTO_{2869} dimers in surface−surface geometrical arrangement. Color maps of σ^{abs} and $|\mathbf{E}|/|\mathbf{E}_0|$ as a function of the PRF and the distance between the two NPs are reported in middle and bottom panels, respectively.

similarly to previous studies.[81] However, to study the effects of structural relaxation we have modeled surface roughness as derived from an atomic adjustment on the surface of one of the two cTO NPs in the surface−surface arrangement (see Figure S7 in the SI).

For the ideal cTO dimers, we investigate both σ^{abs} and $|\mathbf{E}|/|\mathbf{E}_0|$ calculated at the gap's center as a function of the distance d between the two monomers, in the range 1−24 Å. Computed spectra (Figure 5a,b) are characterized by a high energy peak (~3.5 eV for Ag and ~2.2 eV for Au), which red-shifts as d decreases. However, a clear discontinuity occurs at around 4 Å, where quantum tunneling plays a relevant role; in fact, such a distance is close to the Ag−Ag and Au−Au equilibrium distances.

https://doi.org/10.1021/acsphotonics.2c00761
ACS Photonics 2022, 9, 3025−3034

For Au dimers, a second peak at lower energies is visible (d < 2 Å, PRF < 1.5 eV), which blue-shifts as d decreases (see Figure 5b). This band is not present for Ag, because its PRF falls below the investigated frequency range. Highest energy PRF corresponds to the typical Boundary Dipolar Plasmon, BDP, whereas the low-energy peak is associated with a Charge Transfer Plasmon, CTP, where a dipole moment arises in the whole structure (see Figures S8 and S9 in the SI). Note that for distances at which the CT mechanism takes place (for d < 4 Å), the high energy peak is associated with a high-order charge transfer plasmon, usually called CTP′. The clear discontinuity highlighted in σ^{abs} plots is also evident in the case of the computed $|\mathbf{E}|/|\mathbf{E}_0|$ values, which are reported as a color map as a function of the distance in Figure 5, bottom panels. For Ag, the maximum $|\mathbf{E}|/|\mathbf{E}_0|$ is depicted before the two NPs enter in the CT regime, whereas the opposite holds for the Au dimer, for which it corresponds to the CTP peak.

The surface−surface arrangements show similar plasmonic features, independently of the metal nature (see Figure 6a,b). In fact, both spectra are characterized by the presence of two bands when d < 4 Å: a CTP and a CTP′ peak (very low in intensity for Ag and fused with CTP for Au), which blue-shift or red-shift as d decreases, respectively. For d > 4 Å spectra are instead dominated by the BDP mode. The associated $|\mathbf{E}|/|\mathbf{E}_0|$ factors are plotted as a function of the distance in Figure 6, bottom panels. The computed values are of the same order of magnitude as for the previous case. Also, the maximum enhancement for Ag is shown at about 3.3 eV, for a distance of about 4 Å, that is, when CT effects start to dominate the plasmonic response. For Au, the maximum $|\mathbf{E}|/|\mathbf{E}_0|$ occurs at lower distances ($d \sim 3$ Å), however it is associated with the CTP′ plasmonic mode, differently from the tip−substate arrangement. Interestingly, in case of Ag, a clear additional region of enhancement is displayed at energies larger than 3.5 eV, for d > 4 Å. This region is associated with a high-order plasmon, which is indeed dark in the σ^{abs}.

Finally, note that, for both studied geometries, the maximum $|\mathbf{E}|/|\mathbf{E}_0|$ is 3−5 times larger than the corresponding factor obtained for the Ag monomer and even 10 times for Au.

4. SUMMARY AND CONCLUSIONS

We have discussed the prediction of a classical physics based model for nanoplasmonics, ωFQFμ. ωFQFμ is a general atomistic approach to describe the plasmonic features of complex metal nanostructures characterized by interband transitions. In the model, which is formulated in the frequency domain, each atom of the structure is endowed with both a complex-valued charge and dipole, which are determined by solving response equations to an external monochromatic electric field. The two polarization sources conceptually describe the two fundamental mechanisms occurring in d-metals, that is, Drude conduction (charges) and d-electrons polarization (dipoles). Remarkably, charges and dipoles mutually interact; therefore, all physical features of metal nanostructures are considered. ωFQFμ is fully classical, therefore nanostructures of realistic size can be computed with accuracy comparable to full ab initio calculations, but with enormously lower computational cost. Note that the interband polarizability in eq 3 arises from the quantum nature of the system; however, in our approach it is modeled without explicitly considering the quantum nature of the constituting atoms.

From a conceptual point of view, demonstrating that ωFQFμ is able to reproduce the findings of a fully quantum description of the system is clearly questioning the notion that an explicit quantum mechanical treatment is needed to describe the change in plasmonic properties upon shrinking of the nanostructure size. From the results presented in this work, it turns out that only quantum tunneling (relevant for nanoaggregates and nanojunction) is inaccessible by such classical physics, and we had in fact to phenomenologically include the tunneling in ωFQFμ. It is finally worth noting that another relevant quantum effect, Landau damping, is not included in this classical modeling and would in principle require adding a phenomenological correction to ωFQFμ.

From a computational perspective, the developed method paves the way for an investigation of the plasmonic properties of realistic metal nanoparticles, characterized by complex shapes that require an atomistic detail.

■ ASSOCIATED CONTENT

Supporting Information

The Supporting Information is available free of charge at https://pubs.acs.org/doi/10.1021/acsphotonics.2c00761.

Details on ωFQFμ equations and parametrization; Computational details; Ag and Au single NPs absorption cross sections and comparison with reference data; Demonstration of ωFQFμ nonlocality; Plasmon densities for Ag/Au cTO_{2869} dimers (PDF)

■ AUTHOR INFORMATION

Corresponding Authors

Tommaso Giovannini − *Scuola Normale Superiore, 56126 Pisa, Italy*; orcid.org/0000-0002-5637-2853; Email: tommaso.giovannini@sns.it

Chiara Cappelli − *Scuola Normale Superiore, 56126 Pisa, Italy*; orcid.org/0000-0002-4872-4505; Email: chiara.cappelli@sns.it

Authors

Luca Bonatti − *Scuola Normale Superiore, 56126 Pisa, Italy*

Piero Lafiosca − *Scuola Normale Superiore, 56126 Pisa, Italy*

Luca Nicoli − *Scuola Normale Superiore, 56126 Pisa, Italy*

Matteo Castagnola − *Scuola Normale Superiore, 56126 Pisa, Italy*

Pablo Grobas Illobre − *Scuola Normale Superiore, 56126 Pisa, Italy*; orcid.org/0000-0003-2544-9712

Stefano Corni − *Dipartimento di Scienze Chimiche, Università di Padova, 35131 Padova, Italy; Istituto di Nanoscienze del Consiglio Nazionale delle Ricerche CNR-NANO, 41125 Modena, Italy*; orcid.org/0000-0001-6707-108X

Complete contact information is available at: https://pubs.acs.org/10.1021/acsphotonics.2c00761

Funding

This work has received funding from the European Research Council (ERC) under the European Union's Horizon 2020 Research and Innovation Program (Grant Agreement No. 818064). S.C. gratefully acknowledge the European Union's Horizon 2020 FET Project ProID (No. 964363) for funding.

Notes

The authors declare no competing financial interest.

■ ACKNOWLEDGMENTS

We gratefully acknowledge the Center for High Performance Computing (CHPC) at SNS for providing the computational infrastructure.

■ REFERENCES

(1) Junno, T.; Deppert, K.; Montelius, L.; Samuelson, L. Controlled manipulation of nanoparticles with an atomic force microscope. *Appl. Phys. Lett.* **1995**, *66*, 3627−3629.
(2) Ishida, T.; Murayama, T.; Taketoshi, A.; Haruta, M. Importance of size and contact structure of gold nanoparticles for the genesis of unique catalytic processes. *Chem. Rev.* **2020**, *120*, 464−525.
(3) Sau, T. K.; Rogach, A. L. Nonspherical noble metal nanoparticles: colloid-chemical synthesis and morphology control. *Adv. Mater.* **2010**, *22*, 1781−1804.
(4) Liz-Marzán, L. M. Tailoring surface plasmons through the morphology and assembly of metal nanoparticles. *Langmuir* **2006**, *22*, 32−41.
(5) Grzelczak, M.; Pérez-Juste, J.; Mulvaney, P.; Liz-Marzán, L. M. Shape control in gold nanoparticle synthesis. *Chem. Soc. Rev.* **2008**, *37*, 1783−1791.
(6) Willets, K. A.; Van Duyne, R. P. Localized surface plasmon resonance spectroscopy and sensing. *Annu. Rev. Phys. Chem.* **2007**, *58*, 267−297.
(7) Zhang, R.; Zhang, Y.; Dong, Z.; Jiang, S.; Zhang, C.; Chen, L.; Zhang, L.; Liao, Y.; Aizpurua, J.; Luo, Y.; Yang, J. L.; Hou, J. G. Chemical mapping of a single molecule by plasmon-enhanced Raman scattering. *Nature* **2013**, *498*, 82−86.
(8) Jiang, S.; Zhang, Y.; Zhang, R.; Hu, C.; Liao, M.; Luo, Y.; Yang, J.; Dong, Z.; Hou, J. Distinguishing adjacent molecules on a surface using plasmon-enhanced Raman scattering. *Nat. Nanotechnol.* **2015**, *10*, 865−869.
(9) Chiang, N.; Chen, X.; Goubert, G.; Chulhai, D. V.; Chen, X.; Pozzi, E. A.; Jiang, N.; Hersam, M. C.; Seideman, T.; Jensen, L.; Van Duyne, R. P. Conformational contrast of surface-mediated molecular switches yields Ångstrom-scale spatial resolution in ultrahigh vacuum tip-enhanced Raman spectroscopy. *Nano Lett.* **2016**, *16*, 7774−7778.
(10) Langer, J.; et al. Present and Future of Surface-Enhanced Raman Scattering. *ACS Nano* **2020**, *14*, 28−117.
(11) Benz, F.; Schmidt, M. K.; Dreismann, A.; Chikkaraddy, R.; Zhang, Y.; Demetriadou, A.; Carnegie, C.; Ohadi, H.; De Nijs, B.; Esteban, R.; et al. Single-molecule optomechanics in "picocavities. *Science* **2016**, *354*, 726−729.
(12) Yang, B.; Chen, G.; Ghafoor, A.; Zhang, Y.; Zhang, Y.; Zhang, Y.; Luo, Y.; Yang, J.; Sandoghdar, V.; Aizpurua, J.; et al. Sub-nanometre resolution in single-molecule photoluminescence imaging. *Nat. Photonics* **2020**, *14*, 693−699.
(13) Liu, P.; Chulhai, D. V.; Jensen, L. Single-Molecule Imaging Using Atomistic Near-Field Tip-Enhanced Raman Spectroscopy. *ACS Nano* **2017**, *11*, 5094−5102.
(14) Teperik, T. V.; Nordlander, P.; Aizpurua, J.; Borisov, A. G. Quantum effects and nonlocality in strongly coupled plasmonic nanowire dimers. *Opt. Express* **2013**, *21*, 27306−27325.
(15) Zhu, W.; Esteban, R.; Borisov, A. G.; Baumberg, J. J.; Nordlander, P.; Lezec, H. J.; Aizpurua, J.; Crozier, K. B. Quantum mechanical effects in plasmonic structures with subnanometre gaps. *Nat. Commun.* **2016**, *7*, 11495.
(16) Urbieta, M.; Barbry, M.; Zhang, Y.; Koval, P.; Sánchez-Portal, D.; Zabala, N.; Aizpurua, J. Atomic-Scale Lightning Rod Effect in Plasmonic Picocavities: A Classical View to a Quantum Effect. *ACS Nano* **2018**, *12*, 585−595.
(17) Savage, K. J.; Hawkeye, M. M.; Esteban, R.; Borisov, A. G.; Aizpurua, J.; Baumberg, J. J. Revealing the quantum regime in tunnelling plasmonics. *Nature* **2012**, *491*, 574−577.
(18) Marinica, D.; Kazansky, A.; Nordlander, P.; Aizpurua, J.; Borisov, A. G. Quantum plasmonics: nonlinear effects in the field enhancement of a plasmonic nanoparticle dimer. *Nano Lett.* **2012**, *12*, 1333−1339.
(19) Esteban, R.; Borisov, A. G.; Nordlander, P.; Aizpurua, J. Bridging quantum and classical plasmonics with a quantum-corrected model. *Nat. Commun.* **2012**, *3*, 825.
(20) Esteban, R.; Zugarramurdi, A.; Zhang, P.; Nordlander, P.; García-Vidal, F. J.; Borisov, A. G.; Aizpurua, J. A classical treatment of optical tunneling in plasmonic gaps: extending the quantum corrected model to practical situations. *Faraday Discuss.* **2015**, *178*, 151−183.
(21) Campos, A.; Troc, N.; Cottancin, E.; Pellarin, M.; Weissker, H.-C.; Lermé, J.; Kociak, M.; Hillenkamp, M. Plasmonic quantum size effects in silver nanoparticles are dominated by interfaces and local environments. *Nat. Phys.* **2019**, *15*, 275−280.
(22) Scholl, J. A.; García-Etxarri, A.; Koh, A. L.; Dionne, J. A. Observation of quantum tunneling between two plasmonic nanoparticles. *Nano Lett.* **2013**, *13*, 564−569.
(23) Barbry, M.; Koval, P.; Marchesin, F.; Esteban, R.; Borisov, A.; Aizpurua, J.; Sánchez-Portal, D. Atomistic near-field nanoplasmonics: reaching atomic-scale resolution in nanooptics. *Nano Lett.* **2015**, *15*, 3410−3419.
(24) Baumberg, J. J.; Aizpurua, J.; Mikkelsen, M. H.; Smith, D. R. Extreme nanophotonics from ultrathin metallic gaps. *Nat. Mater.* **2019**, *18*, 668−678.
(25) Chen, X.; Liu, P.; Jensen, L. Atomistic electrodynamics simulations of plasmonic nanoparticles. *J. Phys. D Appl. Phys.* **2019**, *52*, 363002.
(26) Mie, G. Beiträge zur Optik trüber Medien, speziell kolloidaler Metallösungen. *Ann. Phys.-Berlin* **1908**, *330*, 377−445.
(27) Draine, B. T.; Flatau, P. J. Discrete-dipole approximation for scattering calculations. *J. Opt. Soc. Am. A* **1994**, *11*, 1491−1499.
(28) Taflove, A.; Hagness, S. C.; Piket-May, M. *Computational Electromagnetics: The Finite-Difference Time-Domain Method*; Elsevier: Amsterdam, The Netherlands, 2005.
(29) Myroshnychenko, V.; Carbó-Argibay, E.; Pastoriza-Santos, I.; Pérez-Juste, J.; Liz-Marzán, L. M.; García de Abajo, F. J. Modeling the optical response of highly faceted metal nanoparticles with a fully 3D boundary element method. *Adv. Mater.* **2008**, *20*, 4288−4293.
(30) García de Abajo, F. J.; Howie, A. Retarded field calculation of electron energy loss in inhomogeneous dielectrics. *Phys. Rev. B* **2002**, *65*, 115418.
(31) Mennucci, B.; Corni, S. Multiscale modelling of photoinduced processes in composite systems. *Nat. Rev. Chem.* **2019**, *3*, 315−330.
(32) Bonatti, L.; Gil, G.; Giovannini, T.; Corni, S.; Cappelli, C. Plasmonic Resonances of Metal Nanoparticles: Atomistic vs Continuum Approaches. *Front. Chem.* **2020**, *8*, 340.
(33) Marcheselli, J.; Chateau, D.; Lerouge, F.; Baldeck, P.; Andraud, C.; Parola, S.; Baroni, S.; Corni, S.; Garavelli, M.; Rivalta, I. Simulating Plasmon Resonances of Gold Nanoparticles with Bipyramidal Shapes by Boundary Element Methods. *J. Chem. Theory Comput.* **2020**, *16*, 3807−3815.
(34) Coccia, E.; Fregoni, J.; Guido, C.; Marsili, M.; Pipolo, S.; Corni, S. Hybrid theoretical models for molecular nanoplasmonics. *J. Chem. Phys.* **2020**, *153*, 200901.
(35) Luo, Y.; Fernandez-Dominguez, A.; Wiener, A.; Maier, S. A.; Pendry, J. Surface plasmons and nonlocality: a simple model. *Phys. Rev. Lett.* **2013**, *111*, 093901.
(36) Ciraci, C.; Pendry, J. B.; Smith, D. R. Hydrodynamic model for plasmonics: a macroscopic approach to a microscopic problem. *ChemPhysChem* **2013**, *14*, 1109−1116.
(37) Raza, S.; Bozhevolnyi, S. I.; Wubs, M.; Mortensen, N. A. Nonlocal optical response in metallic nanostructures. *J. Phys.: Condens. Matter* **2015**, *27*, 183204.
(38) Ciraci, C.; Della Sala, F. Quantum hydrodynamic theory for plasmonics: Impact of the electron density tail. *Phys. Rev. B* **2016**, *93*, 205405.
(39) Toscano, G.; Raza, S.; Jauho, A.-P.; Mortensen, N. A.; Wubs, M. Modified field enhancement and extinction by plasmonic nanowire dimers due to nonlocal response. *Opt. Express* **2012**, *20*, 4176−4188.
(40) David, C.; García de Abajo, F. J. Surface plasmon dependence on the electron density profile at metal surfaces. *ACS Nano* **2014**, *8*, 9558−9566.

https://doi.org/10.1021/acsphotonics.2c00761
ACS Photonics 2022, 9, 3025−3034

(41) Toscano, G.; Straubel, J.; Kwiatkowski, A.; Rockstuhl, C.; Evers, F.; Xu, H.; Asger Mortensen, N.; Wubs, M. Resonance shifts and spill-out effects in self-consistent hydrodynamic nanoplasmonics. *Nat. Commun.* **2015**, *6*, 1−11.
(42) Bonatti, L.; Nicoli, L.; Giovannini, T.; Cappelli, C. In silico design of graphene plasmonic hot-spots. *Nanoscale Adv.* **2022**, *4*, 2294−2302.
(43) Gonçalves, P.; Christensen, T.; Rivera, N.; Jauho, A.-P.; Mortensen, N. A.; Soljačić, M. Plasmon−emitter interactions at the nanoscale. *Nat. Commun.* **2020**, *11*, 1−13.
(44) Echarri, A. R.; Gonçalves, P.; Tserkezis, C.; de Abajo, F. J. G.; Mortensen, N. A.; Cox, J. D. Optical response of noble metal nanostructures: quantum surface effects in crystallographic facets. *Optica* **2021**, *8*, 710−721.
(45) Babaze, A.; Ogando, E.; Stamatopoulou, P. E.; Tserkezis, C.; Mortensen, N. A.; Aizpurua, J.; Borisov, A. G.; Esteban, R. Quantum surface effects in the electromagnetic coupling between a quantum emitter and a plasmonic nanoantenna: time-dependent density functional theory vs. semiclassical Feibelman approach. *Opt. Express* **2022**, *30*, 21159−21183.
(46) Zhu, M.; Aikens, C. M.; Hollander, F. J.; Schatz, G. C.; Jin, R. Correlating the crystal structure of a thiol-protected Au25 cluster and optical properties. *J. Am. Chem. Soc.* **2008**, *130*, 5883−5885.
(47) Rossi, T. P.; Zugarramurdi, A.; Puska, M. J.; Nieminen, R. M. Quantized evolution of the plasmonic response in a stretched nanorod. *Phys. Rev. Lett.* **2015**, *115*, 236804.
(48) Weissker, H.-C.; Mottet, C. Optical properties of pure and core-shell noble-metal nanoclusters from TDDFT: The influence of the atomic structure. *Phys. Rev. B* **2011**, *84*, 165443.
(49) Marchesin, F.; Koval, P.; Barbry, M.; Aizpurua, J.; Sánchez-Portal, D. Plasmonic response of metallic nanojunctions driven by single atom motion: quantum transport revealed in optics. *ACS Photonics* **2016**, *3*, 269−277.
(50) Sinha-Roy, R.; Garcia-Gonzalez, P.; Weissker, H.-C.; Rabilloud, F.; Fernandez-Dominguez, A. I. Classical and ab Initio Plasmonics Meet at Sub-nanometric Noble Metal Rods. *ACS Photonics* **2017**, *4*, 1484−1493.
(51) Morton, S. M.; Jensen, L. A discrete interaction model/quantum mechanical method for describing response properties of molecules adsorbed on metal nanoparticles. *J. Chem. Phys.* **2010**, *133*, 074103.
(52) Morton, S. M.; Jensen, L. A discrete interaction model/quantum mechanical method to describe the interaction of metal nanoparticles and molecular absorption. *J. Chem. Phys.* **2011**, *135*, 134103.
(53) Jensen, L. L.; Jensen, L. Electrostatic interaction model for the calculation of the polarizability of large noble metal nanoclusters. *J. Phys. Chem. C* **2008**, *112*, 15697−15703.
(54) Jensen, L. L.; Jensen, L. Atomistic electrodynamics model for optical properties of silver nanoclusters. *J. Phys. Chem. C* **2009**, *113*, 15182−15190.
(55) Zakomirnyi, V. I.; Rinkevicius, Z.; Baryshnikov, G. V.; Sørensen, L. K.; Ågren, H. Extended discrete interaction model: plasmonic excitations of silver nanoparticles. *J. Phys. Chem. C* **2019**, *123*, 28867−28880.
(56) Rinkevicius, Z.; Li, X.; Sandberg, J. A.; Mikkelsen, K. V.; Ågren, H. A hybrid density functional theory/molecular mechanics approach for linear response properties in heterogeneous environments. *J. Chem. Theory Comput.* **2014**, *10*, 989−1003.
(57) Zakomirnyi, V. I.; Rasskazov, I. L.; Sørensen, L. K.; Carney, P. S.; Rinkevicius, Z.; Ågren, H. Plasmonic nano-shells: atomistic discrete interaction versus classic electrodynamics models. *Phys. Chem. Chem. Phys.* **2020**, *22*, 13467−13473.
(58) Giovannini, T.; Rosa, M.; Corni, S.; Cappelli, C. A classical picture of subnanometer junctions: an atomistic Drude approach to nanoplasmonics. *Nanoscale* **2019**, *11*, 6004−6015.
(59) Giovannini, T.; Bonatti, L.; Polini, M.; Cappelli, C. Graphene plasmonics: Fully atomistic approach for realistic structures. *J. Phys. Chem. Lett.* **2020**, *11*, 7595−7602.
(60) Lafiosca, P.; Giovannini, T.; Benzi, M.; Cappelli, C. Going Beyond the Limits of Classical Atomistic Modeling of Plasmonic Nanostructures. *J. Phys. Chem. C* **2021**, *125*, 23848−23863.
(61) Yamada, A. Classical electronic and molecular dynamics simulation for optical response of metal system. *J. Chem. Phys.* **2021**, *155*, 174118.
(62) Duan, H.; Fernández-Domínguez, A. I.; Bosman, M.; Maier, S. A.; Yang, J. K. Nanoplasmonics: classical down to the nanometer scale. *Nano Lett.* **2012**, *12*, 1683−1689.
(63) Scholl, J. A.; Koh, A. L.; Dionne, J. A. Quantum plasmon resonances of individual metallic nanoparticles. *Nature* **2012**, *483*, 421−427.
(64) Pinchuk, A.; Kreibig, U.; Hilger, A. Optical properties of metallic nanoparticles: influence of interface effects and interband transitions. *Surf. Sci.* **2004**, *557*, 269−280.
(65) Pinchuk, A.; Von Plessen, G.; Kreibig, U. Influence of interband electronic transitions on the optical absorption in metallic nanoparticles. *J. Phys. D: Appl. Phys.* **2004**, *37*, 3133.
(66) Balamurugan, B.; Maruyama, T. Evidence of an enhanced interband absorption in Au nanoparticles: size-dependent electronic structure and optical properties. *Appl. Phys. Lett.* **2005**, *87*, 143105.
(67) Liebsch, A. Surface-plasmon dispersion and size dependence of Mie resonance: silver versus simple metals. *Phys. Rev. B* **1993**, *48*, 11317.
(68) Santiago, E. Y.; Besteiro, L. V.; Kong, X.-T.; Correa-Duarte, M. A.; Wang, Z.; Govorov, A. O. Efficiency of hot-electron generation in plasmonic nanocrystals with complex shapes: surface-induced scattering, hot spots, and interband transitions. *ACS Photonics* **2020**, *7*, 2807−2824.
(69) Giovannini, T.; Puglisi, A.; Ambrosetti, M.; Cappelli, C. Polarizable QM/MM approach with fluctuating charges and fluctuating dipoles: the QM/FQFμ model. *J. Chem. Theory Comput.* **2019**, *15*, 2233−2245.
(70) Giovannini, T.; Riso, R. R.; Ambrosetti, M.; Puglisi, A.; Cappelli, C. Electronic transitions for a fully polarizable qm/mm approach based on fluctuating charges and fluctuating dipoles: linear and corrected linear response regimes. *J. Chem. Phys.* **2019**, *151*, 174104.
(71) Giovannini, T.; Egidi, F.; Cappelli, C. Molecular spectroscopy of aqueous solutions: a theoretical perspective. *Chem. Soc. Rev.* **2020**, *49*, 5664−5677.
(72) Verma, P. Tip-enhanced Raman spectroscopy: technique and recent advances. *Chem. Rev.* **2017**, *117*, 6447−6466.
(73) Zhang, W.; Yeo, B. S.; Schmid, T.; Zenobi, R. Single molecule tip-enhanced Raman spectroscopy with silver tips. *J. Phys. Chem. C* **2007**, *111*, 1733−1738.
(74) Chen, X.; Moore, J. E.; Zekarias, M.; Jensen, L. Atomistic electrodynamics simulations of bare and ligand-coated nanoparticles in the quantum size regime. *Nat. Commun.* **2015**, *6*, 8921.
(75) Ringe, E.; McMahon, J. M.; Sohn, K.; Cobley, C.; Xia, Y.; Huang, J.; Schatz, G. C.; Marks, L. D.; Van Duyne, R. P. Unraveling the effects of size, composition, and substrate on the localized surface plasmon resonance frequencies of gold and silver nanocubes: a systematic single-particle approach. *J. Phys. Chem. C* **2010**, *114*, 12511−12516.
(76) Etchegoin, P. G.; Le Ru, E.; Meyer, M. An analytic model for the optical properties of gold. *J. Chem. Phys.* **2006**, *125*, 164705.
(77) Johnson, P. B.; Christy, R.-W. Optical constants of the noble metals. *Phys. Rev. B* **1972**, *6*, 4370.
(78) Johnson, H. E.; Aikens, C. M. Electronic structure and TDDFT optical absorption spectra of silver nanorods. *J. Phys. Chem. A* **2009**, *113*, 4445−4450.
(79) Bae, G.-T.; Aikens, C. M. Time-dependent density functional theory studies of optical properties of Ag nanoparticles: octahedra, truncated octahedra, and icosahedra. *J. Phys. Chem. C* **2012**, *116*, 10356−10367.
(80) Cottancin, E.; Celep, G.; Lermé, J.; Pellarin, M.; Huntzinger, J.; Vialle, J.; Broyer, M. Optical properties of noble metal clusters as a

https://doi.org/10.1021/acsphotonics.2c00761
ACS Photonics 2022, 9, 3025−3034

function of the size: comparison between experiments and a semi-quantal theory. *Theor. Chem. Acc.* **2006**, *116*, 514−523.
(81) Chen, X.; Jensen, L. Morphology dependent near-field response in atomistic plasmonic nanocavities. *Nanoscale* **2018**, *10*, 11410−11417.
(82) Kreibig, U.; Vollmer, M. *Optical Properties of Metal Clusters*; Springer Science & Business Media, 2013; Vol. *25*.
(83) Novo, C.; Gomez, D.; Perez-Juste, J.; Zhang, Z.; Petrova, H.; Reismann, M.; Mulvaney, P.; Hartland, G. V. Contributions from radiation damping and surface scattering to the linewidth of the longitudinal plasmon band of gold nanorods: a single particle study. *Phys. chem. Chem. Phys.* **2006**, *8*, 3540−3546.
(84) Juvé, V.; Cardinal, M. F.; Lombardi, A.; Crut, A.; Maioli, P.; Pérez-Juste, J.; Liz-Marzán, L. M.; Del Fatti, N.; Vallée, F. Size-dependent surface plasmon resonance broadening in nonspherical nanoparticles: single gold nanorods. *Nano Lett.* **2013**, *13*, 2234−2240.
(85) Foerster, B.; Joplin, A.; Kaefer, K.; Celiksoy, S.; Link, S.; Sönnichsen, C. Chemical interface damping depends on electrons reaching the surface. *ACS Nano* **2017**, *11*, 2886−2893.
(86) Douglas-Gallardo, O. A.; Soldano, G. J.; Mariscal, M. M.; Sánchez, C. G. Effects of oxidation on the plasmonic properties of aluminum nanoclusters. *Nanoscale* **2017**, *9*, 17471−17480.
(87) Kuisma, M.; Sakko, A.; Rossi, T. P.; Larsen, A. H.; Enkovaara, J.; Lehtovaara, L.; Rantala, T. T. Localized surface plasmon resonance in silver nanoparticles: Atomistic first-principles time-dependent density-functional theory calculations. *Phys. Rev. B* **2015**, *91*, 115431.
(88) Iida, K.; Noda, M.; Ishimura, K.; Nobusada, K. First-principles computational visualization of localized surface plasmon resonance in gold nanoclusters. *J. Phys. Chem. A* **2014**, *118*, 11317−11322.
(89) Payton, J. L.; Morton, S. M.; Moore, J. E.; Jensen, L. A hybrid atomistic electrodynamics−quantum mechanical approach for simulating surface-enhanced raman scattering. *Acc. Chem. Res.* **2014**, *47*, 88−99.
(90) Kim, M.; Kwon, H.; Lee, S.; Yoon, S. Effect of nanogap morphology on plasmon coupling. *ACS Nano* **2019**, *13*, 12100−12108.

https://doi.org/10.1021/acsphotonics.2c00761
ACS Photonics 2022, 9, 3025−3034

Chapter 9

QM/Classical Modeling of Surface Enhanced Raman Scattering Based on Atomistic Electromagnetic Models

QM/Classical Modeling of Surface Enhanced Raman Scattering Based on Atomistic Electromagnetic Models

Piero Lafiosca,[†] Luca Nicoli,[†] Luca Bonatti,[†] Tommaso Giovannini,[*,†] Stefano Corni,[‡,¶] and Chiara Cappelli[*,†,§]

†*Scuola Normale Superiore, Piazza dei Cavalieri 7, 56126 Pisa, Italy.*

‡*Dipartimento di Scienze Chimiche, Università di Padova, via Marzolo 1, 35131, Padova, Italy*

¶*Istituto di Nanoscienze del Consiglio Nazionale delle Ricerche CNR-NANO, via Campi 213/A, 41125, Modena, Italy*

§*LENS (European Laboratory for Non-Linear Spectroscopy), Via N. Carrara 1, 50019, Sesto Fiorentino, Italy*

E-mail: tommaso.giovannini@sns.it; chiara.cappelli@sns.it

Abstract

We present quantum mechanics (QM)/frequency dependent fluctuating charge (QM/ωFQ) and fluctuating dipoles (QM/ωFQFμ) multiscale approaches to model Surface-Enhanced Raman Scattering spectra of molecular systems adsorbed on plasmonic nanostructures. The methods are based on a QM/classical partitioning of the system, where the plasmonic substrate is treated by means of the atomistic electromagnetic models ωFQ and ωFQFμ, which are able to describe in a unique fashion and at the same level of accuracy the plasmonic properties of noble metal nanostructures and graphene-based materials. Such methods are based on classical physics, i.e. Drude conduction theory, classical electrodynamics, and atomistic polarizability to account for interband transitions, by also including an ad-hoc phenomenological correction to describe quantum tunneling. QM/ωFQ and QM/ωFQFμ are thus applied to selected

test cases, for which computed results are compared with available experiments, showing the robustness and reliability of both approaches.

Keywords: *Atomistic simulations, SERS, Gold, Silver, Graphene, QM/MM, DFT*

1 Introduction

Surface-enhanced Raman scattering (SERS) takes advantage of the giant enhancement of the Raman scattering cross section of a target molecule in the proximity of plasmonic nanostructured materials.[1] Enhancement factors (i.e. the ratio between the Raman intensity for the nanoaggregate and the isolated/solvated target molecule) can reach values up to 10^{10-11},[2–4] thus allowing single molecule detection, down to submolecular resolution.[5] For this reasons, SERS has gained popularity and is widely used in a plethora of applications,[6–11] because it inherits the general advantages of classical Raman spectroscopy, solves its main weakness, consisting of generally low scattering amplitudes and add, possibly, spatial resolution on the nanometer scale and below.[12–14] From the physico-chemical point of view, it is generally accepted[3,15–17] that SERS enhancement results from the combination of two factors: the so-called electromagnetic (EM) effect (yielding enhancements up to 10^{7-8}), which is caused by the excitation of surface plasmons in the substrate which lead to a strong induced electric field in its proximity; and the so-called chemical (CT) enhancement, for which a holistic theoretical explanation is still missing. CT is associated with 10^{2-3} enhancement factors and is mainly ascribed to charge-transfer excitations between the analyte and the substrate.

Metal nanostructures, such as metal nanoparticles (NPs), have been the most used substrates for SERS because they provide highly confined plasmons and huge enhanced electric field on their surfaces,[15,18–24] also thanks to a substantial advancement in experimental techniques for manipulating the nanoscale.[25–29] Indeed, specific morphological arrangements can be designed, giving rise to *hot-spots*, i.e. regions in space where the electric field is extremely confined and enhanced.[5,12,13,30] Recently, there has been increasing interest in designing novel substrates characterized by high chemical inertness to be used in the investigation of biochemical species. In this context, recent developments of SERS substrates based on carbon allotropes such as graphene and carbon nanotubes (CNTs) are worth being mentioned.[31–33]

A theoretical understanding of the SERS mechanisms can be particularly useful not only for the interpretation of experimental spectra but also for the in-silico design of novel materials and morphologies which can maximize spectral enhancement factors for a specific analyte. For this reason, in the past years, various methodologies have been proposed to simulate SERS signals.[34–46] The huge dimension of typical SERS substrates (tens/hundreds of nanometers) make a full quantum mechanical (QM) description of the molecule-substrate system unfeasible, although small-size model systems can be exploited to deal with spe-

cific features of the SERS phenomenon (mainly related to the CT mechanism).[47–50] To solve this problem, multiscale approaches can be used, where the analyte is described at the QM level, while the substrate is treated classically.[34,35,37–41,51–59] In particular, the nanostructured material can be modeled as a continuum medium, defined in terms of its complex-valued permittivity, or by retaining its atomistic nature. Remarkably, in the latter case a precise description of complex geometries, even characterized by geometrical defects, is obtained.[60,61] Note that both approaches neglect CT effects; however, for usual SERS substrates, EM enhancement is several orders of magnitude higher than CT.[62]

In this paper, we present QM/ωFQ and QM/ωFQFμ fully atomistic multiscale QM/classical approaches to simulate SERS spectra, where the analyte is treated quantum-mechanically. To describe the nanostructured materials, we exploit a family of atomistic models that we have recently developed, which are able to correctly reproduce experimental and *ab-initio* plasmonic features of metal nanoparticles (ωFQ and ωFQFμ),[61] and graphene-based nanostructures (ωFQ).[63,64] These approaches are based on classical physics and text-book concepts, such as Drude conduction theory, classical electrodynamics, and atomistic polarizability to account for interband transitions. In addition, ad-hoc phenomenological correction to describe quantum tunneling is included in the model, so to deal with nanojunctions and aggregates in which *hot-spots* may originate. Within ωFQ and ωFQFμ, each atom of the nanostructure is endowed with a frequency-dependent complex-valued charge and supplemented by a complex-valued dipole in ωFQFμ, which respond to the external radiation, thus mimicking the oscillating electron density.

Differently from previous classical atomistic approaches,[34–36,42–46,59] Drude conduction, i.e. intraband transitions, is taken into account by means of the equation of motion of the charges placed on each atom, while induced dipoles are included so as to model interband transitions.[61] This permits us to correctly catch the physics underlying the plasmonics of generic s,p,d metallic systems, by also allowing for a physical dissection of the two contributions. Moreover, ωFQ(Fμ) is the only atomistic classical method that can treat quantum tunneling in plasmonic materials, which is particularly relevant for nanoaggregates and nanojunctions, where plasmonic hot-spots are created.[61,63] Finally, it is worth noting that ωFQ is the only atomistic classical approach able to physically describe graphene plasmonics in terms of its fundamental physical parameters, such as the Fermi energy, relaxation time, and two-dimensional electron density.[60,64–66]

Here, ωFQ and ωFQFμ are coupled to a density functional theory (DFT) treatment of the QM portion

and the resulting QM/ωFQ and QM/ωFQFμ methods are further extended to the calculation of complex molecular polarizabilities through the linear response theory. The robustness of the approaches is showcased through their application to pyridine adsorbed on noble metal NPs. Thanks to the generality of both approaches, we also apply them to the simulation of Graphene-Enhanced Raman Spectroscopy (GERS), by exploiting graphene-based nanostructures as enhancing substrates. For large pristine graphene sheets, the absence of sharp edges is usually connected to the low enhancement factors reported for GERS.[67,68] Nevertheless, suitably engineered graphene-based nanostructures may enhance several orders of magnitude both the induced electric field and its spatial confinement.[60]

The manuscript is organized as follows. The first section recalls the theoretical foundations of ωFQ and ωFQFμ, and presents their coupling with a DFT Hamiltonian for the ground state and linear response theory. We note that the EM field associated with the induced density in the nanoparticle is neither a purely real nor a purely imaginary perturbation. Therefore, we exploit a general complex linear response formulation. QM/ωFQFμ is then applied to simulate SERS spectra of pyridine adsorbed on different plasmonic substrates (silver, gold, and graphene). Finally, GERS of a widely used anticancer drug, i.e. methotrexate, adsorbed on a graphene disk, is taken as a case study to showcase the potentialities of the method. Summary, conclusions, and future perspectives end the manuscript.

2 Theory

2.1 ωFQ and ωFQFμ

ωFQ endows the atoms of the nanostructure with a charge. In the presence of an external monochromatic electric field $\mathbf{E}^{\text{ext}}(\omega)$, the charge can be exchanged with nearest neighbor atoms as a result of Drude conduction[69] and quantum tunnelling effect.[63] For a system composed of N atoms, charges $\mathbf{q}$ can be calculated by solving the following set of linear equations:[68]

$$(\mathbf{A}^q - z(\omega)\mathbf{I})\mathbf{q} = \mathbf{R}. \tag{1}$$

where $\mathbf{A}^q$ is a real nonsymmetric matrix, which reads:

$$A_{ij}^q = \sum_{k \neq i}^{N} K_{ik}(T_{kj}^{\mathrm{qq}} - T_{ij}^{\mathrm{qq}}), \tag{2}$$

$\mathbf{T}^{\mathrm{qq}}$ is the charge-charge interaction matrix,[70] while $\mathbf{K}$ is defined as:

$$K_{ij} = \begin{cases} [1 - f(r_{ij})]\frac{\mathscr{A}_{ij}}{r_{ij}} & \text{if } i \neq j \\ 0 & \text{otherwise} \end{cases}, \tag{3}$$

Quantum tunneling effects are taken into account by means of the Fermi damping function $f(r_{ij})$, which exponentially decays as a function of the interatomic distance $r_{ij} = \left|\mathbf{r}_i - \mathbf{r}_j\right|$ ($\mathbf{r}_i$ is the position of the i-th atom). $\mathscr{A}_{ij}$ is an effective area connecting atoms i and j. Its value is based on the geometry of the system and has been chosen to best reproduce reference ab-initio values.[61,63,64] It is worth noticing that the $\mathbf{A}^q$ matrix only depends on the geometry of the ωFQ system, because it is a function of the interatomic distance r_{ij} only.

The frequency-dependent complex-valued factor $z(\omega)$ in eq. (1) is defined as:

$$z(\omega) = -\frac{\omega}{2n_0\tau}(\omega\tau + \mathrm{i}), \tag{4}$$

where n_0 is the electron density of the system and τ is the scattering time. The electron density depends on the composition and the morphology of the nanostructure. In general, for 3D systems $n_0 = \frac{\sigma_0/\tau}{m^*}$ where σ_0 is the static conductance of the material and m^* is the effective electron mass, which for metallic systems is usually approximated to 1.[71] For graphene-based structures, this approximation is no longer valid, therefore the electronic density can be written as:[64,72]

$$n_0^{\text{graphene}} = \frac{n_0}{m^*} = \frac{n_{2\mathrm{D}} \cdot a_0}{\sqrt{\pi n_{2\mathrm{D}}}/v_F} \tag{5}$$

$$n_{2\mathrm{D}} = \alpha\frac{N}{S} \tag{6}$$

where $n_{2\mathrm{D}}$ is the 2D numeral electronic density of the system, a_0 is the Bohr radius, v_F is the Fermi velocity,

S is the total surface of the graphene system, while α is the fraction of doping electrons per carbon atom. Such number, and thus graphene plasmonic properties can be tuned by varying the external gating, which is directly related to the Fermi energy (E_F), which determines the numerical value of $n_{2\mathrm{D}}$ (and thus α) by:

$$E_F = \hbar v_F \sqrt{\pi n_{2D}} \tag{7}$$

Finally, the right-hand side in eq. (1) is defined as:[68]

$$R_i = \sum_{j=1}^{N} (V_i^{\mathrm{ext}} - V_j^{\mathrm{ext}}) K_{ij}, \tag{8}$$

where V_i^{ext} is the electric potential associated with the external oscillating field evaluated at position $\mathbf{r}_i$, that implies we are assuming the quasistatic approximation to full EM equations.[63]

ωFQ has successfully been applied to the simulation of the plasmonic response of sodium nanostructures and graphene-based materials.[63–65] However, the underlying Drude conduction mechanism is not able to reproduce the plasmonic response of $d-$metals, as for instance silver and gold nanoparticles, because interband (IB) transitions play an essential role.[73–77] ωFQFμ correctly models such effects.[61] There, each atom is endowed with both an oscillating charge q_i and an oscillating dipole $\boldsymbol{\mu}_i$. The plasmonic response is then assumed to originate from two different mechanisms: the Drude conduction, taken into account by the charges, and the aforementioned IB transitions, which are treated by means of the dipoles, which account for the polarizability of the d-shell. By taking into account both terms, and their interaction, the plasmonic response of metal nanostructures, made by Ag/Au, could be correctly described.[61] The resulting ωFQFμ equation reads:

$$\left[\begin{pmatrix} \mathbf{A}^q & \mathbf{A}^\mu \\ \mathbf{T}^{\mu\mathrm{q}} & \mathbf{T}^{\mu\mu} \end{pmatrix} - \begin{pmatrix} z(\omega)\mathbf{I} & 0 \\ 0 & z'(\omega)\mathbf{I} \end{pmatrix} \right] \begin{pmatrix} \mathbf{q} \\ \boldsymbol{\mu} \end{pmatrix} = \begin{pmatrix} \mathbf{R} \\ -\mathbf{E}^{\mathrm{ext}} \end{pmatrix} \tag{9}$$

where $\mathbf{A}^q$, $z(\omega)$ and $\mathbf{R}$ have been already introduced by eq. (1). $\mathbf{T}^{\mu\mathrm{q}}$ and $\mathbf{T}^{\mu\mu}$ are the dipole-charge and

dipole-dipole interaction tensors,[70] whereas $\mathbf{A}^{\mu}$ and $z'(\omega)$ are defined as follows:

$$A_{ij}^{\mu} = \sum_{k=1}^{N} K_{ij}(T_{kj}^{\mathrm{q}\mu} - T_{ij}^{\mathrm{q}\mu}) \tag{10}$$

$$z'(\omega) = -\frac{1}{\alpha_{\mathrm{IB}}(\omega)} \tag{11}$$

where $\alpha_{\mathrm{IB}}(\omega)$ is the IB polarizability, which is extracted from the experimental permittivity function (after removing the Drude part, see Ref. 61 for further details). Similarly to ωFQ, all the frequency-dependent terms are collected into a diagonal shift through the z, z' functions, and the other terms depend on the geometry of the system only.

2.2 Coupling to a QM Hamiltonian

ωFQ and ωFQFμ can be coupled to a QM description of a molecular system in a QM/MM fashion.[78–85] ωFQ and ωFQFμ describe the response to an external oscillating electric field; thus, they can naturally be translated into a linear response formalism. However, to achieve a physically consistent description of the molecule/substrate system, their interaction needs to be modeled also in the ground state (GS). To this end, the analogous frequency independent force fields, FQ and FQFμ,[70,86–93] can be exploited. In the following, we first briefly recall FQ and FQFμ for the GS; then, we present the linear response formalism for the novel QM/ωFQ(Fμ) approaches.

Description of the ground state

The total energy of a two-layer QM/FQ(Fμ) system can be written as

$$\mathscr{E} = E_{\mathrm{QM}} + E_{\mathrm{QM/FQ(F}\mu)} + E_{\mathrm{FQ(F}\mu)}, \tag{12}$$

where E_{QM} and $E_{\mathrm{FQ(F}\mu)}$ are the self-energies of the QM and FQ(Fμ) portions, whereas $E_{\mathrm{QM/FQ(F}\mu)}$ indicates their interaction energy. The latter term is described as the electrostatic interaction energy between the QM

charge distribution and the classical fluctuating multipoles of the FQ or FQFμ force fields:[70]

$$\begin{aligned} E_{\mathrm{QM/FQ}} &= \sum_{p=1}^{N} q_p V^{\mathrm{QM}}(\mathbf{r}_p) \\ E_{\mathrm{QM/FQF}\mu} &= \sum_{p=1}^{N} \left[q_p V^{\mathrm{QM}}(\mathbf{r}_p) - \boldsymbol{\mu}_p \cdot \mathbf{E}^{\mathrm{QM}}(\mathbf{r}_p) \right], \end{aligned} \tag{13}$$

where the sums run over MM atoms, q_p and $\boldsymbol{\mu}_p$ indicate the p-th FQ and Fμ which are located at position $\mathbf{r}_p$, while V^{QM} and $\mathbf{E}^{\mathrm{QM}}$ are the electric potential and field generated by the QM portion, respectively.

If we exploit a DFT description of the QM portion, the ground state density can be determined by means of the effective Kohn-Sham (KS) equations, which are expressed in terms of the KS operator h_{KS}. In this work, we use the current implementation of QM/FQ and QM/FQFμ in the Amsterdam Density Functional (ADF) module[94] of the Amsterdam Modeling Suite (AMS) software package.[95] There, the solution of KS equations is performed through a numerical integration scheme, in which the KS operator is built over a grid of points $\mathbf{r}$ in the molecular space of the QM portion, i.e.:

$$\begin{aligned} h_{\mathrm{KS}}(\mathbf{r}) &= h^0_{\mathrm{KS}}(\mathbf{r}) + \sum_{p=1}^{N} q_p T^{(0)}(\mathbf{d}_p) \\ h_{\mathrm{KS}}(\mathbf{r}) &= h^0_{\mathrm{KS}}(\mathbf{r}) + \sum_{p=1}^{N} \left(q_p T^{(0)}(\mathbf{d}_p) + \boldsymbol{\mu}_p \cdot \mathbf{T}^{(1)}(\mathbf{d}_p) \right), \end{aligned} \tag{14}$$

In eq. (14) $h^0_{\mathrm{KS}}(\mathbf{r})$ indicates the KS operator associated with the isolated QM system, and the QM/FQ and QM/Fμ interaction tensors are introduced. They are defined in terms of the distance $\mathbf{d}_p$ between the p-th atom and the grid point ($\mathbf{d}_p = \mathbf{r} - \mathbf{r}_p$) as follows:

$$\begin{aligned} T^{(0)}(\mathbf{d}_p) &= \frac{1}{d_p} \mathrm{erf}\left(\frac{d_p}{a} \right) \\ \mathbf{T}^{(1)}(\mathbf{d}_p) &= -\frac{\mathbf{d}_p}{d_p^3} \left[\mathrm{erf}\left(\frac{d_p}{a} \right) - \frac{2 d_p}{\sqrt{\pi} a} \exp\left(-\frac{d_p^2}{a^2} \right) \right]. \end{aligned} \tag{15}$$

where $d_p = |\mathbf{d}_p|$ and $a = 0.2$ a.u.[96] Since the molecular grid is constructed independently of the MM portion, in order to avoid numerical instabilities in eq. (15) a screened interaction tensors between the QM grid points and the MM positions is considered, by analogy to what is reported in Ref. 97.

Linear response theory and SERS spectra

By following the approach reported in Ref. 35, SERS spectral intensities can be evaluated through the frequency-dependent complex polarizability tensor $\bar{\alpha}_{\alpha\beta}(\omega;\omega)$. To this end, the first-order variation of the molecular density under the effect of a time-dependent perturbation is required, which can be accessed by means of the linear response theory. In particular, as a perturbation, we consider a monochromatic uniform electric field $\mathbf{E}^{\text{ext}}(\omega)$, linearly polarized along the direction $\alpha = x,y,z$. The perturbation operator which acts on the electronic density can be written as:

$$V^{\text{pert}}(\mathbf{r},\omega) = V^{\text{ext}}(\mathbf{r},\omega) + V^{\text{loc}}(\mathbf{r},\omega), \tag{16}$$

where V^{ext} is the electric potential associated with the external field $\mathbf{E}^{\text{ext}}$ and V^{loc} is the local field operator, which takes into account the electric field generated by the plasmonic substrate (PS) as induced by the external field.[38] Within ωFQ (Fμ), the local field operator reads:

$$\begin{aligned} V^{\text{loc}}_{\omega\text{FQ}}(\mathbf{r},\omega) &= \sum_{p=1}^{N} q_p^{\text{ext}}(\omega) T^{(0)}(\mathbf{d}_p) \\ V^{\text{loc}}_{\omega\text{FQF}\mu}(\mathbf{r},\omega) &= \sum_{i=p}^{N} q_p^{\text{ext}}(\omega) T^{(0)}(\mathbf{d}_p) + \boldsymbol{\mu}_p^{\text{ext}}(\omega)\cdot\mathbf{T}^{(1)}(\mathbf{d}_p). \end{aligned} \tag{17}$$

$q_p^{\text{ext}}(\omega)$ and $\boldsymbol{\mu}_p^{\text{ext}}(\omega)$ can be calculated from eqs. (1) and (9) by using V^{ext} as source potential. In the following, we use the common notation for identifying the molecular orbitals (MOs): indices i,j for the occupied, a,b for the virtual and r,s,t,u for general MOs; moreover, given a quantity X we will indicate its variation at the first order with respect to the external electric field component α with X^{α}. Given that, the first order density $\rho^{\alpha}(\mathbf{r},\omega)$ can be written as:

$$\rho^{\alpha}(\mathbf{r},\omega) = \sum_{ia} P_{ia}^{\alpha}(\omega)\phi_i(\mathbf{r})\phi_a^*(\mathbf{r}) + P_{ai}^{\alpha}\phi_a(\mathbf{r})\phi_i^*(\mathbf{r}), \tag{18}$$

where $P_{rs}^{\alpha}(\omega)$ is the first-order density matrix expressed on the basis of the KS MOs. The non zero elements of $\mathbf{P}^{\alpha}(\omega)$ are the off-diagonal ones, which are associated to the occupied-virtual and virtual-occupied MOs.

They can be computed through the Time-Dependent Kohn-Sham (TDKS) equations, which read:[98]

$$\left[\begin{pmatrix} \mathbf{A} & \mathbf{B} \\ \mathbf{B}^* & \mathbf{A}^* \end{pmatrix} - (\omega + \mathrm{i}\Gamma)\begin{pmatrix} -\mathbf{I} & \mathbf{0} \\ \mathbf{0} & \mathbf{I} \end{pmatrix}\right]\begin{pmatrix} \mathbf{X} \\ \mathbf{Y} \end{pmatrix} = -\begin{pmatrix} \mathbf{Q} \\ \mathbf{Q}^* \end{pmatrix}, \tag{19}$$

where $X_{ia} = P^{\alpha}_{ia}$ and $Y_{ia} = P^{\alpha}_{ai}$. Also, the phenomenological damping factor Γ, that takes into account the finite lifetime of the QM excited state, is introduced.[99] In addition, the following quantities are defined:

$$\begin{aligned} A_{ai,bj} &= (\varepsilon_a - \varepsilon_i)\delta_{ab}\delta_{ij} + (ai|bj) - c_x(ab|ij) + c_l f^{xc}_{ai,bj} + C^{QM/\omega\mathrm{FQ(F}\mu)}_{ai,bj} \\ B_{ai,bj} &= (ai|bj) - c_x(aj|ib) + C^{QM/\omega\mathrm{FQ(F}\mu)}_{ai,bj} \\ Q_{ia} &= \langle \phi_i | V^{\alpha,\mathrm{pert}}(\mathrm{r},\omega) | \phi_a \rangle , \end{aligned} \tag{20}$$

where ε indicates MO energies, $(rs|tu)$ two-electron integrals, and c_x and c_l define whether a pure ($c_x = 0$) or hybrid ($c_x \neq 0$) DFT functional is exploited. Two additional contributions to TDKS equations arise for QM/ωFQ and QM/ωFQFμ: the local field in the right-hand side (see the definition of Q, and eq. (17)), and the so-called image field or direct contribution to the left-hand side ($C^{QM/\omega\mathrm{FQ(F}\mu)}$).[82] The latter is also introduced in the context of polarizable embedding, such as FQ and FQFμ for non-absorbing media, and determines the response of the MM variables to the perturbed density. Its expression for both QM/FQ and QM/FQFμ methods can be found elsewhere.[89,96,100] On the other hand, the explicit contribution to the right-hand side is associated with the surface plasmon resonance and is responsible for the EM enhancement mechanism in surface-enhanced properties.

Once eq. (19) is solved for the input frequency ω, the frequency-dependent polarizability tensor $\bar{\alpha}_{\alpha\beta}(\omega;\omega')$ is obtained as:[101]

$$\bar{\alpha}_{\alpha\beta}(\omega;\omega') = -\mathrm{tr}\left[\mathbf{H}^{\alpha}(\omega)\mathbf{P}^{\beta}(\omega')\right], \tag{21}$$

where $\mathbf{H}^{\alpha}(\omega)$ is the dipole matrix of the QM system, which involves both the dipole and the local field operator along the direction α, i.e.:

$$H^{\alpha}_{rs}(\omega) = \langle \phi_r | \mu_{\alpha} + V^{\alpha,\mathrm{loc}}(\omega) | \phi_s \rangle \tag{22}$$

From the physical point of view, the presence of the local field operator in eq. (22) can be explained by the fact that the total scattered field from the molecule-nanostructures composite system contains two contributions: the scattered field from the molecule and the reflected field, which is generated by the molecule and reflected on the plasmonic nanostructure. In order to calculate Raman intensities, both fields need to be taken into account.[35,37]

Given the frequency-dependent polarizability tensor $\bar{\alpha}(\omega)$, Raman intensities can finally be evaluated by resorting to Placzek's theory of Raman scattering.[102,103] By assuming the perturbation field to be linearly perpendicular-plane polarized and the scattered light to be collected perpendicularly to the incident direction, the Raman intensity associated to the k-th normal mode can be calculated as:[104]

$$I^k \propto \frac{(\omega-\omega_k)^4}{\omega_k}\{45[\alpha'_k(\omega;\omega)]^2+7[\gamma'_k(\omega;\omega)]^2\}, \tag{23}$$

where ω and ω_k are the frequencies of the external field and of the k-th normal mode, respectively, while α' and γ' are the isotropic and anisotropic polarizability derivatives with respect to the k-th normal mode coordinate Q_k, i.e.:

$$[\alpha'_k(\omega;\omega')]^2 = \frac{1}{9}\left|\sum_{i=x,y,z}\frac{\partial\bar{\alpha}_{ii}(\omega;\omega')}{\partial Q_k}\right|^2 \tag{24}$$

$$[\gamma'_k(\omega;\omega')]^2 = \frac{1}{2}\left(\frac{3}{4}\sum_{ij=x,y,z}\left|\frac{\partial\bar{\alpha}_{ij}(\omega;\omega')}{\partial Q_k}+\frac{\partial\bar{\alpha}_{ji}(\omega;\omega')}{\partial Q_k}\right|^2-9[\alpha'_k(\omega;\omega')]^2\right). \tag{25}$$

The functional form of eq. (23) has been obtained under the assumption that the frequency difference between the incident and scattered light is negligible.[34,104,105] In the general case, the Raman intensity can be calculated as:

$$I^k \propto \frac{(\omega-\omega_k)^4}{\omega_k}\{45[\alpha'_k(\omega-\omega_k;\omega)]^2+7[\gamma'_k(\omega-\omega_k;\omega)]^2+5[\delta'_k(\omega-\omega_k;\omega)]^2\}, \tag{26}$$

in which $[\delta'(\omega)]^2$ is the square of the antisymmetric anisotropy of the polarizability tensor derivative, i.e.:[41]

$$[\delta'_k(\omega;\omega')]^2 = \frac{3}{8}\sum_{ij=x,y,z}\left|\frac{\partial\bar{\alpha}_{ij}(\omega;\omega')}{\partial Q_k}-\frac{\partial\bar{\alpha}_{ji}(\omega;\omega')}{\partial Q_k}\right|^2. \tag{27}$$

In the case in which the incident and scattered frequencies are the same, the latter term is exactly zero and the Raman intensity is reduced to the one reported in eq. (23). If the difference between the frequencies is large with respect to the broadness of the plasmonic absorption peak, this approximation may induce some differences in the final computed SERS intensity. In this work, similarly to other approaches,[34,35] we have relied on this approximation, and its implications will be topic of future communications.

3 Computational details

Silver and gold NPs' geometries are constructed by using OpenMD.[106] In particular, cuboctahedron (cTO), icosahedron (Ih) and ino-decahedron (i-Dh) morphologies are considered. Graphene disks' (GDs) geometries are generated by using VMD package[107] by cutting a graphene sheet in a circular shape with radius r and removing dangling bonds, which only marginally affect GDs' plasmonic response.[68] For both metal NPs and GDs, we study SERS signals as a function of the PS size. To this end, we consider GDs with radius $20 \leq r \leq 160$ Å and metal NPs composed by a maximum of 10179 atoms (see also Tables S2-S3 in the Supporting Information – SI). The dipolar plasmon resonance frequency (PRF) of each PS (see Table S2-S3 in the SI) varies from 3.64 to 3.42 eV for Ag, and from 2.31 to 2.17 eV, for Au. In the case of GDs, the PRF varies from 0.61 to 0.24 eV. In QM/ωFQ (Fμ) calculations, pyridine (PY) is described at the QM level by using BP86 or B3LYP DFT functionals, as coupled with a double$-\zeta$ polarized (DZP) or a triple$-\zeta$ polarized (TZP) basis sets.[108] To simulate Raman/SERS spectra, frequency-dependent polarizabilities $\bar{\alpha}(\omega)$ are calculated[109,110] by setting Γ (see eq. (19)) to 0.10 eV,.[35] $\bar{\alpha}(\omega)$ geometrical derivatives are obtained by means of a numerical differentiation scheme,[111–113] by using a constant step size of 0.001 Å. Similar results are obtained by using a step size of 0.0005 Å (see Fig. S1 in the SI). In this first application, normal modes displacements are calculated on the isolated QM molecule, because we expect vibrational frequencies shifts induced by the nanostructure to be negligible, as shown by previous studies (see for instance Refs. 35,40,105). Frequency-dependent polarizabilities and SERS spectra are calculated by setting the frequency ω as the PRF of each plasmonic substrate (see Tabs. S2-S3 in the SI); moreover, the final SERS spectra are obtained by convoluting raw data with Lorentzian band-shapes (full width at half maximum – FWHM– of 4 cm^{-1}). ωFQ parameters for GDs are taken from Ref. 64, whereas ωFQFμ parameters for silver and gold are

taken from Ref. 61. All QM/ωFQ and QM/ωFQFμ calculations are performed by using a locally modified version of the AMS software.[94,95]

In the following, we evaluate the Raman enhancement associated with the k-th normal mode in terms of the enhancement factor (EF):

$$\mathrm{EF}^k(\omega) = \frac{I^k_{\mathrm{PS}}(\omega)}{I^k_{\mathrm{vac}}(\omega)}, \tag{28}$$

where $I^k_{\mathrm{PS}}(\omega)$ and $I^k_{\mathrm{vac}}(\omega)$ are the Raman intensities of the k-th normal mode evaluated for the molecule-PS and the molecule in gas-phase systems, respectively (see eq. (23)). Since EF clearly depends on the selected normal mode, it is convenient to define a spectrally averaged enhancement factor (AEF) as follows:[49]

$$\mathrm{AEF}(\omega) = \frac{\sum_k I^k_{\mathrm{PS}}(\omega)}{\sum_l I^l_{\mathrm{vac}}(\omega)}, \tag{29}$$

where the indices k, l run over the normal modes of the target molecule (in the selected spectral region). As an additional measurement of calculated enhancement, we also introduce the maximum enhancement factor (MEF), i.e.:

$$\mathrm{MEF}(\omega) = \max_k \mathrm{EF}^k(\omega). \tag{30}$$

4 Numerical results

In this section, we first discuss the capability of QM/ωFQ and QM/ωFQFμ to correctly describe the physico-chemical features of the molecule-plasmonic substrates system. To this end, QM/ωFQ and QM/ωFQFμ approaches are first applied to the simulation of SERS spectra of pyridine (PY, see Fig. 1a), which has been the first molecular system for which SERS was experimentally observed.[1,18,114] Also, thanks to its small size, PY is a perfect prototype to test our novel approach. PY is adsorbed on two PS: metal NPs and graphene disks (GDs). We first validate our novel approach, by studying the dependence of Raman enhancements on the morphology and the PS chemical composition, the molecule-PS distance and spatial arrangement. Finally, we present an application of the approach to the simulation of a real-case scenario, i.e. methotrexate (MTX - see Fig. 1b), adsorbed on a graphene disk.

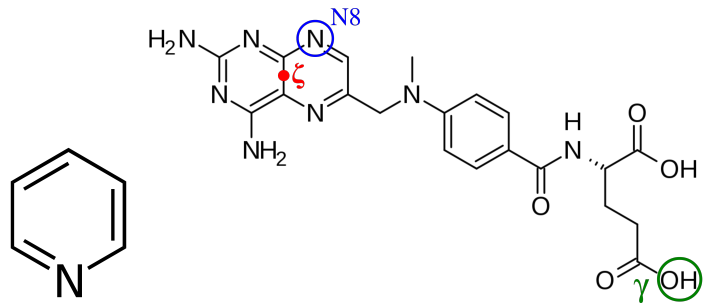

(a) Pyridine (b) Methotrexate

Figure 1: Pyridine (a) and methotrexate (b) molecular structures. In panel b, we highlight the position ζ (red), which indicates the center of MTX aromatic rings, the N8 atom (blue) and the OH (green) of the γ-carboxyl group.

4.1 Model testing

4.1.1 Metal nanoparticles

Dependence of enhancement factors on the nanostructure properties In this section, we study how the morphology, the size and the chemical composition of the PS affect the SERS signal. To this end, PY is adsorbed on silver and gold cTO, Ih and i-Dh NPs with a radius varying from about 6 to 40 Å (see Figs. 2a and 4a and Tab. S2 in the SI). PY is adsorbed standing on the vertex of each structure along the *y* axis, by setting a distance of 3 Å between the Nitrogen atom and the NP vertex, similarly to previous studies.[35] The results obtained by treating PY at the B3LYP/DZP level of theory are graphically reported in Figs. 2 and 4, for Ag and Au NPs, respectively (see Fig. S2 in the SI for their analogous calculated at different levels of theory). In particular, in Figs. 2b and 4b SERS spectra of the three different configurations as a function of the NP radii are reported, whereas in the corresponding c panels, the dependence of both AEF and MEF on the NP radii is graphically depicted. Note that the introduction of such a screening function guarantees the stability of the results by changing the DFT integration grid (see Fig. S3 in the SI).

Let us first discuss the results obtained for Ag NPs. By focusing on Fig. 2b, it can be noticed that SERS intensities strongly depend on the NP size, increasing as the NP size increases. The enhancement is not the same for all normal modes. Indeed, the vibrations modulating the components of the electronic polarizability orthogonal to the NP surface are associated with larger SERS intensity, because both the incident radiation and the scattered field benefit from the EM enhancement. For instance, this is evident for the ring breathing mode at 1008 cm^{-1} (see Fig. S4e in the SI) and the symmetric bending modes of the α-hydrogen atoms at

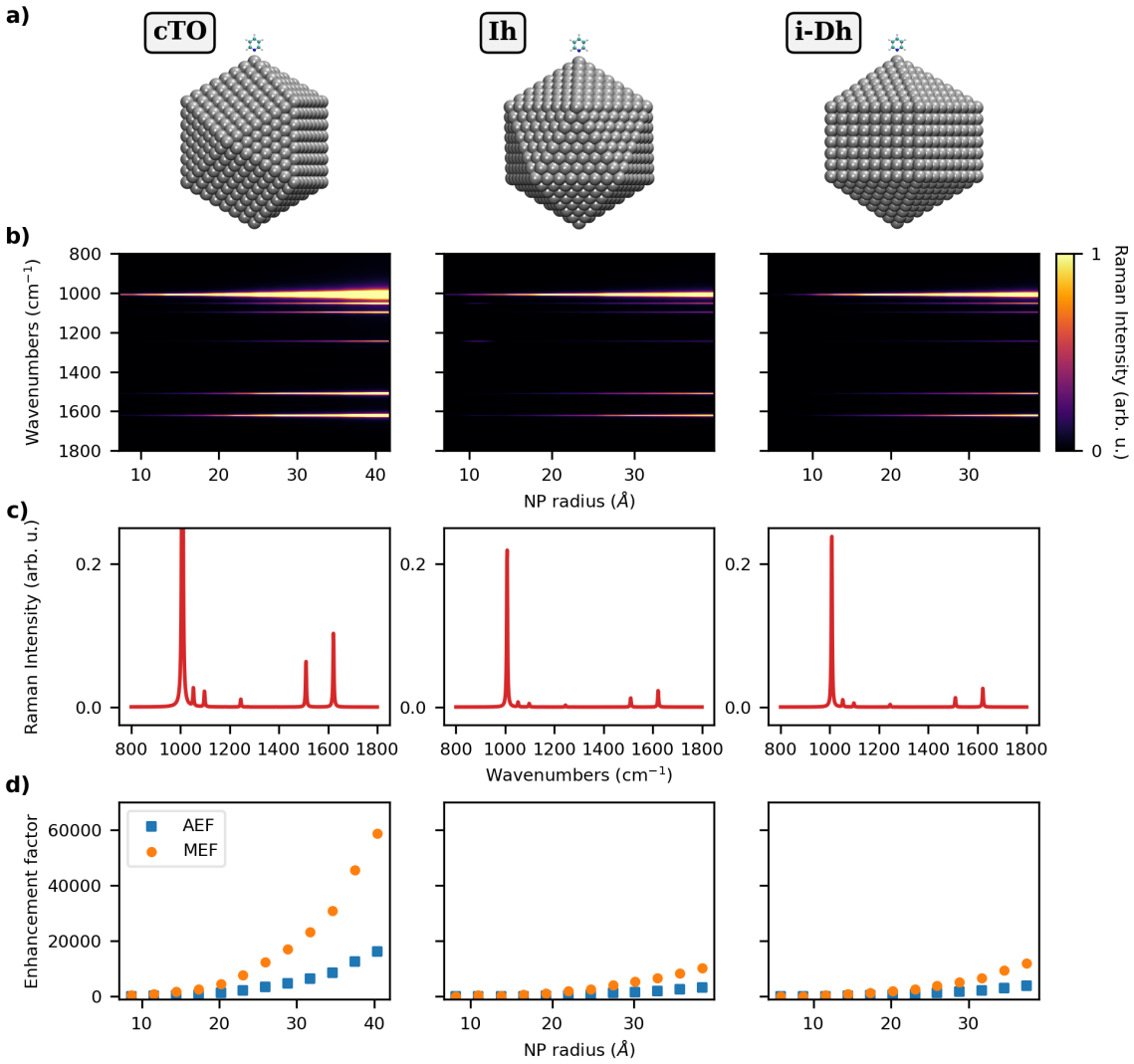

Figure 2: a) Graphical depiction of PY-Ag cTO (left), Ih (middle) and i-Dh (right) systems; (b) color plot of normalized SERS spectra as a function of the NP radius; (c) normalized SERS spectra of PY adsorbed on the largest NP structure for each shape; (d) AEF and MEF as a function of the NP radius. The incident field frequency for the computation of the SERS signal has been set equal to the PRF of each Ag NP, and the numerical ranges are 3.54–3.42 eV (cTO), 3.64–3.51 eV (Ih) and 3.52–3.42 eV (i-Dh), respectively.

1510 and 1622 cm^{-1} (see Figs. S4n and S4p in the SI), which are characterized by the largest SERS intensities (see also Fig. 2c where SERS spectra for the largest NPs are graphically reported). It is also interesting to note that depending on the morphology of the NPs, a different SERS spectrum can be obtained. In fact, fig. 2b shows that SERS spectra obtained by adsorbing PY on Ag Ih and i-Dh NPs display a significantly different relative intensity patterns as compared to PY on Ag cTO SERS spectrum. This is important to remark, as it shows that the details of the local electric field distribution (such as electric field gradients) are accounted for in the modeling and have a visible effect on SERS spectra. A selection of all enhancement factors of PY adsorbed on selected PS is reported in Tab. S4 in the SI.

To further analyze such results, Raman enhancements can be quantified in terms of AEF and MEF (see eqs. (29) and (30)). Their dependence on the NP radius is reported in Fig. 2d, which shows that the shape of the NP strongly affects their values. In particular, cTO-based structures yield to the largest enhancement factors as compared to the other considered morphologies. Interestingly, for small nanostructures, the most enhanced normal mode is the asymmetric bending of α-hydrogen atoms at 1388 cm^{-1} (see Fig. S4l in the SI), while for the largest structures the MEF is associated with the symmetric bending of the same α-hydrogen atoms at 1510 cm^{-1} (see Fig. S4n in the SI). In order to rationalize the differences between the three different shapes, we can resort to the so called E^4 approximation,[15,115] which states that Raman enhancements are proportional to the fourth power of the electric field induced on the NP. Thus, we define $\Upsilon^4_{\mathrm{vol}}$ as follows:

$$\Upsilon^4_{\mathrm{vol}} = \frac{1}{V}\int_V \frac{|\mathbf{E}^{\mathrm{tot}}(\omega)|^4}{|\mathbf{E}^{\mathrm{ext}}(\omega)|^4}\,\mathrm{d}\mathbf{r}, \tag{31}$$

where V is the molecular volume, $\mathbf{E}^{\mathrm{tot}}(\omega)$ is the total electric field, whereas $\mathbf{E}^{\mathrm{ext}}$ is the incident external electric field aligned with NP main axis. $\mathbf{E}^{\mathrm{tot}}(\omega)$ is computed on a box, with sides placed at a distance of 1 Å from each PY atom. It is worth remarking that in ωFQFμ the fluctuating multipoles are associated with a spherical Gaussian distribution,[61,68] which is taken into account in the calculation of the electric field intensity.[60] The AEF-$\Upsilon^4_{\mathrm{vol}}$ correlation as a function of the NP radius is depicted in Fig. 3 for Ag cTO, Ih and i-Dh substrates. Note that $\Upsilon^4_{\mathrm{vol}}$ values are normalized to the largest AEF for each morphology. Absolute AEF and $\Upsilon^4_{\mathrm{vol}}$ values are reported in Tab. S4 in the SI. The two datasets quantitatively differ, probably due to the high inhomogeneity of the electric field in the proximity of the NP surface, in agreement with Ref. 35.

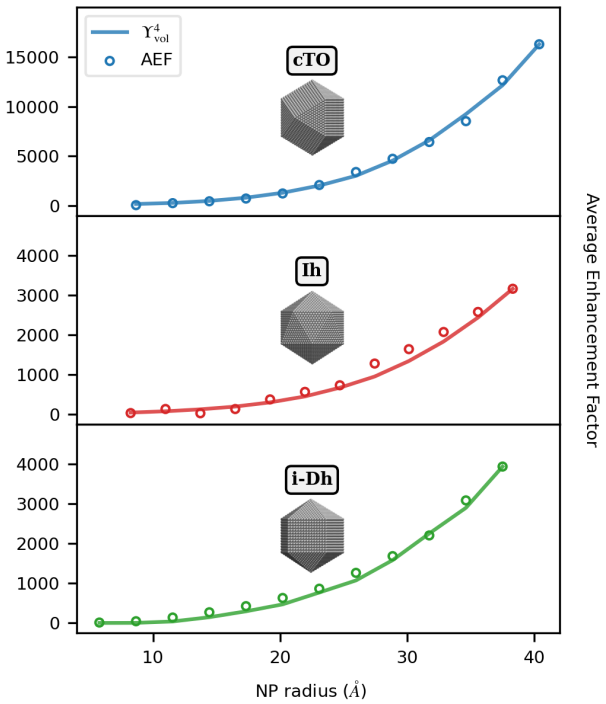

Figure 3: AEF (circles) and normalized Υ^4_{vol} (solid line, see eq. (31)) for PY-Ag as a function of the NP radius and morphology (cTO, Ih and i-Dh). The incident field frequency for the computation of the SERS signal has been set equal to the PRF of each Ag NPs, and the numerical values are 3.42 eV (cTO), 3.51 eV (Ih) and 3.42 eV (i-Dh), respectively.

The agreement between AEF and Υ^4_{vol} is almost perfect, independently of the size and shape of the Ag NPs. Also, we can justify the larger enhancement factors (AEF and MEF) reported in Fig. 2c for cTO with respect to Ih and i-Dh arrangements. Indeed, they are due to a greater induced field, as shown in Fig. 3. This is not surprising and is in line with the results recently reported by us in Ref. 61, which highlighted cTO as the most effective morphology to provide near-field enhancement.

A similar analysis can also be performed by modifying the chemical composition of the NPs. To this end, we consider the same NPs shapes, but made of Au atoms (see Fig. 4a). As recently reported in Ref. 61, ωFQFμ predicts a dipolar PRF only for Au NPs with a radius larger than 15 Å (see also Tab. S2 in the SI). SERS spectra and the AEF/MEF of PY adsorbed on Au cTO, Ih and i-Dh arrangements as a function of the radius are reported in Fig. 4b,c and d, respectively.

Similarly to the Ag case, the most intense SERS signals are associated with the normal modes involving the PY ring (1008 cm^{-1}, see Fig. S4e in the SI) and the α-hydrogen atoms (1510 and 1622 cm^{-1}, see Figs.

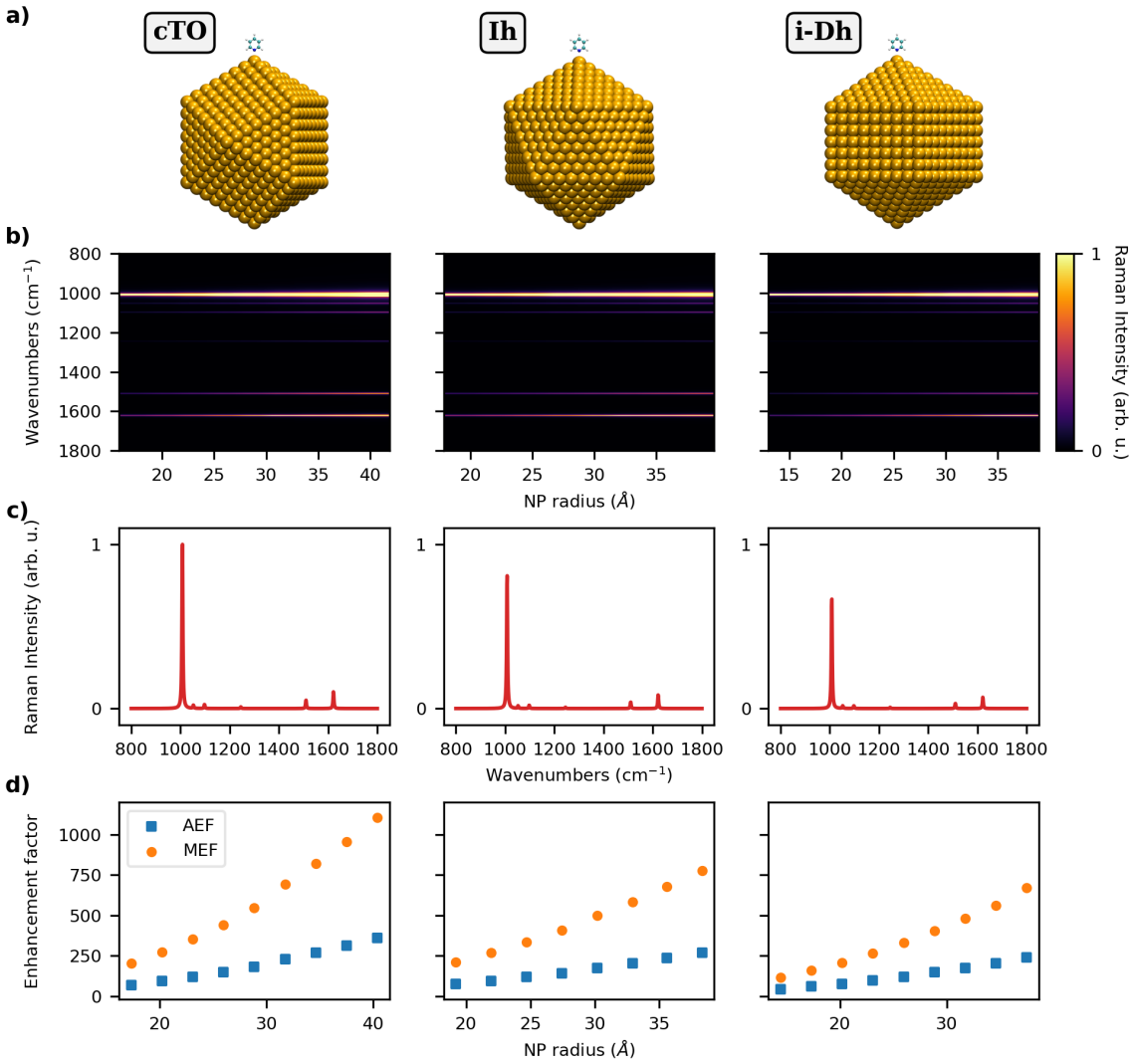

Figure 4: a) Graphical depiction of PY-Au cTO (left), Ih (middle) and i-Dh (right) systems; (b) color plot of normalized SERS spectra as a function of the NP radius (Å); (c) normalized SERS spectra of PY adsorbed on the largest NP structure for each shape; (d) AEF and MEF as a function of the NP radius. The incident field frequency for the computation of the SERS signal has been set equal to the PRF of each Au NP, and the numerical ranges are 2.27–2.17 eV (cTO), 2.29–2.21 eV (Ih) and 2.31–2.17 eV (i-Dh), respectively.

S4n and S4p in the SI, respectively). However, the computed SERS intensities are much lower as compared to the PY-Ag case. By inspecting SERS spectra calculated by considering the largest Au NP (see Fig. 4c), we can indeed notice that slight qualitative discrepancies are reported with respect to PY-Ag (see Fig. 2c). In fact, the SERS spectra of PY on the selected morphologies are characterized by similar relative intensities between the most intense peaks, and the differences between the three spectra are thus less accentuated than the PY-Ag case.

Computed AEF/MEF indices (see Fig. 4d) are also much lower as compared to the PY-Ag case, independently of the NP shape. In this regard, it is worth highlighting that Au PRF is lower than Ag PRF ($\sim$2.2 eV vs. $\sim$3.5 eV), and this also numerically affects the Raman intensities of the molecule in gas-phase. However, the noticeable decrease of AEF/MEF is primarily due to the fact that the electric field generated by the dipolar plasmon of Au NP is much less intense than for Ag; therefore, a smaller enhancement of the Raman intensities is observed. This is demonstrated by the numerical values of AEF, and by the fact that the correlation between AEF and Υ^4_{vol} worsens (see Fig. S5 in the SI). The reported behavior of Au nanoparticles (see Fig. S5 in the SI) has also been previously reported by exploiting other QM/classical approaches.[35]

In case of Au, the E^4 approximation is less accurate, probably because the local field is less intense. In fact, AEF results from the mixing of vibrational normal modes which are enhanced according to different powers of the electric field, up to E^4. When the local field experienced by the molecular system is large, the E^4-dependent vibrational normal modes will dominate the AEF value, thus clearly complying with the E^4 approximation (see Section S1 in the SI for further details).

Dependence of AEF on PY-NP distance As it has been stated in section 2.2, the local field plays a key role in the enhancement of Raman intensities. In this section, we study how AEF behaves as a function of the distance between the molecule and the PS. As a proof of concept, we consider again the case of PY adsorbed on the largest Ih Ag NP (10179 atoms, radius = 38.30 Å, see Tab. S2 in the SI), for which we compute the SERS spectrum by increasing the distance d between the Nitrogen atom and the PS tip. QM/ωFQFμ results are reported in Fig. 5 for $3 \leq d \leq 10$ Å. Analogous results for Au NP are given in Figure S6 of the SI.

As expected, Fig. 5 clearly shows that Raman intensities rapidly decay by increasing d ($\sim d^{-4}$). In particular, AEF decreases from about 1000 at $d = 3$ Å to about 14 at $d = 10$ Å. A similar behavior is observed

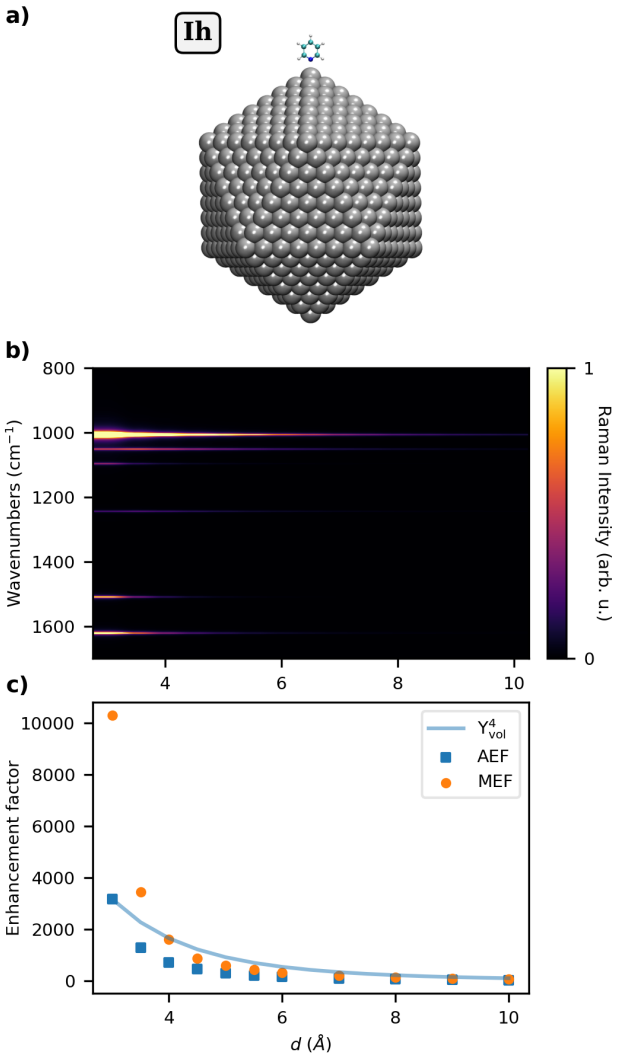

Figure 5: a) Graphical depiction of PY-Ag_{10179} Ih system; (b) color plot of normalized SERS spectra as a function of the PY-NP distance d (Å); (c) AEF, MEF and normalized Υ^4_{vol} as a function of d. The incident field frequency for the computation of the SERS signal has been set equal to the PRF of the Ag NP (3.51 eV).

for MEF. In particular, for $d < 4$ Å, MEF is associated with the symmetric bending of the α-H (1510 cm^{-1}, see Fig. S4n in the SI), while for $d \geq 4$ Å the asymmetric bending of the same hydrogens (1098 cm^{-1}, see Fig. S4h in the SI) yields to the maximum enhancement.

To rationalize these findings, AEF values as a function of d can be compared to the aforementioned E^4 approximation. To this end, we compute the induced electric field in the molecular PY volume as a function of the PY-PS distance. Such values are graphically depicted in Fig. 5c (see Fig. S6c in the SI for the Au NP case). As also commented above for Fig. 3, both the approximated estimation Υ^4_{vol} and computed AEF rapidly vanish as the distance increases. Indeed, it can be noticed that the curves follow a different trend as a function of the distance, which can be ascribed to the fact that AEF comes from the average of different enhancement factors associated with vibrational normal modes according to different powers of the electric field, up to E^4. Also for Au (see Fig. S6c in the SI), small discrepancies are reported, probably related to lower local field effects compared to Ag. AEF and unnormalized Υ^4_{vol} values are reported in Tab. S7 in the SI.

Dependence of AEF on molecule-PS configuration In the previous examples, we have discussed how SERS spectra might depend on the NP morphology and chemical nature of the atoms constituting the NP, and on the mutual molecule-NP distance. In this section, we discuss how the relative configuration of the molecule-PS system affect the SERS spectrum and enhancement. As a proof of concept, we consider three different PY adsorption positions on Ag_{10179} Ih NP. The most representative points of the icosahedral structure are selected (see Fig. 6, bottom): vertex (PY-V, red dot), edge (PY-E, green dot) and face (PY-F, blue dot). In all configurations, PY is adsorbed perpendicularly to the NP surface at a distance of 3 Å, with the nitrogen atom laying closest to the NP. As for the previous cases, the Raman signal is computed by means of eq. (23), by irradiating the PY-Ag_{10179} system with an external electric field polarized along the x, y, z directions. Calculated QM/ωFQFμ SERS spectra are graphically reported in Fig. 6, together with the computed Raman spectrum of PY in the gas-phase.

As a result of the PY-NP interaction, the Raman spectrum undergoes drastic changes when moving from vacuo to the adsorbed case. This can be particularly appreciated by the changes in relative intensities between the two most intense Raman peaks in vacuo, which are associated to the ring breathing (1008 cm^{-1}, see Fig.

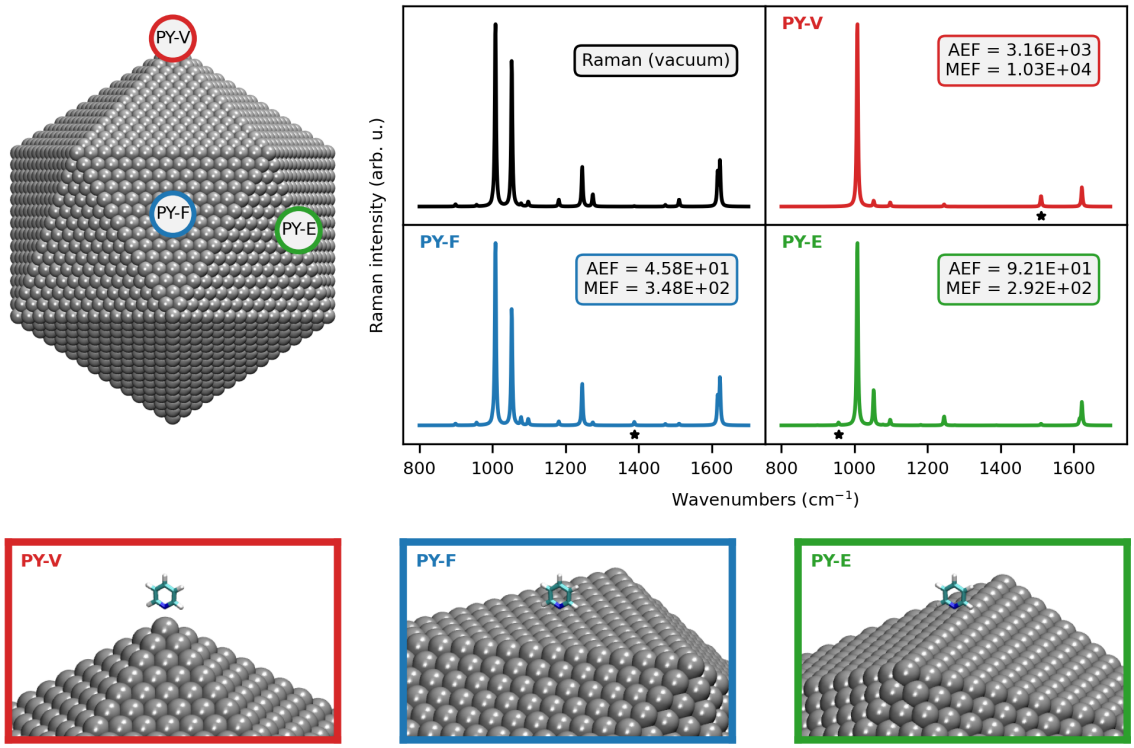

Figure 6: Normalized QM/ωFQFμ PY SERS spectrum as a function of the adsorption site of PY on the Ih Ag_{10179} NP (upper left and bottom panels). AEF and MEF for each configuration are also given. The vibrations associated with the MEF are indicated with a star. The incident field frequency for the computation of the SERS signal has been set equal to the PRF of the Ag NP (3.51 eV).

S4e in the SI) and the symmetric bending of the α-H (1053 cm^{-1}, see Fig. S4f in the SI), respectively. Indeed, for all the selected absorption sites, the relative intensity of the bending mode (1053 cm^{-1}) decreases with respect to that of the ring breathing mode (1008 cm^{-1}), almost vanishing in the case of PY-V (red). Other major differences for PY-F (blue), PY-E (green) and PY-V (red) are reported, for which the relative intensity between the most intense peaks (1000-1100 cm^{-1}) and the other dominant bands completely differ with respect to the gas-phase.

The spatial PY-PS arrangements not only affect the spectral shape, but also enhancement factors. In this respect, AEF for PY-V is two orders of magnitude larger than the values computed for both PY-F and PY-E configurations. The same trend is also observed for MEF, which is interestingly associated with different normal modes depending on the relative PY-PS position. In fact, normal modes involving α-H atoms feature the maximum enhancements for all cases (graphically highlighted in Fig. 6 with a star). More in detail, the symmetric bending (PY-V case, 1588 cm^{-1}, Fig. S4n in the SI), the asymmetric bending (PY-F case, 1388 cm^{-1}, Fig. S4l in the SI) and out-of-plane vibrations (PY-E, 956 cm^{-1}, Fig. S4b in the SI). Such differences are directly related to the relative PY-PS arrangements and are intuitively associated with normal modes providing the largest polarizability variation.

All the reported differences, in both computed SERS spectra and AEF/MEF values, can be related to the inhomogeneity of the electric field induced by the geometrical shape of the Ag NP, which clearly differs by moving for the vertex (PY-V) to a face (PY-F) of the Ih morphology. In fact, the largest changes with respect to the gas-phase spectra/values are predicted for the PY-V configuration (red), for which we observe the largest AEF ($\sim 10^3$) and a drastically different Raman spectrum. Such findings are perfectly explained by the tip effect,[69] which characterizes most plasmonic materials. In fact, in the PY-V configuration, PY is adsorbed to the sharpest region of the Ih NP.

In order to show the effect of the inhomogeneity of the electric field in the surroundings of metal nanoparticles, we have performed additional calculations on the pyridine/Ag_{10179} system in the Ih morphology by changing the relative position of the molecular substrate with respect to the tip of the Ih nanostructure (see Fig. S7 in the SI for more details). For each of these configurations, SERS spectra and AEF values have been computed, and the results are reported in Figs. S7 and S8.

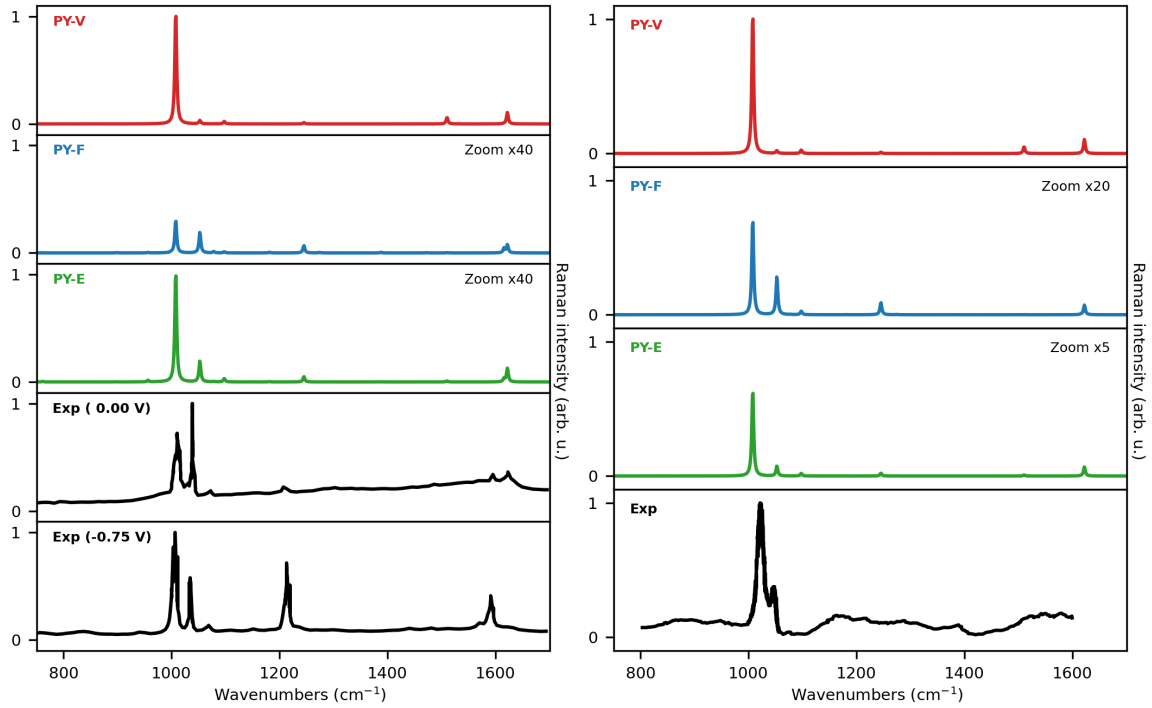

(a) Ag

(b) Au

Figure 7: QM/ωFQFμ SERS spectra of PY adsorbed on Ag (a) and Au (b) Ih NPs (see also Fig. 6). Experimental spectra measured for Ag (a, at 0.0 eV and -0.75 eV external bias) and Au (b, at 0.0 eV) electrodes, reproduced from Refs. 116 (Ag) and 117 (Au), are also reported. The incident field frequency for the computation of the SERS signal has been set equal to the PRF of the Ag NP (3.51 eV) and to the Au NP (2.21 eV), respectively.

Comparison with available experiments To conclude the discussion we compare our QM/ωFQFμ calculations with experimental data available in the literature (Fig. 7 (a-Ag, b-Au).[116,117] We note that our calculations are based on an ideal representation of experimental conditions. Instead, measured spectra result from the interplay between several effects which are not necessarily accounted for in the modeling, such as solvent effects, the coating of the metal electrode, external bias applied, impurities and the roughness of the metal surface. For these reasons, similarly to previous computational studies,[35] the comparison between our results and experiments may only be qualitative.

Let us first focus on PY SERS on Ag electrode, for which experimental spectra at different bias potential have been measured (see Fig. 7).[116] The experimental spectrum at zero bias (0.00 V) is dominated by two bands at about 1000 and 1050 cm^{-1}, whose relative intensities are inverted at higher voltages (see bottom panels). Remarkably, the same bands are also the most intense in computed QM/ωFQFμ SERS spectra, for all investigated PY-PS configurations. Another relevant feature of experimental SERS spectra, is the band at about 1200 cm^{-1}, which only becomes visible by increasing the external bias (see bottom panels in Fig. 7). For this reason, such a band has been commonly associated with a CT mechanism. As stated above, QM/ωFQFμ only accounts for the EM mechanism. Remarkably, and differently from previous models,[35] our approach is able to predict such a feature, because the 1200 cm^{-1} peak is almost absent in the SERS spectrum of the most intense configuration (PY-V, top panel), thus confirming previous hypotheses assigning that band to CT effects.

Similar qualitative trends hold for the Au substrate. Indeed, the experimental SERS spectrum (which refers to an unbiased electrode) is dominated by the bands at about 1000-1050 cm^{-1}. A similar behaviour is observed in the computed spectrum. In addition, the band at about 1200 cm^{-1} is almost absent in both experimental and theoretical SERS spectra.

4.1.2 Graphene disks

In order to show the versatility of QM/ωFQ(Fμ), here we extend the previous study to PY adsorbed on 2D graphene-based substrates.[118,119] To this end, a set of 8 GDs with a radius $20 < r < 160$ Å (see also Tab. S3 in the SI). PY is assumed to be adsorbed on the GD center of mass, parallel to the GD surface at a distance of 3 Å(see Fig. 8a). Such a distance is chosen because it is close to the equilibrium PY-GS distance reported in

the literature.[120] For each PY-GD, GERS spectra are calculated at the B3LYP/DZP level of theory, and the results are reported in Fig. 8b. Note that, in all calculations, $E_F = 0.4$ eV, according to typical reported Fermi energy values.[121,122] We note however that the PRF of graphene-based materials can be tuned by varying the external bias, thus affecting E_F. When applied to GERS, such a feature can be exploited to make the PRF coincide with a molecular excitation of the system under investigation, thus resulting in a pragmatical method to yield resonance Raman assisted by graphene plasmons. Although our approach is general enough to account for such an effect, this is not investigated in this first work.

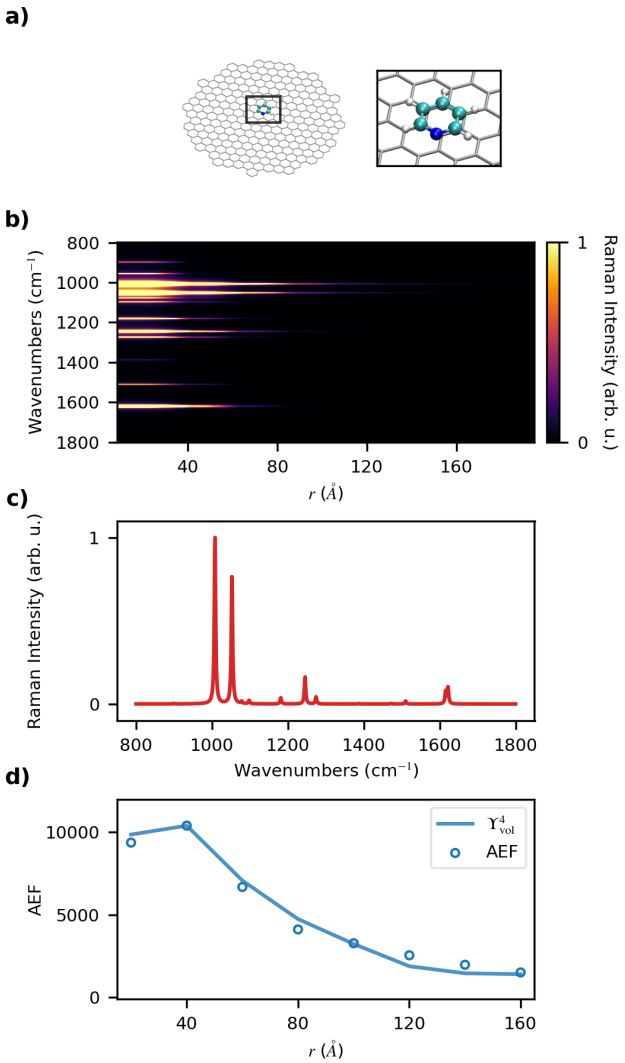

Figure 8: a) Graphical depiction of the PY-GD system; (b) Color plot of normalized SERS spectra as a function of the GD radius r (Å); (c) Normalized SERS spectra of PY adsorbed on a GD with $r = 40$Å; (d) AEF and Υ^4_{vol} as a function of r. The incident field frequency for the computation of the SERS signal has been set equal to the PRF of each GD (0.61–0.24 eV).

From the analysis of GERS spectra, we first note that Raman relative intensities are different from those reported in the case of PY-metal NP systems(see Figs. 2 and 4), with the presence of additional peaks. The latter are mainly related to normal modes involving the vibrations of β and γ H atoms of the pyridine ring (1181 and 1274 cm^{-1}, see Fig. S4i and S4k in the SI). This is the result of the PY-GD morphology under investigation. In fact, the parallel configuration of PY ring with respect to the GD plane allows for a large variation of the polarizability associated to the aforementioned normal modes. Nevertheless, GERS spectra are still dominated by the PY ring breathing and the asymmetric bending of the α hydrogens (1000-1100 cm^{-1}), as already reported for the case of metal NPs. The most relevant dissimilarity between the two substrates is the dependence of GERS spectra on the GD r. In fact, Fig. 8 clearly shows that for large r ($\geq$ 120 Å) the Raman signal vanishes as compared to small r ($\leq$ 40 Å), thus reporting the opposite trend as compared to metal NPs (see Figs. 2b and 4b).

To rationalize this trend, AEF values as a function of r are reported in Fig. 8d. Absolute AEF and Υ^4_{vol} values are given in Tab. S5 in the SI. Differently from metal NPs, in this case the two datasets are almost in perfect agreement, even quantitatively. This is related to the absence of inhomogeneitiesin the induced field in the center of the graphene disk.

A local maximum is observed for $r = 40$ Å, which rapidly decays for larger r values. As for the metal NPs, the electric field generated by the GD increases with the radius, therefore a larger enhancement of the Raman intensity is expected. However, for the specific configuration of the GD system, the electric field is much more intense on the edges (see Ref. 60). Since the distance between PY (adsorbed on the GD center of mass) and the GD edges increases with r, the enhancement factor and the Raman signal decrease as compared with small r (see Fig. 8b). The combination of such effects is responsible for the local maximum in the 40 Å case, in which the electric field at the center of the GD is large enough to substantially increase Raman intensities and therefore PY enhancement factors. Indeed, the trend of AEF as a function of GD r can be explained by means of the Υ^4 approximation, analogously to metal NPs. The correlation between AEF and Υ^4_{vol} is shown by Fig. 8d; the agreement is almost perfect, thus justifying the reported behavior in terms of EM enhancement. We finally remark that our methodology can in principle simulate all possible PY-GD configurations. However, in this work we have restricted the analysis to the selected geometry because it better represents, from the physico-chemical point of view, the most favorable configuration of

a target molecule adsorbed on a graphene sheet, i.e. far from the edges. Within this picture, in fact, we aim to mimic the common experimental setup that is generally constituted of a graphene substrate with intrinsic dimensions much larger than those considered in this work.[67] We point out that different PY-GD configurations can provide higher enhancements, as we have recently reported in Ref. 60.

4.2 Increasing the chromophore complexity: methotrexate adsorbed on graphene disks

In this section, we discuss the application of the model to a realistic case, i.e. methotrexate adsorbed on a graphene disk (see Fig. 1b for the molecular structure). Differently from PY, MTX is a flexible molecule, therefore reliable modeling needs to account for the different conformations. To this end, we perform molecular dynamics (MD) simulations by using ReaxFF,[123,124] within its dedicated engine[125] in the Amsterdam Modeling Suite (AMS).[95] The ReaxFF force field developed in Ref. 126 and which has been reported to reliably describe graphene-based systems is employed.[127] Temperature is maintained at 300K by using a Nosé-Hoover chains (NHC) thermostat,[128] with a damping constant of 100 fs. In NPT simulations, constant pressure is enforced by using the Martyna-Tobias-Klein barostat with a damping constant of 100 fs.[129] 20 layers of graphite, composed of 50 atoms each, are prepared in a 3-D hexagonal periodic cell with lattice parameters $a = b = 12.3$ Å and $c = 67.1$ Å. A 100 ps NPT calculation is then run, by imposing a pressure of 1 atm in all directions. At this point, the simulation box is enlarged so that $a = b = 62.52$ Å and $c = 100$ Å and only 10 layers of graphite, formed by 1250 carbon atoms each, are kept. Then a 50 ps NPT simulation is performed by imposing a pressure of 1 atm in the planar directions. No substantial changes in the values of a and b are detected during pressure equilibration. After this, MTX is thermalized in an empty 3-D hexagonal periodic box with lattice parameters $a = b = 62.52$ Å and $c = 100$ Å by means of a 62.5 ps NVT simulation. Thermalized MTX is then placed at a distance of ~ 10 Å from the equilibrated graphitic surface and a production NVT simulation of 375 ps is performed. After 125 ps, the temperature is equilibrated and the center of the aromatic rings of MTX (ζ-point in Fig 1b) is adsorbed at an average distance of ~ 3.42 Å from the first graphitic layer, in agreement with previous studies.[130] Notably, during the adsorption process, we observe the intramolecular hydrogen transfer between the γ-carboxyl group (green circle in Fig. 1b) and the N8 atom (blue circle in Fig. 1b).

After MTX adsorption, we extract 5000 snapshots from the remaining 250 ps of the production run. MTX geometries are processed by means of the GROMOS[131] clustering approach as it is implemented in the 2020.3 version of the GROMACS[132,133] software. As a result, only two MTX geometries are selected, representing 68.7 % (MTX1) and 28.8 % (MTX2) of the total configurational space. The two structures are reported in Fig. 9b (see also Fig. S9 in the SI).

To simulate MTX GERS, we remove the graphitic substrate, and we substitute the first layer by a perfect GD with $r = 16$ nm on the center of which MTX is adsorbed. MTX1 and MTX2 Raman (in gas-phase) and GERS spectra are finally computed at the B3LYP/DZP level of theory, by setting $E_F = 0.4$ eV (PRF = 0.24 eV). Spectra are reported in Fig. 9a.

MTX1 and MTX2 Raman spectra, both in gas-phase and adsorbed on GD, qualitatively differ, as they are characterized by a shift in vibrational frequencies, and in relative intensities of the main bands. Indeed, while MTX1 Raman spectrum is dominated by the presence of intense bands in the low energy region (between 600 and 800 cm^{-1}), MTX2 spectrum reports diverse intense peaks in the whole considered spectral range. The different MTX1 and MTX2 spectral fingerprints reflect the intrinsic dissimilarity in MTX conformations, as expected from the clustering process. When moving from the gas-phase to the adsorbed configuration, both MTX1 and MTX2 Raman spectra are enhanced by an AEF of about 900. However, Raman spectra undergo small qualitative variations. Such findings can be rationalized by considering that the plasmonic electric field generated by the GD is strongly inhomogeneous at the GD edges, while at the GD center it is almost uniform. Therefore, we expect that the electric field felt by each normal mode is essentially uniform, although more intense than in vacuo. To analyze from a quantitative point of view this hypothesis, we compute for both structures the EFs associated to each normal mode (see eq. (28)), which are graphically depicted in Fig. 10a. In particular, for each normal mode, EFs are plotted with a color scale that follows the intensities of the corresponding Raman peak.

Except for a few outliers, all computed EFs are almost equal independently of the normal mode, and fall around AEF (about 900). The normal modes featuring the highest EF are depicted in Fig. 10b. However, these modes are associated with rather low-intensity bands. On the contrary, EFs computed for the most intense Raman peaks, which dominate the computed spectra, are almost constant at a value of around 900. As it can be noticed, it is difficult to find a correlation between the most intense normal modes of both

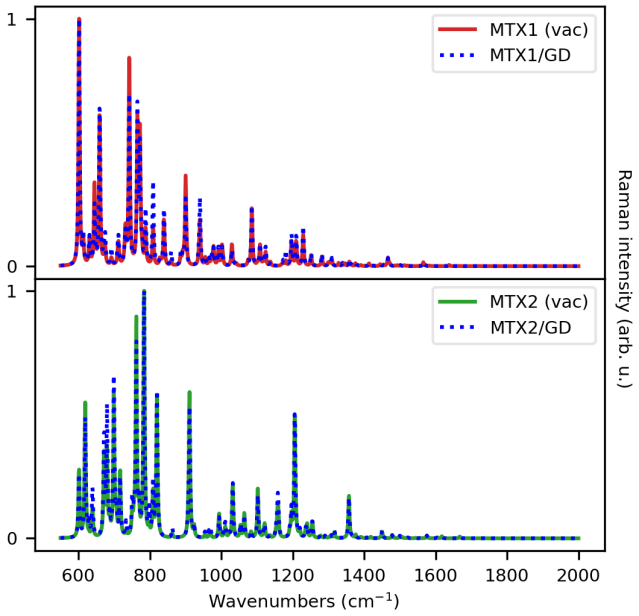

(a)

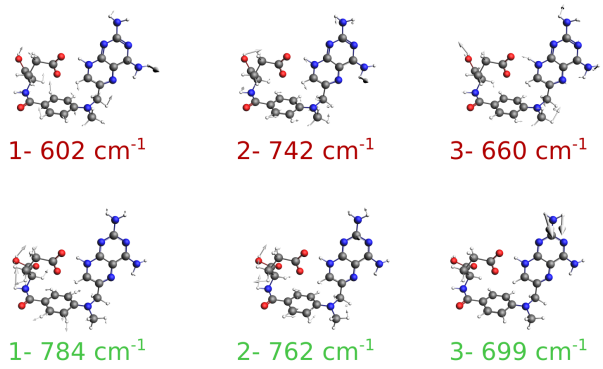

(b)

Figure 9: (a) Normalized MTX1 and MTX2 Raman spectra as computed in vacuo (solid line) and adsorbed on GD (dashed line). (b) MTX1 and MTX2 normal modes associated with the highest Raman intensities. The incident field frequency for the computation of the Raman/GERS signal has been set equal to the PRF of the GD (0.24 eV).

conformers, because they are localized on separated regions of the MTX structure, independently of the distance with respect to the GD surface. In light of the above discussion, this is not surprising. In fact, the presence of GD yields an almost uniform increase of the Raman bands as compared to the case in vacuo, without greatly affecting their relative intensities. Thus, the most intense peaks are related to the same normal modes which provide the most intense bands in the gas-phase Raman spectrum.

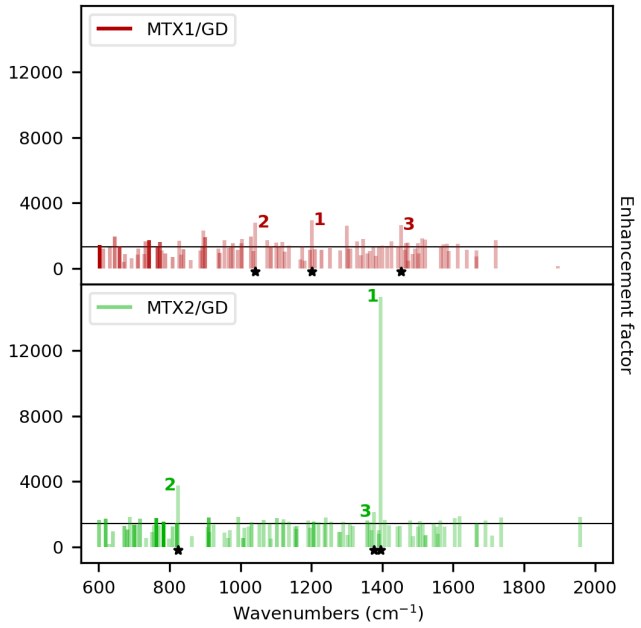

(a)

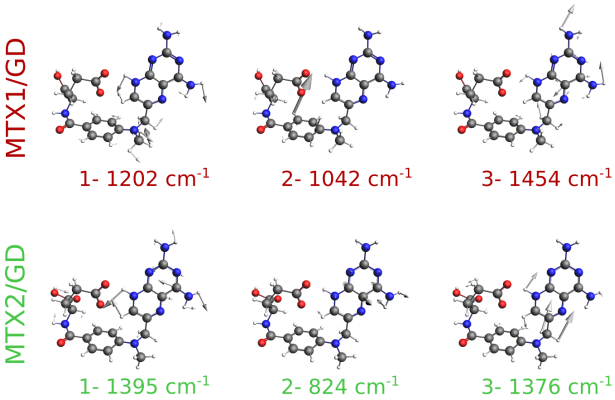

(b)

Figure 10: (a) Computed QM/ωFQ MTX1/GD (top) and MTX2/GD (bottom) normal modes' EFs and AEF reported as horizontal black lines. The darkness of each bar is proportional to the Raman intensity. (b) MTX1 and MTX2 normal modes associated with the largest EFs.

To conclude the discussion, in Fig. 11 we report the MTX/GD GERS spectrum as obtained by averaging MTX1 and MTX2 spectra, which are also graphically depicted.

The most important contribution to the Raman spectrum is due to the MTX1 structure (68.7%), therefore only the most intense peaks of MTX2 arise noticeably in the averaged spectrum. MTX2 bands, however, drastically affect the final GERS spectrum, which do not present anymore the spectral fingerprints related only to MTX1 or MTX2. Moreover, the final spectrum is particularly noisy, especially in the high-frequency

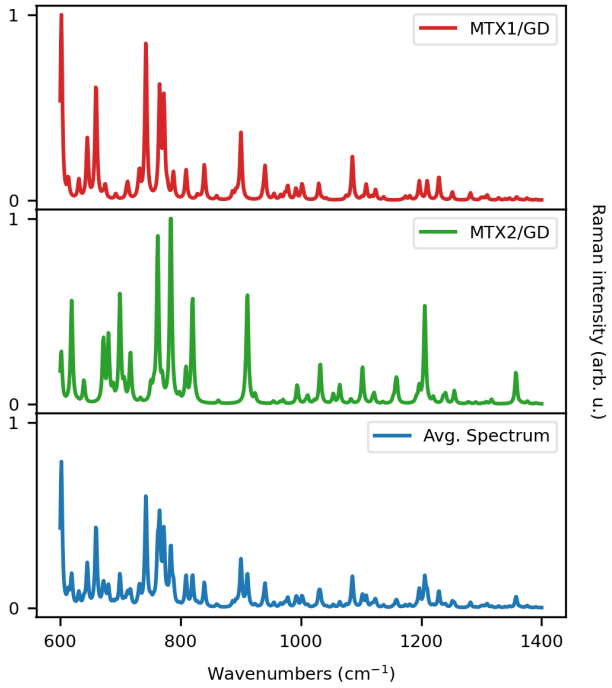

Figure 11: Normalized QM/ωFQFμ GERS spectra of MTX1 and MTX2. The weighted average spectrum is also displayed (bottom panel). The incident field frequency for the computation of the GERS signal has been set equal to the PRF of the GD (0.24 eV).

region. This is essentially due to mall differences between the vibrational frequencies of the two conformers.

Finally, it is worth pointing out that, for the system under consideration, graphene is able to provide significant EM enhancement, comparable to specific metal NPs, such as Au surfaces.[134]

5 Summary, Conclusions and Future Perspectives

In this work, we have presented a new methodology to simulate the Raman spectrum of molecular systems, described at the QM level, adsorbed on plasmonic substrates, treated in terms of the ωFQ and ωFQFμ classical atomistic and frequency-dependent force fields. The resulting multiscale approach is particularly versatile because the underlying ωMM approach is able to accurately describe the plasmonic response of both metallic nanostructures and 2D graphene-based substrates.[63–65,68] The performance of QM/ωFQ(Fμ) has been tested on PY adsorbed on Ag/Au nanostructures and graphene disks. The enhancement factors of the Raman intensities have been studied as a function of the PS size, the PY-PS distance, and the relative

PY-PS orientation, and the qualitative trend has been compared with the E^4 approximation. The largest enhancement has been obtained for silver cTO structures, with an average enhancement factor of about 5000. Such an analysis has allowed confirming that the developed approach is able to correctly describe the EM enhancement in SERS/GERS spectroscopies. Thus, as a final application, we have presented an application of the approach to a realistic case, i.e. methothrexate adsorbed on a graphene disk, for which we also investigate the configurational populations as computed by means of ReaxFF MD simulations. The computed GERS spectrum shows that, although GD is able to enhance the Raman bands by a non-negligible factor of about 900, GD substrate is not able to discriminate between vibrational normal modes.

Our approach has the potential to become a reliable and efficient tool for the simulation of optical properties of molecular systems adsorbed on plasmonic substrates, and might become a viable tool for the experimental design of innovative nanostructured materials able to maximize the enhancement of Raman intensities of a target molecule. To this end, it is worth noting that the current computational bottleneck in QM/ωFQFμ is the cost associated with the solution of ωFQ/ωFQFμ linear systems (see eqs. (1) and (9)), which can be overcome by resorting to efficient approaches that have been recently tested by some of the authors.[68] In particular, with the aid of on-the-fly iterative techniques, we can largely increase the size of the treatable plasmonic nanostructures, up to reach the typical dimensions exploited in real experiments. The latter would also benefit from taking into account the interaction of the molecular system and substrate with a solvating environment.

6 Acknowledgments

This work has received funding from the European Research Council (ERC) under the European Union's Horizon 2020 research and innovation programme (grant agreement No. 818064). SC acknowledges funding from EU under the H2020 grant ProID N. 964363. CC acknowledges funding from PNRR MUR project PE0000023-NQSTI. We gratefully acknowledge the Center for High-Performance Computing (CHPC) at SNS for providing the computational infrastructure.

7 Supporting Information

List of abbreviations introduced in the main text. Geometrical details and PRFs on the PS presented in the main text. Robustness of the computed EFs with respect to the numerical differentiation step size. Raman spectra of PY-NP composite system with different levels of theory. Numerical consistency of the computed SERS spectra and AEF with respect to the DFT integration grid. Graphical representation of the isolated PY normal modes computed at the B3LYP/DZP level of theory. EFs for selected PY-PS configurations. AEF and unnormalized Υ^4_{vol} values for PY adsorbed on Ag NPs and GDs. Correlation of AEF and E^4 approximation for Au NPs with respect to the size of the PS. AEF and unnormalized Υ^4_{vol} values for PY adsorbed on Ag_{10179} in the Ih morphology. Correlation of AEF and E^4 approximation for the NPs with respect to the PY-Au distance. AEF and SERS spectra of PY adsorbed on Ag_{10179} in the Ih morphology by changing the relative position of the two moieties. Comparison of MTX1 and MTX2 structures. Comment on the range of validity of the E^4 approximation with respect to the AEF estimate.

References

(1) Fleischmann, M.; Hendra, P. J.; McQuillan, A. J. Raman spectra of pyridine adsorbed at a silver electrode. *Chem. Phys. Lett.* **1974**, *26*, 163–166.

(2) Le Ru, E. C.; Blackie, E.; Meyer, M.; Etchegoin, P. G. Surface enhanced Raman scattering enhancement factors: a comprehensive study. *J. Phys. Chem. C* **2007**, *111*, 13794–13803.

(3) LeRu, E.; Etchegoin, P. Principles of Surface Enhanced Raman Spectroscopy Elsevier. 2009.

(4) Ding, S.-Y.; You, E.-M.; Tian, Z.-Q.; Moskovits, M. Electromagnetic theories of surface-enhanced Raman spectroscopy. *Chem. Soc. Rev.* **2017**, *46*, 4042–4076.

(5) Zrimsek, A. B.; Chiang, N.; Mattei, M.; Zaleski, S.; McAnally, M. O.; Chapman, C. T.; Henry, A.-I.; Schatz, G. C.; Van Duyne, R. P. Single-molecule chemistry with surface-and tip-enhanced Raman spectroscopy. *Chem. Rev.* **2017**, *117*, 7583–7613.

(6) Wang, X.; Shi, W.; She, G.; Mu, L.; Lee, S. High-performance surface-enhanced Raman scattering sensors based on Ag nanoparticles-coated Si nanowire arrays for quantitative detection of pesticides. *Appl. Phys. Lett.* **2010**, *96*, 053104.

(7) Wang, Y.; Wang, Y.; Wang, W.; Sun, K.; Chen, L. Reporter-embedded SERS tags from gold nanorod seeds: selective immobilization of reporter molecules at the tip of nanorods. *ACS Appl. Mater.* **2016**, *8*, 28105–28115.

(8) Zhang, X.; Young, M. A.; Lyandres, O.; Van Duyne, R. P. Rapid detection of an anthrax biomarker by surface-enhanced Raman spectroscopy. *J. Am. Chem. Soc.* **2005**, *127*, 4484–4489.

(9) Jarvis, R. M.; Goodacre, R. Discrimination of bacteria using surface-enhanced Raman spectroscopy. *Anal. Chem.* **2004**, *76*, 40–47.

(10) Huh, Y. S.; Chung, A. J.; Erickson, D. Surface enhanced Raman spectroscopy and its application to molecular and cellular analysis. *Microfluid. Nanofluidics* **2009**, *6*, 285–297.

(11) Cailletaud, J.; De Bleye, C.; Dumont, E.; Sacré, P.-Y.; Netchacovitch, L.; Gut, Y.; Boiret, M.; Ginot, Y.-M.; Hubert, P.; Ziemons, E. Critical review of surface-enhanced Raman spectroscopy applications in the pharmaceutical field. *J. Pharm. Biomed. Anal.* **2018**, *147*, 458–472.

(12) Han, X. X.; Rodriguez, R. S.; Haynes, C. L.; Ozaki, Y.; Zhao, B. Surface-enhanced Raman spectroscopy. *Nat. Rev. Methods Primers* **2022**, *1*, 1–17.

(13) Sharma, B.; Frontiera, R. R.; Henry, A.-I.; Ringe, E.; Van Duyne, R. P. SERS: Materials, applications, and the future. *Mater. Today* **2012**, *15*, 16–25.

(14) Le Ru, E. C.; Etchegoin, P. G. Single-molecule surface-enhanced Raman spectroscopy. *Annu. Rev. Phys. Chem.* **2012**, *63*, 65–87.

(15) Langer, J.; Jimenez de Aberasturi, D.; Aizpurua, J.; Alvarez-Puebla, R. A.; Auguié, B.; Baumberg, J. J.; Bazan, G. C.; Bell, S. E.; Boisen, A.; Brolo, A. G., et al. Present and future of surface-enhanced Raman scattering. *ACS Nano* **2019**, *14*, 28–117.

(16) Pilot, R.; Signorini, R.; Durante, C.; Orian, L.; Bhamidipati, M.; Fabris, L. A review on surface-enhanced Raman scattering. *Biosensors* **2019**, *9*, 57.

(17) Zong, C.; Xu, M.; Xu, L.-J.; Wei, T.; Ma, X.; Zheng, X.-S.; Hu, R.; Ren, B. Surface-enhanced Raman spectroscopy for bioanalysis: reliability and challenges. *Chem. Rev.* **2018**, *118*, 4946–4980.

(18) Albrecht, M. G.; Creighton, J. A. Anomalously intense Raman spectra of pyridine at a silver electrode. *J. Am. Chem. Soc.* **1977**, *99*, 5215–5217.

(19) Jeanmaire, D. L.; Van Duyne, R. P. Surface Raman spectroelectrochemistry: Part I. Heterocyclic, aromatic, and aliphatic amines adsorbed on the anodized silver electrode. *J. Electroanal. Chem. Interf. Electrochem.* **1977**, *84*, 1–20.

(20) Campion, A.; Kambhampati, P. Surface-enhanced Raman scattering. *Chem. Soc. Rev.* **1998**, *27*, 241–250.

(21) Willets, K. A.; Van Duyne, R. P. Localized surface plasmon resonance spectroscopy and sensing. *Annu. Rev. Phys. Chem.* **2007**, *58*, 267–297.

(22) Alvarez-Puebla, R.; Liz-Marzán, L. M.; García de Abajo, F. J. Light concentration at the nanometer scale. *J. Phys. Chem. Lett.* **2010**, *1*, 2428–2434.

(23) Le Ru, E.; Etchegoin, P. *Principles of Surface-Enhanced Raman Spectroscopy: and related plasmonic effects*; Elsevier, 2008.

(24) Maier, S. A. *Plasmonics: fundamentals and applications*; Springer Science & Business Media, 2007.

(25) Junno, T.; Deppert, K.; Montelius, L.; Samuelson, L. Controlled manipulation of nanoparticles with an atomic force microscope. *Appl. Phys. Lett.* **1995**, *66*, 3627–3629.

(26) Ishida, T.; Murayama, T.; Taketoshi, A.; Haruta, M. Importance of size and contact structure of gold nanoparticles for the genesis of unique catalytic processes. *Chem. Rev.* **2019**, *120*, 464–525.

(27) Sau, T. K.; Rogach, A. L. Nonspherical noble metal nanoparticles: colloid-chemical synthesis and morphology control. *Adv. Mater.* **2010**, *22*, 1781–1804.

(28) Liz-Marzán, L. M. Tailoring surface plasmons through the morphology and assembly of metal nanoparticles. *Langmuir* **2006**, *22*, 32–41.

(29) Grzelczak, M.; Pérez-Juste, J.; Mulvaney, P.; Liz-Marzán, L. M. Shape control in gold nanoparticle synthesis. *Chem. Soc. Rev.* **2008**, *37*, 1783–1791.

(30) Blackie, E. J.; Le Ru, E. C.; Etchegoin, P. G. Single-molecule surface-enhanced Raman spectroscopy of nonresonant molecules. *J. Am. Chem. Soc.* **2009**, *131*, 14466–14472.

(31) Fesenko, O.; Dovbeshko, G.; Dementjev, A.; Karpicz, R.; Kaplas, T.; Svirko, Y. Graphene-enhanced Raman spectroscopy of thymine adsorbed on single-layer graphene. *Nanoscale Res. Lett.* **2015**, *10*, 1–7.

(32) Lai, H.; Xu, F.; Zhang, Y.; Wang, L. Recent progress on graphene-based substrates for surface-enhanced Raman scattering applications. *J. Mater. Chem. B* **2018**, *6*, 4008–4028.

(33) Chen, N.; Xiao, T.-H.; Luo, Z.; Kitahama, Y.; Hiramatsu, K.; Kishimoto, N.; Itoh, T.; Cheng, Z.; Goda, K. Porous carbon nanowire array for surface-enhanced Raman spectroscopy. *Nat. Commun.* **2020**, *11*, 1–8.

(34) Payton, J. L.; Morton, S. M.; Moore, J. E.; Jensen, L. A discrete interaction model/quantum mechanical method for simulating surface-enhanced Raman spectroscopy. *J. Chem. Phys.* **2012**, *136*, 214103.

(35) Payton, J. L.; Morton, S. M.; Moore, J. E.; Jensen, L. A hybrid atomistic electrodynamics–quantum mechanical approach for simulating surface-enhanced Raman scattering. *Acc. Chem. Res.* **2014**, *47*, 88–99.

(36) Hu, Z.; Chulhai, D. V.; Jensen, L. Simulating surface-enhanced hyper-Raman scattering using atomistic electrodynamics-quantum mechanical models. *J. Chem. Theory Comput.* **2016**, *12*, 5968–5978.

(37) Corni, S.; Tomasi, J. Enhanced response properties of a chromophore physisorbed on a metal particle. *J. Chem. Phys.* **2001**, *114*, 3739–3751.

(38) Corni, S.; Tomasi, J. Surface enhanced Raman scattering from a single molecule adsorbed on a metal particle aggregate: A theoretical study. *J. Chem. Phys.* **2002**, *116*, 1156–1164.

(39) Corni, S.; Tomasi, J. Excitation energies of a molecule close to a metal surface. *J. Chem. Phys.* **2002**, *117*, 7266–7278.

(40) Corni, S.; Tomasi, J. Theoretical evaluation of Raman spectra and enhancement factors for a molecule adsorbed on a complex-shaped metal particle. *Chem. Phys. Lett.* **2001**, *342*, 135–140.

(41) Corni, S.; Tomasi, J. Erratum to: Theoretical evaluation of Raman spectra and enhancement factors for a molecule adsorbed on a complex-shaped metal particle [Chem. Phys. Lett. 342 (2001) 135-140]. *Chem. Phys. Lett.* **2002**, *365*, 552–553.

(42) Chen, R.; Jensen, L. Interpreting the chemical mechanism in SERS using a Raman bond model. *J. Chem. Phys.* **2020**, *152*, 024126.

(43) Chen, R.; Jensen, L. Understanding chemical enhancements of surface-enhanced Raman scattering using a Raman bond model for extended systems. *J. Chem. Phys.* **2022**,

(44) Becca, J. C.; Chen, X.; Jensen, L. A discrete interaction model/quantum mechanical method for simulating surface-enhanced Raman spectroscopy in solution. *J. Chem. Phys.* **2021**, *154*, 224705.

(45) Liu, P.; Chulhai, D. V.; Jensen, L. Single-molecule imaging using atomistic near-field tip-enhanced Raman spectroscopy. *ACS nano* **2017**, *11*, 5094–5102.

(46) Chulhai, D. V.; Chen, X.; Jensen, L. Simulating ensemble-averaged surface-enhanced Raman scattering. *J. Phys. Chem. C* **2016**, *120*, 20833–20842.

(47) Zhao, L.; Jensen, L.; Schatz, G. C. Pyridine- Ag20 cluster: a model system for studying surface-enhanced Raman scattering. *J. Am. Chem. Soc.* **2006**, *128*, 2911–2919.

(48) Jensen, L.; Aikens, C. M.; Schatz, G. C. Electronic structure methods for studying surface-enhanced Raman scattering. *Chem. Soc. Rev.* **2008**, *37*, 1061–1073.

(49) Morton, S. M.; Jensen, L. Understanding the molecule- surface chemical coupling in SERS. *J. Am. Chem. Soc.* **2009**, *131*, 4090–4098.

(50) Morton, S. M.; Silverstein, D. W.; Jensen, L. Theoretical studies of plasmonics using electronic structure methods. *Chem. Rev.* **2011**, *111*, 3962–3994.

(51) Jørgensen, S.; Ratner, M. A.; Mikkelsen, K. V. Heterogeneous solvation: An ab initio approach. *J. Chem. Phys.* **2001**, *115*, 3792–3803.

(52) Neuhauser, D.; Lopata, K. Molecular nanopolaritonics: Cross manipulation of near-field plasmons and molecules. I. Theory and application to junction control. *J. Chem. Phys.* **2007**, *127*, 154715.

(53) Masiello, D. J.; Schatz, G. C. Many-body theory of surface-enhanced Raman scattering. *Phys. Rev. A* **2008**, *78*, 042505.

(54) Vukovic, S.; Corni, S.; Mennucci, B. Fluorescence enhancement of chromophores close to metal nanoparticles. Optimal setup revealed by the polarizable continuum model. *J. Phys. Chem. C* **2009**, *113*, 121–133.

(55) Lopata, K.; Neuhauser, D. Multiscale Maxwell–Schrödinger modeling: A split field finite-difference time-domain approach to molecular nanopolaritonics. *J. Chem. Phys.* **2009**, *130*, 104707.

(56) Arcisauskaite, V.; Kongsted, J.; Hansen, T.; Mikkelsen, K. V. Charge transfer excitation energies in pyridine–silver complexes studied by a QM/MM method. *Chem. Phys. Lett.* **2009**, *470*, 285–288.

(57) Masiello, D. J.; Schatz, G. C. On the linear response and scattering of an interacting molecule-metal system. *J. Chem. Phys.* **2010**, *132*, 064102.

(58) Chen, H.; McMahon, J. M.; Ratner, M. A.; Schatz, G. C. Classical electrodynamics coupled to quantum mechanics for calculation of molecular optical properties: a RT-TDDFT/FDTD approach. *J. Phys. Chem. C* **2010**, *114*, 14384–14392.

(59) Hao, Q.; Morton, S. M.; Wang, B.; Zhao, Y.; Jensen, L.; Jun Huang, T. Tuning surface-enhanced Raman scattering from graphene substrates using the electric field effect and chemical doping. *Applied Physics Letters* **2013**, *102*, 011102.

(60) Bonatti, L.; Nicoli, L.; Giovannini, T.; Cappelli, C. In silico design of graphene plasmonic hot-spots. *Nanoscale Advances* **2022**, *4*, 2294–2302.

(61) Giovannini, T.; Bonatti, L.; Lafiosca, P.; Nicoli, L.; Castagnola, M.; Illobre, P. G.; Corni, S.; Cappelli, C. Do We Really Need Quantum Mechanics to Describe Plasmonic Properties of Metal Nanostructures? *ACS Photonics* **2022**,

(62) Lombardi, J. R.; Birke, R. L.; Lu, T.; Xu, J. Charge-transfer theory of surface enhanced Raman spectroscopy: Herzberg–Teller contributions. *J. Chem. Phys.* **1986**, *84*, 4174–4180.

(63) Giovannini, T.; Rosa, M.; Corni, S.; Cappelli, C. A classical picture of subnanometer junctions: an atomistic Drude approach to nanoplasmonics. *Nanoscale* **2019**, *11*, 6004–6015.

(64) Giovannini, T.; Bonatti, L.; Polini, M.; Cappelli, C. Graphene plasmonics: Fully atomistic approach for realistic structures. *J. Phys. Chem. Lett.* **2020**, *11*, 7595–7602.

(65) Bonatti, L.; Gil, G.; Giovannini, T.; Corni, S.; Cappelli, C. Plasmonic resonances of metal nanoparticles: atomistic vs. Continuum approaches. *Front. Chem.* **2020**, *8*, 340.

(66) Zanotto, S.; Bonatti, L.; Pantano, M. F.; Mišeikis, V.; Speranza, G.; Giovannini, T.; Coletti, C.; Cappelli, C.; Tredicucci, A.; Toncelli, A. Strain-Induced Plasmon Confinement in Polycrystalline Graphene. *ACS Photonics* **2023**,

(67) Barros, E. B.; Dresselhaus, M. S. Theory of Raman enhancement by two-dimensional materials: Applications for graphene-enhanced Raman spectroscopy. *Phys. Rev. B* **2014**, *90*, 035443.

(68) Lafiosca, P.; Giovannini, T.; Benzi, M.; Cappelli, C. Going Beyond the Limits of Classical Atomistic Modeling of Plasmonic Nanostructures. *J. Phys. Chem. C* **2021**,

(69) Jackson, J. D. Classical electrodynamics. 1999.

(70) Giovannini, T.; Puglisi, A.; Ambrosetti, M.; Cappelli, C. Polarizable QM/MM approach with fluctuating charges and fluctuating dipoles: the QM/FQFμ model. *J. Chem. Theory Comput.* **2019**, *15*, 2233–2245.

(71) Pelton, M.; Bryant, G. W. *Introduction to metal-nanoparticle plasmonics*; John Wiley & Sons, 2013; Vol. 5.

(72) Neto, A. C.; Guinea, F.; Peres, N. M.; Novoselov, K. S.; Geim, A. K. The electronic properties of graphene. *Rev. Mod. Phys.* **2009**, *81*, 109.

(73) Pinchuk, A.; Kreibig, U.; Hilger, A. Optical properties of metallic nanoparticles: influence of interface effects and interband transitions. *Surf. Sci.* **2004**, *557*, 269–280.

(74) Pinchuk, A.; Von Plessen, G.; Kreibig, U. Influence of interband electronic transitions on the optical absorption in metallic nanoparticles. *J. Phys. D: Appl. Phys.* **2004**, *37*, 3133.

(75) Balamurugan, B.; Maruyama, T. Evidence of an enhanced interband absorption in Au nanoparticles: size-dependent electronic structure and optical properties. *Appl. Phys. Lett.* **2005**, *87*, 143105.

(76) Liebsch, A. Surface-plasmon dispersion and size dependence of Mie resonance: silver versus simple metals. *Phys. Rev. B* **1993**, *48*, 11317.

(77) Santiago, E. Y.; Besteiro, L. V.; Kong, X.-T.; Correa-Duarte, M. A.; Wang, Z.; Govorov, A. O. Efficiency of hot-electron generation in plasmonic nanocrystals with complex shapes: surface-induced scattering, hot spots, and interband transitions. *ACS Photonics* **2020**, *7*, 2807–2824.

(78) Warshel, A.; Levitt, M. Theoretical studies of enzymic reactions: dielectric, electrostatic and steric stabilization of the carbonium ion in the reaction of lysozyme. *J. Mol. Biol.* **1976**, *103*, 227–249.

(79) Lin, H.; Truhlar, D. G. QM/MM: what have we learned, where are we, and where do we go from here? *Theor. Chem. Acc.* **2007**, *117*, 185–199.

(80) Senn, H. M.; Thiel, W. QM/MM methods for biomolecular systems. *Angew. Chem. Int. Ed.* **2009**, *48*, 1198–1229.

(81) Mennucci, B.; Corni, S. Multiscale modelling of photoinduced processes in composite systems. *Nat. Rev. Chem.* **2019**, *3*, 315–330.

(82) Morton, S. M.; Jensen, L. A discrete interaction model/quantum mechanical method for describing response properties of molecules adsorbed on metal nanoparticles. *J. Chem. Phys.* **2010**, *133*, 074103.

(83) Guido, C. A.; Rosa, M.; Cammi, R.; Corni, S. An open quantum system theory for polarizable continuum models. *J. Chem. Phys.* **2020**, *152*, 174114.

(84) Coccia, E.; Fregoni, J.; Guido, C.; Marsili, M.; Pipolo, S.; Corni, S. Hybrid theoretical models for molecular nanoplasmonics. *J. Chem. Phys.* **2020**, *153*, 200901.

(85) Corni, S.; Pipolo, S.; Cammi, R. Equation of motion for the solvent polarization apparent charges in the polarizable continuum model: Application to real-time TDDFT. *J. Phys. Chem. A* **2015**, *119*, 5405–5416.

(86) Rick, S. W.; Stuart, S. J.; Bader, J. S.; Berne, B. Fluctuating charge force fields for aqueous solutions. *J. Mol. Liq.* **1995**, *65*, 31–40.

(87) Cappelli, C. Integrated QM/polarizable MM/continuum approaches to model chiroptical properties of strongly interacting solute–solvent systems. *Int. J. Quantum Chem.* **2016**, *116*, 1532–1542.

(88) Giovannini, T.; Egidi, F.; Cappelli, C. Molecular spectroscopy of aqueous solutions: a theoretical perspective. *Chem. Soc. Rev.* **2020**, *49*, 5664–5677.

(89) Giovannini, T.; Egidi, F.; Cappelli, C. Theory and algorithms for chiroptical properties and spectroscopies of aqueous systems. *Physical Chemistry Chemical Physics* **2020**, *22*, 22864–22879.

(90) Giovannini, T.; Riso, R. R.; Ambrosetti, M.; Puglisi, A.; Cappelli, C. Electronic transitions for a fully polarizable qm/mm approach based on fluctuating charges and fluctuating dipoles: linear and corrected linear response regimes. *J. Chem. Phys.* **2019**, *151*, 174104.

(91) Giovannini, T.; Grazioli, L.; Ambrosetti, M.; Cappelli, C. Calculation of ir spectra with a fully polarizable qm/mm approach based on fluctuating charges and fluctuating dipoles. *J. Chem. Theory Comput.* **2019**, *15*, 5495–5507.

(92) Giovannini, T.; Ambrosetti, M.; Cappelli, C. Quantum confinement effects on solvatochromic shifts of molecular solutes. *J. Phys. Chem. Lett.* **2019**, *10*, 5823–5829.

(93) Marrazzini, G.; Giovannini, T.; Egidi, F.; Cappelli, C. Calculation of linear and non-linear electric response properties of systems in aqueous solution: A polarizable quantum/classical approach with quantum repulsion effects. *J. Chem. Theory Comput.* **2020**, *16*, 6993–7004.

(94) te Velde, G.; Bickelhaupt, F. M.; Baerends, E. J.; Fonseca Guerra, C.; van Gisbergen, S. J. A.; Snijders, J. G.; Ziegler, T. Chemistry with ADF. *J. Comput. Chem.* **2001**, *22*, 931–967.

(95) Baerends, E.; et. al, ADF *(version 2020.x)*. 2020; Theoretical Chemistry, Vrije Universiteit, Amsterdam, The Netherlands, http://www.scm.com.

(96) Nicoli, L.; Giovannini, T.; Cappelli, C. Assessing the Quality of QM/MM Approaches to Describe Vacuo-to-water Solvatochromic Shifts. *J. Chem. Phys.* **2022**, DOI: 10.1063/5.0118664.

(97) Jensen, L.; Van Duijnen, P. T.; Snijders, J. G. A discrete solvent reaction field model within density functional theory. *J. Chem. Phys.* **2003**, *118*, 514–521.

(98) Casida, M. E. *Recent Advances In Density Functional Methods: (Part I)*; World Scientific, 1995; pp 155–192.

(99) Norman, P.; Ruud, K.; Saue, T. *Principles and practices of molecular properties: Theory, modeling, and simulations*; John Wiley & Sons, 2018.

(100) Giovannini, T.; Ambrosetti, M.; Cappelli, C. A polarizable embedding approach to second harmonic generation (SHG) of molecular systems in aqueous solutions. *Theoretical Chemistry Accounts* **2018**, *137*, 1–11.

(101) Morton, S. M.; Jensen, L. A discrete interaction model/quantum mechanical method to describe the interaction of metal nanoparticles and molecular absorption. *J. Chem. Phys.* **2011**, *135*, 134103.

(102) Placzek, G.; Teller, E. Die Rotationsstruktur der Ramanbanden mehratomiger Moleküle. *Zeitschrift für Physik* **1933**, *81*, 209–258.

(103) Placzek, G. Handbuch der Radiologie, vol. *Ed. G. Marx, Akademische Verlagsgesellschaft, Leipzig* **1934**,

(104) Jensen, L.; Zhao, L.; Autschbach, J.; Schatz, G. Theory and method for calculating resonance Raman scattering from resonance polarizability derivatives. *J. Chem. Phys.* **2005**, *123*, 174110.

(105) Corni, S.; Tomasi, J. Studying SERS from metal nanoparticles and nanoparticles aggregates with continuum models. *Surface-Enhanced Raman Scattering: Physics and Applications* **2006**, 105–123.

(106) Louden, P.; Bhattarai, H.; Neidhart, S.; Lin, T.; Vardeman II, C. F.; Fennell, C. J.; Meineke, M. A.; Kuang, S.; Lamichhane, M.; Michalka, J., et al. OPENMD-2.5: molecular dynamics in the open. *OpenMD http://openmd. org* **2017**,

(107) Humphrey, W.; Dalke, A.; Schulten, K. VMD – Visual Molecular Dynamics. *Journal of Molecular Graphics* **1996**, *14*, 33–38.

(108) Van Lenthe, E.; Baerends, E. J. Optimized Slater-type basis sets for the elements 1–118. *Journal of computational chemistry* **2003**, *24*, 1142–1156.

(109) Van Gisbergen, S.; Snijders, J.; Baerends, E. A density functional theory study of frequency-dependent polarizabilities and Van der Waals dispersion coefficients for polyatomic molecules. *J. Chem. Phys.* **1995**, *103*, 9347–9354.

(110) Van Gisbergen, S.; Snijders, J.; Baerends, E. Implementation of time-dependent density functional response equations. *Comput. Phys. Commun.* **1999**, *118*, 119–138.

(111) Fan, L.; Ziegler, T. Application of density functional theory to infrared absorption intensity calculations on main group molecules. *J. Chem. Phys.* **1992**, *96*, 9005–9012.

(112) Fan, L.; Ziegler, T. Application of density functional theory to infrared absorption intensity calculations on transition-metal carbonyls. *J. Phys. Chem.* **1992**, *96*, 6937–6941.

(113) Van Gisbergen, S.; Snijders, J.; Baerends, E. Application of time-dependent density functional response theory to Raman scattering. *Chem. Phys. Lett.* **1996**, *259*, 599–604.

(114) Van Duyne, R.; Jeanmaire, D. Surface Raman spectroelectochemistry: part1. heterocyclic, aromatic, and aliphatic Amines adsorbed on the anodized silver electrode. *J. Electroanal. Chem* **1977**, *84*, 1–20.

(115) Le Ru, E.; Etchegoin, P. Rigorous justification of the| E| 4 enhancement factor in surface enhanced Raman spectroscopy. *Chem. Phys. Lett.* **2006**, *423*, 63–66.

(116) Arenas, J. F.; López Tocón, I.; Otero, J. C.; Marcos, J. I. Charge transfer processes in surface-enhanced raman scattering. Franck- condon active vibrations of pyridine. *J. Phys. Chem.* **1996**, *100*, 9254–9261.

(117) Khaing Oo, M. K.; Guo, Y.; Reddy, K.; Liu, J.; Fan, X. Ultrasensitive vapor detection with surface-enhanced Raman scattering-active gold nanoparticle immobilized flow-through multihole capillaries. *Anal. Chem.* **2012**, *84*, 3376–3381.

(118) Dresselhaus, M. S.; Jorio, A.; Hofmann, M.; Dresselhaus, G.; Saito, R. Perspectives on carbon nanotubes and graphene Raman spectroscopy. *Nano Lett.* **2010**, *10*, 751–758.

(119) Ling, X.; Xie, L.; Fang, Y.; Xu, H.; Zhang, H.; Kong, J.; Dresselhaus, M. S.; Zhang, J.; Liu, Z. Can graphene be used as a substrate for Raman enhancement? *Nano Lett.* **2010**, *10*, 553–561.

(120) Voloshina, E.; Mollenhauer, D.; Chiappisi, L.; Paulus, B. Theoretical study on the adsorption of pyridine derivatives on graphene. *Chem. Phys. Lett.* **2011**, *510*, 220–223.

(121) Kim, J.; Son, H.; Cho, D. J.; Geng, B.; Regan, W.; Shi, S.; Kim, K.; Zettl, A.; Shen, Y.-R.; Wang, F. Electrical control of optical plasmon resonance with graphene. *Nano Lett.* **2012**, *12*, 5598–5602.

(122) Thongrattanasiri, S.; de Abajo, F. J. G. Optical field enhancement by strong plasmon interaction in graphene nanostructures. *Phys. Rev. Lett.* **2013**, *110*, 187401.

(123) Van Duin, A. C.; Dasgupta, S.; Lorant, F.; Goddard, W. A. ReaxFF: a reactive force field for hydrocarbons. *J. Phys. Chem. A* **2001**, *105*, 9396–9409.

(124) Chenoweth, K.; Van Duin, A. C.; Goddard, W. A. ReaxFF reactive force field for molecular dynamics simulations of hydrocarbon oxidation. *J. Phys. Chem. A* **2008**, *112*, 1040–1053.

(125) ReaxFF 2021.1, SCM, Theoretical Chemistry, Vrije Universiteit, Amsterdam, The Netherlands. `http://www.scm.com`.

(126) Monti, S.; Corozzi, A.; Fristrup, P.; Joshi, K. L.; Shin, Y. K.; Oelschlaeger, P.; Van Duin, A. C.; Barone, V. Exploring the conformational and reactive dynamics of biomolecules in solution using an extended version of the glycine reactive force field. *Phys. Chem. Chem. Phys.* **2013**, *15*, 15062–15077.

(127) Golkaram, M.; van Duin, A. C. Revealing graphene oxide toxicity mechanisms: A reactive molecular dynamics study. *Mater. Discov.* **2015**, *1*, 54–62.

(128) Martyna, G. J.; Klein, M. L.; Tuckerman, M. Nosé–Hoover chains: The canonical ensemble via continuous dynamics. *J. Chem. Phys.* **1992**, *97*, 2635–2643.

(129) Martyna, G. J.; Tobias, D. J.; Klein, M. L. Constant pressure molecular dynamics algorithms. *J. Chem. Phys.* **1994**, *101*, 4177–4189.

(130) Umadevi, D.; Sastry, G. N. Impact of the chirality and curvature of carbon nanostructures on their interaction with aromatics and amino acids. *ChemPhysChem* **2013**, *14*, 2570–2578.

(131) Daura, X.; Gademann, K.; Jaun, B.; Seebach, D.; Van Gunsteren, W. F.; Mark, A. E. Peptide folding: when simulation meets experiment. *Angew. Chem. Int. Ed.* **1999**, *38*, 236–240.

(132) Abraham, M. J.; Murtola, T.; Schulz, R.; Páll, S.; Smith, J. C.; Hess, B.; Lindahl, E. GROMACS: High performance molecular simulations through multi-level parallelism from laptops to supercomputers. *SoftwareX* **2015**, *1*, 19–25.

(133) Abraham, L.; Hess, B.; Spoel, V. GROMACS 2020.3 source code. Zenodo. 2020.

(134) Abdelsalam, M. E.; Bartlett, P. N.; Baumberg, J. J.; Cintra, S.; Kelf, T. A.; Russell, A. E. Electrochemical SERS at a structured gold surface. *Electrochem. Commun.* **2005**, *7*, 740–744.

TOC graphic

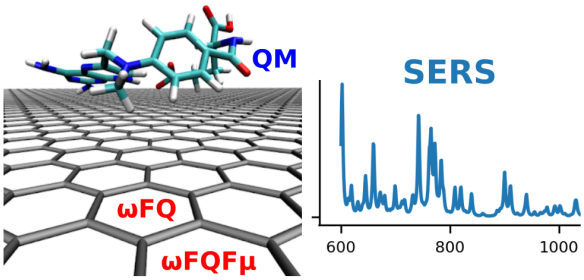

Supporting Information: QM/Classical Modeling of Surface Enhanced Raman Scattering Based on Atomistic Electromagnetic Models

Piero Lafiosca,[†] Luca Nicoli,[†] Luca Bonatti,[†] Tommaso Giovannini,[*,†] Stefano Corni,[‡,¶] and Chiara Cappelli[*,†,§]

†*Scuola Normale Superiore, Piazza dei Cavalieri 7, 56126 Pisa, Italy.*

‡*Dipartimento di Scienze Chimiche, Università di Padova, via Marzolo 1, 35131, Padova, Italy*

¶*Istituto di Nanoscienze del Consiglio Nazionale delle Ricerche CNR-NANO, via Campi 213/A, 41125, Modena, Italy*

§*LENS (European Laboratory for Non-Linear Spectroscopy), Via N. Carrara 1, 50019, Sesto Fiorentino, Italy*

E-mail: tommaso.giovannini@sns.it; chiara.cappelli@sns.it

Table S1: List of abbreviations used in the manuscript

ωFQ	Frequency dependent Fluctuating Charges
ωFQFμ	Frequency dependent Fluctuating Charges and Fluctuating Dipoles
EM	electromagnetic
CT	chemical enhancement
NP	metal nanoparticles
IB	interband (transitions)
PS	plasmonic substrate
cTO	cuboctahedron
Ih	icosahedron
i-Dh	ino-decahedron
GD	graphene disk
PY	pyridine
PRF	plasmon resonance frequency
EF	enhancement factor
AEF	(spectrally) averaged enhancement factor
MEF	maximum enhancement factor
MTX	methotrexate
PY-V	pyridine adsorbed on the vertex of a plasmonic substrate
PY-E	pyridine adsorbed on the edge of a plasmonic substrate
PY-F	pyridine adsorbed on the face of a plasmonic substrate
MTX1, MTX2	conformers of methotrexate

Shape	Number of atoms	Radius (Å)	PRF (eV)	
			Ag	Au
cTO	147	8.66	3.54	-
	309	11.54	3.49	-
	561	14.43	3.46	2.27
	923	17.31	3.47	-
	1415	20.20	3.45	2.23
	2057	23.08	3.44	2.21
	2869	25.97	3.43	2.20
	3871	28.85	3.43	2.19
	5083	31.74	3.43	2.17

	6525	34.62	3.43	2.17
	8217	37.51	3.42	2.17
	10179	40.39	3.42	2.17
Ih	147	8.23	3.64	-
	309	10.98	3.58	-
	561	13.72	3.56	-
	923	16.46	3.54	-
	1415	19.21	3.53	2.29
	2057	21.95	3.52	2.26
	2869	24.69	3.52	2.24
	3871	27.44	3.51	2.23
	5083	30.13	3.51	2.21
	6525	32.87	3.51	2.21
	8217	35.57	3.51	2.21
	10179	38.30	3.51	2.21
i-Dh	85	5.770	3.52	-
	207	8.655	3.48	-
	409	11.54	3.47	-
	711	14.43	3.46	2.31
	1133	17.31	3.45	2.25
	1695	20.20	3.44	2.22
	2417	23.08	3.44	2.20
	3319	25.97	3.43	2.19
	4421	28.85	3.43	2.18
	5743	31.74	3.43	2.18
	7305	34.62	3.42	2.18
	9127	37.50	3.42	2.17

Table S2: Geometrical parameters (number of atoms and radius) of Ag and Au nanoparticles used in this work. The associated plasmon resonance frequencies (PRF) are also given.

Table S3: Geometrical parameters (number of atoms and radius) of graphene disks used in this work. The associated plasmon resonance frequencies (PRF) are also given.

Shape	Number of atoms	Radius (Å)	PRF (eV)
	469	20	0.61
	1909	40	0.46
	4294	60	0.38
	7669	80	0.33
GD	11980	100	0.30
	17269	120	0.28
	23485	140	0.26
	30724	160	0.24

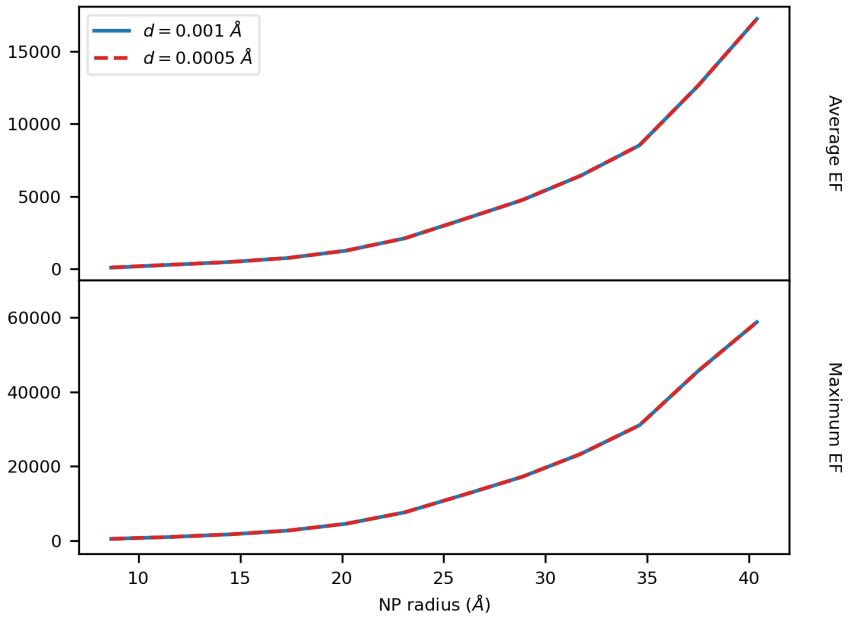

Figure S1: Dependence of AEF and MEF on the numerical differentiation step (d=0.001 Å or d=0.0005 Å) used in the calculation of complex polarizability derivatives. PY adsorbed on Ag cTO systems.

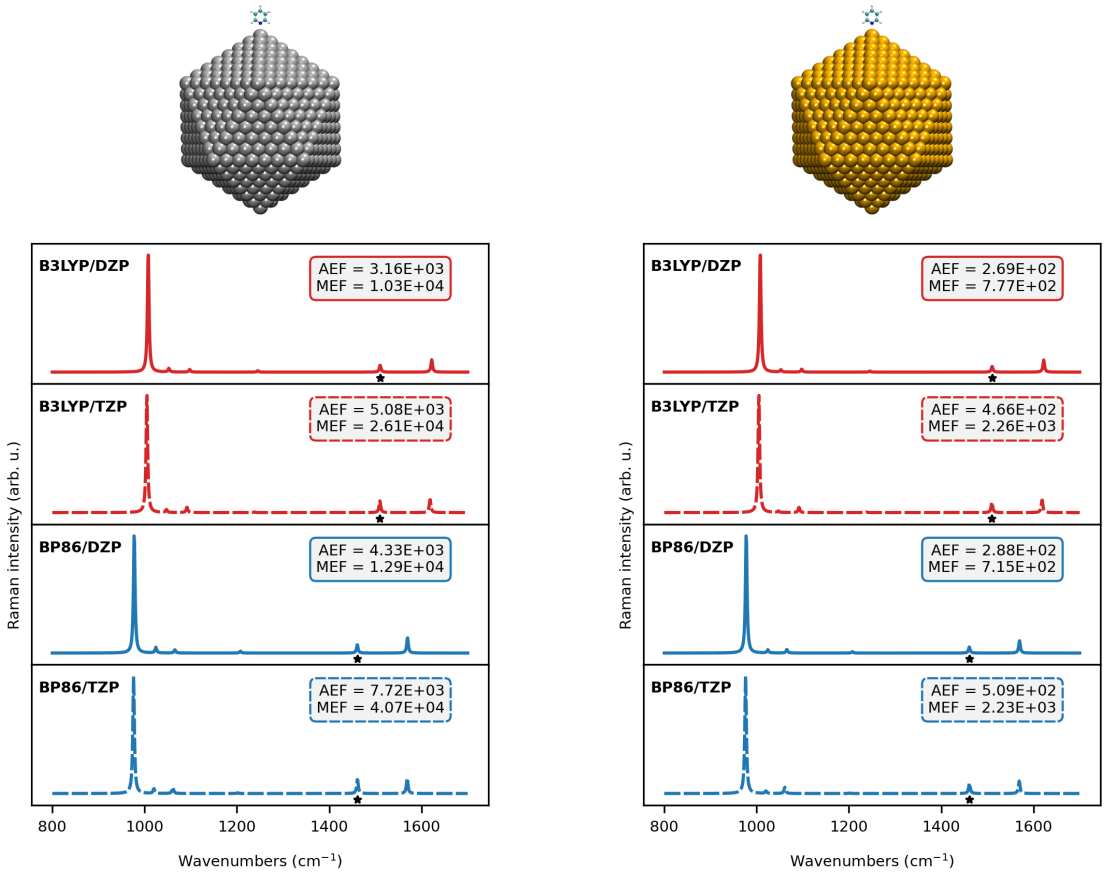

(a) Silver

(b) Gold

Figure S2: Dependence of SERS spectra of PY adsorbed on Ih Ag_{10179} (left) and Au_{10179} (left) on the level of theory. The vibrational frequency associated with the MEF is highlighted by a black star.

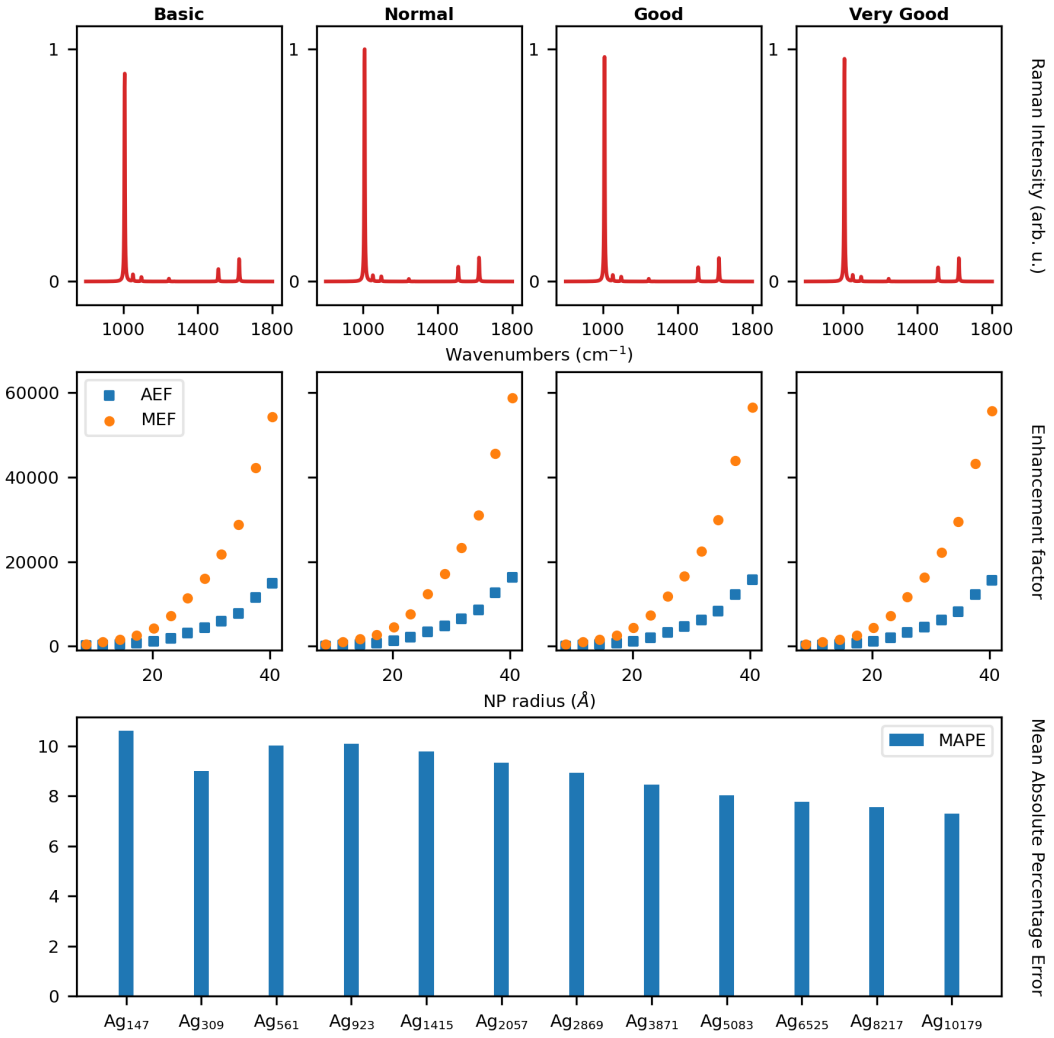

Figure S3: Analysis of the numerical results of the QM/ωFQFμcalculations on the pyridine/Ag system in the cTO morphology with respect to the accuracy of the DFT integration grid. Top panel: normalized SERS spectra of pyridine adsorbed on the largest cTO structure (Ag_{10179}). Middle panel: AEF and MEF with respect to the NP radius. Bottom panel: Mean Absolute Percentage Error (MAPE) of the AEF computed with Numerical Quality Normal with respect to the Numerical Quality VeryGood for each NP size. All the calculations have been performed at the B3LYP/DZP level of theory.

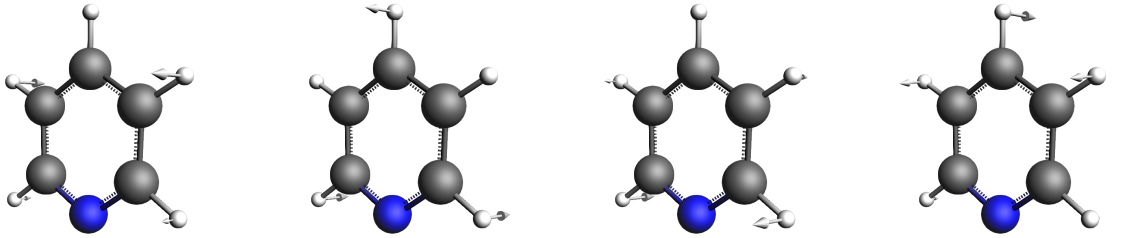

(a) 899 cm^{-1} (b) 956 cm^{-1} (c) 1000 cm^{-1} (d) 1008 cm^{-1}

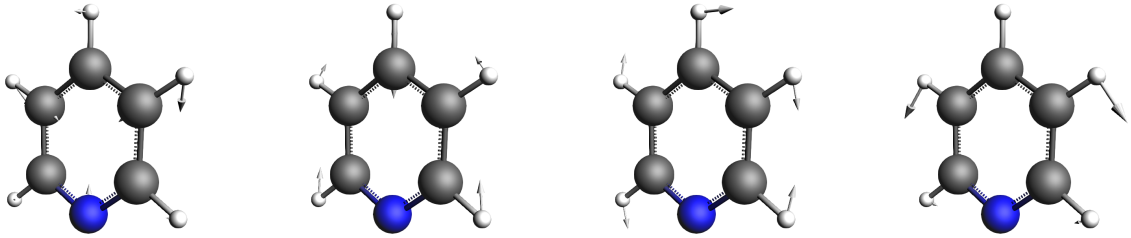

(e) 1008 cm^{-1} (f) 1053 cm^{-1} (g) 1078 cm^{-1} (h) 1098 cm^{-1}

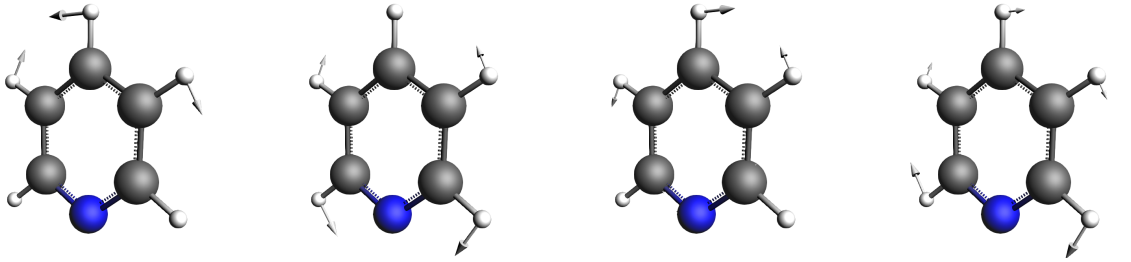

(i) 1181 cm^{-1} (j) 1245 cm^{-1} (k) 1274 cm^{-1} (l) 1388 cm^{-1}

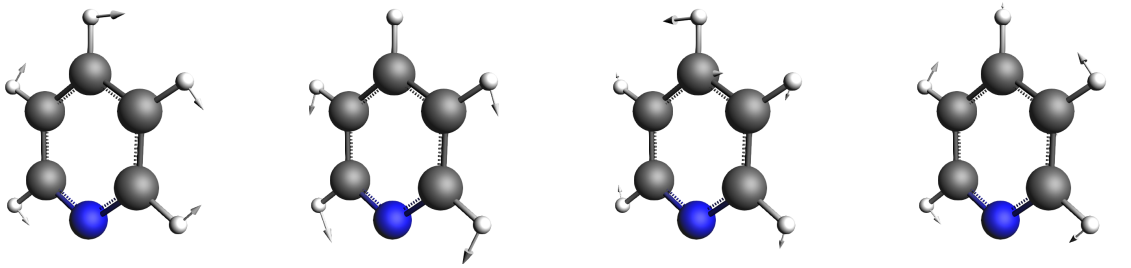

(m) 1473 cm^{-1} (n) 1510 cm^{-1} (o) 1616 cm^{-1} (p) 1622 cm^{-1}

Figure S4: Vibrational normal modes of PY in vacuo calculated at B3LYP/DZP level of theory.

Table S4: Enhancement factors of PY adsorbed on Ag_{10179}, Au_{10179} and $GD_{R=4nm}$.

Wavenumber (cm^{-1})	Ag			Au			GD
	cTO	Ih	i-Dh	cTO	Ih	i-Dh	$R = 40$ Å
898.64	1.35	0.94	2.17	0.04	0.04	0.04	2244.46
956.44	197.71	148.12	226.37	14.18	9.42	8.13	70093.32
999.92	0.90	0.78	1.55	0.01	0.00	0.01	871.76
1007.84	34527.07	6705.84	8218.10	666.05	568.87	443.33	14329.97
1007.85	34828.44	6769.42	8297.90	769.05	573.70	512.51	10043.62
1052.58	1098.16	258.18	427.98	18.90	14.33	15.56	10947.63
1078.03	416.86	57.03	114.94	2.26	1.01	1.47	11209.79
1097.74	30026.28	5966.64	7533.43	714.95	539.00	485.58	8956.54
1181.17	136.27	34.49	53.14	3.44	3.14	2.84	10502.80
1245.18	1718.09	370.70	573.17	33.54	23.59	24.20	9723.70
1274.20	201.59	32.92	55.93	2.70	1.93	1.99	9395.24
1387.78	1993.79	333.95	530.69	0.98	1.21	0.63	12150.37
1472.56	146.16	45.13	43.48	4.47	3.99	3.37	12347.82
1510.30	58738.36	10286.44	11988.96	1106.07	776.91	671.46	10587.33
1615.76	253.79	60.30	93.51	4.11	3.85	3.41	11134.33
1622.08	15235.88	2980.92	3850.27	360.65	268.83	242.29	11183.74
AEF	15218.65	2954.27	3681.90	334.26	249.00	222.84	10520.91

Table S5: Average Enhancement Factors (AEF) and unnormalized Υ^4_{vol} values associated with the external field aligned along the pyridine molecular axis for the case of Ag nanostructures.

Structure	cTO		Ih		i-Dh	
	AEF	Υ^4_{vol}	AEF	Υ^4_{vol}	AEF	Υ^4_{vol}
1	71.49	20842.90	33.48	11764.20	10.41	11764.20
2	270.54	32820.81	136.26	20015.08	43.61	20015.08
3	458.77	55400.45	28.86	32425.23	136.97	32425.23
4	737.30	91651.60	135.04	50134.76	269.37	50134.76
5	1246.36	147054.50	377.41	76897.12	423.28	76897.12
6	2098.16	228347.38	567.14	114971.62	628.98	114971.62
7	3407.28	338220.33	733.55	170596.26	862.55	170596.26
8	4738.77	509599.52	1279.95	242233.09	1261.68	242233.09
9	6427.08	737693.47	1643.09	341402.32	1682.09	155968.96
10	8525.95	1032631.53	2074.32	466134.52	2203.65	222169.56
11	12646.52	1357815.07	2579.17	619243.56	3085.70	619243.56
12	16269.71	1819201.17	3163.13	803358.62	3936.84	803358.62

Table S6: Average Enhancement Factors (AEF) and unnormalized Υ^4_{vol} values associated with the external field aligned along the graphene plane.

Structure	AEF	Υ^4_{vol}
1	9375.43	11260.83
2	10402.45	11876.37
3	6687.45	8079.50
4	4115.87	5417.91
5	3278.32	3696.09
6	2550.34	2153.59
7	1976.16	1666.88
8	1509.64	1605.28

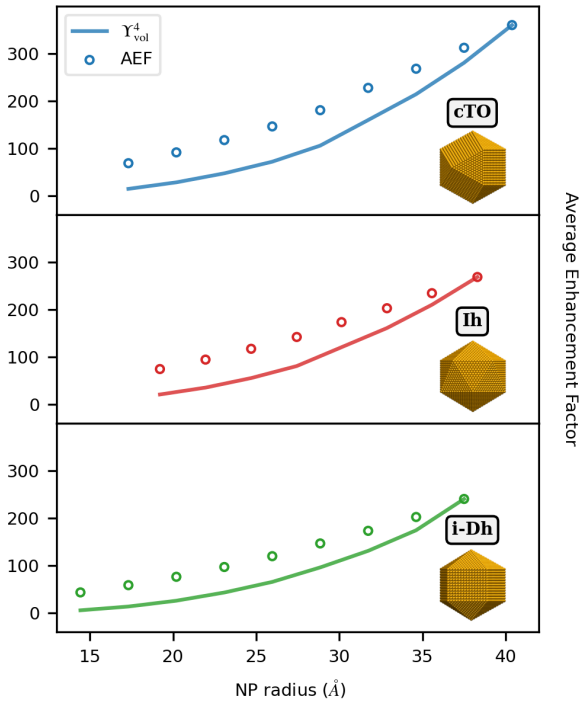

Figure S5: AEF (circles) and Υ^4_{vol} (solid line) as a function of the Au NP radius.

Table S7: Average Enhancement Factors (AEF) and unnormalized Υ^4_{vol} values associated with the external field aligned along the NP axis for different values of the N-Ag distance.

Distance (Å)	AEF	Υ^4_{vol}
3.0	3163.13	803358.62
3.5	1278.98	576391.98
4.0	715.43	419288.14
4.5	448.03	309808.78
5.0	302.43	232696.42
5.5	214.56	177537.96
6.0	157.86	137394.02
7.0	92.49	85348.18
8.0	58.66	55199.50
9.0	39.45	36888.75
10.0	27.81	25331.77

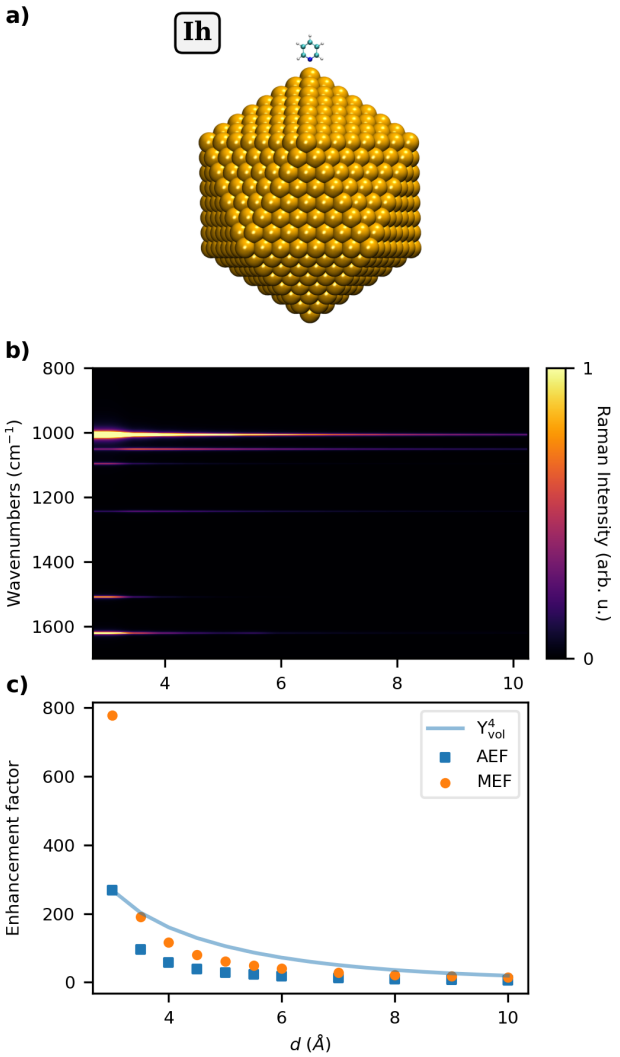

Figure S6: a) Graphical depiction of PY-Au_{10179} Ih system; (b) color plot of normalized SERS spectra as a function of the PY-NP distance d (Å); (c) AEF, MEF and normalized Υ^4_{vol} as a function of d.

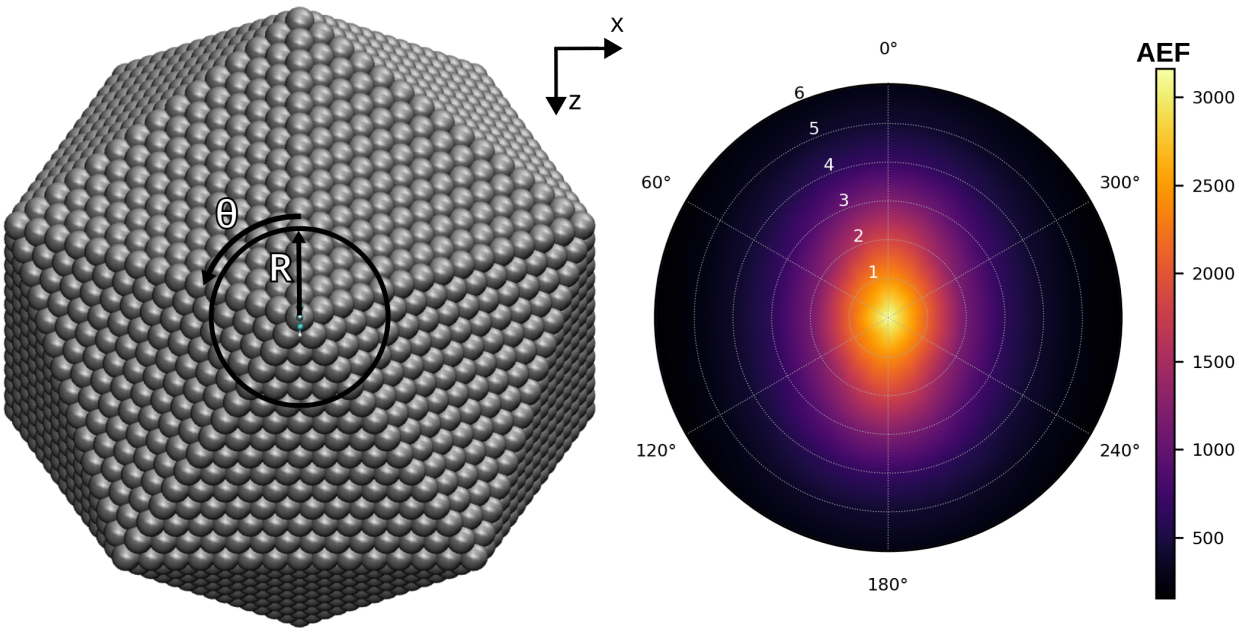

Figure S7: Dependence of the SERS signal on the PY-Ag_{10179} in the Ih morphology on the relative position. Left panel: graphical depiction of the Py-Ag system with indication of the polar coordinates system. Right panel: AEF of the PY-Ag system computed at different values of the radius R (from 1 to 6 Åwith a step of 1 Å) and the angle θ (from 0 to 180 degrees with a step of 10 degrees). Since the system is symmetric, the values from $\theta = 180$ degrees to $\theta = 360$ degrees have been obtained by reflection with respect to the yz plane.

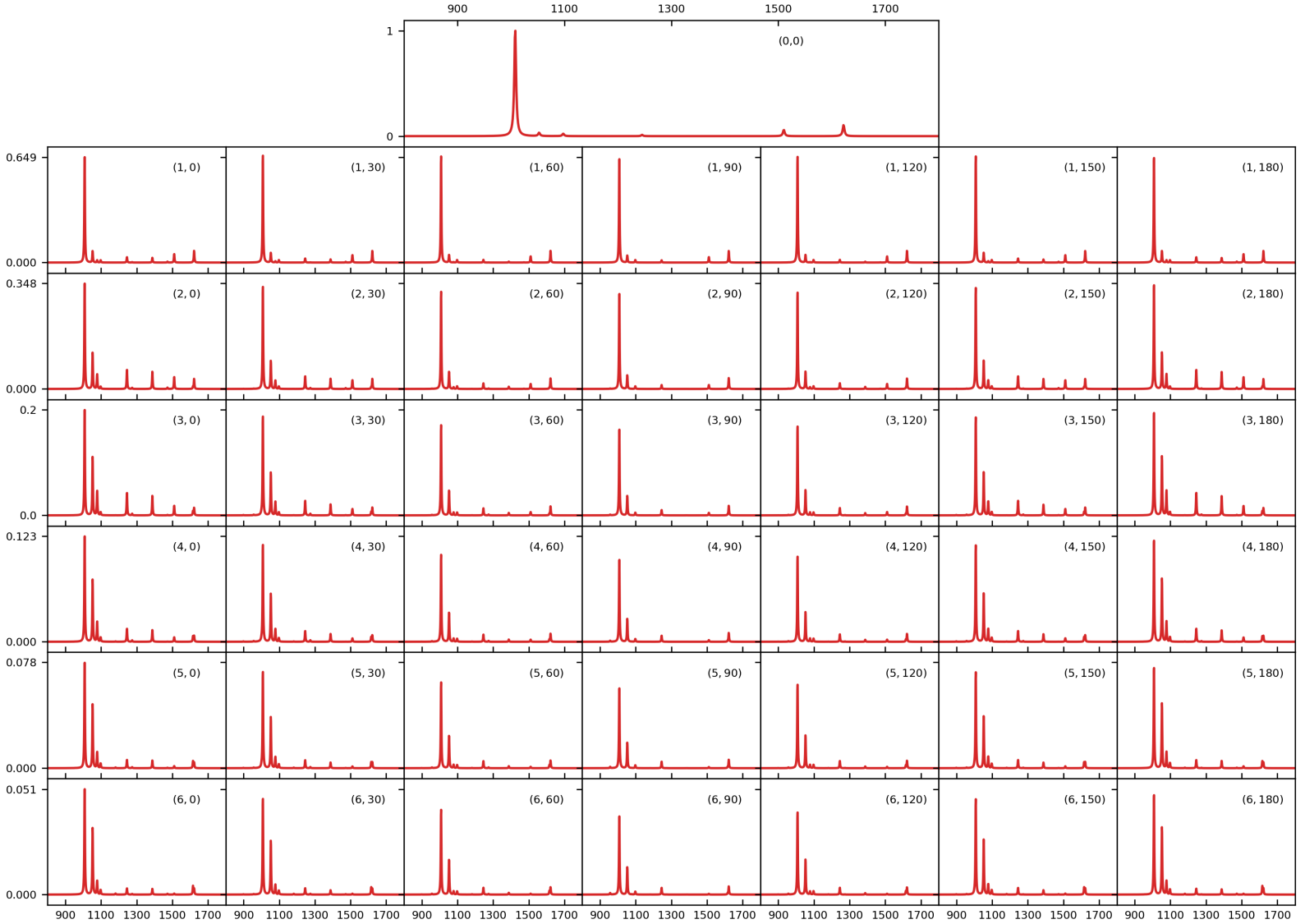

Figure S8: SERS spectra computed at different relative positions of the PY-Ag_{10179} PS in the Ih morphology. Each spectra has been obtained at specific values of the (R, θ) coordinates (see Fig. S7 for the definition) that have been reported in each panel. In the top row the reference spectra on the tip of the Ih system, corresponding to the coordinates $(R, \theta) = (0, 0)$ is reported as a reference.

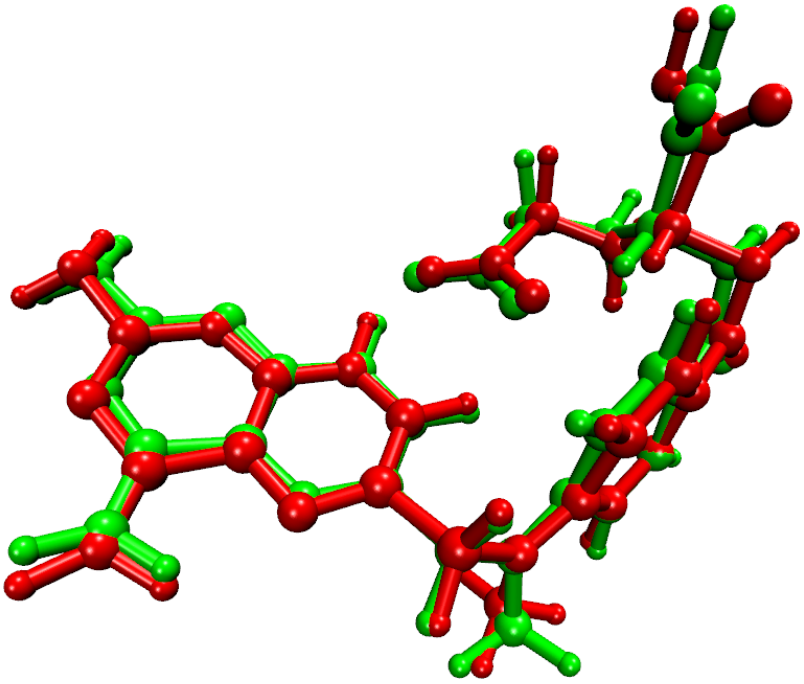

Figure S9: Superposition of MTX1 and MTX2 geometries (see main text).

S1 Dependence of AEF on electric field intensity

Let us consider a molecular system adsorbed on a plasmonic substrate, both interacting with an external field aligned along the z direction. The Raman signal of the molecular vibrational normal modes is enhanced by the presence of the plasmonic substrate as a result of the increase of the incident and/or scattered fields. The vibrational normal modes can be partitioned into three subsets:

- The vibrational normal modes Q_a (total number N_a) whose intensity is dominated by the contribution $\left|\frac{\partial\overline{\alpha}_{zz}(\omega;\omega)}{\partial Q_a}\right|^2$, which are enhanced by the plasmonic substrate via both the incident and scattered fields, yielding a total enhancement factor of $|E|^4$;
- The vibrational normal modes Q_b (total number N_b) whose intensity is dominated by the contribution $\left|\frac{\partial\overline{\alpha}_{iz}(\omega;\omega)}{\partial Q_b}\right|^2$ or $\left|\frac{\partial\overline{\alpha}_{zi}(\omega;\omega)}{\partial Q_b}\right|^2$ with $i \neq z$, which are enhanced by the

plasmonic substrate via the incident or the scattered fields only, yielding a total enhancement factor of $|E|^2$;

- The vibrational normal modes Q_c (total number N_c) whose intensity is dominated by the contribution $\left|\frac{\partial \overline{\alpha}_{ij}(\omega;\omega)}{\partial Q_c}\right|^2$ with $i, j \neq z$, which are not enhanced by the plasmonic substrate.

Therefore, the AEF can be computed as follows:

$$\text{AEF} = \frac{N_a|E|^4 + N_b|E|^2 + N_c}{N_a + N_b + N_c} \overset{|E|^2 \gg 1}{\approx} |E|^4 \frac{N_a}{N_a + N_b + N_c},$$

where the second equality is true when $|E|^2 \gg 1$, thus $|E|^4 \gg |E|^2$. Therefore, the AEF follows the E^4 approximation for strong electric field intensities.

Chapter 10

Summary, Conclusions and Future Perspectives

In this Thesis, a theoretical framework and the related computational tools to describe the optical properties of metal and graphene-based plasmonic substrates, and their interaction with molecules adsorbed on their surfaces, have been developed, implemented, and tested. The work has been divided into two main steps. First, ωFQ[92] has been applied to the calculation of the optical properties of metal and graphene-based nanostructures with complex shapes and to the study of conductivity in polycrystalline graphene samples. Then, ωFQ has been improved to describe interband transitions in noble metals and to compute enhanced Raman spectra of molecular systems adsorbed on plasmonic substrates.

The advantages of using a fully atomistic approach to describe nanomaterials have been demonstrated in Paper 1, Paper 2, and Paper 3. These papers highlight how atomistic models are suitable for describing finite-size nanostructures with surfaces defined by defects, disorder, tips, and edges. Such structures cannot be described by continuum models. Morover, these papers demonstrate that ωFQ returns results in excellent agreement with *ab initio* reference values for both metal and graphene-based substrates. Remarkably, the low computational cost of our method permits us to afford real-size systems, which can not be treated by *ab initio* methods. Therefore, atomistic models appear as a competitive approach between continuum and *ab initio* models, able to combine their strengths in one method. The extreme flexibility and reliability of ωFQ in describing complex nanostructures pave the way for its extensive application to even more complex structures, such as noble metal nanostars NPs[204–206] and graphene nanopores.[207–209]

An important limitation of ωFQ is solved in Paper 4, where ωFQFμ is first introduced. It extends ωFQ to account for interband transitions in noble metal NPs. The paper also highlights the agreement between ωFQFμ results and *ab initio* data, while also showing how the optical properties of the plasmonic substrate change with the size, up to real-size systems. Another important feature of ωFQ(Fμ) resides in its ability to accurately model the physics of metal nanojunctions, capturing the effect of NPs edges and gap's width on the overall optical response of the system and on the electric field enhancement at the *hot spots*. Paper 4 also paves the way to further parameterizations, for instance for aluminum,

iron, and copper. Furthermore, the description of interband transitions could be extended to the case of graphene, so as to model the optical phenomena occurring in twisted bilayer graphene.[210]

Finally, in Paper 5 ωFQ(Fμ) is coupled to a quantum mechanical (QM) Hamiltonian,[194] so to allow the calculation of Raman spectra of molecular targets adsorbed on plasmonic substrates, in a multiscale QM/molecular mechanics (QM/MM) fashion.[97,179] Although surface-enhanced Raman scattering (SERS) is nowadays one of the most used techniques in biosensing, other spectroscopic techniques can exploit plasmons, such as the surface-enhanced infrared absorption (SEIRA)[143] and the surface-enhanced fluorescence (SEF).[144,145] They will all be treated with our model in future works.

Bibliography

[1] Lukas Novotny and Bert Hecht. *Principles of nano-optics*. Cambridge university press, 2012.

[2] William L Barnes, Alain Dereux, and Thomas W Ebbesen. Surface plasmon subwavelength optics. *Nature*, 424(6950):824–830, 2003.

[3] Stefan Alexander Maier. *Plasmonics: fundamentals and applications*. Springer Science & Business Media, 2007.

[4] Stefan A Maier, Mark L Brongersma, Pieter G Kik, Sheffer Meltzer, Ari AG Requicha, and Harry A Atwater. Plasmonics—a route to nanoscale optical devices. *Adv. Mater.*, 13(19):1501–1505, 2001.

[5] Surbhi Lal, Stephan Link, and Naomi J Halas. Nano-optics from sensing to waveguiding. *Nanosci. Technol.*, pages 213–220, 2010.

[6] Jon A Schuller, Edward S Barnard, Wenshan Cai, Young Chul Jun, Justin S White, and Mark L Brongersma. Plasmonics for extreme light concentration and manipulation. *Nat. Mater.*, 9(3):193–204, 2010.

[7] Harry A Atwater and Albert Polman. Plasmonics for improved photovoltaic devices. *Nat. Mater.*, 9(3):205, 2010.

[8] Suljo Linic, Phillip Christopher, and David B Ingram. Plasmonic-metal nanostructures for efficient conversion of solar to chemical energy. *Nat. Mater.*, 10(12):911–921, 2011.

[9] Mark W Knight, Heidar Sobhani, Peter Nordlander, and Naomi J Halas. Photodetection with active optical antennas. *Science*, 332(6030):702–704, 2011.

[10] Palash Bharadwaj, Bradley Deutsch, and Lukas Novotny. Optical antennas. *Adv. Opt. Photonics*, 1(3):438–483, 2009.

[11] Vincenzo Giannini, Antonio I Fernández-Domínguez, Susannah C Heck, and Stefan A Maier. Plasmonic nanoantennas: fundamentals and their use in controlling the radiative properties of nanoemitters. *Chem. Rev.*, 111(6):3888–3912, 2011.

[12] Zhaowei Liu, Hyesog Lee, Yi Xiong, Cheng Sun, and Xiang Zhang. Far-field optical hyperlens magnifying sub-diffraction-limited objects. *Science*, 315(5819):1686–1686, 2007.

[13] Darrick E Chang, Anders S Sørensen, Eugene A Demler, and Mikhail D Lukin. A single-photon transistor using nanoscale surface plasmons. *Nat. Phys.*, 3(11):807, 2007.

[14] Mark S Tame, KR McEnery, ŞK Özdemir, Jinhyoung Lee, Stefan A Maier, and MS Kim. Quantum plasmonics. *Nat. Phys.*, 9(6):329–340, 2013.

[15] Christopher Loo, Amanda Lowery, Naomi Halas, Jennifer West, and Rebekah Drezek. Immunotargeted nanoshells for integrated cancer imaging and therapy. *Nano Lett.*, 5(4):709–711, 2005.

[16] Xiaohua Huang, Ivan H El-Sayed, Wei Qian, and Mostafa A El-Sayed. Cancer cell imaging and photothermal therapy in the near-infrared region by using gold nanorods. *J. Am. Chem. Soc.*, 128(6):2115–2120, 2006.

[17] Prashant K Jain, Kyeong Seok Lee, Ivan H El-Sayed, and Mostafa A El-Sayed. Calculated absorption and scattering properties of gold nanoparticles of different size, shape, and composition: applications in biological imaging and biomedicine. *J. Phys. Chem. B*, 110(14):7238–7248, 2006.

[18] Prashant K Jain, Xiaohua Huang, Ivan H El-Sayed, and Mostafa A El-Sayed. Noble metals on the nanoscale: optical and photothermal properties and some applications in imaging, sensing, biology, and medicine. *Acc. Chem. Res.*, 41(12):1578–1586, 2008.

[19] Erik C Dreaden, Alaaldin M Alkilany, Xiaohua Huang, Catherine J Murphy, and Mostafa A El-Sayed. The golden age: gold nanoparticles for biomedicine. *Chem. Soc. Rev.*, 41(7):2740–2779, 2012.

[20] Jeffrey N Anker, W Paige Hall, Olga Lyandres, Nilam C Shah, Jing Zhao, and Richard P Van Duyne. Biosensing with plasmonic nanosensors. *Nanosci. Technol.*, pages 308–319, 2010.

[21] Katherine A Willets and Richard P Van Duyne. Localized surface plasmon resonance spectroscopy and sensing. *Annu. Rev. Phys. Chem.*, 58(1):267–297, 2007.

[22] Katrin Kneipp, Yang Wang, Harald Kneipp, Lev T Perelman, Irving Itzkan, Ramachandra R Dasari, and Michael S Feld. Single molecule detection using surface-enhanced raman scattering (sers). *Phys. Rev. Lett.*, 78(9):1667, 1997.

[23] Shuming Nie and Steven R Emory. Probing single molecules and single nanoparticles by surface-enhanced raman scattering. *Science*, 275(5303):1102–1106, 1997.

[24] Kevin J Savage, Matthew M Hawkeye, Rubén Esteban, Andrei G Borisov, Javier Aizpurua, and Jeremy J Baumberg. Revealing the quantum regime in tunnelling plasmonics. *Nature*, 491(7425):574–577, 2012.

[25] Darya Radziuk and Helmuth Moehwald. Prospects for plasmonic hot spots in single molecule sers towards the chemical imaging of live cells. *Phys. Chem. Chem. Phys.*, 17(33):21072–21093, 2015.

[26] Calin Hrelescu, Tapan K Sau, Andrey L Rogach, Frank Jäckel, Guillaume Laurent, Ludovic Douillard, and Fabrice Charra. Selective excitation of individual plasmonic hotspots at the tips of single gold nanostars. *Nano Lett.*, 11(2):402–407, 2011.

[27] Renhe Zhang, Yao Zhang, ZC Dong, S Jiang, C Zhang, LG Chen, L Zhang, Y Liao, J Aizpurua, Y ea Luo, et al. Chemical mapping of a single molecule by plasmon-enhanced raman scattering. *Nature*, 498(7452):82–86, 2013.

[28] Joonhee Lee, Kevin T Crampton, Nicholas Tallarida, and V Apkarian. Visualizing vibrational normal modes of a single molecule with atomically confined light. *Nature*, 568(7750):78–82, 2019.

[29] Rohit Chikkaraddy, Bart De Nijs, Felix Benz, Steven J Barrow, Oren A Scherman, Edina Rosta, Angela Demetriadou, Peter Fox, Ortwin Hess, and Jeremy J Baumberg. Single-molecule strong coupling at room temperature in plasmonic nanocavities. *Nature*, 535(7610):127–130, 2016.

[30] Felix Benz, Christos Tserkezis, Lars O Herrmann, Bart De Nijs, Alan Sanders, Daniel O Sigle, Laurynas Pukenas, Stephen D Evans, Javier Aizpurua, and Jeremy J Baumberg. Nanooptics of molecular-shunted plasmonic nanojunctions. *Nano Lett.*, 15(1):669–674, 2015.

[31] Judith Langer, Dorleta Jimenez de Aberasturi, Javier Aizpurua, Ramon A Alvarez-Puebla, Baptiste Auguié, Jeremy J Baumberg, Guillermo C Bazan, Steven EJ Bell, Anja Boisen, Alexandre G Brolo, et al. Present and future of surface-enhanced raman scattering. *ACS Nano*, 14(1):28–117, 2019.

[32] Felix Benz, Mikolaj K Schmidt, Alexander Dreismann, Rohit Chikkaraddy, Yao Zhang, Angela Demetriadou, Cloudy Carnegie, Hamid Ohadi, Bart De Nijs, Ruben Esteban, et al. Single-molecule optomechanics in "picocavities". *Science*, 354(6313):726–729, 2016.

[33] Jeremy J Baumberg, Javier Aizpurua, Maiken H Mikkelsen, and David R Smith. Extreme nanophotonics from ultrathin metallic gaps. *Nat. Mater.*, 18(7):668–678, 2019.

[34] Raoul M Stöckle, Yung Doug Suh, Volker Deckert, and Renato Zenobi. Nanoscale chemical analysis by tip-enhanced raman spectroscopy. *Chem. Phys. Lett.*, 318(1-3):131–136, 2000.

[35] Mark S Anderson. Locally enhanced raman spectroscopy with an atomic force microscope. *Appl. Phys. Lett.*, 76(21):3130–3132, 2000.

[36] Felix Benz, Rohit Chikkaraddy, Andrew Salmon, Hamid Ohadi, Bart De Nijs, Jan Mertens, Cloudy Carnegie, Richard W Bowman, and Jeremy J Baumberg. Sers of individual nanoparticles on a mirror: size does matter, but so does shape. *J. Phys. Chem. Lett.*, 7(12):2264–2269, 2016.

[37] Andreas Trügler. *Optical properties of metallic nanoparticles*. Springer, 2011.

[38] Kostya S Novoselov, Andre K Geim, Sergei V Morozov, De-eng Jiang, Yanshui Zhang, Sergey V Dubonos, Irina V Grigorieva, and Alexandr A Firsov. Electric field effect in atomically thin carbon films. *Science*, 306(5696):666–669, 2004.

[39] Kostya S Novoselov, Andre K Geim, Sergei Vladimirovich Morozov, Dingde Jiang, Michail I Katsnelson, IVa Grigorieva, SVb Dubonos, and andAA Firsov. Two-dimensional gas of massless dirac fermions in graphene. *Nature*, 438(7065):197–200, 2005.

[40] Andre K Geim and Konstantin S Novoselov. The rise of graphene. In *Nanosci. Technol.*, pages 11–19. World Scientific, 2010.

[41] Frank HL Koppens, Darrick E Chang, and F Javier García de Abajo. Graphene plasmonics: a platform for strong light–matter interactions. *Nano Lett.*, 11(8):3370–3377, 2011.

[42] Francesco Bonaccorso, Zhipei Sun, TA Hasan, and AC Ferrari. Graphene photonics and optoelectronics. *Nat. Photonics*, 4(9):611–622, 2010.

[43] Ashkan Vakil and Nader Engheta. Transformation optics using graphene. *Science*, 332(6035):1291–1294, 2011.

[44] Alexander N Grigorenko, Marco Polini, and KS Novoselov. Graphene plasmonics. *Nat. Photonics*, 6(11):749–758, 2012.

[45] Fengnian Xia, Thomas Mueller, Yu-ming Lin, Alberto Valdes-Garcia, and Phaedon Avouris. Ultrafast graphene photodetector. *Nat. Nanotechnol.*, 4(12):839–843, 2009.

[46] FHL Koppens, T Mueller, Ph Avouris, AC Ferrari, MS Vitiello, and M Polini. Photodetectors based on graphene, other two-dimensional materials and hybrid systems. *Nat. Nanotechnol.*, 9(10):780–793, 2014.

[47] Nikitas Papasimakis, Zhiqiang Luo, Ze Xiang Shen, Francesco De Angelis, Enzo Di Fabrizio, Andrey E Nikolaenko, and Nikolay I Zheludev. Graphene in a photonic metamaterial. *Opt. Express*, 18(8):8353–8359, 2010.

[48] Fred Schedin, Elefterios Lidorikis, Antonio Lombardo, Vasyl G Kravets, Andre K Geim, Alexander N Grigorenko, Kostya S Novoselov, and Andrea C Ferrari. Surface-enhanced raman spectroscopy of graphene. *ACS Nano*, 4(10):5617–5626, 2010.

[49] Weigao Xu, Xi Ling, Jiaqi Xiao, Mildred S Dresselhaus, Jing Kong, Hongxing Xu, Zhongfan Liu, and Jin Zhang. Surface enhanced raman spectroscopy on a flat graphene surface. *Proc. Natl. Acad. Sci. U.S.A.*, 109(24):9281–9286, 2012.

[50] Guosong Hong, Shuo Diao, Alexander L Antaris, and Hongjie Dai. Carbon nanomaterials for biological imaging and nanomedicinal therapy. *Chem. Rev.*, 115(19):10816–10906, 2015.

[51] Weigao Xu, Nannan Mao, and Jin Zhang. Graphene: a platform for surface-enhanced raman spectroscopy. *Small*, 9(8):1206–1224, 2013.

[52] Xi Ling, Liming Xie, Yuan Fang, Hua Xu, Haoli Zhang, Jing Kong, Mildred S Dresselhaus, Jin Zhang, and Zhongfan Liu. Can graphene be used as a substrate for raman enhancement? *Nano Lett.*, 10(2):553–561, 2010.

[53] Viktor Myroshnychenko, Jessica Rodríguez-Fernández, Isabel Pastoriza-Santos, Alison M Funston, Carolina Novo, Paul Mulvaney, Luis M Liz-Marzán, and F Javier García De Abajo. Modelling the optical response of gold nanoparticles. *Chem. Soc. Rev.*, 37(9):1792–1805, 2008.

[54] Mikael Kuisma, Arto Sakko, Tuomas P Rossi, Ask H Larsen, Jussi Enkovaara, Lauri Lehtovaara, and Tapio T Rantala. Localized surface plasmon resonance in silver nanoparticles: Atomistic first-principles time-dependent density-functional theory calculations. *Phys. Rev. B*, 91(11):115431, 2015.

[55] Kenji Iida, Masashi Noda, Kazuya Ishimura, and Katsuyuki Nobusada. First-principles computational visualization of localized surface plasmon resonance in gold nanoclusters. *J. Phys. Chem. A*, 118(47):11317–11322, 2014.

[56] Yu Shao, Jing Jing Yang, and Ming Huang. A review of computational electromagnetic methods for graphene modeling. *Int. J. Antennas Propag.*, 2016, 2016.

[57] Sukosin Thongrattanasiri, Alejandro Manjavacas, and F Javier García de Abajo. Quantum finite-size effects in graphene plasmons. *ACS Nano*, 6(2):1766–1775, 2012.

[58] Gustav Mie. Beiträge zur optik trüber medien, speziell kolloidaler metallösungen. *Ann. Phys.*, 330(3):377–445, 1908.

[59] Hendrik Christoffel Hulst and Hendrik C van de Hulst. *Light scattering by small particles*. Courier Corporation, 1981.

[60] Bruce T Draine and Piotr J Flatau. Discrete-dipole approximation for scattering calculations. *J. Opt. Soc. Am. A*, 11(4):1491–1499, 1994.

[61] Mark W Knight, Nicholas S King, Lifei Liu, Henry O Everitt, Peter Nordlander, and Naomi J Halas. Aluminum for plasmonics. *ACS Nano*, 8(1):834–840, 2014.

[62] Yeon-Hwa Kim, Hongjin Choi, Jeahoon Cho, and Kyung-Young Jung. Fdtd modeling for the accurate electromagnetic wave analysis of graphene. *J. Electr. Eng. Technol.*, 15(3):1281–1286, 2020.

[63] FJ Garcia De Abajo and A Howie. Retarded field calculation of electron energy loss in inhomogeneous dielectrics. *Phys. Rev. B*, 65(11):115418, 2002.

[64] Ulrich Hohenester and Andreas Trügler. Mnpbem–a matlab toolbox for the simulation of plasmonic nanoparticles. *Comput. Phys. Commun.*, 183(2):370–381, 2012.

[65] Ulrich Hohenester. Simulating electron energy loss spectroscopy with the mnpbem toolbox. *Comput. Phys. Commun.*, 185(3):1177–1187, 2014.

[66] S Corni and J Tomasi. Enhanced response properties of a chromophore physisorbed on a metal particle. *J. Chem. Phys.*, 114(8):3739–3751, 2001.

[67] S Corni and J Tomasi. Surface enhanced raman scattering from a single molecule adsorbed on a metal particle aggregate: A theoretical study. *J. Chem. Phys.*, 116(3):1156–1164, 2002.

[68] Silvio Pipolo and Stefano Corni. Real-time description of the electronic dynamics for a molecule close to a plasmonic nanoparticle. *J. Phys. Chem. C*, 120(50):28774–28781, 2016.

[69] Giulia Dall'Osto, Gabriel Gil, Silvio Pipolo, and Stefano Corni. Real-time dynamics of plasmonic resonances in nanoparticles described by a boundary element method with generic dielectric function. *J. Chem. Phys.*, 153(18):184114, 2020.

[70] Jacopo Marcheselli, Denis Chateau, Frederic Lerouge, Patrice Baldeck, Chantal Andraud, Stephane Parola, Stefano Baroni, Stefano Corni, Marco Garavelli, and Ivan Rivalta. Simulating plasmon resonances of gold nanoparticles with bipyramidal shapes by boundary element methods. *J. Chem. Theory Comput.*, 16(6):3807–3815, 2020.

[71] Ulrich Hohenester and Joachim Krenn. Surface plasmon resonances of single and coupled metallic nanoparticles: A boundary integral method approach. *Phys. Rev. B*, 72(19):195429, 2005.

[72] Ruben Esteban, Andrei G Borisov, Peter Nordlander, and Javier Aizpurua. Bridging quantum and classical plasmonics with a quantum-corrected model. *Nat. Commun.*, 3(1):1–9, 2012.

[73] Marc Barbry, P Koval, Federico Marchesin, Ruben Esteban, Andrei G Borisov, Javier Aizpurua, and Daniel Sánchez-Portal. Atomistic near-field nanoplasmonics: reaching atomic-scale resolution in nanooptics. *Nano Lett.*, 15(5):3410–3419, 2015.

[74] Mattin Urbieta, Marc Barbry, Yao Zhang, Peter Koval, Daniel Sánchez-Portal, Nerea Zabala, and Javier Aizpurua. Atomic-scale lightning rod effect in plasmonic picocavities: a classical view to a quantum effect. *ACS Nano*, 12(1):585–595, 2018.

[75] Sukosin Thongrattanasiri and F Javier García de Abajo. Optical field enhancement by strong plasmon interaction in graphene nanostructures. *Phys. Rev. Lett.*, 110(18):187401, 2013.

[76] Stephanie Reich, Janina Maultzsch, Christian Thomsen, and Pablo Ordejon. Tight-binding description of graphene. *Phys. Rev. B*, 66(3):035412, 2002.

[77] Deborah Prezzi, Daniele Varsano, Alice Ruini, Andrea Marini, and Elisa Molinari. Optical properties of graphene nanoribbons: The role of many-body effects. *Phys. Rev. B*, 77(4):041404, 2008.

[78] Rajarshi Sinha-Roy, Pablo García-González, Hans-Christian Weissker, Frank Rabilloud, and Antonio I. Fernández-Domínguez. Classical and ab initio plasmonics meet at sub-nanometric noble metal rods. *ACS Photonics*, 4(6):1484–1493, 2017.

[79] Tuomas P Rossi, Asier Zugarramurdi, Martti J Puska, and Risto M Nieminen. Quantized evolution of the plasmonic response in a stretched nanorod. *Phys. Rev. Lett.*, 115(23):236804, 2015.

[80] Giovanni Barcaro, Luca Sementa, Alessandro Fortunelli, and Mauro Stener. Optical properties of silver nanoshells from time-dependent density functional theory calculations. *J. Phys. Chem. C*, 118(23):12450–12458, 2014.

[81] Giovanni Barcaro, Michel Broyer, Nicola Durante, Alessandro Fortunelli, and Mauro Stener. Alloying effects on the optical properties of ag–au nanoclusters from tddft calculations. *J. Phys. Chem. C*, 115(49):24085–24091, 2011.

[82] Giovanni Barcaro, Luca Sementa, Alessandro Fortunelli, and Mauro Stener. Optical properties of nanoalloys. *Phys. Chem. Chem. Phys.*, 17(42):27952–27967, 2015.

[83] Nicola Durante, Alessandro Fortunelli, Michel Broyer, and Mauro Stener. Optical properties of au nanoclusters from td-dft calculations. *J. Phys. Chem. C*, 115(14):6277–6282, 2011.

[84] GiovanniMaria Piccini, Remco WA Havenith, Ria Broer, and Mauro Stener. Gold nanowires: a time-dependent density functional assessment of plasmonic behavior. *J. Phys. Chem. C*, 117(33):17196–17204, 2013.

[85] Oscar Baseggio, Giovanna Fronzoni, and Mauro Stener. A new time dependent density functional algorithm for large systems and plasmons in metal clusters. *J. Chem. Phys.*, 143(2):024106, 2015.

[86] Nicola Danielis, Lorena Vega, Giovanna Fronzoni, Mauro Stener, Albert Bruix, and Konstantin M Neyman. Agpd, aupd, and aupt nanoalloys with ag-or au-rich

compositions: Modeling chemical ordering and optical properties. *J. Phys. Chem. C*, 125(31):17372–17384, 2021.

[87] Xing Chen, Justin E Moore, Meserret Zekarias, and Lasse Jensen. Atomistic electrodynamics simulations of bare and ligand-coated nanoparticles in the quantum size regime. *Nat. Commun.*, 6:8921, 2015.

[88] Xing Chen and Lasse Jensen. Morphology dependent near-field response in atomistic plasmonic nanocavities. *Nanoscale*, 10(24):11410–11417, 2018.

[89] Xing Chen, Pengchong Liu, and Lasse Jensen. Atomistic electrodynamics simulations of plasmonic nanoparticles. *J. Phys. D: Appl. Phys.*, 52(36):363002, 2019.

[90] Lin Lin Jensen and Lasse Jensen. Electrostatic interaction model for the calculation of the polarizability of large noble metal nanoclusters. *J. Phys. Chem. C*, 112(40):15697–15703, 2008.

[91] Lin Lin Jensen and Lasse Jensen. Atomistic electrodynamics model for optical properties of silver nanoclusters. *J. Phys. Chem. C*, 113(34):15182–15190, 2009.

[92] Tommaso Giovannini, Marta Rosa, Stefano Corni, and Chiara Cappelli. A classical picture of subnanometer junctions: an atomistic drude approach to nanoplasmonics. *Nanoscale*, 11(13):6004–6015, 2019.

[93] Tommaso Giovannini, Luca Bonatti, Marco Polini, and Chiara Cappelli. Graphene plasmonics: Fully atomistic approach for realistic structures. *J. Phys. Chem. Lett.*, 11(18):7595–7602, 2020.

[94] Steven W Rick, Steven J Stuart, Joel S Bader, and BJ Berne. Fluctuating charge force fields for aqueous solutions. *J. Mol. Liq.*, 65:31–40, 1995.

[95] Steven W Rick and BJ Berne. Dynamical fluctuating charge force fields: the aqueous solvation of amides. *J. Am. Chem. Soc.*, 118(3):672–679, 1996.

[96] Tommaso Giovannini, Franco Egidi, and Chiara Cappelli. Molecular spectroscopy of aqueous solutions: a theoretical perspective. *Chem. Soc. Rev.*, 49(16):5664–5677, 2020.

[97] Chiara Cappelli. Integrated qm/polarizable mm/continuum approaches to model chiroptical properties of strongly interacting solute–solvent systems. *Int. J. Quantum Chem.*, 116(21):1532–1542, 2016.

[98] Paul Drude. Zur elektronentheorie der metalle. *Ann. Phys.*, 306(3):566–613, 1900.

[99] Tommaso Giovannini, Luca Bonatti, Piero Lafiosca, Luca Nicoli, Matteo Castagnola, Pablo Grobas Illobre, Stefano Corni, and Chiara Cappelli. Do we really need quantum mechanics to describe plasmonic properties of metal nanostructures? *ACS photonics*, 9(9):3025–3034, 2022.

[100] Piero Lafiosca, Luca Nicoli, Luca Bonatti, Tommaso Giovannini, Stefano Corni, and Chiara Cappelli. Qm/classical modeling of surface enhanced raman scattering based on atomistic electromagnetic models. *submitted*.

[101] Luca Bonatti, Luca Nicoli, Tommaso Giovannini, and Chiara Cappelli. In silico design of graphene plasmonic hot-spots. *Nanoscale Adv.*, 4(10):2294–2302, 2022.

[102] Luca Bonatti, Gabriel Gil, Tommaso Giovannini, Stefano Corni, and Chiara Cappelli. Plasmonic resonances of metal nanoparticles: atomistic vs. continuum approaches. *Front. Chem.*, 8:340, 2020.

[103] Andreas Trügler. *Optical properties of metallic nanoparticles: basic principles and simulation*, volume 232. Springer, 2016.

[104] AH Castro Neto, Francisco Guinea, Nuno MR Peres, Kostya S Novoselov, and Andre K Geim. The electronic properties of graphene. *Rev. Mod. Phys.*, 81(1):109, 2009.

[105] Tony Low and Phaedon Avouris. Graphene plasmonics for terahertz to mid-infrared applications. *ACS Nano*, 8(2):1086–1101, 2014.

[106] NV Smith. Classical generalization of the drude formula for the optical conductivity. *Phys. Rev. B*, 64(15):155106, 2001.

[107] Peter B Johnson and R-WJPrB Christy. Optical constants of the noble metals. *Phys. Rev. B*, 6(12):4370, 1972.

[108] HRPH Ehrenreich and HR Philipp. Optical properties of ag and cu. *Phys. Rev.*, 128(4):1622, 1962.

[109] H Ehrenreich, HR Philipp, and B Segall. Optical properties of aluminum. *Phys. Rev.*, 132(5):1918, 1963.

[110] Aleksandar D Rakić, Aleksandra B Djurišić, Jovan M Elazar, and Marian L Majewski. Optical properties of metallic films for vertical-cavity optoelectronic devices. *Appl. Opt.*, 37(22):5271–5283, 1998.

[111] MI Marković and AD Rakić. Determination of optical properties of aluminium including electron reradiation in the lorentz-drude model. *Opt. Laser Technol.*, 22(6):394–398, 1990.

[112] Alexandre Vial, Anne-Sophie Grimault, Demetrio Macías, Dominique Barchiesi, and Marc Lamy De La Chapelle. Improved analytical fit of gold dispersion: Application to the modeling of extinction spectra with a finite-difference time-domain method. *Phys. Rev. B*, 71(8):085416, 2005.

[113] R Brendel and D Bormann. An infrared dielectric function model for amorphous solids. *J. Appl. Phys.*, 71(1):1–6, 1992.

[114] Tasnim Gharbi, Dominique Barchiesi, Sameh Kessentini, and Ramzi Maalej. Fitting optical properties of metals by drude-lorentz and partial-fraction models in the [0.5; 6] ev range. *Opt. Mater. Express.*, 10(5):1129–1162, 2020.

[115] Pablo G Etchegoin, EC Le Ru, and M Meyer. An analytic model for the optical properties of gold. *J. Chem. Phys.*, 125(16):164705, 2006.

[116] Martin G Blaber, Anne-Isabelle Henry, Julia M Bingham, George C Schatz, and Richard P Van Duyne. Lspr imaging of silver triangular nanoprisms: correlating scattering with structure using electrodynamics for plasmon lifetime analysis. *J. Phys. Chem. C*, 116(1):393–403, 2012.

[117] Hannah J Joyce, Jessica L Boland, Christopher L Davies, Sarwat A Baig, and Michael B Johnston. A review of the electrical properties of semiconductor nanowires: insights gained from terahertz conductivity spectroscopy. *Semicond. Sci. Technol.*, 31(10):103003, 2016.

[118] DG Cooke, AN MacDonald, A Hryciw, J Wang, Q Li, A Meldrum, and FA Hegmann. Transient terahertz conductivity in photoexcited silicon nanocrystal films. *Phys. Rev. B*, 73(19):193311, 2006.

[119] Han-Kwang Nienhuys and Villy Sundström. Influence of plasmons on terahertz conductivity measurements. *Appl. Phys. Lett.*, 87(1):012101, 2005.

[120] Hynek Němec, Petr Kužel, and Villy Sundström. Far-infrared response of free charge carriers localized in semiconductor nanoparticles. *Phys. Rev. B*, 79(11):115309, 2009.

[121] Tyler L Cocker, Devin Baillie, Miles Buruma, Lyubov V Titova, Richard D Sydora, Frank Marsiglio, and Frank A Hegmann. Microscopic origin of the drude-smith model. *Phys. Rev. B*, 96(20):205439, 2017.

[122] Mark A Ordal, Robert J Bell, Ralph W Alexander, Larry L Long, and Marvin R Querry. Optical properties of fourteen metals in the infrared and far infrared: Al, co, cu, au, fe, pb, mo, ni, pd, pt, ag, ti, v, and w. *Appl. Opt.*, 24(24):4493–4499, 1985.

[123] John David Jackson. Classical electrodynamics, 1999.

[124] Andre K Geim and Konstantin S Novoselov. The rise of graphene. *Nat. Mater.*, 6(3):183–191, 2007.

[125] Harold W Kroto, James R Heath, Sean C O'Brien, Robert F Curl, and Richard E Smalley. C60: Buckminsterfullerene. *Nature*, 318(6042):162–163, 1985.

[126] Sumio Iijima. Helical microtubules of graphitic carbon. *Nature*, 354(6348):56–58, 1991.

[127] Sumio Iijima. Carbon nanotubes: past, present, and future. *Phys. B: Condens. Matter*, 323(1-4):1–5, 2002.

[128] Andrea C Ferrari, Francesco Bonaccorso, Vladimir Fal'Ko, Konstantin S Novoselov, Stephan Roche, Peter Bøggild, Stefano Borini, Frank HL Koppens, Vincenzo Palermo, Nicola Pugno, et al. Science and technology roadmap for graphene, related two-dimensional crystals, and hybrid systems. *Nanoscale*, 7(11):4598–4810, 2015.

[129] Philip Richard Wallace. The band theory of graphite. *Phys. Rev.*, 71(9):622, 1947.

[130] RS Deacon, K-C Chuang, RJ Nicholas, KS Novoselov, and AK Geim. Cyclotron resonance study of the electron and hole velocity in graphene monolayers. *Phys. Rev. B*, 76(8):081406, 2007.

[131] Choongyu Hwang, David A Siegel, Sung-Kwan Mo, William Regan, Ariel Ismach, Yuegang Zhang, Alex Zettl, and Alessandra Lanzara. Fermi velocity engineering in graphene by substrate modification. *Sci. Rep.*, 2(1):1–4, 2012.

[132] Kerson Huang. *Introduction to statistical physics*. Chapman and Hall/CRC, 2009.

[133] MF Craciun, S Russo, M Yamamoto, and S Tarucha. Tuneable electronic properties in graphene. *Nano Today*, 6(1):42–60, 2011.

[134] Hugen Yan, Xuesong Li, Bhupesh Chandra, George Tulevski, Yanqing Wu, Marcus Freitag, Wenjuan Zhu, Phaedon Avouris, and Fengnian Xia. Tunable infrared plasmonic devices using graphene/insulator stacks. *Nat. Nanotechnol.*, 7(5):330–334, 2012.

[135] Sukosin Thongrattanasiri, Frank HL Koppens, and F Javier Garcia De Abajo. Complete optical absorption in periodically patterned graphene. *Phys. Rev. Lett.*, 108(4):047401, 2012.

[136] Long Ju, Baisong Geng, Jason Horng, Caglar Girit, Michael Martin, Zhao Hao, Hans A Bechtel, Xiaogan Liang, Alex Zettl, Y Ron Shen, et al. Graphene plasmonics for tunable terahertz metamaterials. *Nat. Nanotechnol.*, 6(10):630–634, 2011.

[137] SJ Allen Jr, HL Störmer, and JCM Hwang. Dimensional resonance of the two-dimensional electron gas in selectively doped gaas/algaas heterostructures. *Phys. Rev. B*, 28(8):4875, 1983.

[138] Kin Fai Mak, Matthew Y Sfeir, Yang Wu, Chun Hung Lui, James A Misewich, and Tony F Heinz. Measurement of the optical conductivity of graphene. *Phys. Rev. Lett.*, 101(19):196405, 2008.

[139] Rahul Raveendran Nair, Peter Blake, Alexander N Grigorenko, Konstantin S Novoselov, Tim J Booth, Tobias Stauber, Nuno MR Peres, and Andre K Geim. Fine structure constant defines visual transparency of graphene. *Science*, 320(5881):1308–1308, 2008.

[140] Alexey B Kuzmenko, Erik Van Heumen, Fabrizio Carbone, and Dirk Van Der Marel. Universal optical conductance of graphite. *Phys. Rev. Lett.*, 100(11):117401, 2008.

[141] ZhiQuan Li, Eric A Henriksen, Zhifang Jiang, Zhao Hao, Michael C Martin, Phaly Kim, Horst Ludwig Stormer, and Dimitri N Basov. Dirac charge dynamics in graphene by infrared spectroscopy. *Nat. Phys.*, 4(7):532–535, 2008.

[142] Richard P Leavitt and JW Little. Absorption and emission of radiation by plasmons in two-dimensional electron-gas disks. *Phys. Rev. B*, 34(4):2450, 1986.

[143] Masatoshi Osawa. Surface-enhanced infrared absorption. In *Near-field optics and surface plasmon polaritons*, pages 163–187. Springer, 2001.

[144] Emmanuel Fort and Samuel Grésillon. Surface enhanced fluorescence. *J. Phys. D: Appl. Phys.*, 41(1):013001, 2007.

[145] Jian-Feng Li, Chao-Yu Li, and Ricardo F Aroca. Plasmon-enhanced fluorescence spectroscopy. *Chem. Soc. Rev.*, 46(13):3962–3979, 2017.

[146] David L Jeanmaire and Richard P Van Duyne. Surface raman spectroelectrochemistry: Part i. heterocyclic, aromatic, and aliphatic amines adsorbed on the anodized silver electrode. *J. Electroanal. Chem. Interfacial Electrochem.*, 84(1):1–20, 1977.

[147] M Grant Albrecht and J Alan Creighton. Anomalously intense raman spectra of pyridine at a silver electrode. *J. Am. Chem. Soc.*, 99(15):5215–5217, 1977.

[148] Alan Campion and Patanjali Kambhampati. Surface-enhanced raman scattering. *Chem. Soc. Rev.*, 27(4):241–250, 1998.

[149] Karen E Shafer-Peltier, Christy L Haynes, Matthew R Glucksberg, and Richard P Van Duyne. Toward a glucose biosensor based on surface-enhanced raman scattering. *J. Am. Chem. Soc.*, 125(2):588–593, 2003.

[150] Jonathan M Yuen, Nilam C Shah, Joseph T Walsh Jr, Matthew R Glucksberg, and Richard P Van Duyne. Transcutaneous glucose sensing by surface-enhanced spatially offset raman spectroscopy in a rat model. *Anal. Chem.*, 82(20):8382–8385, 2010.

[151] Xiaoyu Zhang, Matthew A Young, Olga Lyandres, and Richard P Van Duyne. Rapid detection of an anthrax biomarker by surface-enhanced raman spectroscopy. *J. Am. Chem. Soc.*, 127(12):4484–4489, 2005.

[152] YunWei Charles Cao, Rongchao Jin, and Chad A Mirkin. Nanoparticles with raman spectroscopic fingerprints for dna and rna detection. *Science*, 297(5586):1536–1540, 2002.

[153] Derek Albert Long and DA Long. *The Raman effect: a unified treatment of the theory of Raman scattering by molecules*, volume 8. Wiley Chichester, 2002.

[154] Katrin Kneipp, Harald Kneipp, Irving Itzkan, Ramachandra R Dasari, and Michael S Feld. Surface-enhanced raman scattering and biophysics. *J. Phys. Condens. Matter*, 14(18):R597, apr 2002.

[155] Bhavya Sharma, Renee R Frontiera, Anne-Isabelle Henry, Emilie Ringe, and Richard P Van Duyne. Sers: Materials, applications, and the future. *Mater. Today*, 15(1-2):16–25, 2012.

[156] Roberto Pilot, Raffaella Signorini, Christian Durante, Laura Orian, Manjari Bhamidipati, and Laura Fabris. A review on surface-enhanced raman scattering. *Biosensors*, 9(2):57, 2019.

[157] Song-Yuan Ding, En-Ming You, Zhong-Qun Tian, and Martin Moskovits. Electromagnetic theories of surface-enhanced raman spectroscopy. *Chem. Soc. Rev.*, 46(13):4042–4076, 2017.

[158] Eric C Le Ru, Evan Blackie, Matthias Meyer, and Pablo G Etchegoin. Surface enhanced raman scattering enhancement factors: a comprehensive study. *J. Phys. Chem. C*, 111(37):13794–13803, 2007.

[159] Rebecca LM Gieseking, Joonhee Lee, Nicholas Tallarida, Vartkess Ara Apkarian, and George C Schatz. Bias-dependent chemical enhancement and nonclassical stark effect in tip-enhanced raman spectromicroscopy of co-terminated ag tips. *J. Phys. Chem. Lett.*, 9(11):3074–3080, 2018.

[160] Seth M Morton and Lasse Jensen. Understanding the molecule- surface chemical coupling in sers. *J. Am. Chem. Soc.*, 131(11):4090–4098, 2009.

[161] Lasse Jensen, Christine M Aikens, and George C Schatz. Electronic structure methods for studying surface-enhanced raman scattering. *Chem. Soc. Rev.*, 37(5):1061–1073, 2008.

[162] Justin E Moore, Seth M Morton, and Lasse Jensen. Importance of correctly describing charge-transfer excitations for understanding the chemical effect in sers. *J. Phys. Chem. Lett.*, 3(17):2470–2475, 2012.

[163] Won-Hwa Park and Zee Hwan Kim. Charge transfer enhancement in the sers of a single molecule. *Nano Lett.*, 10(10):4040–4048, 2010.

[164] Richard P Van Duyne. Laser excitation of raman scattering from adsorbed molecules on electrode surfaces. *Chemical and biochemical applications of lasers*, 4:101–185, 2012.

[165] Milton Kerker, D-S Wang, and H Chew. Surface enhanced raman scattering (sers) by molecules adsorbed at spherical particles. *Appl. Opt.*, 19(19):3373–3388, 1980.

[166] Xi Ling and Jin Zhang. First-layer effect in graphene-enhanced raman scattering. *Small*, 6(18):2020–2025, 2010.

[167] Shengxi Huang, Xi Ling, Liangbo Liang, Yi Song, Wenjing Fang, Jin Zhang, Jing Kong, Vincent Meunier, and Mildred S Dresselhaus. Molecular selectivity of graphene-enhanced raman scattering. *Nano Lett.*, 15(5):2892–2901, 2015.

[168] Xi Ling, LG Moura, Marcos A Pimenta, and Jin Zhang. Charge-transfer mechanism in graphene-enhanced raman scattering. *J. Phys. Chem. C*, 116(47):25112–25118, 2012.

[169] Xi Ling, Juanxia Wu, Weigao Xu, and Jin Zhang. Probing the effect of molecular orientation on the intensity of chemical enhancement using graphene-enhanced raman spectroscopy. *Small*, 8(9):1365–1372, 2012.

[170] I Mrozek and A Otto. Long and short-range effects in sers from silver. *EPL*, 11(3):243, 1990.

[171] FJ García De Abajo and A Howie. Relativistic electron energy loss and electron-induced photon emission in inhomogeneous dielectrics. *Phys. Rev. Lett.*, 80(23):5180, 1998.

[172] Ulrich Hohenester. Quantum corrected model for plasmonic nanoparticles: A boundary element method implementation. *Phys. Rev. B*, 91(20):205436, 2015.

[173] Jacopo Tomasi, Benedetta Mennucci, and Roberto Cammi. Quantum mechanical continuum solvation models. *Chem. Rev.*, 105(8):2999–3094, 2005.

[174] Alexandre Mayer. Formulation in terms of normalized propagators of a charge-dipole model enabling the calculation of the polarization properties of fullerenes and carbon nanotubes. *Phys. Rev. B*, 75(4):045407, 2007.

[175] Steven W Rick, Steven J Stuart, and Bruce J Berne. Dynamical fluctuating charge force fields: Application to liquid water. *J. Chem. Phys.*, 101(7):6141–6156, 1994.

[176] Tommaso Giovannini, Marta Olszowka, and Chiara Cappelli. Effective fully polarizable qm/mm approach to model vibrational circular dichroism spectra of systems in aqueous solution. *J. Chem. Theory Comput.*, 12(11):5483–5492, 2016.

[177] Tommaso Giovannini, Marta Olszowka, Franco Egidi, James R Cheeseman, Giovanni Scalmani, and Chiara Cappelli. Polarizable embedding approach for the analytical calculation of raman and raman optical activity spectra of solvated systems. *J. Chem. Theory Comput.*, 13(9):4421–4435, 2017.

[178] Tommaso Giovannini, Marina Macchiagodena, Matteo Ambrosetti, Alessandra Puglisi, Piero Lafiosca, Giulia Lo Gerfo, Franco Egidi, and Chiara Cappelli. Simulating vertical excitation energies of solvated dyes: From continuum to polarizable discrete modeling. *Int. J. Quantum Chem.*, 119(1):e25684, 2019.

[179] Tommaso Giovannini, Matteo Ambrosetti, and Chiara Cappelli. A polarizable embedding approach to second harmonic generation (shg) of molecular systems in aqueous solutions. *Theor. Chem. Acc.*, 137(6):1–11, 2018.

[180] Filippo Lipparini, Chiara Cappelli, and Vincenzo Barone. Linear response theory and electronic transition energies for a fully polarizable qm/classical hamiltonian. *J. Chem. Theory Comput.*, 8(11):4153–4165, 2012.

[181] Filippo Lipparini, Chiara Cappelli, Giovanni Scalmani, Nicola De Mitri, and Vincenzo Barone. Analytical first and second derivatives for a fully polarizable qm/classical hamiltonian. *J. Chem. Theory Comput.*, 8(11):4270–4278, 2012.

[182] Filippo Lipparini and Vincenzo Barone. Polarizable force fields and polarizable continuum model: A fluctuating charges/pcm approach. 1. theory and implementation. *J. Chem. Theory Comput.*, 7(11):3711–3724, 2011.

[183] RT Sanderson. An interpretation of bond lengths and a classification of bonds. *Science*, 114(2973):670–672, 1951.

[184] Darrin M York and Weitao Yang. A chemical potential equalization method for molecular simulations. *J. Chem. Phys.*, 104(1):159–172, 1996.

[185] Riccardo Chelli and Piero Procacci. A transferable polarizable electrostatic force field for molecular mechanics based on the chemical potential equalization principle. *J. Chem. Phys.*, 117(20):9175–9189, 2002.

[186] Riccardo Chelli, Vincenzo Schettino, and Piero Procacci. Comparing polarizable force fields to ab initio calculations reveals nonclassical effects in condensed phases. *J. Chem. Phys.*, 122(23):234107, 2005.

[187] A Pinchuk, U Kreibig, and A Hilger. Optical properties of metallic nanoparticles: influence of interface effects and interband transitions. *Surf. Sci.*, 557(1-3):269–280, 2004.

[188] Anatoliy Pinchuk, Gero Von Plessen, and Uwe Kreibig. Influence of interband electronic transitions on the optical absorption in metallic nanoparticles. *J. Phys. D: Appl. Phys.*, 37(22):3133, 2004.

[189] B Balamurugan and Toshiro Maruyama. Evidence of an enhanced interband absorption in au nanoparticles: size-dependent electronic structure and optical properties. *Appl. Phys. Lett.*, 87(14):143105, 2005.

[190] A Liebsch. Surface-plasmon dispersion and size dependence of mie resonance: silver versus simple metals. *Phys. Rev. B*, 48(15):11317, 1993.

[191] Eva Yazmin Santiago, Lucas V Besteiro, Xiang-Tian Kong, Miguel A Correa-Duarte, Zhiming Wang, and Alexander O Govorov. Efficiency of hot-electron generation in plasmonic nanocrystals with complex shapes: surface-induced scattering, hot spots, and interband transitions. *ACS Photonics*, 7(10):2807–2824, 2020.

[192] Tommaso Giovannini, Franco Egidi, and Chiara Cappelli. Theory and algorithms for chiroptical properties and spectroscopies of aqueous systems. *Phys. Chem. Chem. Phys.*, 22(40):22864–22879, 2020.

[193] Luca Nicoli, Tommaso Giovannini, and Chiara Cappelli. Assessing the quality of qm/mm approaches to describe vacuo-to-water solvatochromic shifts. *J. Chem. Phys.*, 157(21):214101, 2022.

[194] Mark E Casida. Time-dependent density functional response theory for molecules. In *Recent Advances In Density Functional Methods: (Part I)*, pages 155–192. World Scientific, 1995.

[195] John A Jaszczak, George W Robinson, Svetlana Dimovski, and Yury Gogotsi. Naturally occurring graphite cones. *Carbon*, 41(11):2085–2092, 2003.

[196] Cheng-Te Lin, Chi-Young Lee, Hsin-Tien Chiu, and Tsung-Shune Chin. Graphene structure in carbon nanocones and nanodiscs. *Langmuir*, 23(26):12806–12810, 2007.

[197] Stine Nalum Naess, Arnljot Elgsaeter, Geir Helgesen, and Kenneth D Knudsen. Carbon nanocones: wall structure and morphology. *Sci. Technol. Adv. Mater.*, 2009.

[198] Natalie Wohner, Pui Lam, and Klaus Sattler. Energetic stability of graphene nanoflakes and nanocones. *Carbon*, 67:721–735, 2014.

[199] Oleg V Yazyev and Steven G Louie. Electronic transport in polycrystalline graphene. *Nat. Mater.*, 9(10):806–809, 2010.

[200] Oleg V Yazyev and Yong P Chen. Polycrystalline graphene and other two-dimensional materials. *Nat. Nanotechnol.*, 9(10):755–767, 2014.

[201] Kwanpyo Kim, Zonghoon Lee, William Regan, C Kisielowski, MF Crommie, and A Zettl. Grain boundary mapping in polycrystalline graphene. *ACS Nano*, 5(3):2142–2146, 2011.

[202] Florian Banhart, Jani Kotakoski, and Arkady V Krasheninnikov. Structural defects in graphene. *ACS Nano*, 5(1):26–41, 2011.

[203] Pinshane Y Huang, Carlos S Ruiz-Vargas, Arend M Van Der Zande, William S Whitney, Mark P Levendorf, Joshua W Kevek, Shivank Garg, Jonathan S Alden, Caleb J Hustedt, Ye Zhu, et al. Grains and grain boundaries in single-layer graphene atomic patchwork quilts. *Nature*, 469(7330):389–392, 2011.

[204] Calin Hrelescu, Tapan K Sau, Andrey L Rogach, Frank Jäckel, and Jochen Feldmann. Single gold nanostars enhance raman scattering. *Appl. Phys. Lett.*, 94(15):153113, 2009.

[205] Feng Hao, Colleen L Nehl, Jason H Hafner, and Peter Nordlander. Plasmon resonances of a gold nanostar. *Nano Lett.*, 7(3):729–732, 2007.

[206] Andrés Guerrero-Martínez, Silvia Barbosa, Isabel Pastoriza-Santos, and Luis M Liz-Marzán. Nanostars shine bright for you: colloidal synthesis, properties and applications of branched metallic nanoparticles. *Curr. Opin. Colloid Interface Sci.*, 16(2):118–127, 2011.

[207] Yoshikazu Ito, Yoichi Tanabe, H-J Qiu, Katsuaki Sugawara, Satoshi Heguri, Ngoc Han Tu, Khuong Kim Huynh, Takeshi Fujita, Takashi Takahashi, Katsumi Tanigaki, et al. High-quality three-dimensional nanoporous graphene. *Angew. Chem.*, 126(19):4922–4926, 2014.

[208] Haibo Huang, Haodong Shi, Pratteek Das, Jieqiong Qin, Yaguang Li, Xiao Wang, Feng Su, Pengchao Wen, Suyuan Li, Pengfei Lu, et al. The chemistry and promising applications of graphene and porous graphene materials. *Adv. Funct. Mater.*, 30(41):1909035, 2020.

[209] Susanna Monti, Giovanni Barcaro, William A Goddard III, and Alessandro Fortunelli. Diverse phases of carbonaceous materials from stochastic simulations. *ACS Nano*, 15(4):6369–6385, 2021.

[210] Niels CH Hesp, Iacopo Torre, Daniel Rodan-Legrain, Pietro Novelli, Yuan Cao, Stephen Carr, Shiang Fang, Petr Stepanov, David Barcons-Ruiz, Hanan Herzig Sheinfux, et al. Observation of interband collective excitations in twisted bilayer graphene. *Nat. Phys.*, 17(10):1162–1168, 2021.